UNIVERSITY OF SILESIA
IN KATOWICE

FACULTY OF SCIENCE AND TECHNOLOGY

INSTITUTE OF CHEMISTRY

Fullerenes – theranostic nanoparticles in anticancer therapy

PhD thesis

Julia Korzuch

Student ID number: 8748

Supervisor: Prof. dr hab. Robert Musioł

Katowice 2025

The work presented in this thesis was carried out within the framework of the research project OPUS 2019/35/B/NZ7/02459, titled:

„The [60]fullerene-based theranostic agent for pancreatic cancers treatment and diagnosis”, funded by

NATIONAL SCIENCE CENTRE
POLAND

Acknowledgements

I would like to express my sincere gratitude to prof. dr hab. Robert Musioł and dr hab. inż. Maciej Serda prof. UŚ for their kindness, commitment, and unwavering support throughout this research and the preparation of this thesis. I am truly grateful for the opportunity to balance science with professional sports. I would also like to thank the “Drug Design and Nanopharmacology” team for their friendly atmosphere, as well as everyone I had the pleasure of collaborating with over the past few years.

Contents

List of Abbreviations and Symbols

Ala - alanine

APOA-1 - apolipoprotein A-1

ASGPR - asialoglycoprotein receptor

AuNPs - gold nanoparticles

BCR - signalling pathway - B cell receptor signalling pathway

Boc - tert-butoxycarbonyl protecting group

BSA - bovine serum albumin

BTK - Burton's tyrosine kinases

BUT - n-butylamine

CT - computed tomography

CRISP - clustered regularly-interspaced short palindromic repeats

DBU - 1,8-Diazabicyclo[5.4.0]undec-7-e

DCC - N,N'-dicyclohexylcarbodiimide

DIC - N,N'-diisopropylcarbodiimide

DCM - dichloromethylene

DOX - doxorubicine

DIPEA - N,N-Diisopropylethylamine

DLS - dynamic light scattering

DMSO - dimetlylsulfoxide

DTPA - diethylenetriamine pentaacetate

ECM - extracellular matrix

EDC - 1-Ethyl-3-(3-dimethylaminopropyl)carbodiimide hydrochloride

EDS - energy-dispersive spectroscopy

eGFP - enhanced green fluorescent protein

EFGR - epidermal grow factor receptor

EPR - enhanced paermability and retention effect (also electron paramagnetic resonance)

ERL - erlotinib

FDA - Food and Drug Agency

^{18}F-FDG - iludeoxyglucose

GalNac - N-Acetylgalactosamine

Gem - gemcitabine

GLUT 1 - glucose 1 transporter

GO - graphene oxide

HDAC 1 - histone deacetylase 1

HDGF - hexakis-diglycinemethanofullerene

HIF 1α - hypoxia-inducible factor

HoBt - 1-hydroxybenzotriazole

HOMO - highest occupied molecular orbital

HBA - human serum albumin

HSA - human serum albumin

HCuS - hollow copper sulphide

HMDPA - hollow mesoporous polydopamine

IBR - ibrutinib

ICG - indocyanine green

IONPs - iron oxide nanoparticles

IPR - isolated pentagonal rule

ISC - intersystem crossing

LUMO - lowest occupied molecular orbital

MAPK - mitogen-activated protein kinases

MDR - multidrug resistance

MMP - matrix metalloproteinases

MPA - main pulmonary artery

MPI - magnetic particle imaging

MPS - mononuclear phagocytic system

MRI - magnetic resonance imaging

MYH9 - myosin heavy chain

NHS - N- hydroxysuccinimide

NIR - near-infrared

NPs - nanoparticles

NSCLC - non-small cell lung cancer

PAI - photoacoustic imaging

PDAC – pancreatic ductal adenocarcinoma

PDT - photodynamic therapy

PEG - polyethylene glycol

PEI - polyethylene diamine

PET - positron emission tomography

PI3K - phosphoinositide 3-kinase

PS - photosensitiser

PTT - photothermal terapy

P@ - pheophorbide-a

RES - reticuloendothelial system

RGD - arginyl-glycyl-aspartic acid

RISC - RNA-induced silencing complex

RNAi - RNA interference

ROS - reactive oxygen species

SA - sialic acid

SEM - Scanning Electron Microscopy

SC-5 - sulfo Cyanine5

SPECT - single-photon emission computed tomography

SR-BI - scavenger receptor class B type I

SWCNT - single-walled carbon nanotube

TAM - tumour associated macrophage

TEM - transmission electron microscopy

TME - tumour microenvironment

TPFE - tetra(piperazino)fullerene epoxide

UI - ultrasound imaging

VDA - vascular disrupting agent

XPS - X-ray photoelectron spectroscopy

5-FU - 5-fluorouracil

Introduction

Nanoparticles in cancer therapy

For over three decades, scientific attention has been focused on using the potential of nanotechnology in oncology medicine. Small particles with a size controlled at the nanometer scale have been engineered to direct medicine towards higher precision for both early diagnosis and treatment. New nanomaterials for drugs and nucleic acid transport, bioimaging and photothermal or photodynamic therapy have been investigated[1-4]. Moreover, theranostic particles have been designed to simultaneously perform therapeutic and diagnostic functions[5-7]. Conventional methods like chemo-, radiotherapy, and surgical resection of tumours have limited efficacy for malignant cancers in the progressed stadium. Even immunotherapy, a turning point in advanced cases, is struggling with poor patient responses[8]. Both mentioned methods are non-targeted cancer therapies and eliminate cancer cells at the expense of normal cells, causing unpleasant or sometimes fatal side effects[1,9]. Besides monoclonal antibodies, gene innovative modalities like iRNA and CRISPR, although they provide a significant breakthrough in some diseases, have not been applied against cancer yet[10-12]. The systems for precise drug delivery to the cancer environment, capable of selective recognition of cancer tissue, specifically the cancer cell or subcellular site of action, are still being investigated[13-15]. For this purpose, it is essential to broaden the knowledge about differences between cancer cells and normal cells on the molecular levels and the cross-correlation between them.

Until 2023, the Food and Drug Agency (FDA) had accepted at least fifteen nanotherapeutics for cancer treatment to be used globally[1,16]. The subsequent eighty are being investigated in clinical trials. The broadest group is represented by nanodelivery systems, including medicines accepted before with polimiceles, dendrimers, liposomes and other transport-facilitating particles (Lipo-DOX, Nanoxel, Abraxane, Onivyde) as well as platforms with controlled drug release systems (Eligard, Genexol-PM)[1,17,18]. Recent advances significantly improved therapeutic efficacy and reduced off-target toxicity by changing the drug's pharmacokinetics, bioavailability and biodistribution. Essentially, all the enhancements refer to increasing the solubility of existing drugs, prolonging their retention times, plasma circulation half-life and enhanced tumour accumulation thanks to invented nanoplatforms[9,13,14].

Targeted drug delivery to tumour tissue may occur through two mechanisms. Passive targeting uses a unique phenomenon known as the Enhanced Permeability and Retention (EPR) effect[18,19]. Nanotherapeutic could accumulate nearby tumours thanks to leaky blood vessels produced during angiogenesis. The lymphatic system cannot drain tumoral fluids, thus facilitating medicine retention. The optimal size of nanoparticles for EPR-mediated tumour targeting ranking from 50-150 nm[19]. Except for NPs physiochemical properties, the efficacy of passive targeting depends on factors like the extent of vascular and lymphatic vessel generation, perivascular tumour invasion, and intra-tumour pressure. Nearly all the nanomedicines approved for clinical use can employ EPR to reach the tumour site. However, utilizing this effect remains constrained by interpatient and intratumoural heterogeneity[20]. Concerning these limitations, the emphasis was on a more pragmatic approach, like active targeting. The second generation is represented by particles functionalised by targeting moieties, including antibodies, nucleic acids, aptamers, peptides, carbohydrates, and small particles that bind specific antigens or receptors expressed on the cell membrane[1,13,21]. The multiple nanoparticles conjugated with actively targeted medicines like cetuximab, erlotinib, and afatinib were developed to act more selectively on kinase receptors that are overexpressed in cancer cells[22]. The biomimetic strategies based on covering the NPs by the plasma membrane of cancer cells or stem cells are also evaluated[23-26]. Following the introduction of cancer cells, the NPs must be directed accurately to the side of action mainly localized in the nucleus, mitochondria and lysosomes. Organelle-targeted NPs are considered to be the third generation of nanoparticles[27].

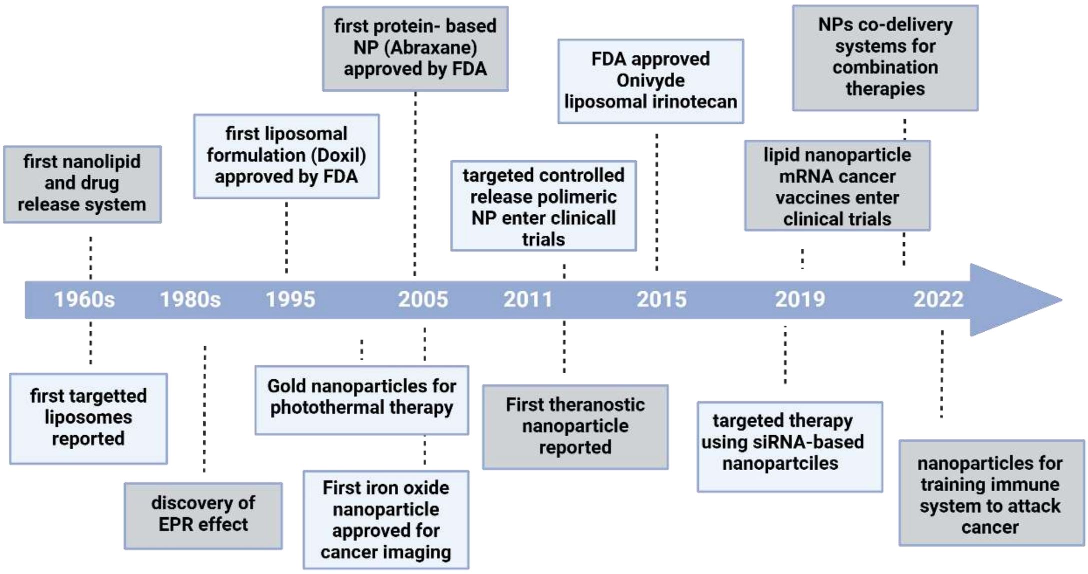

Fig 1. The timeline of progression in cancer nanotherapy[1]

To pursue their destination, nanoparticles must cross several physiological barriers, including travelling in the bloodstream and extravasate to the tumour microenvironment, binding to the target on the tumour cells, internalising into the intracellular compartment, and performing their action[19]. Parameters like shape, size, charge, surface modifications, and biocompatibility directly influence the outcomes of the journey[28,29]. The positive charge on the nanoparticle surface promotes NPs uptake by negatively charged phospholipids on the cell membranes and the endosomal escape through the proton sponge effect. It is also connected with fast clearance due to interaction with the mononuclear phagocytic system (MPS) or reticuloendothelial system (RES) and cellular uptake rates. The anionic particles have longer circulation times and enhanced tumour accumulation[30,31]. The perfect situation assumes NPs' slightly negative or neutral charge at the beginning in the bloodstream and switches the charge to positive after reaching the tumour environment. Optimising the interplay of nanomaterials with biological systems through property modification is one of the most significant opportunities that nanomedicine presents[1]. The standard strategy to prolong the circulation time and retard RES clearance of positively charged nanoparticles is to cover them with polyethene glycol (PEG). PEG-ylated liposomes are the nanoplatforms employed in Doxil and Oncospar[32]. Recently, charge reversal systems have been developed. The disconnection of the PEG corona and the ligand exposition occurs near the tumour site. The trigger for releasing the polymer fragment is usually the pH change to more acidic or tumour-overexpressed enzymes like matrix metalloproteinases. Thereby, using alterations of the tumour microenvironment (acidic pH, hypoxic conditions, an altered redox environment, and elevated level of reactive oxygen species), size and charge switchable particles or controlled release systems are engineered, representing the potential of stimuli-responsive nanomedicine[33,34].

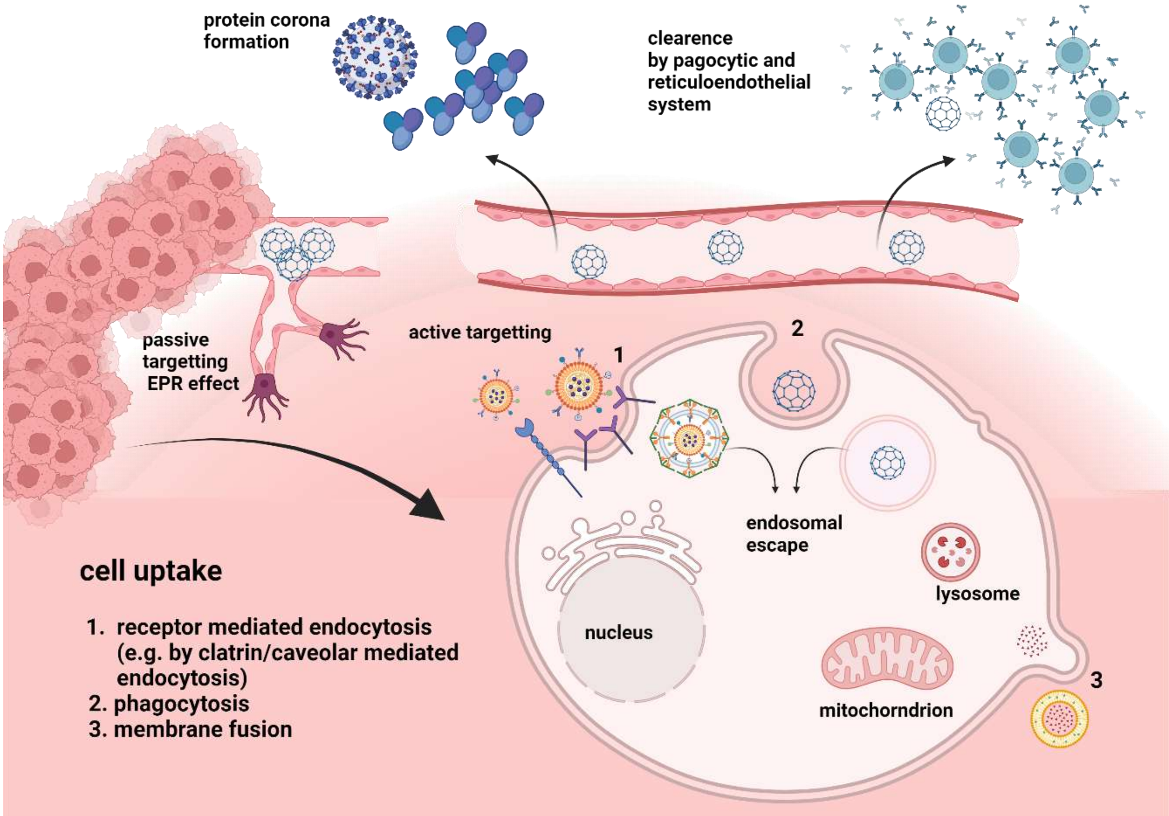

Fig. 2. Nanomedicine journey.

The heterogeneous nature of cancer often makes a single therapeutic approach insufficient. For example, the dense stroma hampers medicine accumulation in the tumour site of pancreatic cancer.[35] Moreover, cancer cells may develop resistance to the medicine treatment (MDR – multidrug resistance) or create hypoxic conditions to disable photodynamic therapy. Biological diversity requires a variety of therapeutic approaches. Nanoplatforms offer the possibility to combine targeting delivery with other therapeutic strategies, which have to overcome physiological barriers, improve the drug's efficacy and decrease side effects[35,36]. Over the past decade, research has shown that tumour microenvironment (TME) plays a crucial role in cancer formation and treatment resistance, making it an important target. Cancer is not a simply localized disease but forms a complex adaptive system involving inflammation, metabolism, and genetics tangled with each other. Novel therapeutic strategies involve targeting tumour microenvironment's related targets like tumour immunosuppressive components, cancer-associated fibroblasts, tumour extracellular matrix or vasculature[37].

Using vascular disrupting agents (VDAs) to restrict blood flow to the tumour is a practical technique for tackling tumour growth. The NIR-laser-activated "nanobomb" consisting of vinyl azide enclosed in peptide-functionalised, hollow copper sulfide (HCuS) nanoparticles targeting $\alpha_v\beta_3$ integrin has been "armed" by Gao et al. Upon the signal, N_2 is released and destroys angiogenic vessels and surrounding tumour tissue. Photoacoustic angiography in vivo enables precise detonation[38]. Another strategy involves a drug delivery system based on gold nanoparticles combined with the vascular angiogenesis-inhibitor, used to treat non-small cell lung cancer and normalize the tumour vascular system. Combining this therapy with 5-fluorouracil (5-FU) results in better accumulation of the chemotherapeutic agent in the tumour site, thus improving treatment effectiveness[39].

The rapid growth of cancer cells and the associated neovascularisation cause insufficient oxygen delivery and an acidic pH in the tumour microenvironment. These conditions can enhance tumour angiogenesis and metastasis, leading to therapeutic resistance and treatment failure, particularly photodynamic therapy. Chen et al. designed a pH/H_2O_2-responsive nanodelivery system using albumin-decorated MnO_2. Nanoparticulated MnO_2 interacts with hydrogen peroxide to alleviate hypoxia. Albumin was conjugated with the photosensitiser or the pro-drug of cis-platinum, which activates in a reductive environment. This approach enhances the effectiveness of chemotherapy and PDT by increasing oxygen levels in hypoxic tumour areas[40].

Bruton's tyrosine kinases are nonreceptor tyrosine kinases expressed in B-cells, myeloid cells and tumour-associated macrophages. BTK plays an essential role in antigen-dependent BCR signalling pathway, regulating B cell proliferation and survival, participates in antigen-independent Toll-like receptor and chemokine receptor signalling pathway, regulating B cell adhesion, migration, and tumour microenvironment. Aberrant signalling of the B-cell receptor pathway is responsible for the aetiology of B-cell malignancies, making it one of the therapeutic targets. BTK is also expressed in tumour-associated macrophages. Developing a strategy to inhibit BTK is critical for eliminating TAM-induced immunosuppression and establishing persistent antitumour immunity. Ibrutinib (IBR), the first irreversible, small-molecule BTK inhibitor, has shown therapeutic effects in patients with B-cell lymphoma and possesses anticancer mechanisms that reduce macrophage contribution to cancer cell proliferation and survival. However, Ibrutinib has a short circulation time, resulting in poor tumour accumulation and limited therapeutic efficacy in solid tumours. A strategy to improve Ibrutinib's pharmacokinetics was presented by Quijun et al., involving conjugation with sialic acid-based nanocomposite. His research resulted in the effective infiltration of macrophages and inhibition of BTK with minimal side effects[41].

Except for constantly improved delivery systems, nanoparticles are applicable in molecular imaging using modern imaging techniques like magnetic resonance imaging (MRI), Computed Tomography (CT), Ultrasound Imaging (UI), Positron Emission Tomography (PET), Single-Photon Emission Computed Tomography (SPECT), Photoacoustic Imaging (PAI)[42-44]. Each imaging modality has its advantages and limitations, and the choice of technique depends on various factors, including tissue characteristics. For example, optical bioluminescence and fluorescence imaging are highly sensitive methods but have limited tissue penetration. In contrast, SPECT and PET have no tissue penetration limit but exhibit low spatial resolution. MRI and CT offer high spatial resolution but low sensitivity. To meet all the requirements for in vivo bioimaging, multimodal imaging strategies have been developed. These systems can assess disease stages, detect metastasis, and predict treatment response. Due to their exceptional sensitivity and resolution, multimodal imaging techniques are powerful diagnostic tools that can detect early disease symptoms (e.g., specific biomarkers), enhance targeted therapy, and significantly advance personalized medicine. In this area, gold nanoparticles (AuNPs), iron oxide nanoparticles (IONPs), and carbon nanoparticles prevailed due to their optical or paramagnetic properties, which are suitable for the above techniques[36]. Imaging agents based on these nanoparticles have already been employed clinically to complement diagnostics, for example, as a guide for surgical tumour resection and improved radiation-based treatment methods (Lymphoseek^{TM}, Nanocoll) and for improving existing therapy - NanoTherm (iron oxide nanoparticles for thermal ablation responsive to quickly-changing electromagnetic field) and AuroLase (gold nanoshells for thermal ablation under NIR laser illumination)[17,45,46]. Iron oxide nanoparticles additionally have been clinically approved as MRI contrast agents - Feridex, Resovist, Combidex, Gastromark, and Feraheme[47]. However, the first one was removed from the market in relation to safety issues.

Until today, only PET-CT multimodal techniques have been clinically effective. Unak et al. conjugated AuNPs with ^{18}F-FDG antibody specifically targeted breast cancer cells and obtained nanoplatforms for PET-CT multimodal imaging that collect information about glucose metabolism, which higher uptake is characteristic for cancer cells[48]. The dual modalities, such as MRI-optical, MRI-PET/SPECT, MRI-CT, MRI-MPI, and MRI-MPA, are still in the preclinical phases and have shown encouraging results[43].

The dual-modality system based on IONP nanoparticles has been presented by Hen et al. to detect small tumours in preoperative diagnosis. They encapsulated superparamagnetic iron oxide nanoparticles (SPIONs) in liposomes containing PEG, a tumour-targeted peptide (RGD sequence), and indocyanine green (ICG) - the only NIR dye approved by the FDA in the United States for clinical usage. The hybrid nanosystem was able to detect small tumours using the MRI approach. In addition, active targeting and a prolonged clearance rate enabled fluorescence imaging to detect considerably smaller tumour metastatic lesions[49].

MRI-PET diagnosis system has been used by Lee et al. for tumour detection *in vitro* and in vivo. Polyaspartic acid coated IONPs nanoplatform was combined with a ^{64}Cu radionuclide (for PET imaging) through a DOTA chelator and conjugated with arginine–glycine–aspartic (RGD) peptide targeting agent. Nanoparticle targeted tumours with integrin $\alpha_v\beta_3$ expression demonstrating their relevance for accurate tumour identification using dual-imaging methods[50]. One of the most significant benefits of MRI-PET is the high contrast of soft tissue provided by MRI, which, alongside the sensitivity of PET, can be highly beneficial in the assessment and biopsy planning of primary tumours such as those in the prostate, lung, or breast. The radiation dose is lower than for CT-PET[51].

The primary obstacle in translating nanoparticles for clinical application is their behaviour under physiological conditions. Opsonization and protein corona formation, for instance, impact the biodistribution of nanoparticles[52,53]. To gain better insights into the nanoparticle behaviour in response to physiological processes, nanodelivery platforms have been adjusted to adopt at least one of the imaging techniques. This solution allows to understand the kinetics of the drug, which is altered depending on the tumour environment. Based on these findings, the physicochemical properties of the nanoparticle can be modulated to achieve favourable outcomes[54]. Personalized therapy concerning personal differences in cancer characteristics is required if maximal efficacy is an aim. Simultaneous targeted delivery, diagnosis, and treatment monitoring allow for capturing these deviations and improving therapeutic response with minimal side effects. Although multifunctional platforms should increase therapeutic potential, it is essential to consider that every functionalisation may influence system pharmacokinetics, including delivered medicine, which should be regarded during synthesis planning. Nanoparticles engineered as theranostic agents, including liposomes, polymeric nanoparticles, and protein nanoparticles, are already in phase II clinical trials[5]. New strategies are still being developed; here are a few examples: Li et al. performed real-time monitoring of siRNA-loaded lipid-polymer nanoparticles with NIR fluorescent core and ApoA-1 mimetic peptide for natural targeting in an orthotropic prostate tumour model. The targeting specificity was confirmed only in malignant cells with SR-BI protein expression, and the effective gene knockdown was observed. The image co-registration of in vivo fluorescent molecular tomography with computed tomography (CT) affords a non-invasive technique to examine the selectivity and efficiency of siRNA administration in tumour[55]. In another study Yu et al. created P@-Gem-HSA (human serum albumin) nanoparticles loaded with gemcitabine and pheophorbide-a (P@) – a chlorophyll-related photosynthesiser to treat lymphatic PDAC metastases. This system allows for tracking the delivery of gemcitabine and provides synergistic PDT efficacy (Gem, @P) and chemotherapy (Gem)[56].

Nanomaterials that already display imaging possibilities are suitable for theranostic materials as they do not require to be loaded with imaging agents. The gold and iron oxide nanoparticles have already been approved for cancer diagnosis, which may speed up the translational process[5]. Based on iron oxide nanoparticles, a theranostic, tumour-targeted siRNA vector was designed to fight against cell cycle-specific serine-threonine-kinase and Polo-like kinase-1. In vivo, tumour growth was monitored by MRI on small animal models. The accumulation in PDAC cells and in vivo and *in vitro* gene silencing efficacy was confirmed, followed by tumour growth inhibition and increased apoptosis[57].

Maesoporus-based theranostic agent, including doxorubicin, iron superoxide SPION for MRI imaging and sialic acid as targeting agent (DOX)-loaded SAPEG-MPDA@SPIO/Fe^{3+}), was tested against hepatic cancer and for dual magnetic resonance imaging (MRI-guided cancer chemo-photothermal therapy). Nanoparticles effectively encapsulated chemotherapeutic agents and performed dual-triggered release (pH and temperature). This proposed theranostic agent possessed excellent photothermal conversion capability, photostability and relaxivity (contrasting sensitivity) values compared to clinically used contrast agents. MRI visualisation in vivo displayed NPs accumulation only in hepatic cells with E-selectin overexpression. Combining therapy revealed higher efficacy than separate chemotherapy with DOX or photothermal therapy with SAPEG-MPDA@SPIO/Fe^{3+} [58].

Li et al. presented hollow mesoporous polydopamine (HMPDA) microcapsules modified with gold (Au) nanoparticles (NPs) as photothermal-responsive nanodrug carriers. This nanocomplex synergizes photothermal therapy with doxorubicin delivery. Such therapeutic approach is characterized by high photothermal conversion efficiency, strong loading capacity and release system responsive to the acidic pH of the tumour environment or NIR laser irradiation (800 nm). *In vitro* cytotoxicity experiments showed a more robust inhibitory effect on tumour cells (the cell survival rate was reduced to nearly 20%) than healthy ones (80%)[59].

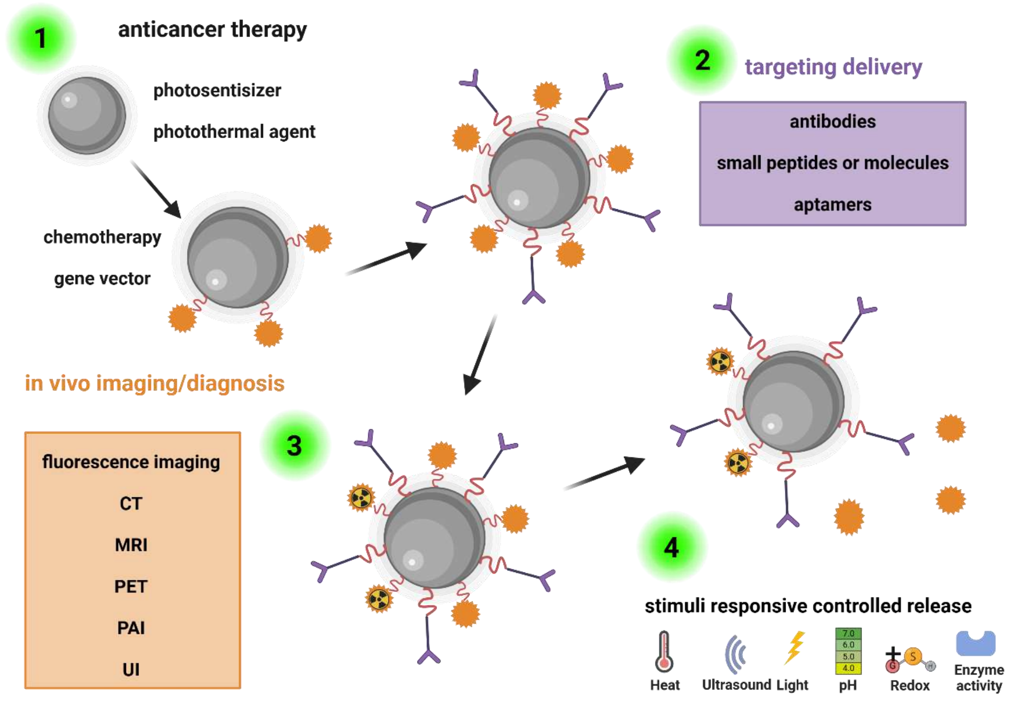

Fig. 3. Theranostic nanoparticles engineering. 1 - attaching the therapeutic agent, 2 - functionalisation with targeting moiety, 3 - linking with bioimaging fragment (if required) or specific antennae to improve visualisation, 4 - stimuli responsive releasing of the drug.

Carbon nanoparticles, including graphene oxide (GO) and single-walled carbon nanotubes (SWCNTs), have optical properties required for PET, SPECT or PAI imaging. The drug loading capacity and modification potential allowed the development of multimodal imaging and multifunctional therapy nanosystems as they perform characteristics for both PDT and PTT[60]. Yang et al. functionalised SWCNTs with polyethylene glycol (PEG) and poliethylenamine (PEI) and evaluated this nanocarrier for drug loading capacity, *in vitro* release and killing MCF-7 cells effectively[61]. Guo et al. presented a new platform consisting of graphene-oxide with PEGylated and oxidised sodium alginate, which was employed to load the anticancer agent paclitaxel with additional suppression of drug resistance to this chemotherapeutic by a synergistic PTT/PDT impact. This conjugated system achieved better therapeutic efficacy on paclitaxel-resistant gastric cancer cells[62].

Among numerous designed nanotherapeutic agents facing challenges, carbon nanoparticles remain an alternative to be used as one of them in the future. They represent an excellent platform for chemical modifications with prospective applications in nanomedicine. Due to a wide range of synthetic possibilities, they can combine delivery and imaging strategies and photodynamic potential. However, a broader knowledge of their behaviour in the physiological environment is still needed. Currently, two carbon-based nanoparticles are in phase III of clinical trials (NCT02123407, NCT06791005)[63]. They are tested for lymph node staining, which allows tracking of tumour metastasis and provides valuable information on treatment efficacy.

Fullerenes

The uniqueness of fullerenes among nanotherapeutics lies in their multifunctionality stemming from inherent susceptibility to chemical modifications and optical characteristics. The fullerene cage serves as an excellent, tunable nanoplatform while also exhibiting its own intrinsic therapeutic potential. Moreover, the metal ions inside metallofullerenes enable particle imaging and play a key role in designing multimodal diagnosis systems. Thus, fullerenes represent three-dimensional platforms where both internal and external modifications can further enhance their medical applications.

Fullerenes are spherical particles, one of the most fundamental allotropic forms of carbon, along with graphite, diamond, graphene[64] and nanotubes[65]. Their discovery is attributed to Kroto, Smalley and Curl in 1985, who were honoured with the Nobel Prize for this discovery[66]. Carbon has a particular property: in high temperatures, where other molecules become one or two atomic, it begins to form multiatomic clusters. The chemical characteristics and reactivity of a 60-atomic carbon cluster produced by condensate carbon steam after laser sublimation of graphite ruled out a planar shape. Based on Eurler's theory of pentagons, Kroto, Curl, and Smalley concluded that it must be a closed structure. Fullerene was named after the architect Buckminster Fuller, who created a geodesic dome with that shape several years before[67,68]. The unique symmetry and properties of fullerenes have aroused interest in many areas of science, including photovoltaic, nanomedicine and optics[69,70,71-74].

Structure of fullerenes

The fullerene cage is formed by carbon atoms shaped into pentagonal and hexagonal rings[68,75]. According to Euler's theory, pentagonal rings are required to introduce curvature to the carbon network - the net containing only hexagonal rings is planar. The isolated pentagonal rule (IPR) must be fulfilled to maintain particle stability[76,77]. It implies that the pentagonals cannot remain in a close neighbourhood and are separated by hexagonals. The smallest fullerene particles that adhered to this principle are C_{60} and C_{70}. The member of the fullerene family with the lowest carbon number, C_{20}, does not meet the IPR theory, and his lifetime is very short – 0,4 ms[78]. In C_{60} fullerene, twelve pentagon rings are surrounded by twenty hexagon rings. C_{70} fullerene contains 12 pentagonal rings and 25 hexagonal rings. Except for the fact that C_{70} adheres to the pentagonal rule, the magical numbers ensure its stability[68,79].

C_{60} fullerene contains two bound types – single with 0,144 nm length between hexagonal and pentagonal rings and double with 0,139 nm between two hexagonal rings. All carbon atoms are equivalent and connected with neighbours with two longer and one shorter bound are sp^2. The other 60 π electrons create resonance structures[80]. The C_{70} molecule consists of eight types of bonds. The structure is tightening up on the equator due to the curvature of hexagon rings called "melted" hexagons. Five bounds around the equator are not in the direct surroundings of pentagons[79].

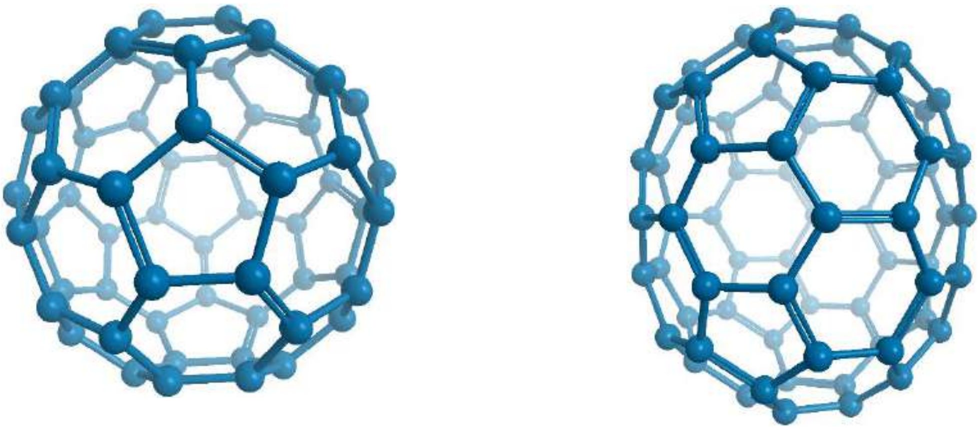

Fig. 4. The C_{60} and C_{70} fullerene structure.

Fullerenes, despite their spherical shape, can be regarded as three-dimensional analogues of benzene and other planar aromatic compounds. Initially, it was thought that in C_{60} fullerene π electrons are strongly delocalized, which makes particles superaromatic[81]. However, an aberration from planarity affects rehybridizing the sp^2 s and p orbitals, while only the pure p orbitals appear for strictly planar conditions[82,83]. As mentioned, the C_{60} fullerenes have two types of bounds with different lengths. The [6,6] bond is shorter and has the property of a double bond, while the single [5,6] bond is formed at the edge of the contact between hexagonal and pentagonal rings. In this regard, the fullerene ball is created by [5]-radialene and 1,2,3-cyclohexatriens. They are conjugated molecules with completely localized double bonds. The ring currents from π electrons in hexagonal rings are responsible for diamagnetic properties, while the currents from pentagonal rings correspond to paramagnetic behaviour. In C_{60}, both currents are almost cancelling out each other. The uncompensated ones determine the weak magnetic susceptibility of fullerene. The C_{70} exhibit more aromatic character due to a more significant number of hexagonal rings, which leads to increased diamagnetic ring currents[84,85].

Reactivity of fullerenes

Contrary to planar aromatics, fullerenes conjugated p-system has no hydrogens that can be replaced via substitution reactions. As a result, these chemical compounds' reactivity is substantially different from classical aromatics. The chemical behaviour of fullerenes is considered shape-dependent as the sphericity excludes aromaticity and causes the pyramidalization of carbon atoms. Consequently, a closed fullerene cage is responsible for solid tensions of energy 484 kJ/mol, and the molecule is determined to eliminate these tensions. Therefore, fullerenes act similarly to alkenes and arenes and undergo nucleophilic reactions with the centres at [6,6] double bonds. Theoretically, the four positions are possible for monofunctionalised fullerenes: [5,6]-open, [5,6]-closed, [6,6]-open and [6,6]-closed. However, thermodynamically, the most stable is [6,6] isomer due to maintaining energetically beneficial energy levels[85]. The most common reactions on the fullerene cage include dehydrogenation, hydroxylation, and cycloadditions like Diels-Alder, Friedel-Crafts, Bingel-Hirsch and Prato. In cycloaddition reactions [6,6], double bonds act like dienophiles. Almost every functional group can be attached to a fullerene cage via cycloaddition reactions of appropriate compounds. For biological applications, stable, nontoxic, water-soluble fullerene derivatives are desired. The primary goal is to provide practical and facile approaches for organic modification, preferably with high yields and mild conditions. Fullerenes are also prone to radical addition - they act like a sponge for free radicals, which can be attached to 30 double bounds of C_{60}. C_{60} and C_{70} undergo nucleophilic reduction and collect electrons from nucleophiles. The reduction reactions of fullerenes are also a strain relief process since the formed carbanions prefer pyramidalized geometry. Addition and redox reactions generate exohedral adducts and salts. Subsequent transformations of particular adducts open the path for various fullerene derivatives[84].

During my work I was focused on functionalising the fullerene cage and providing its solubility in polar solvents for enabling interactions with biological environment. For this purpose, I decided to use an optimise Bingel-Hirsch reaction and amination.

Bingel- Hirsch reaction

From a variety of cycloaddition reactions ([2+n] (n=1,2,3,4)), the [2+1] cyclopropanations, which incorporate three-membered rings into a fullerene cage, are one of the most popular functionalisation procedures[85]. Between them, the Bingel reaction stands out as the efficient method of obtaining methanofullerenes. The mechanism consists of deprotonating the malonate's α-halogen derivative by a base and forming an anion, which attacks [6,6] the double bond of fullerene and creates carbanion. Carbanion reacts with malonate derivative according to nucleophilic substitution, cyclization, and methanofullerene formation. The one-pot version of Bingel-Hirsch reaction requires the presence of generated in situ diethyl bromomalonate with a non-nucleophilic base[86]. The process is simple, takes place under mild conditions and generates relatively high yields. As a result, one to six malonates could attach. The required time of reaction increases with the level of substitution. In the Bingel-Hirsch reaction, only monoadduct and octahedral hexakis adducts of C_{60} fullerene exist in one isomer form. The remaining adducts (bis, tris, etc.) create isomeric mixtures. For biological purposes, one stable isomeric form is necessary.

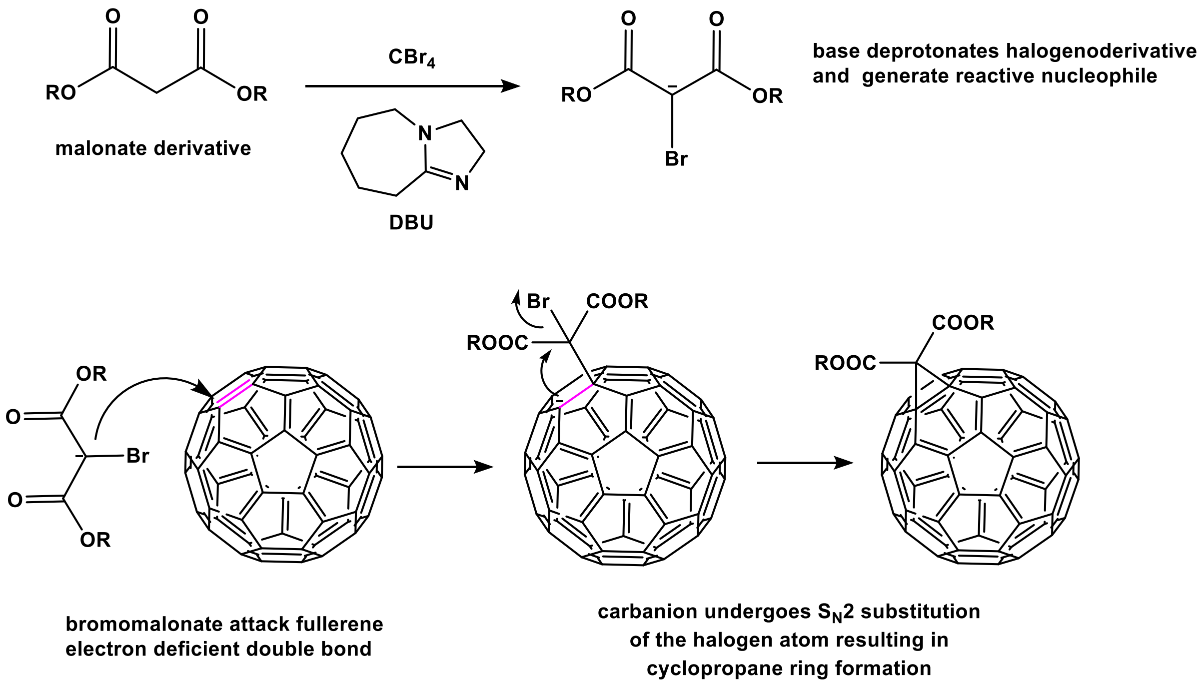

Fig. 5. Bingel-Hirsch reaction mechanism[85].

The functionalisation of fullerene results in the breakup of its conjugated π system, which causes changes in fullerene's ability to oxidation and reduction. The number of substituents increases the particle's reduction potentials. The disturbance of the π-electron system affects the UV-VIS spectrum and the reactivity against nucleophiles. Nevertheless, the substituents' character is irrelevant to the electronic properties of the fullerene cage due to sp^3 carbon in the methylene bridge acting as an isolator[87].

Addition of amines

The nucleophilic character of primary and secondary amines allows them to undergo nucleophilic addition with electron-poor fullerene. The mechanism of the reaction is based on electron transfer from amine to C_{60} followed by recombination of C_{60} radical anion. The created zwitterion could be stabilized by proton transfer from amine to C_{60}

or oxidation succeeded by radical recombination. The resultant aminofullerenes are therefore generated through a complex, mostly unknown sequence of radical recombination, deprotonation, and redox processes[88,89].

The regiochemistry of this reaction complies with nucleophilic addition rules, where the most preferable positions are [6,6] double bonds. The addition of subsequent ligands occurs in the 1,2 position unless there is a steric hindrance. The other available positions are 1,4 and 1,16[84].

Metallofullerenes

The hollowed fullerene cage can entrap atoms inside, thus creating endohedral complexes. The most abundant endohedral fullerene is not Me@C_{60} but Me@C_{82}, since the encapsulated metal atom influences the fullerene electron structure. The high formal charge of metal and strong interactions with metal-fullerene violate the IPR principle - hexagons don't need to surround pentagonal rings to provide a stabilized structure[90]. The coordinate metal ion is usually not in the middle of the fullerene cage but closer to the shell, which can affect ligands distribution during addition reactions. As the charge of the metal is positive the fullerene cage becomes anionic. The endohedral complexes are an example of permanent ion pairs, which cannot separate without breaking up the whole system - in this case, a fullerene cage - which is not achievable under physiological conditions.

One of the most explored endohedral fullerenes is Gd@C_{82} due to its potential for magnetic resonance application. Gadofullerenes exhibit remarkably high proton relaxivity, owning seven unpaired 4f Gd electrons delocalized on the fullerene cage's surface and long electron-spin relaxation time. Proton relaxivity values exceed the gadolinium chelate-based products and the commercially available Gd-DTPA (Magnevist^{TM}), allowing a lower contrast agent dose[91]. Most significantly, the carbon cage isolates the gadolinium metal from the biological environment, avoiding the release of hazardous Gd ions in vivo and resulting in negligible toxicity, even at high concentrations. The modification of metallofullerene with functional groups like hydroxyl, amines, and carboxyl provides water solubility. The electron transfer from gadolinium to carbon cage induces charge alteration, which influences interactions with the biological environment, including functional groups of proteins[91,92]

Fullerenes application in cancer nanomedicine

The optical properties of fullerenes and their synthetic potential create the path for application in photodynamic therapy and delivery platforms. The characteristics of fullerene particles in these roles will be presented below. The behaviour in the biological environment and possible interactions with molecular, cancer-related targets will be described.

Fullerenes for photodynamic therapy

Photodynamic therapy is an alternative method for cancer treatment based on selective photoactivation of photosensitiser (PS), resulting in the generation of cytotoxic agents[93,94]. The photochemical reaction requires the simultaneous presence of three factors: photosensitiser, oxygen and light. Upon internalisation, the PS accumulates in the affected area and becomes activated when exposed to light of a particular wavelength. This activation generates reactive oxygen species, causing oxidative stress, destroying cell membranes, and leading to cell death through apoptosis, necrosis, or autophagy. Furthermore, new pathways for damaging angiogenic blood vessels and activating immunogenic responses may arise as a complementary response to PDT therapy. Because none of the applied factors is individually toxic and reactive oxygen species with a short lifetime are generated only in illuminated areas, the phototoxic effect is time- and spatially-limited, making the therapy exceptionally efficient and precise. It should be noted that the ROS selectivity is not restricted to the pathological cells but implies the relative accumulation of PS in cancer tissue and selective photoactivation[95,96].

The earliest chemical compounds used as photosensitisers were haematoporphyrins illuminated with red light[97]. The presence of a long-lived triplet state, caused by intersystem crossing from an excited state when the particle absorbs a photon, has been determined to be a fundamental property of dyads. The second generation of photosensitisers includes porphyrins and phthalocyanines, which are non-toxic in darkness and absorb in the near-infrared (NIR) region. The third generation continues to enhance PS specificity against cancer cells and improve NIR absorption. Currently, agents like Photofrin, Levulan, Foscan, and Fotolon are used in clinical treatments[95,98].

The molecular oxygen ground state is a triplet state with two unpaired electrons with opposite spins, which leads to the following values of quantum number $I = ½+½ = 1$[99]. According to quantum mechanics, a particle with integer spin 1 exhibits three orientations relative to an external magnetic field, corresponding to three energy levels. To achieve complete reduction, oxygen must absorb 2x2 electrons with spins antiparallel to its own. Since most biological particles exist in the singlet state, oxygen's reactivity in this environment is limited.

Following light absorption at the specific wavelength, the photosensitiser particle is excited to an unstable singlet state with a short lifetime[95]. The release of energy can be achieved in three ways[100]. The particle can return to the ground state by fluorescence with an excess energy emission. In intramolecular conversion, molecules can release energy radiationlessly through interactions with surrounding molecules. Alternatively, the intersystem crossing (ISC) into an excited triplet state is possible. The multiplicity change occurs during this transition, rendering this process prohibited and, therefore, very unlikely. The ISC is more probable to happen when the band gap between the HOMO and LUMO orbitals is low or when the states are intercrossing. A long-life triplet state increases the probability of exploiting the energy. The particle can revert to its ground state through phosphorescence.

There are two classes of photochemical reactions[100]. In the first type, the particles in the triplet state react directly with the environment, transfer the electron to the surrounding organelles or tissues, and generate mainly hydroxyl radicals and superoxide anions. The second type applies to transferring the energy directly to the oxygen particle, leading to singlet oxygen generation. Singlet oxygen is highly reactive and can oxide lipids, proteins and nucleic acids, but importantly, it destroys tissues only in close proximity.

The perfect photosensitiser should comply with followed characteristics[101]:

- Generates high concentrations of ROS upon irradiation to induce targeted cell death.
- Exhibit low cytotoxicity in the darkness, good photostability and high quantum yield of the triplet state.
- Absorb in the optical window, which allows for better tissue penetration.
- Have a high absorption band to minimise the photosensitiser dose.
- Provide imaging contrast for biodistribution monitoring.
- Display intrinsic fluorescence for detection using optical imaging techniques.

Fullerenes display features that characterise good photosensitisers[102,103,104]. They are not cytotoxic in the dark and have good photostability as well as high resistance to photobleaching. The low-lying triply degenerate LUMO orbital of fullerene molecule can exist for up to 500-1000 ns. The C_{60} particle is an excellent spin converter with efficient intersystem crossing (nearly 100% quantum yield), essential in high-performance ROS generation. Moreover, while many common PS structures are destroyed or lose their photoactivity under relatively modest energy doses, fullerenes maintain PDT activity even at high fluence levels. In the electron absorbing spectrum of fullerene C_{60}, several bands in 200 - 650 nm can be distinguished. The strongest two bands have a maximum of 265 nm and 330 nm, corresponding with a comprehensive π electron conjugation system on the particle surface. The absorption in the NIR is the most desirable for medical applications due to the deep tissue penetration capacity of this light wavelength. However, applying relevant synthetic strategies can overcome this disadvantage of fullerene particles and tune the absorption to the desired wavelength. Attaching light-harvesting antennae or optical clearing agents to the carbon cage allows the shift of the absorption spectrum towards the NIR region[105]. Also, two-photon excitation, where two photons of near-infrared wavelength are simultaneously delivered to a particle as the equivalent of one photon with twice higher energy, can be used to get around the unfavourable absorption spectrum. When modifying fullerene to adapt to the physiological conditions, it has to be considered that functionalisation for improving particle solubility may decrease their optical properties.

Fullerenes can perform two types of PDT reactions, with the type depending on solvent polarity. In photodynamic therapy, the most significant are the II type reactions due to high cytotoxicity and local exposure to singlet oxygen. The relaxation from the triplet state of fullerene can be performed through two alternative pathways – emission of a photon with $h\nu$ energy or quenching of the triplet state by oxygen particle. The reactive singlet oxygen is then generated. Photochemical properties of fullerenes, especially electron affinity, show that not only does the energy transfer from $^3C_{60}$ to oxygen appear, but anionic radicals can also be formed in the presence of an electron donor (I-type PDT reaction), as the excited triplet state of fullerene is excellent electron acceptor[106]. Reduced fullerene forms interact with oxygen to generate superoxide radicals. Due to high electron affinity, fullerenes can also perform oxygen-independent photokilling, which may be essential in some challenging tumour microenvironments like pancreatic cancer, where hypoxic areas appear[107].

For the first time, the phototoxicity of fullerenes was reported for carboxylic acid-functionalised fullerenes[108]. Hamblin and Wilson demonstrated the effectiveness of PDT in amino-C_{60} monoadduct and pyrrolidinofullerenes[101-103,109]. Besides tuning the adsorption wavelength, the carbon cage is functionalised to improve tumour accumulation using pegylated ligands or structures captured by receptors overexpressed in cancer cells, such as GLUT and folate receptors. Multimodal fullerene platforms, including drug transporters and light-harvesting antennae, have also been engineered to perform drug release and ROS generation in response to specific light illumination[6-98]. Gd@C_{82} and Gd@C_{82}-Ala nanoparticles which are prone to accumulate in oxygen-rich angiogenic blood vessels finds potential in new strategy for anticancer therapy - tumour vasculature disruption after irradiation (V-PDT) with additional MRI imaging potential. Despite the superiority of fullerenes over the traditional photosensitisers the important restriction is aggregation phenomena[110]. Fullerenes are prone to create clusters in biological environments, which has a significant impact on their PDT potential. The excited $^3C_{60}$ quenched each other which reducing the lifetime of the triplet state and decrease the possibility to transfer the electron to the oxygen particle. Moreover, the fullerenes inside multiparticle clusters cannot interact with environment so the reaction area is substantially reduced. Di Giosia et al. face the aggregation problem and proposed innovative solution. They discovered that when using sonification technique fullerene can be surround by protein molecule in 1:1 ratio[111]. C_{60}@lysosyme after illumination decreased cell viability to about 60% in the short time. No cytotoxicity was observed in the dark. C_{60}@lysozyme shows an excellent singlet oxygen quantum yields higher than Rose Bengal.

ROS detection is a complex procedure due to its short lifetime and low concentration. However, the formation of $^1O_2$ may be documented by a specific and sensitive method – time-resolved detection of characteristic luminescence at 1270 nm[112]. This method allows us to estimate if the second type of photochemical reaction is performed. In the case of free radicals, indirect methods are required. The sensitive method of ROS detection is EPR spin trapping, where radicals are scavenged by a spin trap, forming a spin adduct from whose EPR spectra information about the original radical may be obtained[113]. Another method for singlet oxygen detection performed in the cells is an estimation of lipid peroxidation[114,115]. Cholesterol plays a crucial role in peroxidation processes. This steroid lipid exists in every mammalian cell, and lipoproteins are a member of the cell membrane. Regarding the presence of double bonds in cholesterol structure, this particle is prone to spontaneous oxidation. During peroxidation, in the presence of free radicals, the characteristic products of cholesterol peroxidation are generated - 5α-OOH, 6α-OOH and 6β-OOH. They can be easily separated and indicated by specific chromatographic methods. Cholesterol acts as a molecular probe that detects the mechanisms of photosensitisation reactions.

Fullerene-based delivery systems

Pristine C_{60} is insoluble in water and most polar solvents. However, various modifications increase its hydrophilicity[83,116]. These include synthesising fullerene derivatives such as dendrimers and polymers and chemically modifying them by adding hydrophilic functional groups like polyhydroxylation, amination, carboxylation, and ligands such as amphiphilic polymers. Appropriately functionalised fullerenes can cross biological barriers via endocytosis, achieve endosomal escape, and even cross cell membranes[117-119]. These structural characteristics make fullerenes promising nanoplatforms capable of combining multiple therapeutic strategies, thereby enhancing selectivity.

Several attempts have been made to use fullerenes and their derivatives for pharmaceutical delivery, including doxorubicin, gemcitabine, paclitaxel, and docetaxel[120-125]. Synthesised complexes have improved the water solubility of these drugs, enhanced their adsorption and circulation times, or reduced their side effects. Various strategies have been employed to attach drugs to fullerene scaffolds. For instance, Shi et al. conjugated a ROS-sensitive thioketal linker with doxorubicin's amine functional group and aminofullerene using NHS/EDC amide coupling reactions. They employed an "on-off" strategy for drug release and ROS generation in response to 532 nm laser irradiation[126]. The docetaxel–fullerene complex was obtained through esterification with acylated fullerene[127]. The gemcitabine C_{60}-hexakisadduct was synthesised by Nalepa et al., introducing malonyl diglycine to C_{60} through the Bingel-Hirsch reaction. Monoadduct received at the initial stage was attached to the cytosine fragment of gemcitabine using an amide coupling reaction[128].

Fullerene functionalisation has a significant influence on size and charge distribution. Attaching carboxyl and hydroxyl groups is associated with shifting the zeta potential towards highly negative values, while amine functionalisation notably shifts charge values towards positive ones. Particles are considered stable in solution when the zeta potential is below -30 mV or above +30 mV[129-131] . Values in between are associated with weak repulsive forces between nanoparticles and an increased tendency to aggregate. The positive charge of aminofullerenes is linked to their ultrahigh cellular uptake. It is also noteworthy that the conjugation of the π system of the carbon cage is better preserved in aminofullerenes compared to their hydroxylated analogues due to fewer substituents[132].

Aminofullerenes as erlotinib carriers

EGFR (epidermal growth factor receptor) belongs to the family of tyrosine receptor kinases and plays a crucial role in various cellular processes such as cell growth, division, and survival[133,134]. EGFR is frequently overexpressed in pancreatic cancer, contributing to its aggressive and treatment-resistant nature. Binding specific growth factors to EGFR triggers cellular events promoting cancer cell growth and survival. Several downstream signalling pathways, including Ras/MAPK and PI3K/Akt, are activated in response. EGFR dysregulation in pancreatic cancer makes it a promising target for therapy. Research on specific kinase inhibitors has led to several FDA-approved drugs, including erlotinib.

Erlotinib, approved in 2016 for pancreatic cancer treatment, is a first-generation EGFR kinase inhibitor[135,136]. It reversibly binds the ATP-binding pocket of the EGFR kinase domain, preventing ATP binding and thereby potentially reducing tumour growth and slowing pancreatic cancer progression. Additionally, erlotinib may enhance the effectiveness of chemotherapy, particularly when combined with gemcitabine. However, a limitation of erlotinib therapy is the development of cancer cell resistance, often due to mutations in the ATP-binding pocket, such as threonine-to-methionine substitutions, observed in 50% of cases[137].

Attaching drugs to nanocarriers must maintain their chemical activity. Therefore, strategic functional groups should remain intact. Erlotinib targets the hydrophobic ATP-binding pockets, stabilizing inhibitor binding through hydrophobic, hydrogen bonding, and π-π stacking interactions of aromatic rings, which are crucial[138]. Erlotinib offers two strategic points for structural modification and carrier connection: the amine group, facilitating hydrogen atom substitution, and the triple bond suitable for Sonogashira or “click” chemistry. Various synthetic approaches aim to overcome erlotinib resistance. For instance, ferrocenyl-erlotinib derivatives synthesised via “click” chemistry were tested against both erlotinib-sensitive and resistant NSCLC cells (A549, H1395, H1975, H1650)[138]. Docking studies showed that the modified drug binds to EGFR, forming a conformation similar to unmodified particles. Additionally, the number of carbons in the ferrocene-triazole bridge is significant. Modified particles can generate ROS, which, according to Biegański et al., makes their anticancer activity superior to erlotinib. Zhao et al. and Ravindra et al. designed erlotinib derivatives with photosensitisers obtained through “click” and Sonogashira reactions for PDT-mediated therapy. A phthalocyanine analogue was obtained by addition to the amine group of the erlotinib moiety. Molecular docking calculations indicate that these modifications have a negligible effect on the erlotinib’s binding affinity[139,140].

Click chemistry is widely used in medicine due to the crucial role of ligand chemistry in nanotechnology. Linkers are used to conjugate medicine to the photoactive agent and attach or load medicine to its vehicle. Nanotherapeutic systems are often labelled with probes for biodistribution evaluation. Click reactions can be conducted in water, in mild conditions, so fragile molecule structures are unaffected[141].

The CuI-catalysed Huisgen 1,3-dipolar cycloaddition of azides and terminal alkynes to form 1,2,3-triazoles is the model example of a click reaction. This reaction exclusively forms 1,4-substituted products, making it regiospecific. It does not require temperature alterations and can be performed in various solvents with a wide range of pH values. Both primary, secondary, tertiary, and aromatic azides can be involved in this reaction. Tolerance for variations in the acetylene component is also exceptional[141-143]. The reaction is independent of steric factors, occurs rapidly, and processing is usually based on filtration. Triazole ring unit is non-toxic and stable in a biological environment. Moreover, it binds the molecular targets easily through hydrogen bonds and co-dipole interactions. In the case of triazole erlotinib derivatives, a molecular docking study reveals additional cationic - π stacking interactions between triazole ring and ATP binding pocket amino acids residues[138].

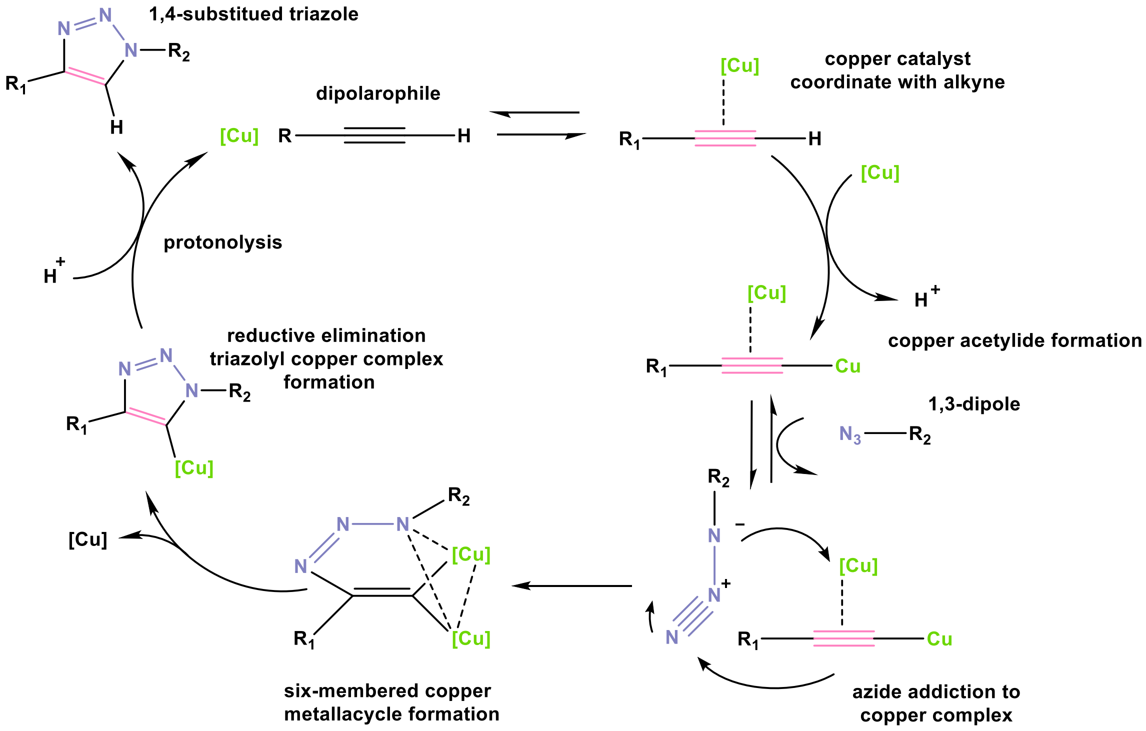

Fig. 7. Copper catalysed click reaction mechanism [144].

Aminofullerenes for siRNA tranfection

RNA interference (RNAi) is a regulatory mechanism found in most eukaryotic cells, using small, double-stranded RNA molecules to control gene activity at the transcriptional level[145-148]. This process silences genes involved in cancerogenesis or disease processes by introducing suitably modified siRNA (short interfering RNA), typically about 20-25 nucleotides long, allowing precise gene expression control. The enzymatic machinery involves the Dicer protein, which has endonuclease activity, and the RNA-induced silencing complex (RISC). Exogenous siRNA is directly loaded onto the RISC complex, where its antisense strand recognizes complementary mRNA. Upon binding, the mRNA is cleaved into fragments by the Ago-2 protein, the catalytic centre of RISC, leading to silencing of the targeted gene expression.

RNAi has emerged as a powerful tool in gene therapy, expanding the targeting potential to include “undruggable proteins” that lack suitable docking sites for small-molecule drugs.[149] The FDA has approved five siRNA-based agents to this date. Patisiran, the first siRNA drug approved, is a liposomal nanoparticle formulation targeting transthyretin for amyloid polyneuropathy. The other four agents utilize siRNA bioconjugates, such as N-acetyl galactosamine (GalNac siRNA), which binds to the asialoglycoprotein receptor (ASGPR) expressed on hepatocytes[150]. Therefore, drugs like Givosiran, Lumasiran, and Inclisiran are used for treating acute hepatic porphyria and other liver-related disorders. GalNac is currently the leading conjugated vector in this field[151].

siRNA can be engineered to directly target dominant oncogenes involved in cancerogenesis, such as KRAS mutants, currently in clinical trials[152]. For instance, G12D siRNA is formulated in biodegradable polymer matrices to prolong local release time. Research on advanced pancreatic cancer patients involves combining it with gemcitabine and paclitaxel-based chemotherapy[153]. Effective use siRNA in cancer pharmacology requires suitable vectors that safely deliver siRNA to target sites. Under physiological conditions, siRNA is unstable and susceptible to degradation by endonucleases. Its negative charge and hydrophobic nature prevent it from crossing biological membranes, which further worsening its pharmacokinetics. Various solutions have been developed to facilitate siRNA distribution, with aminofullerenes emerging as a promising alternative[154-157]. Their positive charge allows for stable complex formation with negatively charged siRNA. The binding affinity of siRNA is influenced by factors such as the ratio of terminal amines to phosphate groups. Higher aminofullerene ratios enhance binding potential but may also promote aggregation. Tested siRNA-fullerene complexes typically maintain an aminofullerene to base ratio of around twenty. The R-value, calculated by dividing the nitrogen-to-phosphorus ratio by two, affects their stability and aggregation propensity.

Fullerenes are preferred over nanolipids due to their lower toxicity and higher hydrophilicity, enabling stable complex formation and better nuclease protection[158,159]. Their amphiphilic nature makes them effective delivery vectors for lung tissue as they are less prone to interact with erythrocytes, which, in the case of liposomes, can induce toxic effects[160]. Studies by Minami et al. suggest that fullerene particles can aggregate with genetic material, forming globular structures similar to histone proteins. Aminofullerene complexes of the Minami team with an N/P ratio of 20 remained stable in buffer solutions for up to 6 hours, indicating their potential in gene therapy. In vivo biodistribution studies of TPFE-siRNA complexes show accumulation in lung tissue, followed by complete clearance within 24 hours after successful gene silencing. Released siRNA binds to RISC instantly, initiating gene knockdown, while residual fullerene is cleared due to its smaller diameter[159]. Recently, light-induced controllable ROS production siRNA-amino fullerene complexes have been developed to enhance lysosomal escape. Although the cationic character of nanoparticles induces a proton sponge effect, which leads to lysozyme membrane rupture, the process is not fully controlled. Wang et al. designed a system in which aminofullerenes generate ROS upon visible light irradiation. This process enables endosomal escape without damaging genetic material, thereby achieving higher transfection efficacy both *in vitro* and in vivo[117].

The aim of the project

My research work mainly concerns the synthesis of water-soluble fullerene nanomaterials and their further functionalisation to enable applications depicted below:

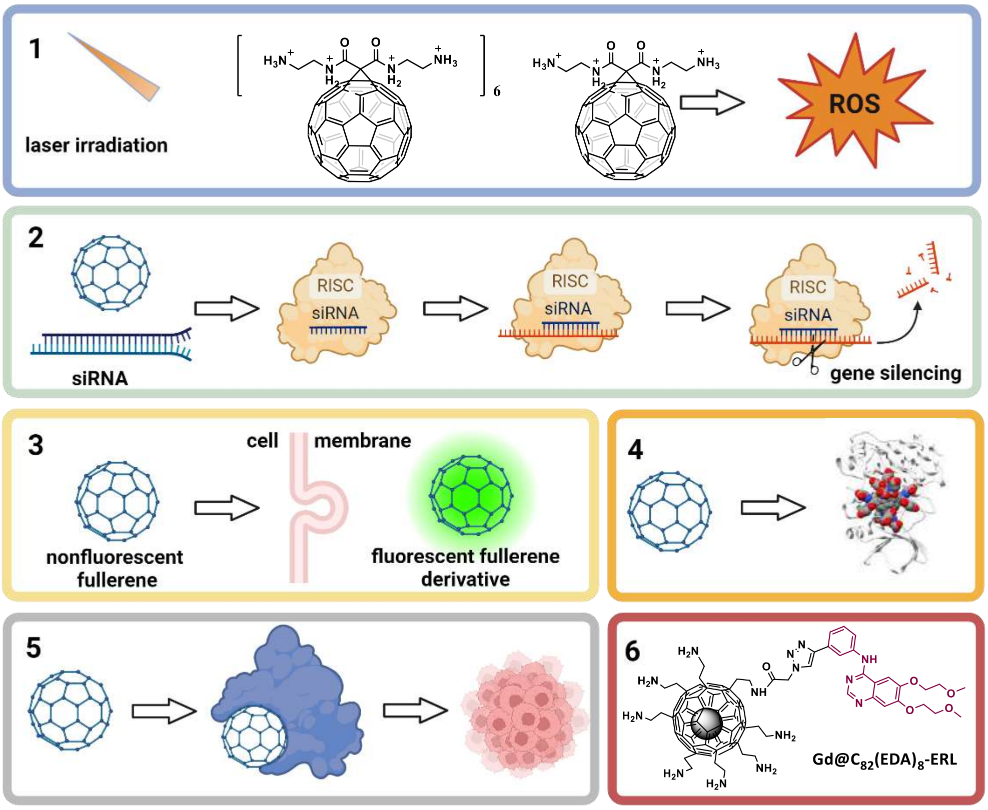

Fig. 9. 1 - (blue box) - photosensitisers in photodynamic therapy, 2 - (green box) - siRNA transfection vectors, 3 - (yellow box) – fullerenes for in vivo bioorthogonal click and visualisation in cancer cells, 4 - (orange box) - BTK protein inhibitors, 5 - (grey box) fullerene-protein interaction review, 6 - (red box) - fullerenes as theranostic erlotinib delivery system.

The goal was to develop fullerene materials suitable for theranostic applications, enabling simultaneous use in multiple therapeutic techniques. This included determining the PDT potential of fullerene derivatives, presenting their siRNA and drug delivery capabilities, and evaluating their imaging potential. Additionally, interactions with selected proteins of the fullerene derivative itself were assessed.

The objectives also included:

- Optimising conditions for synthesising mono- and hexakis-fullerene C_{60} adducts and malonic acid derivatives to obtain water-soluble materials.
- Covalently attaching the EGFR inhibitor; erlotinib to the fullerene core.
- Conducting a comprehensive physicochemical characterization of the obtained adducts.
- Determining the *in vitro* cytotoxicity of fullerene nanomaterials.
- Evaluating their behaviour in cells, including their ability to cross cell membranes, their aggregation under physiological conditions, and their colocalization within cell organelles or structures.
- Assessing the efficacy of their therapeutic effects, imaging capabilities, and interactions with particular proteins on *in vitro* model using cancer cell lines.
- Expanding the knowledge about these nanoparticles to evaluate their therapeutic potential.

All biological experiments were conducted in cooperation. In particular colocalization studies, cellular activity and cytotoxicity *in vitro*. Cell lines were assessed by the group of Professor Anna Mrozek-Wilczkiewicz. The collaboration in the area of ROS detection was implemented with the group of Professor Tadeusz Sarna, siRNA transfection experiments were conducted by dr Monika Rak, the group of Professor Calvaresi from Bologna performed *in silico* studies, and Professor Magdalena Rost-Roszkowska evaluated in vivo cytotoxicity on Drosophila Melangoster model. The relaxation times of gadolinium fullerene derivatives were estimated by Fernando Herranz research team from Madrid.

Publication overview

My research was published in several following articles:

1. Serda M., Szewczyk G., Krzysztyńska-Kuleta O., Korzuch J., Dulski M., Musioł, R., Sarna T., (2020) Developing [60]fullerene nanomaterials for better photodynamic treatment of non-melanoma skin cancer, *ACS Biomaterials Science & Engineering,* 6, 5930-5940.

2. Korzuch J., Rak M., Balin K., Zubko M., Głowacka E., Dulski M., Musioł R., Madeja Z., Serda M., (2021) Towards water-soluble [60]fullerenes for efficient siRNA delivery in a prostate cancer model, *Scientific Reports,* 11, 10565.

3. Serda M., Malarz K., Korzuch J., Szubka M., Zubko M., Musioł R. (2022) In situ cellular localization of non-fluorescent [60]fullerene nanomaterial in MCF-7 breast cancer cells, *Biomaterials Science and Engeneering,* 8, 3450–3462.

4. Malarz K, Korzuch J, Marforio TD, Balin K, Calvaresi M, Mrozek-Wilczkiewicz A, Musioł R, Serda M., (2023) Identification and Biological Evaluation of a Water-Soluble Fullerene Nanomaterial as BTK Kinase Inhibitor, *Int J Nanomedicine*, 18:1709-1724.

5. Serda M, Korzuch J, Dreszer D, Krzykawska-Serda M, Musioł R., (2023) Interactions between modified fullerenes and proteins in cancer nanotechnology, *Drug Discovery Today*, (9):103704.

6. Malarz K, Korzuch J, Mrozek-Wilczkiewicz A, Szubka M, Rurka P, Małota K, Herraiz A, Dreszer D, Kocot K, Herranz F, Rost-Roszkowska M, Sun T, Musioł R, Serda M., (2025) Aminofullerenes as targeted inhibitors of EGFR: from pancreatic cancer inhibitors to *Drosophila m*. Toxicology, *Nanomedicine* (Lond) 20(6):585-601.

Bingel-Hirsch reaction

As mentioned before, the essential issue in medical chemistry is receiving a pure, mono-isomeric reaction product since a regioisomeric mixture can result in different biological responses. By using the optimised, time-controlled Bingel-Hirsch reaction protocol, the pure one isomeric mono- and hexakis-fullerene adducts were obtained.

According to the literature methodology, toluene or 1,4-dichlorobenzene are typically used as reaction solvents. Superbase as 1,8-Diazabicyclo[5.4.0]undec-7-e (DBU), a non-nucleophilic reagent capable of detaching the proton from bromomalonic acid without participating in nucleophilic side reactions, facilitates the process[86]. To obtain monoadduct, the ratio of particular reagents C_{60}/malonate/DBU/carbon tetrabromide (CBr_4) should stand at 1/1,25/1,25/2 equivalents. The reaction runs at room temperature for about 12 hours. Studies have also been conducted with iodine (I_2) as a halogenic agent[85]. Finally, toluene as a reaction solvent was used due to its easier evaporation than 1,4-dichlorobenzene. The iodine as halogenic agent generates multiple by-products, which impair the purification process; therefore, CBr_4 was used.

After dissolving C_{60} in toluene, the flask was placed inside an ultrasonic bath for 20 minutes to minimise aggregation phenomena. The malonates and CBr_4, and also DBU separately, were dissolved in a small amount of dichloromethane before being added to the mixture. The reaction was time-controlled by every hour of TLC analysis. When a higher adduct signal appeared, the reaction was terminated. According to our experiments, the 3-hour procedure was sufficient to obtain monoadduct. The mixture purification included removing unreacted C_{60} with toluene flush on the Buchner tunnel packed with silica gel (silica plug). It was easy to observe the progress of the purification process due to the characteristic purple colour of C_{60} fullerene. The product remaining on the top of the silica was eluted with DCM. Despite TLC control, optionally formed bisadducts were removed using column chromatography. A larger number of malonate groups increases particle polarity and their retention time on silica gel. To limit the polydispersity of fullerene aggregates, larger clusters were removed using centrifugal membranes with 1 kDa filters.

The further optimisations of monoadduct synthesis, which have not yet been published, were directed towards water-free conditions. The glass used in the reaction was heated prior to the reaction to remove the water residual, the toluene was freshly dried, and the inert atmosphere was applied. Firstly, the Bingel-Hirsch reaction with iodine was evaluated at different times and temperatures. The best results for the reaction were obtained at 0 °C for 4 hours. The unreacted C_{60} and iodine were removed on the Buchner tunnel flush. Next, the three-step extraction procedure using Na_2SiO_3, 1M HCl and brine was utilised to remove the iodine residual and unreacted substrates. The pure final product was the first fraction collected from the column chromatography. Higher yields have been observed for the reaction using CBr_4 when water-free conditions and room temperature were applied. The extraction was reduced to two steps with HCl and brine. The applied procedure gives up to 15% higher final yields of fullerene monoadducts.

Hexakisadduct can be received in one step during a longer reaction time and the higher reagents ratio, counting 1/12/12/20 eq. In our studies, we used a two-step reaction version where the monoadduct undergoes subsequent Bingel-Hirsch reaction due to addition of different malonates. Double cyclopropanation ensured higher yields of the final hexakisadduct, which is related to better reactivity of [60]fullerene monoadduct compared to unmodified C_{60}. Therefore, this reaction protocol was also applied for uniform (with only one kind of malonate derivative) hexakisadducts.

The significant advantage of this part of synthetic works is clarity of isomers identification by ^{13}C NMR spectroscopy. For monoadducts with C_v symmetry, 16 signals of sp^2 carbon atoms are observed between 120 ppm and 150 ppm, and one signal of sp^3 carbon from the cyclopropane bridge is observed at 70 ppm. High symmetry (T_h) of hexakisadduct reduces the signal number to three, with two sp^2 signals between 150-135 ppm and one sp^3 at 70 ppm.

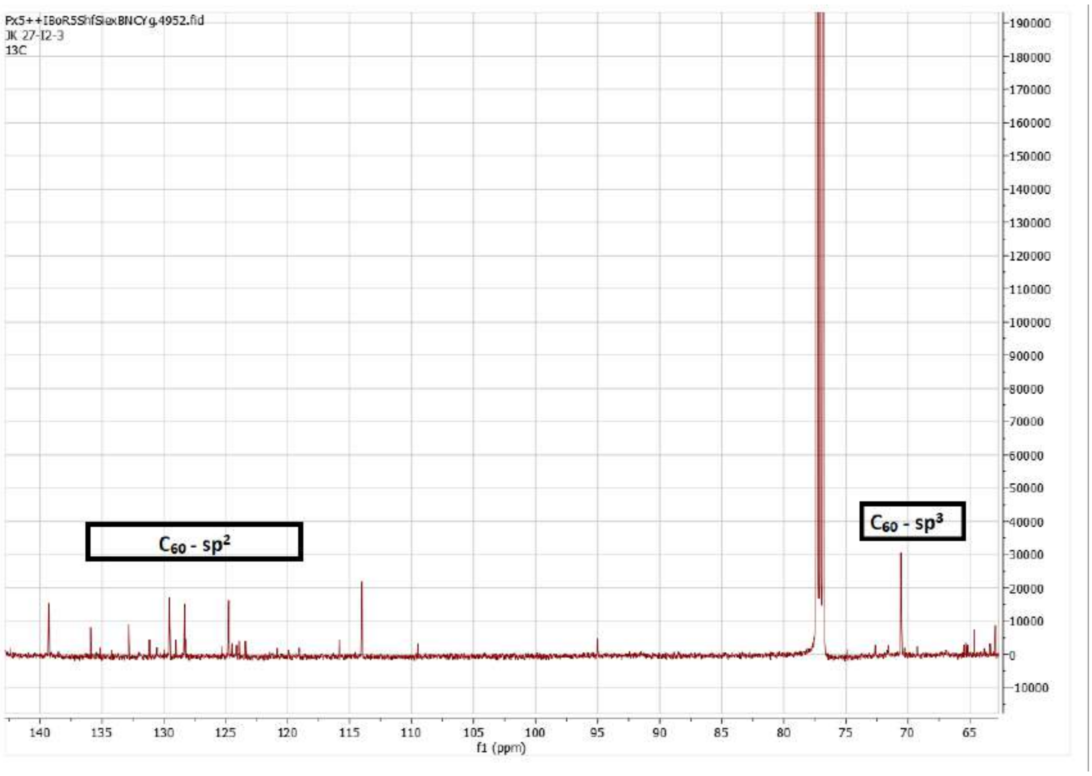

Fig.10. Illustrative spectra of monoadduct of C_{60} fullerene

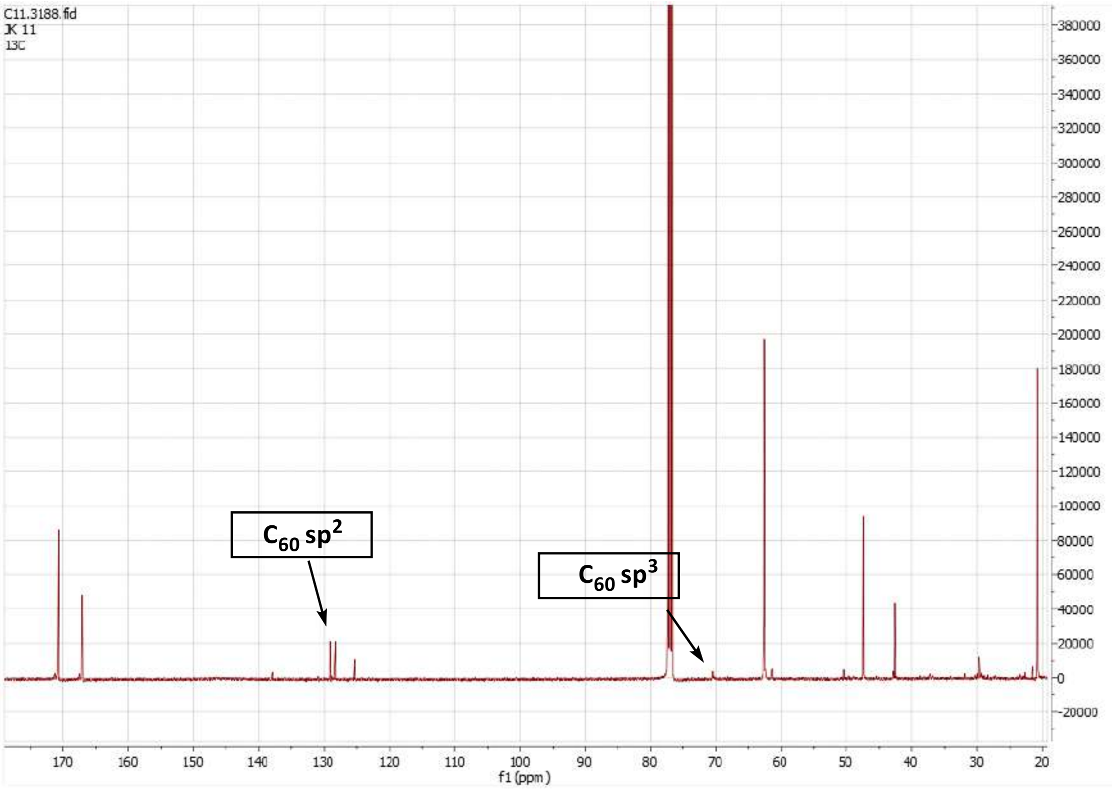

Fig. 11. Illustrative spectra of fullerene C_{60} hexakisadduct.

Modifications of malonic acid and malonic acid esters

The primary substrates for the Bingel-Hirsch reaction are malonates. The initial step in synthesising fullerene derivatives through this method involves attaching the desired functional groups to malonic acid or malonic acid esters, which can be further modified. These basic malonate modifications are commonly employed in nearly all the publications mentioned above and are, therefore, central to the overall process. Below, the approaches for synthesising malonate derivatives, which will serve as intermediates in further reactions, are presented.

Malonic acid derivatives were obtained using followed reactions:

1. Carbodiimide coupling (DCC, DIC, EDC)
2. Amidation with malonyl dichlorides
3. Reaction of dimethyl malonate with amines
4. Esterification catalysed by para-toulenosulfonic acid

Carbodiimides represent a widely adopted and versatile method for crosslinking carboxylic acids. Among the most frequently used carbodiimides are the water-soluble EDC, suitable for aqueous crosslinking as previously discussed, and the water-insoluble N,N'-dicyclohexylcarbodiimide (DCC) or N,N'-diisopropylcarbodiimide (DIC), preferred for non-aqueous organic synthesis techniques. Amidation or esterification reactions utilising these compounds are straightforward, proceeding rapidly under mild conditions at room temperature, and applicable to a diverse range of carboxylic acids, amines, and alcohols. Carbodiimides contain two nitrogen atoms, which are weakly alkaline and enable them to react with carboxylic acid and form unstable O-acylisourea. This intermediate is very reactive and instantly undergoes aminolysis in the presence of primary amine. The most common side reactions involve the cyclisation of intermediate to give oxazolone or the formation of N-acylurea, which can pose challenges for removal in certain solvents. N-acylurea is a stable form of carboxylic acid, and the rate of this irreversible reaction depends on the type of solvent - it undergoes faster in DMF and slower in DCM[161]. To avoid this process, the stabilisers of the O-acylisourea intermediate, such as NHS (N-hydroxysuccinimide) and HoBt (1-hydroxybenzotriazole), are used. They suppress the formation of N-acylurea by protonating the O-acylisourea, thereby preventing intramolecular reaction and shifting the reaction towards the formation of active esters. The last undesirable possibility involves the reaction of O-acylisourea with another carboxyl group in case of excess carboxylic acid. In brief, carbodiimide activates the carboxyl group by creating an intermediate that is more prone to nucleophilic attack and can be stabilised by 1-hydroxybenzotriazole or N-hydroxysuccinimide to avoid undesired products and lower yields[162,163].

The amide coupling using EDC/NHS (1-Ethyl-3-(3-dimethylaminopropyl)carbodiimide hydrochloride/ N-hydroxysuccinimide) is a straightforward method performed between primary amines and carboxylic acids, applicable at physiological pH. This carboxyl-to-amine crosslinking is commonly used for peptide and protein conjugation, covalent binding to surface materials or carriers, labelling amines with carboxylic ligands, and vice versa. It serves as a robust appliance in nanoparticle engineering. The reaction mechanism involves EDC activating carboxylic acid groups to form an unstable O-acylisourea intermediate in aqueous solutions. NHS enhances reaction efficiency by coupling to the EDC carboxyl intermediate and forming an amino-reactive NHS ester[163-167].

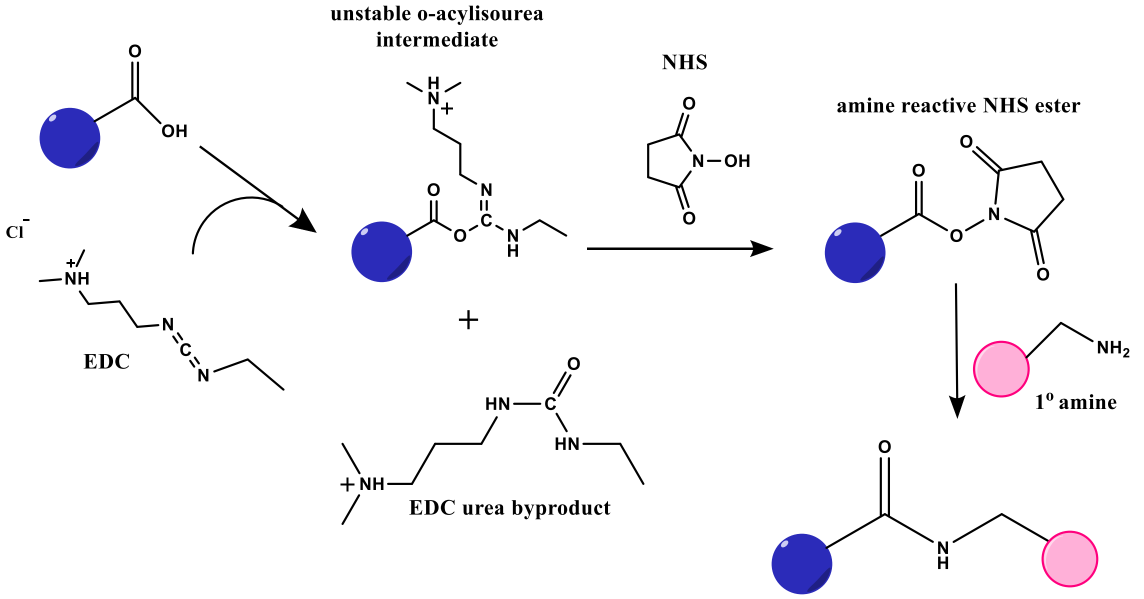

Fig. 12. EDC/NHS amide coupling mechanism.

In organic solvents, the counterpart of this reaction is DCC or DIC coupling, where carbodiimide attacks the carboxylic group to render it a good leaving group, quickly displaced by primary amines in nucleophilic substitution reactions. The reaction processing typically involves only filtration to remove urea and other by-products. The traces of DCC urea are more challenging to remove[162,163,168].

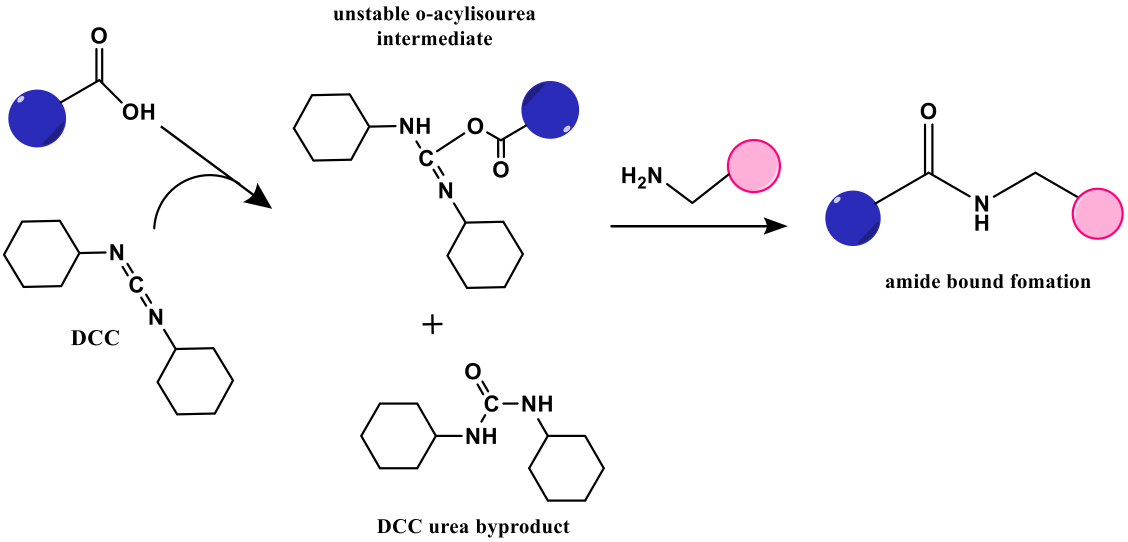

Fig. 13. Mechanism of DCC coupling.

If residual urea can be effectively removed via filtration, a carbodiimide coupling reaction was employed (**Articles 2 and 3**); otherwise, an alternative method was selected. To obtain the best possible yields, the reactions were run at -10 °C to prevent the decomposition of DCC or DIC and provide better reaction control. For Boc-protected aminomalonate and diserinolmalonate, Reaction 2 proved optimal due to straightforward purification: the final product precipitated within days, followed by filtration and crystallisation to acquire a pure malonate derivative (**Articles 2 and 3**). Amidation with malonic acid chlorides necessitates harsher conditions; however, for diglycine malonate, which yields poorly via acylation and exhibits similar solubility to DCC urea, it represents the most efficient approach (**Article 4**). Esterification catalysed by para-toluenesulfonic acid was utilised for triple-bonded malonate, generating the highest purity and yield (**Article 3**). Extraction of the organic phase with a sodium hydrogen carbonate ($NaHCO_3$) solution removes residual malonic acid or its mono-substituted ester. For double-substituted derivatives (excluding Reaction 2), column chromatography was required to eliminate trace amounts of mono-substituted compounds.

The products structures were confirmed and characterized by ^{1}H NMR, ^{13}C NMR and UV-VIS spectra. FT-IR and X-ray photoelectron spectroscopy (XPS) proved the presence of characteristic functional groups. These analytical methods were used to characterise both malonic acid derivatives and the final fullerene adducts. MALDI-TOF spectrometry was utilised for the water-insoluble fullerene monoadducts, while ESI-MS was employed for the final water-soluble products. Particle size measurements for all fullerene nanomaterials were conducted using Dynamic Light Scattering (DLS) and Transmission Electron Microscopy (TEM). Additionally, zeta potential was determinate for all final fullerene adducts.

Commentary on published results

In our studies, the predominant focus was on describing aminofullerenes. As mentioned, fullerene particles decorated with amine functional groups are known for excellent solubility and ultra-high cellular uptake since cationic nanoparticles have a better affinity for anionic residues on the cell surface. The colocalization studies of some aminofullerenes derivatives indicate lysosomes and mitochondria as their main sites of accumulation in cells. In physiological pH, functional amine groups are typically protonated. The positive charge of amines enables electrostatic interactions with various targets and increases the particle zeta potential, implying better particle stability. It is known that many substituents change the electronic properties of fullerenes due to the disturbance of the π-electronic system. However, the aggregation phenomena, which also impair PDT efficacy, could be reduced by the electrostatic repulsions of the positively charged amine groups.

In the first work (**Article 1**), water-soluble fullerenes were synthesised and studied for PDT applications against squamous skin carcinoma. Their effectiveness in ROS generation and lipid oxidation was compared to glycofullerenes previously described by Serda et al.[169]. As fullerenes are prone to interact with serum albumin and others protein in physiological environments, a protein corona is formed on the fullerene surface. The generation of singlet oxygen and anionic superoxide radicals was tested in the presence of bovine serum albumin. Similar studies have been performed before for tris-malonic acid C_{60} complexed with human serum albumin, where HSA significantly shortened the triplet state lifetime[170].

The synthetic part required obtaining amino derivatives of malonic acid and their incorporation into the C_{60} core using a two-step Bingel-Hirsch reaction. Aminomalonate was obtained by the malonic acid methyl ester reaction with ethylenediamine (EDA), which was previously protected on one side with a trityl group to avoid nucleophilic addition to the fullerene double bonds. Next, the fullerene mono- and hexakisadducts were obtained using the Bingel-Hirsch approach, followed by hydrolytic removal of the protecting groups (fig. 13).

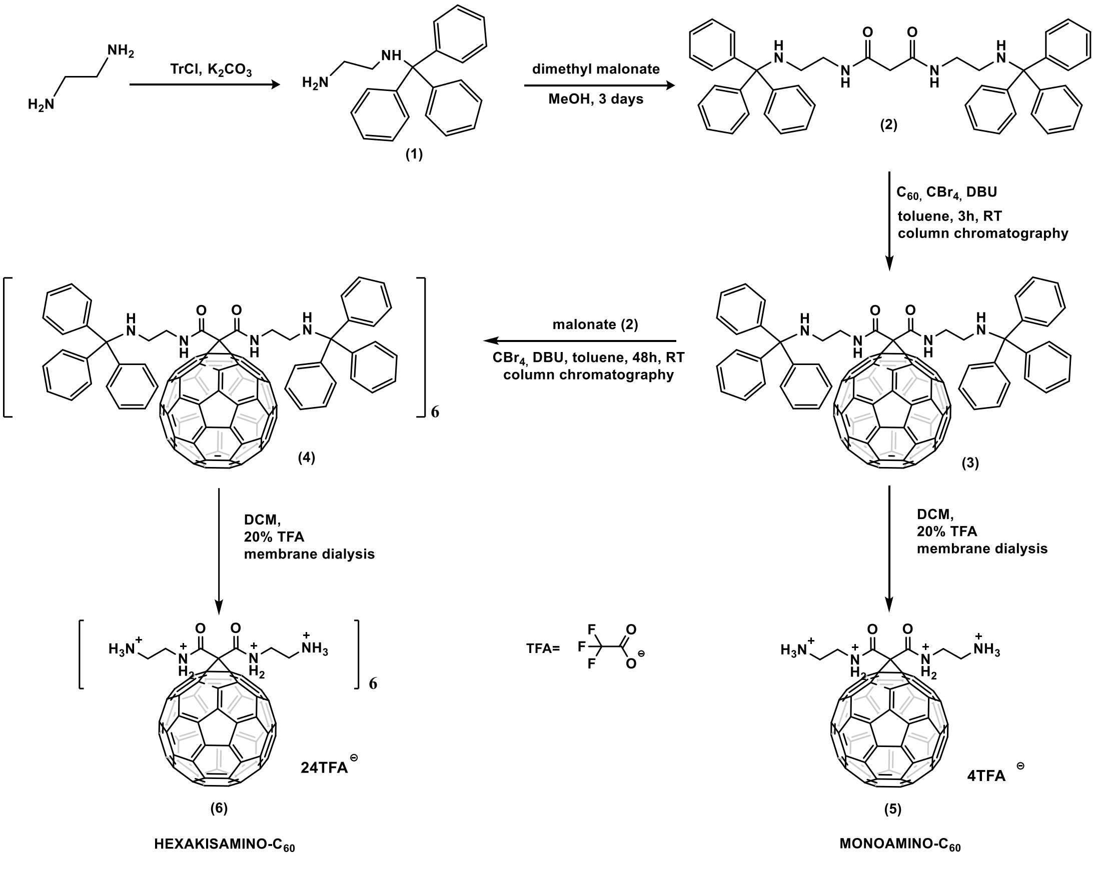

Fig. 14. The synthetic route for monoamino-C_{60} and hexakisamino-C_{60} from **Article 1**.

All four fullerenes, including glucosaminofullerenes, exhibit photoactive potential. The formation of singlet oxygen was confirmed by measuring the phosphorescence of $^1O_2$ at

1270 nm. The quantum yield of photogeneration was low, around 0.1 for hexakisamino-C_{60} and 0.062 for monoamino- C_{60}.These results differ from Bingel-type malonic acid and malonic acid ester fullerene adducts, where the quantum yield of singlet oxygen production decreases as the number of addends increases. The lower quantum yield for monoamino-C_{60} can be related to the formation of larger aggregates (345 nm) while hexakisamino-C_{60} forms smaller clusters (99 nm). Although complexation with albumin usually reduces the ability of singlet oxygen photogeneration, in the case of hexakisamino-C_{60}, the formation of $^1O_2$ was increased. Since this dependency was not observed for the other three derivatives, it might be related to different binding modes of BSA. The type I PDT reaction was also confirmed by EPR spin trapping. According to the literature, type II photodynamic reactions prevailed. Cholesterol peroxidation studies confirm singlet oxygen as the main perpetrator. Protein oxidation was also confirmed. Biological studies determined that hexakisamino-C_{60} decreases cell viability by 20%. Both biological and physical studies were performed in cooperation.

The same hexakisamino fullerene was tested as a siRNA vector in companion with a new D-glucosamine fullerene (**Article 2**). As mentioned before, positively charged aminofullerenes form electrostatic complexes with the negatively charged phosphate groups of genetic material. Cationic fullerene hexakisadducts have already been used as DNA transfection agents for *in vitro* studies, whereas siRNA transfection using fullerenes has only been reported for the tetra(piperazino)fullerene[171,159]. The D-glucosamine moiety was selected based on the premise that the sugar fragment enhances interactions with nucleic acids in chitosan-based transfection agents[172]. Additionally, sugar moiety may increase particle uptake by neoplastic cells. According to the observation of Warburg[173], cancer cells display an elevated rate of glycolysis and, for this purpose, absorb substantial amounts of glucose. Glucose transporter 1 (GLUT1) is a receptor overexpressed in a broad spectrum of cancers and has become a target for the third generation of photosensitisers[174]. Serda et al. determined that another sugar fullerene analogue, SweetC_{60}, mainly accumulates in the nucleus of stellate cells, which confirms good penetrability of the barrier[175]. Otake et al. previously developed glycoconjugate fullerenes as promising PDT agents. D-glucose was attached to the fullerene double bonds via nucleophilic addition. They assumed that glycofullerenes might produce a more significant effect than porphyrin derivatives due to their lower phosphorescence and fluorescence, which allows for more efficient energy transfer to oxygen[176]. Serda et al. determined that another sugar analogue, SweetC_{60} reveals no toxicity in the dark and is photoactive while illuminated with blue and green light[175]. Considering these literature reports, synthesised fullerene siRNA vectors may simultaneously be used in photodynamic therapy and, in the case of JK39, utilize a higher affinity of sugar moiety towards cancer cells.

The synthesis of new fullerene nanomaterial is presented in Fig15. The coupling between sugar glucosamine and malonate mono ethyl ester was performed via DIC/HoBt coupling. The HexakisaminoC_{60} synthetic route was similar as in the first article, with one exception. The trityl protecting group was replaced with tert-butyloxycarbonyl protection which facilitate purification of obtained malonate. After the Bingel-Hirsch reactions and hydrolysis, the cationic fullerene nanomaterials were obtained. The measure of effective fullerene-siRNA complexation is an alteration in fullerene zeta potential, which decreases after ribonucleic acid conjugation. In comparison to HexakisaminoC_{60} (from +28,6 mV to +19,1 mV after siRNA binding), the high positive charge of JK39 (form +54 and +90 mV to + 32,7 mV) resulted in strong binding to the siRNA particle, impeding cargo release inside the cell. The transfection efficacy was evaluated on prostate cancer cell lines DU145 encoding the EGFP protein. This model allowed the process validation by observing the fluorescence loss using fluorescence microscopy. The studies imply that hexakisamino-C_{60} decreases the fluorescence signal by around 50%. Both HexakisaminoC_{60} and JK39 exhibit PDT potential and can be further functionalised. All biological experiments were conducted by Dr. Monika Rak from Jagiellonian University.

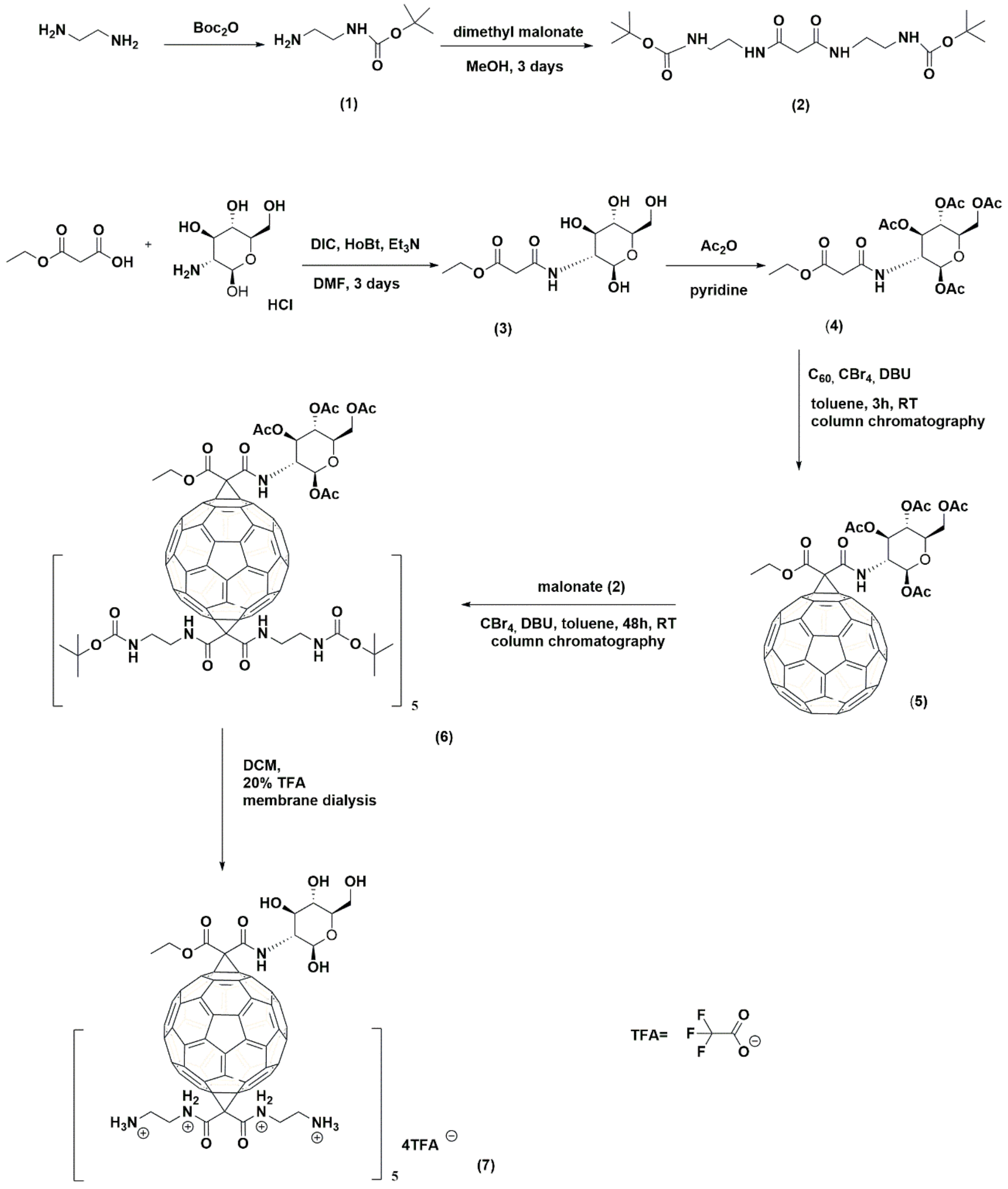

Fig. 15. JK39 synthesis route (**Article 2**). For HexakisaminoC$_{60}$, trityl protection was replaced by tert-butyloxycarbonyl (Boc) group. The reaction work-up was more straightforward, and the final product yield was higher. D-glucosamine malonic acid ester was obtained in DIC/HoBt amide coupling.

Considering fullerenes as theranostic nanoparticles, their visualisation in vivo is a crucial issue. As mentioned, gadolinium fullerene NPs are allowed to be monitored by MRI, but C_{60} and C_{70} particles must be adequately functionalised. Several approaches have been evaluated to allow fullerene tracking inside living systems, including complexation with fluorophores, labelling with fluorescent moieties or using fullerene antibody[177,178]. Even conjugation with medicine (e.g. fluorescent DOX) is sufficient to obtain a complex that can be visualised[179]. Li et al. tracked the pharmacokinetics of ^{64}Cu-labelled fullerenes in vivo on the standard mouse model using PET/CT tomography[180]. However, every functionalisation influences nanoparticle properties and behaviour in a physiological environment. The biorthogonal click chemistry allowed molecules to remain untouched when introducing to living systems and perform fluorescing after conjugation with a specific ligand. The non-fluorescent nature of both substrates is favourable as it does not require the clearance of unreacted particles.

Using bioorthogonal chemistry, we developed a simple method for in situ visualisation of water-soluble TBC_{60}ser derivative (**Article 3**). The synthetic route was in line with the synthetic scheme used before. The malonate derivatives were obtained in esterification catalysed by para-toluenesulfonic acid (A – fig.14) and nucleophilic substitution of malonic acid methyl ester (B - fig. 14). Triple bond malonate and serinol malonate were attached to the fullerene core by a double-step Bingel-Hirsch reaction.

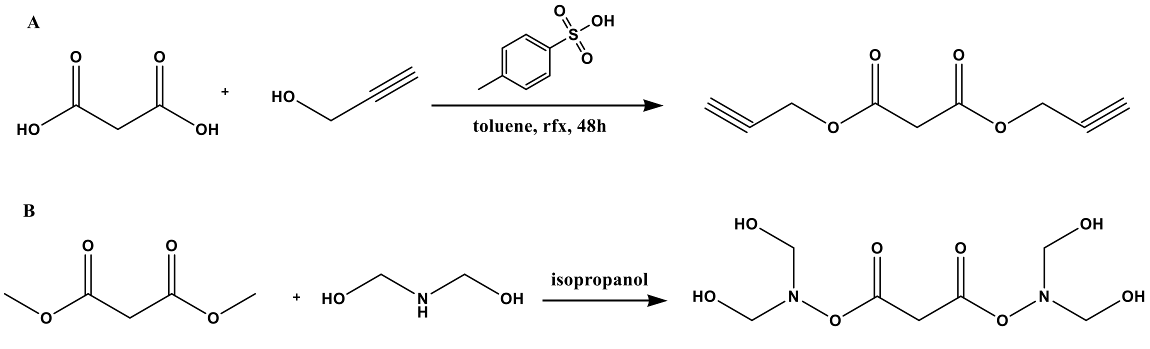

Fig. 16. Malonate derivative (from **Article 3**) synthesis scheme.

Further functionalisation was achieved using "click" copper-catalysed 1,4-Huisgen cycloaddition between the triple bond of the fullerene derivative and the azide group of non-fluorescent 3-azido hydroxycoumarin, as well as commercially available fluorescent azido-SC5 as a control. The project aimed to carry out the reaction in cells, where two non-fluorescent substrates would form a fluorescent fullerene triazole and determine their cellular localisation.

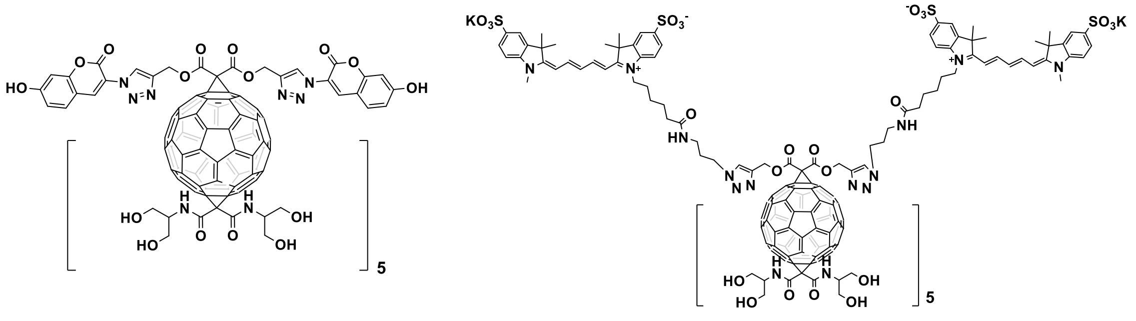

HYDROXYCOUMARIN-C$_{60}$ser TRIAZOLE
(HCC$_{60}$serTRIAZOLE)

SULFOCYANINE5-C$_{60}$ser TRIAZOLE
(SC5C$_{60}$serTRIAZOLE)

Fig. 17. The fullerene nanomaterials for cellular imaging (**Article 3**)

The final *in vitro* experiment was conducted in MCF-7 breast cancer cells. All compounds, including copper sulphate ($CuSO_4$), were used in non-toxic concentrations. The *in situ* click was successful. Colocalisation studies indicate lysosomes as the primary accumulation site, with low affinity observed for mitochondria, consistent with studies on other fullerene derivatives[181,182]. Attempts were also made with an azide fullerene derivative, but it did not penetrate the cell membrane and remained in the medium. This remains a puzzle for me as the amphiphilic character of fullerene derivatives, especially containing cationic amino groups, has been sufficient before passing the biological barriers (e.g., HexakisaminoC60). The azide functional group used in biorthogonal click is indifferent to biomolecules and should not interfere with this process.

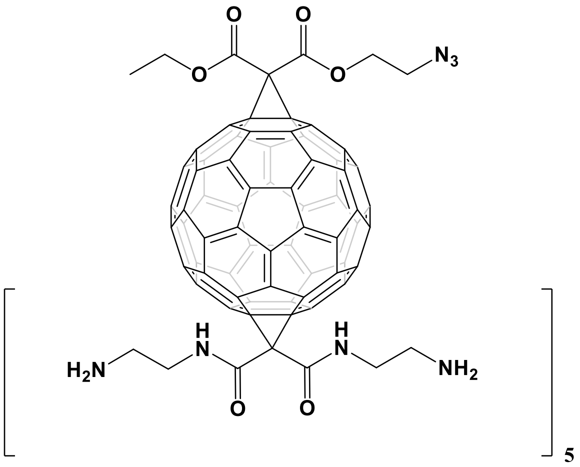

AZIDOAMINO-C$_{60}$FULLERENE

Fig. 18. The azidoaminofullere structure

The fullerene-protein interaction, introduced in previous chapters, plays a crucial role in the behaviour of fullerenes within biological systems. These interactions define both the potential and limitations of fullerenes. Their inherent activity makes them exceptional nanomaterials, serving not only in drug delivery and photodynamic functions but also as potential drug candidates targeting specific proteins directly through carbon shell. This capability may enhance their therapeutic profile, although it complicates their pharmacokinetic characteristics. Interactions with serum proteins also influence their fate inside the living systems. The phenomenon of protein adsorption onto nanoparticle surfaces is referred to as protein corona formation.

In three of my works, the topic of fullerene-protein interactions is explored. One of these is a review article which introduces this subject and will be discussed first.

Our review (**Article 5**), which compiles knowledge from the past thirteen years, provides a comprehensive overview of fullerene-protein interactions, including:

- How protein adsorption onto the fullerene surface influences their behaviour in biological fluids, and how complexation with specific proteins can improve bioavailability while maintaining desired properties.
- The potential for direct inhibition of cancer-related proteins.

It is widely recognized that when nanoparticles enter a biological environment, biomolecules like proteins, sugars, and lipids immediately form a surrounding layer. This biomolecular shell, primarily composed of proteins, is difficult to predict and evolves over time, which can lead to misinterpretations of nanoparticle behaviour and alter their biological activity. The formation of a protein corona can induce aggregation, reduce stability, interfere with molecular targets, or cause a complete loss of specificity. It can also affect cellular uptake and phagocyte recognition, potentially leading to faster clearance from the system. However, the adsorbed shell may also benefit by increasing bioavailability and reducing nanoparticle toxicity. Efforts to control this phenomenon have included nanoparticle surface modifications, such as polymeric or zwitterionic coatings, to reduce the randomness of biomolecule adsorption[183-187].

Despite these exertions, the wide variety of factors influencing the composition of absorbed biomolecules complicates the development of a consistent solution. To date, the only study investigating protein corona formation on fullerene surfaces was conducted by Wu et al.[188] Their research confirmed that protein adsorption induced aggregation, although no changes in protein charge were observed after binding to C_{60}. However, the secondary structure of the proteins was altered. Given the challenges in controlling the association of proteins with fullerene cages, the solution proposed by the Calvaresi research team remains a promising alternative[189,190]. As discussed in the previous chapters, their approach effectively addresses the issue of random protein organization. Fullerene “buckyballs” specifically interact with proteins’ binding pockets through guest-host interactions, in which the protein binds the hydrophobic fullerene scaffold via π-π stacking, hydrophobic interactions, surfactant-like behaviour, or charge-π interactions. This complex prevents fullerene aggregation, enhances solubility in biological fluids, preserves its electronic properties, and prevents the excited state from being deactivated by its surroundings. It is a significant step towards using fullerenes as photosynthesisers in PDT. In articles by di Giosia et al., fullerene-protein complexes have already been studied for these applications[111,182,191]. Calvaressi and colleagues also created a Protein Database, where proteins that potentially may interact with fullerenes are identified based on a developed algorithm that quantitively evaluates interactions between these particles[190].

Dozens of studies have described the interaction of fullerene buckyballs with cancer-related proteins. The mechanism of action has been deeply analysed in literature only for certain enzymes and proteins, such as matrix metalloproteinases 9/2[192,193], myosin heavy chain (MYH-9)[194], hypoxia-inducible factor (HIF-1α), metastasis-associated protein 1 (MTA1), histone deacetylase 1 (HDAC1)[195], F-actin, G-actin[196,197] and collagen[198,199]. Except for the above proteins, in most cases, studies are limited to determining the cytotoxicity of fullerene derivatives. A detailed understanding of these interactions is necessary for fullerenes to be effectively used as nanotherapeutic systems.

Prevalence of the interactions between C_{60} and functional proteins prompted us to evaluate whether similar phenomena will be observed in case of our compounds. Among cancer related protein, which are studied for protein interactions significant role is played by tyrosine kinases. The analysis of fullerenes-protein interactions with these proteins was reviewed in two publications (**Article 4 and Article 6**).

We have selected hexakis-diglycinemethanofullerene (HDGF) and tested it against non-receptor tyrosine kinases, specifically BTK (Bruton's tyrosine kinase) as published in **Article 4**.

The inhibition capacity of HDGF was compared to clinically available therapeutics such as ibrutinib. The studies conducted by Dr Katarzyna Malarz assessed inhibitory effects against a panel of non-receptor tyrosine kinases, including ABL, BRK, BTK, and Src family kinases, in both water and culture medium (DMEM), where protein corona formation is expected. HDGF demonstrated strong inhibitory capacity against BTK kinases; however, significant divergences in activity were observed with other proteins. This research confirmed that protein corona significantly influences the activity of nanomaterials towards biological targets.

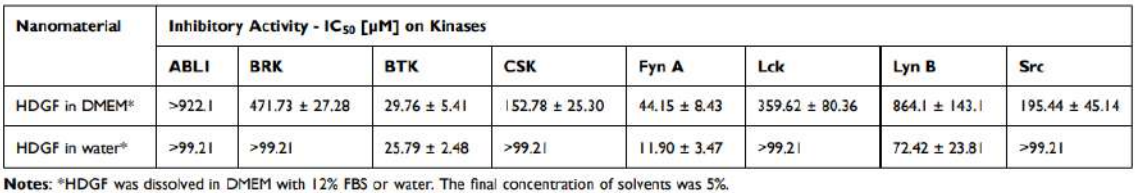

Nanomaterial	Inhibitory Activity - IC_{50} [μM] on Kinases							
	ABL1	BRK	BTK	CSK	Fyn A	Lck	Lyn B	Src
HDGF in DMEM*	>922.1	471.73 ± 27.28	29.76 ± 5.41	152.78 ± 25.30	44.15 ± 8.43	359.62 ± 80.36	864.1 ± 143.1	195.44 ± 45.14
HDGF in water*	>99.21	>99.21	25.79 ± 2.48	>99.21	11.90 ± 3.47	>99.21	72.42 ± 23.81	>99.21

Notes: *HDGF was dissolved in DMEM with 12% FBS or water. The final concentration of solvents was 5%.

Table 1. HDGF inhibitory activity (IC_{50}) against tyrosine kinases (from **Article 4**)

The docking experiments of diglycinefullerene were conducted by the cooperating research group from the University of Bologna. *In silico* studies established that negatively charged HDGF binds to the positively charged active site of BTK and significantly reduces the availability of Tyr551. As mentioned earlier, phosphorylation of tyrosine residues leads to the activation of BTK kinase; therefore, the Tyr551 position is crucial for the modulation of BTK activity. HDGF also interacts directly with the catalytic residue Arg525 and Cys148, which covalently binds the clinically used BTK inhibitor ibrutinib. Cytotoxicity studies performed on RAJI and K526 cells indicated that autophagosomes and caspases 3/9 were the main pathways for cell death. High-resolution transmission electron microscopy (HR-TEM) and cryogenic transmission electron microscopy (cryo-TEM) were used for morphological characterization.

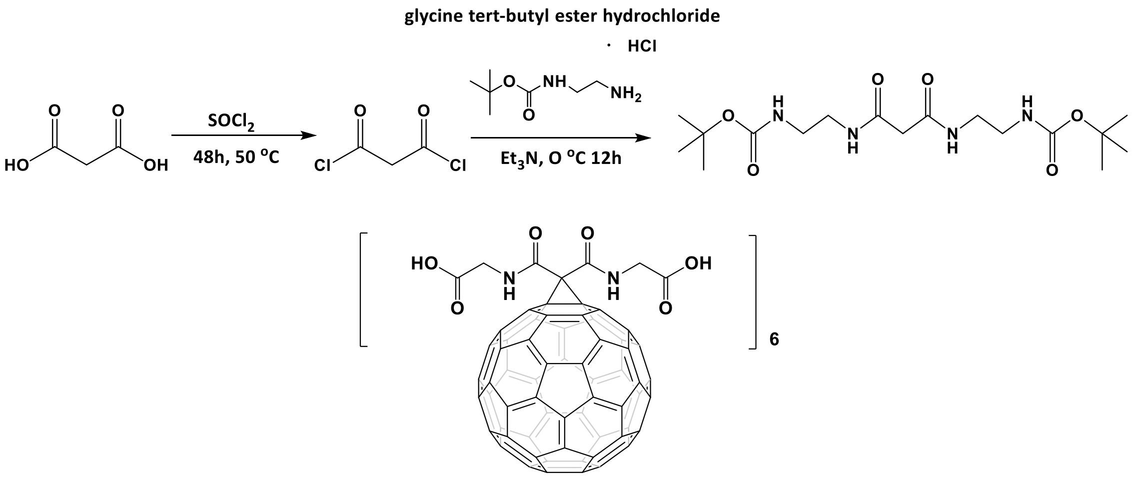

HEXAKIS DIGLICINEMETHANOFULLERNE (HDGF)

Fig. 19. Synthesis of diglycine malonate and structure of hexakis diglycinemethanofullerene (**Article 4**)

In the next effort, fullerene ornamented with erlotinib was used for the anti-EGRF strategy. Erlotinib, as mentioned, is an EGFR kinase inhibitor approved for combination therapy towards pancreatic cancer and small cell lung carcinoma. Moreover, the fullerene core was represented by gadolinium fullerene, which exhibited MRI imaging potential. The intrinsic Gd@C_{82} fullerene activity has appeared in several articles over the last few years. To my knowledge, hydroxylated and aminated derivatives of Gd@C_{82} are the best described fullerenes for cancer-related protein inhibition[72,90,200,201].

The antineoplastic activity of gadofullerenes includes inhibition of tumour growth, invasion and metastasis. Additionally, it was noticed that they could resume blocked immune response in the tumour microenvironment by reprograming tumour-associated macrophages and suppresses angiogenesis by direct interaction with angiogenic factors but may also destroy the existing tumour vasculature under radiofrequency irradiation[201-203]. Research findings indicate that Gd@C_{82} derivatives reduce cell proliferation, reverse drug resistance, regulate the cell cycle, and induce apoptosis in cancer cells[90,200,204]. Some studies explain the mechanism of action in detail; in others, it remains unknown. For example, Gd@$C_{82}(OH)_{22}$ was reported to interact with two matrix metalloproteinases, MMP9 and MMP2 trough specified bindings[192,193,205]. In pancreatic cancer, MMPs show high expression levels relative to normal cells. MPs initiate an invasion-metastatic cascade, but from a broader perspective, they are pathing the way for all six cancer's hallmarks to develop[206]. Gadofullerenes are also engaged in the degradation of extracellular matrix (ECM), which allows cancer cell migration and provides a prerequisite to angiogenesis[199,207]. They also participate in inflammation processes and impact Interleukin-6, TMF-α, Notch and other signalling pathways[72,90].

Three-dimensional gadofullerene potential: antineoplastic activity of Gd@C_{82} particle, MRI imaging potential and their specificity towards EGFR-signalling pathway proteins was evaluated in **Article 6**. Using click reaction, tyrosine kinase inhibitor erlotinib was attached to gadolinium containing fullerene, C_{60}BUT and C_{70}BUT aminofullerenes, and assess the activity of these theranostic nanocomplexes on pancreatic cancer cell lines.

Using a click chemistry approach, a carboxylic functional group was introduced into the erlotinib moiety to obtain substrate for further amide coupling reaction. A click reaction was conducted between the terminal triple bound of erlotinib and synthesised earlier (in modified Dyke's procedure) with 2-azidocarboxylic acid. For this purpose, several attempts have been made to establish the most preferable reaction conditions. Two approaches have been tested: i) with sodium ascorbate and copper sulphate ($CuSO_4$) in water and tert-butanol mixture, and ii) CuI/DIPEA (N,N-Diisopropylethylamine) in DMSO. Different reaction times, temperatures and solvents were examined (Fig.19). Erlotinib hydrochloride exhibits poor solubility in broad range of organic solvents. Finally, the best yield (91%) was obtained at 60 °C with sodium ascorbate and $CuSO_4$ (H_2O/t-BuOH 4:1).

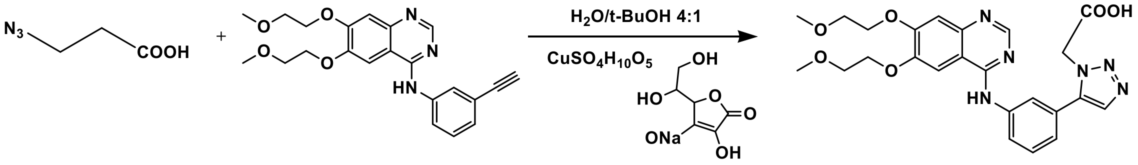

	Equivalents	Catalytic system	Solvent	Reaction time	Temperature	Yield
i	1/1/0,1/0,1	$CuSO_4$/sodium ascorbate	H_2O/t-BuOH 2:1	1h	40 °C	15%
			H_2O/t-BuOH 2:1	48h	40 °C	20%
			H_2O/t-BuOH 4:1	48h	50 °C	70%
			H_2O/t-BuOH 4:1	48h	60 °C	92%
ii	1/1/0,1/0,2	CuI/DIPEA	DCM	48h	30°C	15%
			DMF	48h	50 °C	20%
			DMSO	48h	50 °C	50%

Fig. 19. The synthesis scheme of ERL-COOH. Table shows evaluation of click reaction.

The amide coupling was performed using one equivalent of EDC/NHS and ERL-COOH to achieve a single substitution while maintaining the water solubility and stability of the fullerene nanomaterials. Morphological studies included Cryo-TEM, Scanning Electron Microscopy (SEM), and additional structure confirmation of Gd@C82EDA-ERL using SEM energy-dispersive spectroscopy (EDS) mapping. The PDI factor indicated a narrow size distribution of 0.3.

The toxicological properties of all fullerene nanomaterials were tested *in vitro* on PANC-1, AsPC-1, and PAN02 cancer cells. In vivo studies for the gadofullerene nanoconjugate Gd@C_{82}EDA-ERL were performed using a *Drosophila Melanogaster* model. All biological studies were conducted by Dr Katarzyna Malarz from the

University of Silesia. The antiproliferative properties of the compounds were evaluated *in vitro*. C_{60}BUT exhibited the highest activity on the erlotinib-resistant PANC-1 cell line (IC_{50} - 16,88 μM) and showed similar biological activity to erlotinib (IC_{50} - 6,45 μM) in AsPC-1 cancer cell lines. Further cellular experiments revealed that the tested fullerene nanomaterials could arrest the cell cycle in the G0/G1 phase, as evidenced by changes in p27 and cyclin E1 expression. Most importantly, it was shown that the tested fullerene nanomaterials inhibited the EGFR signalling pathway by reducing the production of p-EGFR, p-Akt, PI3K, and Ras proteins.

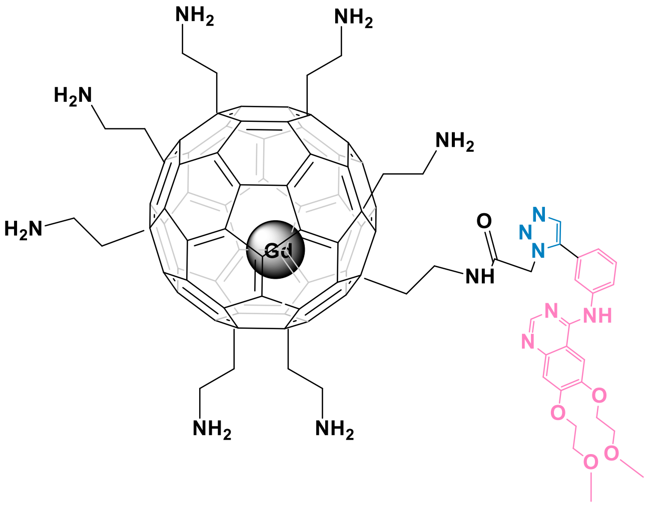

Fig. 20. Schematic presentation of Gd@C_{82}EDA-ERL nanoparticle.

Final conclusions

The amphiphilic fullerene derivatives soluble in physiological fluids and exhibiting high bioavailability were obtained. It was achieved via series of synthetic works as following:

- Synthesis of malonate derivatives using optimised reaction conditions, including amide coupling, esterification and aminolysis.
- Synthesis of fullerene mono- and hexakisadducts by using the Bingel-Hirsch reaction.
- Synthesis of ethylenediamine- and butyldiamine-substituted fullerenes, which enables further conjugation with erlotinib.
- Attaching the erlotinib to corresponding aminofullerenes via alkyne fragment, using 1,4 - Huisgen cycloaddiction

Malonate functional groups were selected to enable multiblock nanomaterial engineering. The fullerene carbon cage forms the first block, while the second consists of malonate functional groups, which can be further modified towards specific applications or combined therapy, following the theranostic approach.

- All obtained structures were confirmed and fully characterised using ^{1}H NMR, ^{13}C NMR, UV-VIS, FT-IR, XPS, and ESI-MS. It applies to malonate derivatives, mono- and hexakisadducts, modified erlotinib and erlotinib-conjugated aminofullerenes. Where required the particle size and aggregate forms of the final fullerene nanomaterials were analysed using DLS and TEM. Zeta potential measurements were used to determine the charge, which changes depending on functionalisation.
- All the synthesised fullerene nanomaterials exist in one isomeric form.
- All the synthesised nanomaterials can cross the cell membranes (except azidoamino-C_{60} fullerene) and localise primarily in lysosomes, consistent with previously published data.
- In physiological fluids, the obtained fullerene derivatives form spherical or fluffy-like aggregates with varying polydispersity.

- All fullerene derivatives exhibit no cytotoxicity in the dark, which was evaluated *in vitro* and for Gd@C_{82}EDA-ERL also in vivo on the *D. Melanogaster* model.

The investigation towards fullerenes' potential application in anticancer therapies, including photodynamic therapy, gene and drug delivery and protein inhibition, yielded the following results:

- Amino and glycofullerenes were confirmed as potential photosynthesisers, being non-toxic in the dark and cytotoxic after blue light laser irradiation (weaker effect was observed for green light). For HexakisaminoC_{60}, the presence of bovine serum albumin increased singlet oxygen production, suggesting that this protein may serve as a suitable host and boost the photodynamic effect.
- The same HexakisaminoC_{60} passed the green fluorescent protein (GFP) fluorescence quenching test, confirming its siRNA transfection efficacy. It forms a stable complex with siRNA and effectively delivers and releases it into cancer cells *in vitro*.
- The *in situ* click experiment provided a simple method to track fullerene nanomaterials within living systems without prior functionalisation, which could otherwise alter their pharmacokinetic profile. Fluorescence microscopy identified lysosomes as the primary accumulation site.

The inherent activity of fullerenes toward tyrosine kinases was analysed, leading to the following conclusions:

- The glycine derivative HDGF shows inhibitory potential against the BTK protein. The absorbed protein corona has minimal impact on its activity. The molecular mechanism suggests that the negatively charged regions of fullerene nanomaterials associated with glycine fragments are primarily responsible for BTK inactivation. These regions interact with the positively charged ATP-binding pocket, thereby blocking BTK autophosphorylation and its subsequent activation.
- The EGFR inhibition capacity of Gd@C_{82}-ERL and C_{70}BUT was confirmed. In the case of C_{70}BUT, its inhibition was comparable to erlotinib, supporting the premise of fullerenes' activity against tyrosine kinases. However, the conjugation of erlotinib with Gd@C_{82}EDA reduced its inhibitory effect, despite simulations

showing additional interactions between the ATP-binding pocket of the EGFR domain and the triazole ring connecting erlotinib to fullerene. The high positive charge likely prevented fullerene from approaching the ATP-binding pocket or the formation of aggregates limited the accessibility of erlotinib. Further studies are needed to better understand the interactions between C_{70}BUT and EGFR. Additionally, Gd@C_{82}EDA-ERL exhibited good relaxation times and no cytotoxicity in in vivo studies on *D. Melanogaster*, indicating its potential as a theranostic agent. However, functionalisation of fullerene carrier or erlotinib conjugation needs to be optimised.

The primary challenges in advancing fullerenes to clinical trials have been their insolubility in physiological solvents and their tendency to aggregate. While solubility issues have largely been addressed through the chemical modifications discussed in this dissertation, aggregation remains a significant hurdle to fully realizing the therapeutic potential of fullerenes. Methods employed for solubilization (also in our studies) often result in polydisperse aggregates. One promising approach involves using suitable, non-toxic carriers, referred to as supramolecular hosts, in which fullerene is complexed with host molecules in a 1:1 ratio.

The research team from Bologna University, which focuses on fullerene-protein guest-host interactions, has developed solutions to alleviate aggregation. Their approach enables the maintenance of the photophysical and photochemical properties of the particles while addressing the protein corona issue. However, fullerene functionalisation may hinder the selective binding of fullerenes to binding pockets, which limits the potential for synthetic modifications. Nevertheless, attaching appropriately sized antennae to the fullerene scaffold, extending beyond the protein, may enable fullerene in vivo interactions. These findings indicate that such fullerene derivatives preserving their unique properties, could enhance drug delivery precision and efficacy by targeting specific cellular components.

The prospects of this research underscore the importance of designing biocompatible fullerene-based compounds that not only improve therapeutic targeting but also reduce off-target effects. Additionally, by exploring the potential of fullerenes as enzyme inhibitors, I believe my work opens new avenues for developing alternative therapeutic strategies at a molecular level to combat resistant cancer cells. Continued exploration in this field could ultimately contribute to the broader field of nanomedicine and the development of more effective, fine-tuned treatments with applications extending beyond oncology.

References

1. Fan D, Cao Y, Cao M, Wang Y, Cao Y, Gong T. (2023) Nanomedicine in cancer therapy. *Signal Transduction and Targeted Therapy*. 2023;8,293.
2. Nirmala MJ, Kizhuveetil U, Johnson A, G B, Nagarajan R, Muthuvijayan V. (2023) Cancer nanomedicine: a review of nano-therapeutics and challenges ahead. *RSC Advances*. 2023;13,8606-8629.
3. Bodunde OP, Ikumapayi OM, Akinlabi ET, Oladapo BI, Adeoye AOM, Fatoba SO. (2021) A futuristic insight into a “nano-doctor”: A clinical review on medical diagnosis and devices using nanotechnology. *Materials Today: Proceedings*. 2021;44,1144-1153.
4. Mundekkad D, Cho WC. (2022) Nanoparticles in Clinical Translation for Cancer Therapy. *Int J Mol Sci*. 2022;23,
5. Kashyap BK, Singh VV, Solanki MK, Kumar A, Ruokolainen J, Kesari KK. (2023) Smart Nanomaterials in Cancer Theranostics: Challenges and Opportunities. *ACS Omega*. 2023;8,14290-14320.
6. Raheem MA, Rahim MA, Gul I, Zhong X, Xiao C, Zhang H, et al. (2023) Advances in nanoparticles-based approaches in cancer theranostics. *OpenNano*. 2023;12,100152.
7. Johnson KK, Koshy P, Yang J-L, Sorrell CC. (2021) Preclinical Cancer Theranostics—From Nanomaterials to Clinic: The Missing Link. *Advanced Functional Materials*. 2021;31,2104199.
8. Nam J, Son S, Park KS, Zou W, Shea LD, Moon JJ. (2019) Cancer nanomedicine for combination cancer immunotherapy. *Nature Reviews Materials*. 2019;4,398-414.
9. Giri PM, Banerjee A, Layek B. (2023) A Recent Review on Cancer Nanomedicine. *Cancers*. 2023;15,2256.
10. Hou S, Hasnat M, Chen Z, Liu Y, Faran Ashraf Baig MM, Liu F, et al. (2022) Application Perspectives of Nanomedicine in Cancer Treatment. *Frontiers in Pharmacology*. 2022;13,
11. Rafii S, Tashkandi E, Bukhari N, Al-Shamsi HO. (2022) Current Status of CRISPR/Cas9 Application in Clinical Cancer Research: Opportunities and Challenges. *Cancers (Basel)*. 2022;14,
12. Hu B, Zhong L, Weng Y, Peng L, Huang Y, Zhao Y, et al. (2020) Therapeutic siRNA: state of the art. *Signal Transduction and Targeted Therapy*. 2020;5,101.
13. Mitchell MJ, Billingsley MM, Haley RM, Wechsler ME, Peppas NA, Langer R. (2021) Engineering precision nanoparticles for drug delivery. *Nature Reviews Drug Discovery*. 2021;20,101-124.
14. Manzari MT, Shamay Y, Kiguchi H, Rosen N, Scaltriti M, Heller DA. (2021) Targeted drug delivery strategies for precision medicines. *Nat Rev Mater*. 2021;6,351-370.
15. Hare JI, Lammers T, Ashford MB, Puri S, Storm G, Barry ST. (2017) Challenges and strategies in anti-cancer nanomedicine development: An industry perspective. *Advanced Drug Delivery Reviews*. 2017;108,25-38.

16. Rodríguez F, Caruana P, De la Fuente N, Español P, Gámez M, Balart J, et al. (2022) Nano-Based Approved Pharmaceuticals for Cancer Treatment: Present and Future Challenges. *Biomolecules*. 2022;12,

17. Shi J, Kantoff PW, Wooster R, Farokhzad OC. (2017) Cancer nanomedicine: progress, challenges and opportunities. *Nature Reviews Cancer*. 2017;17,20-37.

18. Nirmala MJ, Kizhuveetil U, Johnson A, G B, Nagarajan R, Muthuvijayan V. (2023) Cancer nanomedicine: a review of nano-therapeutics and challenges ahead. *RSC Adv*. 2023;13,8606-8629.

19. Blanco E, Shen H, Ferrari M. (2015) Principles of nanoparticle design for overcoming biological barriers to drug delivery. *Nature Biotechnology*. 2015;33,941-951.

20. Golombek SK, May JN, Theek B, Appold L, Drude N, Kiessling F, et al. (2018) Tumor targeting via EPR: Strategies to enhance patient responses. *Adv Drug Deliv Rev*. 2018;130,17-38.

21. Bertrand N, Wu J, Xu X, Kamaly N, Farokhzad OC. (2014) Cancer nanotechnology: the impact of passive and active targeting in the era of modern cancer biology. *Adv Drug Deliv Rev*. 2014;66,2-25.

22. Smidova V, Michalek P, Goliasova Z, Eckschlager T, Hodek P, Adam V, et al. (2021) Nanomedicine of tyrosine kinase inhibitors. *Theranostics*. 2021;11,1546-1567.

23. Soprano E, Polo E, Pelaz B, del Pino P. (2022) Biomimetic cell-derived nanocarriers in cancer research. *Journal of Nanobiotechnology*. 2022;20,538.

24. Issaka E, Amu-Darko JNO. (2024) Biomimetic Nanoparticles for Cancer Therapy: A Review of Recent Advances, Applications, and Bottlenecks. *Biomedical Materials & Devices*. 2024;

25. Ghosh AK, Ghosh A, Das PK. (2024) Nanotechnology Meets Stem Cell Therapy for Treating Glioblastomas: A Review. *ACS Applied Nano Materials*. 2024;7,2430-2460.

26. Oroojalian F, Beygi M, Baradaran B, Mokhtarzadeh A, Shahbazi M-A. (2021) Immune Cell Membrane-Coated Biomimetic Nanoparticles for Targeted Cancer Therapy. *Small*. 2021;17,2006484.

27. Sakhrani NM, Padh H. (2013) Organelle targeting: third level of drug targeting. *Drug Des Devel Ther*. 2013;7,585-99.

28. Fröhlich E. (2012) The role of surface charge in cellular uptake and cytotoxicity of medical nanoparticles. *Int J Nanomedicine*. 2012;7,5577-91.

29. Hoshyar N, Gray S, Han H, Bao G. (2016) The effect of nanoparticle size on in vivo pharmacokinetics and cellular interaction. *Nanomedicine (Lond)*. 2016;11,673-92.

30. Augustine R, Hasan A, Primavera R, Wilson RJ, Thakor AS, Kevadiya BD. (2020) Cellular uptake and retention of nanoparticles: Insights on particle properties and interaction with cellular components. *Materials Today Communications*. 2020;25,101692.

31. Fang J, Islam W, Maeda H. (2020) Exploiting the dynamics of the EPR effect and strategies to improve the therapeutic effects of nanomedicines by using EPR effect enhancers. *Adv Drug Deliv Rev*. 2020;157,142-160.

32. Hussain Z, Khan S, Imran M, Sohail M, Shah SWA, de Matas M. (2019) PEGylation: a promising strategy to overcome challenges to cancer-targeted nanomedicines: a review of challenges to clinical transition and promising resolution. *Drug Deliv Transl Res*. 2019;9,721-734.

33. Raza A, Rasheed T, Nabeel F, Hayat U, Bilal M, Iqbal HMN. (2019) Endogenous and Exogenous Stimuli-Responsive Drug Delivery Systems for Programmed Site-Specific Release. *Molecules*. 2019;24,

34. Al-Zoubi MS, Al-Zoubi RM. (2022) Nanomedicine tactics in cancer treatment: Challenge and hope. *Critical Reviews in Oncology/Hematology*. 2022;174,103677.

35. Jia M, Zhang D, Zhang C, Li C. (2021) Nanoparticle-based delivery systems modulate the tumor microenvironment in pancreatic cancer for enhanced therapy. *Journal of Nanobiotechnology*. 2021;19,384.
36. Roma-Rodrigues C, Pombo I, Raposo L, Pedrosa P, Fernandes AR, Baptista PV. (2019) Nanotheranostics Targeting the Tumor Microenvironment. *Frontiers in Bioengineering and Biotechnology*. 2019;7,
37. Raju GSR, Pavitra E, Varaprasad GL, Bandaru SS, Nagaraju GP, Farran B, et al. (2022) Nanoparticles mediated tumor microenvironment modulation: current advances and applications. *J Nanobiotechnology*. 2022;20,274.
38. Gao W, Li S, Liu Z, Sun Y, Cao W, Tong L, et al. (2017) Targeting and destroying tumor vasculature with a near-infrared laser-activated “nanobomb” for efficient tumor ablation. *Biomaterials*. 2017;139,1-11.
39. Li W, Zhao X, Du B, Li X, Liu S, Yang XY, et al. (2016) Gold Nanoparticle-Mediated Targeted Delivery of Recombinant Human Endostatin Normalizes Tumour Vasculature and Improves Cancer Therapy. *Sci Rep*. 2016;6,30619.
40. Chen Q, Feng L, Liu J, Zhu W, Dong Z, Wu Y, et al. (2016) Intelligent Albumin-MnO2 Nanoparticles as pH-/H2 O2 -Responsive Dissociable Nanocarriers to Modulate Tumor Hypoxia for Effective Combination Therapy. *Adv Mater*. 2016;28,7129-36.
41. Qiu Q, Li C, Song Y, Shi T, Luo X, Zhang H, et al. (2019) Targeted delivery of ibrutinib to tumor-associated macrophages by sialic acid-stearic acid conjugate modified nanocomplexes for cancer immunotherapy. *Acta Biomater*. 2019;92,184-195.
42. Wu M, Shu J. (2018) Multimodal Molecular Imaging: Current Status and Future Directions. *Contrast Media & Molecular Imaging*. 2018;2018,1382183.
43. Luengo Morato Y, Ovejero Paredes K, Lozano Chamizo L, Marciello M, Filice M. (2021) Recent Advances in Multimodal Molecular Imaging of Cancer Mediated by Hybrid Magnetic Nanoparticles. *Polymers (Basel)*. 2021;13,
44. Zlitni A, Gambhir SS. (2018) Molecular imaging agents for ultrasound. *Current Opinion in Chemical Biology*. 2018;45,113-120.
45. Wallace AM, Hoh CK, Vera DR, Darrah DD, Schulteis G. (2003) Lymphoseek: A Molecular Radiopharmaceutical for Sentinel Node Detection. *Annals of Surgical Oncology*. 2003;10,531-538.
46. Gommans GMM, Gommans E, van der Zant FM, Teule GJJ, van der Schors TG, de Waard JWD. (2009) 99mTc Nanocoll: A radiopharmaceutical for sentinel node localisation in breast cancer—In vitro and in vivo results. *Applied Radiation and Isotopes*. 2009;67,1550-1558.
47. Paredes KO, Ruiz-Cabello J, Alarcón DI, Filice M, (2019) *Chapter 14 - The State of the Art of Investigational and Approved Nanomedicine Products for Nucleic Acid Delivery.* 2019; 421-456
48. Unak G, Ozkaya F, Medine EI, Kozgus O, Sakarya S, Bekis R, et al. (2012) Gold nanoparticle probes: design and in vitro applications in cancer cell culture. *Colloids Surf B Biointerfaces*. 2012;90,217-26.
49. Chen Q, Shang W, Zeng C, Wang K, Liang X, Chi C, et al. (2017) Theranostic imaging of liver cancer using targeted optical/MRI dual-modal probes. *Oncotarget*. 2017;8,
50. Lee H-Y, Li Z, Chen K, Hsu AR, Xu C, Xie J, et al. (2008) PET/MRI Dual-Modality Tumor Imaging Using Arginine-Glycine-Aspartic (RGD)–Conjugated Radiolabeled Iron Oxide Nanoparticles. *Journal of Nuclear Medicine*. 2008;49,1371-1379.
51. Mannheim JG, Schmid AM, Schwenck J, Katiyar P, Herfert K, Pichler BJ, et al. (2018) PET/MRI Hybrid Systems. *Seminars in Nuclear Medicine*. 2018;48,332-347.
52. Mahmoudi M, Landry MP, Moore A, Coreas R. (2023) The protein corona from nanomedicine to environmental science. *Nature Reviews Materials*. 2023;8,422-438.

53. Wani TU, Raza SN, Khan NA. (2020) Nanoparticle opsonization: forces involved and protection by long chain polymers. *Polymer Bulletin*. 2020;77,3865-3889.
54. Dasgupta A, Biancacci I, Kiessling F, Lammers T. (2020) Imaging-assisted anticancer nanotherapy. *Theranostics*. 2020;10,956-967.
55. Lin Q, Jin CS, Huang H, Ding L, Zhang Z, Chen J, et al. (2014) Nanoparticle-enabled, image-guided treatment planning of target specific RNAi therapeutics in an orthotopic prostate cancer model. *Small*. 2014;10,3072-82.
56. Yu X, Zhu W, Di Y, Gu J, Guo Z, Li H, et al. (2017) Triple-functional albumin-based nanoparticles for combined chemotherapy and photodynamic therapy of pancreatic cancer with lymphatic metastases. *Int J Nanomedicine*. 2017;12,6771-6785.
57. Mahajan UM, Teller S, Sendler M, Palankar R, van den Brandt C, Schwaiger T, et al. (2016) Tumour-specific delivery of siRNA-coupled superparamagnetic iron oxide nanoparticles, targeted against PLK1, stops progression of pancreatic cancer. *Gut*. 2016;65,1838-1849.
58. Shu G, Chen M, Song J, Xu X, Lu C, Du Y, et al. (2021) Sialic acid-engineered mesoporous polydopamine nanoparticles loaded with SPIO and Fe3+ as a novel theranostic agent for T1/T2 dual-mode MRI-guided combined chemo-photothermal treatment of hepatic cancer. *Bioactive Materials*. 2021;6,1423-1435.
59. Li H, Lin L, Su S, Wen X, Yan R, Liu H, et al. (2022) Enhanced photothermal effect of functionalized HMPDA@AuNPs microcapsules for near-infrared theranostic treatment of tumor. *Journal of Materials Science*. 2022;57,7694-7705.
60. Hosseini SM, Mohammadnejad J, Najafi-Taher R, Zadeh ZB, Tanhaei M, Ramakrishna S. (2023) Multifunctional Carbon-Based Nanoparticles: Theranostic Applications in Cancer Therapy and Diagnosis. *ACS Applied Bio Materials*. 2023;6,1323-1338.
61. Yang S, Wang Z, Ping Y, Miao Y, Xiao Y, Qu L, et al. (2020) PEG/PEI-functionalized single-walled carbon nanotubes as delivery carriers for doxorubicin: synthesis, characterization, and in vitro evaluation. *Beilstein J Nanotechnol*. 2020;11,1728-1741.
62. Guo W, Chen Z, Feng X, Shen G, Huang H, Liang Y, et al. (2021) Graphene oxide (GO)-based nanosheets with combined chemo/photothermal/photodynamic therapy to overcome gastric cancer (GC) paclitaxel resistance by reducing mitochondria-derived adenosine-triphosphate (ATP). *Journal of Nanobiotechnology*. 2021;19,146.
63. Li Z, Ao S, Bu Z, Wu A, Wu X, Shan F, et al. (2016) Clinical study of harvesting lymph nodes with carbon nanoparticles in advanced gastric cancer: a prospective randomized trial. *World J Surg Oncol*. 2016;14,88.
64. Novoselov KS, Geim AK, Morozov SV, Jiang D, Zhang Y, Dubonos SV, et al. (2004) Electric field effect in atomically thin carbon films. *Science*. 2004;306,666-9.
65. Iijima S. (1991) Helical microtubules of graphitic carbon. *Nature*. 1991;354,56-58.
66. Kroto HW, Heath JR, O'Brien SC, Curl RF, Smalley RE. (1985) C60: Buckminsterfullerene. *Nature*. 1985;318,162-163.
67. Hirsch A, Brettreich M, (2006) *Discovery of fullerenes.* 2006; 4-6
68. Ghavanloo E, Rafii-Tabar H, Kausar A, Giannopoulos GI, Fazelzadeh SA. (2023) Experimental and computational physics of fullerenes and their nanocomposites: Synthesis, thermo-mechanical characteristics and nanomedicine applications. *Physics Reports*. 2023;996,1-116.
69. Paukov M, Kramberger C, Begichev I, Kharlamova M, Burdanova M. (2023) Functionalized Fullerenes and Their Applications in Electrochemistry, Solar Cells, and Nanoelectronics. *Materials (Basel)*. 2023;16,
70. Collavini S, Delgado JL. (2018) Fullerenes: the stars of photovoltaics. *Sustainable Energy & Fuels*. 2018;2,2480-2493.

71. Shetti NP, Mishra A, Basu S, Aminabhavi TM. (2021) Versatile fullerenes as sensor materials. *Materials Today Chemistry*. 2021;20,100454.
72. Fernandes NB, Shenoy RUK, Kajampady MK, Dcruz CEM, Shirodkar RK, Kumar L, et al. (2022) Fullerenes for the treatment of cancer: an emerging tool. *Environmental Science and Pollution Research*. 2022;29,58607-58627.
73. Hou W, Shen L, Zhu Y, Wang X, Du T, Yang F, et al. (2024) Fullerene Derivatives for Tumor Treatment: Mechanisms and Application. *International Journal of Nanomedicine*. 2024;19,9771-9797.
74. Goodarzi S, Da Ros T, Conde J, Sefat F, Mozafari M. (2017) Fullerene: biomedical engineers get to revisit an old friend. *Materials Today*. 2017;20,460-480.
75. Hirsch A, Brettreich M, (2005) *Properties.* 2005; 29-33
76. Li H, Zhang H. (2018) The isolated-pentagon rule and nice substructures infullerens. *Ars Mathematica Contemporanea*. 2018;15,487-497.
77. Kroto HW. (1987) The stability of the fullerenes Cn, with n = 24, 28, 32, 36, 50, 60 and 70. *Nature*. 1987;329,529-531.
78. Prinzbach H, Weiler A, Landenberger P, Wahl F, Wörth J, Scott LT, et al. (2000) Gas-phase production and photoelectron spectroscopy of the smallest fullerene, C20. *Nature*. 2000;407,60-63.
79. McKenzie DR, Davis CA, Cockayne DJH, Muller DA, Vassallo AM. (1992) The structure of the C70 molecule. *Nature*. 1992;355,622-624.
80. Hirsch A, (1999) *Principles of Fullerene Reactivity.* 1999; 4-10
81. Chen Z, Wu JI, Corminboeuf C, Bohmann J, Lu X, Hirsch A, et al. (2012) Is C60 buckminsterfullerene aromatic? *Physical Chemistry Chemical Physics*. 2012;14,14886-14891.
82. Hirsch A, (1999) *Structure and Electronic Properties of C60* 1999; 4-10
83. Rašović I. (2017) Water-soluble fullerenes for medical applications. *Materials Science and Technology*. 2017;33,777-794.
84. Hirsch A, (1999) *Principles of Fullerene Reactivity.* 1999; 4-10
85. Biglova YN, Mustafin AG. (2019) Nucleophilic cyclopropanation of [60]fullerene by the addition-elimination mechanism. *RSC Adv*. 2019;9,22428-22498.
86. Camps X, Hirsch A. (1997) Efficient cyclopropanation of C60 starting from malonates. *Journal of the Chemical Society, Perkin Transactions 1*. 1997;1595-1596.
87. Boudon C, Gisselbrecht J-P, Gross M, Isaacs L, Anderson HL, Faust R, et al. (1995) Electrochemistry of Mono- through Hexakis-adducts of C60. *Helvetica Chimica Acta*. 1995;78,1334-1344.
88. Miller GP. (2006) Reactions between aliphatic amines and [60]fullerene: a review. *Comptes Rendus Chimie*. 2006;9,952-959.
89. A. Hirsch MB, (2004) *Addition of amines.* 2004; 87-91
90. Grebowski J, Litwinienko G. (2022) Metallofullerenols in biomedical applications. *European Journal of Medicinal Chemistry*. 2022;238,114481.
91. Mikawa M, Kato H, Okumura M, Narazaki M, Kanazawa Y, Miwa N, et al. (2001) Paramagnetic water-soluble metallofullerenes having the highest relaxivity for MRI contrast agents. *Bioconjug Chem*. 2001;12,510-4.
92. Bolskar RD, (2008) *Gadolinium Endohedral Metallofullerene-Based MRI Contrast Agents.* 2008; 157-180
93. Dolmans DE, Fukumura D, Jain RK. (2003) Photodynamic therapy for cancer. *Nat Rev Cancer*. 2003;3,380-7.
94. Sharman WM, Allen CM, van Lier JE. (1999) Photodynamic therapeutics: basic principles and clinical applications. *Drug Discovery Today*. 1999;4,507-517.

95. Chen J, Fan T, Xie Z, Zeng Q, Xue P, Zheng T, et al. (2020) Advances in nanomaterials for photodynamic therapy applications: Status and challenges. *Biomaterials*. 2020;237,119827.
96. Yu X-T, Sui S-Y, He Y-X, Yu C-H, Peng Q. (2022) Nanomaterials-based photosensitizers and delivery systems for photodynamic cancer therapy. *Biomaterials Advances*. 2022;135,212725.
97. Dougherty TJ, Grindey GB, Fiel R, Weishaupt KR, Boyle DG. (1975) Photoradiation Therapy. II. Cure of Animal Tumors With Hematoporphyrin and Light23. *JNCI: Journal of the National Cancer Institute*. 1975;55,115-121.
98. Yano S, Hirohara S, Obata M, Hagiya Y, Ogura S-i, Ikeda A, et al. (2011) Current states and future views in photodynamic therapy. *Journal of Photochemistry and Photobiology C: Photochemistry Reviews*. 2011;12,46-67.
99. Bartosz G. (2004) Druga twarz tlenu. *Wolne rodniki w przyrodzie*. 2004;358-359.
100. Kozinska A, Oles T, Sarna T. (2012) Photoactivation and Detection of Photoexcited Molecules and Photochemical Products. *Israel Journal of Chemistry*. 2012;52,745-756.
101. Huang YY, Sharma SK, Yin R, Agrawal T, Chiang LY, Hamblin MR. (2014) Functionalized fullerenes in photodynamic therapy. *J Biomed Nanotechnol*. 2014;10,1918-36.
102. Mroz P, Tegos GP, Gali H, Wharton T, Sarna T, Hamblin MR. (2007) Photodynamic therapy with fullerenes. *Photochem Photobiol Sci*. 2007;6,1139-49.
103. Hamblin MR. (2018) Fullerenes as photosensitizers in photodynamic therapy: pros and cons. *Photochem Photobiol Sci*. 2018;17,1515-1533.
104. Jain R, Mohanty S, Sarode I, Biswas S, Singhvi G, Dubey SK. (2023) Multifunctional Photoactive Nanomaterials for Photodynamic Therapy against Tumor: Recent Advancements and Perspectives. *Pharmaceutics*. 2023;15,109.
105. Sharma SK, Chiang LY, Hamblin MR. (2011) Photodynamic therapy with fullerenes in vivo: reality or a dream? *Nanomedicine (Lond)*. 2011;6,1813-25.
106. Guldi DM, Prato M. (2000) Excited-State Properties of C60 Fullerene Derivatives. *Accounts of Chemical Research*. 2000;33,695-703.
107. Hou W, Shi G, Wu S, Mo J, Shen L, Zhang X, et al. (2022) Application of Fullerenes as Photosensitizers for Antimicrobial Photodynamic Inactivation: A Review. *Frontiers in Microbiology*. 2022;13,
108. Tokuyama H, Yamago S, Nakamura E, Shiraki T, Sugiura Y. (1993) Photoinduced biochemical activity of fullerene carboxylic acid. *Journal of the American Chemical Society*. 1993;115,7918-7919.
109. Cho M, Lee J, Mackeyev Y, Wilson LJ, Alvarez PJJ, Hughes JB, et al. (2010) Visible Light Sensitized Inactivation of MS-2 Bacteriophage by a Cationic Amine-Functionalized C60 Derivative. *Environmental Science & Technology*. 2010;44,6685-6691.
110. Chae SR, Badireddy AR, Farner Budarz J, Lin S, Xiao Y, Therezien M, et al. (2010) Heterogeneities in fullerene nanoparticle aggregates affecting reactivity, bioactivity, and transport. *ACS Nano*. 2010;4,5011-8.
111. Soldà A, Cantelli A, Di Giosia M, Montalti M, Zerbetto F, Rapino S, et al. (2017) C60@lysozyme: a new photosensitizing agent for photodynamic therapy. *Journal of Materials Chemistry B*. 2017;5,6608-6615.
112. Jiménez-Banzo A, Ragàs X, Kapusta P, Nonell S. (2008) Time-resolved methods in biophysics. 7. Photon counting vs. analog time-resolved singlet oxygen phosphorescence detection. *Photochemical & Photobiological Sciences*. 2008;7,1003-1010.
113. Finkelstein E, Rosen GM, Rauckman EJ. (1980) Spin trapping of superoxide and hydroxyl radical: practical aspects. *Arch Biochem Biophys*. 1980;200,1-16.

114. Korytowski W, Girotti AW. (1999) Singlet oxygen adducts of cholesterol: photogeneration and reductive turnover in membrane systems. *Photochem Photobiol*. 1999;70,484-9.

115. Girotti AW. (2001) Photosensitized oxidation of membrane lipids: reaction pathways, cytotoxic effects, and cytoprotective mechanisms. *Journal of Photochemistry and Photobiology B: Biology*. 2001;63,103-113.

116. Pochkaeva EI, Podolsky NE, Zakusilo DN, Petrov AV, Charykov NA, Vlasov TD, et al. (2020) Fullerene derivatives with amino acids, peptides and proteins: From synthesis to biomedical application. *Progress in Solid State Chemistry*. 2020;57,100255.

117. Wang J, Xie L, Wang T, Wu F, Meng J, Liu J, et al. (2017) Visible light-switched cytosol release of siRNA by amphiphilic fullerene derivative to enhance RNAi efficacy in vitro and in vivo. *Acta Biomater*. 2017;59,158-169.

118. Biswas R, Batista Da Rocha C, Bennick RA, Zhang J. (2023) Water-Soluble Fullerene Monoderivatives for Biomedical Applications. *ChemMedChem*. 2023;18,e202300296.

119. Kazemzadeh H, Mozafari M. (2019) Fullerene-based delivery systems. *Drug Discovery Today*. 2019;24,898-905.

120. Zakharian TY, Seryshev A, Sitharaman B, Gilbert BE, Knight V, Wilson LJ. (2005) A fullerene-paclitaxel chemotherapeutic: synthesis, characterization, and study of biological activity in tissue culture. *J Am Chem Soc*. 2005;127,12508-9.

121. Butowska K, Kozak W, Zdrowowicz M, Makurat S, Rychłowski M, Hać A, et al. (2019) Cytotoxicity of doxorubicin conjugated with C60 fullerene. Structural and in vitro studies. *Structural Chemistry*. 2019;30,2327-2338.

122. Grebinyk A, Prylutska S, Chepurna O, Grebinyk S, Prylutskyy Y, Ritter U, et al. (2019) Synergy of Chemo- and Photodynamic Therapies with C60 Fullerene-Doxorubicin Nanocomplex. *Nanomaterials*. 2019;9,1540.

123. Grebinyk A, Prylutska S, Grebinyk S, Prylutskyy Y, Ritter U, Matyshevska O, et al. (2019) Complexation with C60 Fullerene Increases Doxorubicin Efficiency against Leukemic Cells In Vitro. *Nanoscale Research Letters*. 2019;14,61.

124. Misra C, Kumar M, Sharma G, Kumar R, Singh B, Katare OP, et al. (2017) Glycinated fullerenes for tamoxifen intracellular delivery with improved anticancer activity and pharmacokinetics. *Nanomedicine (Lond)*. 2017;12,1011-1023.

125. Lynchak OV, Prylutskyy YI, Rybalchenko VK, Kyzyma OA, Soloviov D, Kostjukov VV, et al. (2017) Comparative Analysis of the Antineoplastic Activity of C(60) Fullerene with 5-Fluorouracil and Pyrrole Derivative In Vivo. *Nanoscale Res Lett*. 2017;12,8.

126. Shi J, Wang B, Wang L, Lu T, Fu Y, Zhang H, et al. (2016) Fullerene (C60)-based tumor-targeting nanoparticles with “off-on” state for enhanced treatment of cancer. *Journal of Controlled Release*. 2016;235,245-258.

127. Misra C, Thotakura N, Kumar R, Singh B, Sharma G, Katare OP, et al. (2017) Improved cellular uptake, enhanced efficacy and promising pharmacokinetic profile of docetaxel employing glycine-tethered C60-fullerenes. *Materials Science and Engineering: C*. 2017;76,501-508.

128. Nalepa P, Gawecki R, Szewczyk G, Balin K, Dulski M, Sajewicz M, et al. (2020) A [60]fullerene nanoconjugate with gemcitabine: synthesis, biophysical properties and biological evaluation for treating pancreatic cancer. *Cancer Nanotechnology*. 2020;11,2.

129. Pochapski DJ, Carvalho dos Santos C, Leite GW, Pulcinelli SH, Santilli CV. (2021) Zeta Potential and Colloidal Stability Predictions for Inorganic Nanoparticle Dispersions: Effects of Experimental Conditions and Electrokinetic Models on the Interpretation of Results. *Langmuir*. 2021;37,13379-13389.

130. Honary S, Zahir F. (2013) Effect of zeta potential on the properties of nano-drug delivery systems-a review (Part 1). *Tropical journal of pharmaceutical research*. 2013;12,255-264.

131. Honary S, Zahir F. (2013) Effect of zeta potential on the properties of nano-drug delivery systems-a review (Part 2). *Tropical journal of pharmaceutical research*. 2013;12,265-273.

132. Li J, Guan M, Wang T, Zhen M, Zhao F, Shu C, et al. (2016) Gd@C82-(ethylenediamine)8 Nanoparticle: A New High-Efficiency Water-Soluble ROS Scavenger. *ACS Applied Materials & Interfaces*. 2016;8,25770-25776.

133. Williams M, Lomberk G, Urrutia R, (2018) *EGFR (ErbB) Signaling Pathways in Pancreatic Cancer Pathogenesis.* 2018; 383-408

134. Oliveira-Cunha M, Newman WG, Siriwardena AK. (2011) Epidermal Growth Factor Receptor in Pancreatic Cancer. *Cancers*. 2011;3,1513-1526.

135. Moore MJ, Goldstein D, Hamm J, Figer A, Hecht JR, Gallinger S, et al. (2007) Erlotinib plus gemcitabine compared with gemcitabine alone in patients with advanced pancreatic cancer: a phase III trial of the National Cancer Institute of Canada Clinical Trials Group. *J Clin Oncol*. 2007;25,1960-6.

136. Shin S, Park CM, Kwon H, Lee K-H. (2016) Erlotinib plus gemcitabine versus gemcitabine for pancreatic cancer: real-world analysis of Korean national database. *BMC Cancer*. 2016;16,443.

137. Pao W, Miller VA, Politi KA, Riely GJ, Somwar R, Zakowski MF, et al. (2005) Acquired resistance of lung adenocarcinomas to gefitinib or erlotinib is associated with a second mutation in the EGFR kinase domain. *PLoS Med*. 2005;2,e73.

138. Biegański P, Godel M, Riganti C, Kawano DF, Kopecka J, Kowalski K. (2022) Click ferrocenyl-erlotinib conjugates active against erlotinib-resistant non-small cell lung cancer cells in vitro. *Bioorganic Chemistry*. 2022;119,105514.

139. Zhao X, Ma H, Chen J, Zhang F, Jia X, Xue J. (2019) An epidermal growth factor receptor-targeted and endoplasmic reticulum-localized organic photosensitizer toward photodynamic anticancer therapy. *European Journal of Medicinal Chemistry*. 2019;182,111625.

140. Cheruku RR, Cacaccio J, Durrani FA, Tabaczynski WA, Watson R, Marko A, et al. (2019) Epidermal Growth Factor Receptor-Targeted Multifunctional Photosensitizers for Bladder Cancer Imaging and Photodynamic Therapy. *Journal of Medicinal Chemistry*. 2019;62,2598-2617.

141. Hein CD, Liu XM, Wang D. (2008) Click chemistry, a powerful tool for pharmaceutical sciences. *Pharm Res*. 2008;25,2216-30.

142. Amblard F, Cho JH, Schinazi RF. (2009) Cu(I)-catalyzed Huisgen azide-alkyne 1,3-dipolar cycloaddition reaction in nucleoside, nucleotide, and oligonucleotide chemistry. *Chem Rev*. 2009;109,4207-20.

143. Meldal M, Tornøe CW. (2008) Cu-Catalyzed Azide−Alkyne Cycloaddition. *Chemical Reviews*. 2008;108,2952-3015.

144. Worrell BT, Malik JA, Fokin VV. (2013) Direct evidence of a dinuclear copper intermediate in Cu(I)-catalyzed azide-alkyne cycloadditions. *Science*. 2013;340,457-60.

145. Dong Y, Siegwart DJ, Anderson DG. (2019) Strategies, design, and chemistry in siRNA delivery systems. *Advanced Drug Delivery Reviews*. 2019;144,133-147.

146. Alshaer W, Zureigat H, Al Karaki A, Al-Kadash A, Gharaibeh L, Hatmal MmM, et al. (2021) siRNA: Mechanism of action, challenges, and therapeutic approaches. *European Journal of Pharmacology*. 2021;905,174178.

147. Dammes N, Peer D. (2020) Paving the Road for RNA Therapeutics. *Trends in Pharmacological Sciences*. 2020;41,755-775.

148. Li Z, Rana TM. (2012) Molecular Mechanisms of RNA-Triggered Gene Silencing Machineries. *Accounts of Chemical Research*. 2012;45,1122-1131.
149. Xie X, Yu T, Li X, Zhang N, Foster LJ, Peng C, et al. (2023) Recent advances in targeting the “undruggable” proteins: from drug discovery to clinical trials. *Signal Transduction and Targeted Therapy*. 2023;8,335.
150. Springer AD, Dowdy SF. (2018) GalNAc-siRNA Conjugates: Leading the Way for Delivery of RNAi Therapeutics. *Nucleic Acid Ther*. 2018;28,109-118.
151. Ahn I, Kang CS, Han J. (2023) Where should siRNAs go: applicable organs for siRNA drugs. *Experimental & Molecular Medicine*. 2023;55,1283-1292.
152. Hattab D, Gazzali AM, Bakhtiar A. (2021) Clinical Advances of siRNA-Based Nanotherapeutics for Cancer Treatment. *Pharmaceutics*. 2021;13,
153. Huang R, Du H, Cheng L, Zhang P, Meng F, Zhong Z. (2023) Targeted nanodelivery of siRNA against KRAS G12D inhibits pancreatic cancer. *Acta Biomater*. 2023;168,529-539.
154. Ferdows BE, Patel DN, Chen W, Huang X, Kong N, Tao W. (2022) RNA cancer nanomedicine: nanotechnology-mediated RNA therapy. *Nanoscale*. 2022;14,4448-4455.
155. Mostafavi E, Zare H. (2022) Carbon-based nanomaterials in gene therapy. *OpenNano*. 2022;7,100062.
156. Bholakant R, Qian H, Zhang J, Huang X, Huang D, Feijen J, et al. (2020) Recent Advances of Polycationic siRNA Vectors for Cancer Therapy. *Biomacromolecules*. 2020;21,2966-2982.
157. Chen M, Dong C, Shi S. (2021) Nanoparticle-Mediated siRNA Delivery and Multifunctional Modification Strategies for Effective Cancer Therapy. *Advanced Materials Technologies*. 2021;6,2001236.
158. Isobe H, Nakanishi W, Tomita N, Jinno S, Okayama H, Nakamura E. (2006) Gene Delivery by Aminofullerenes: Structural Requirements for Efficient Transfection. *Chemistry – An Asian Journal*. 2006;1,167-175.
159. Minami K, Okamoto K, Doi K, Harano K, Noiri E, Nakamura E. (2014) siRNA delivery targeting to the lung via agglutination-induced accumulation and clearance of cationic tetraamino fullerene. *Scientific Reports*. 2014;4,4916.
160. Sakurai F, Nishioka T, Yamashita F, Takakura Y, Hashida M. (2001) Effects of erythrocytes and serum proteins on lung accumulation of lipoplexes containing cholesterol or DOPE as a helper lipid in the single-pass rat lung perfusion system. *European Journal of Pharmaceutics and Biopharmaceutics*. 2001;52,165-172.
161. Rich DH, Singh J, (1979) *Chapter 5 - The Carbodiimide Method.* 1979; 1, 241-261
162. El-Faham A, Albericio F. (2011) Peptide Coupling Reagents, More than a Letter Soup. *Chemical Reviews*. 2011;111,6557-6602.
163. Hermanson GT, (2013) *Chapter 4 - Zero-Length Crosslinkers.* 2013; 259-273
164. Staros JV, Wright RW, Swingle DM. (1986) Enhancement by N-hydroxysulfosuccinimide of water-soluble carbodiimide-mediated coupling reactions. *Analytical Biochemistry*. 1986;156,220-222.
165. Wickramathilaka MP, Tao BY. (2019) Characterization of covalent crosslinking strategies for synthesizing DNA-based bioconjugates. *Journal of Biological Engineering*. 2019;13,63.
166. Bartczak D, Kanaras AG. (2011) Preparation of Peptide-Functionalized Gold Nanoparticles Using One Pot EDC/Sulfo-NHS Coupling. *Langmuir*. 2011;27,10119-10123.
167. Keleştemur S, Altunbek M, Culha M. (2017) Influence of EDC/NHS coupling chemistry on stability and cytotoxicity of ZnO nanoparticles modified with proteins. *Applied Surface Science*. 2017;403,455-463.
168. Hunter JH, Anderson MJ, Castan IFSF, Graham JS, Salvini CLA, Stanway-Gordon HA, et al. (2021) Highly efficient on-DNA amide couplings promoted by micelle forming surfactants for the synthesis of DNA encoded libraries. *Chemical Science*. 2021;12,9475-9484.

169. Serda M, Malarz K, Mrozek-Wilczkiewicz A, Wojtyniak M, Musioł R, Curley SA. (2020) Glycofullerenes as non-receptor tyrosine kinase inhibitors- towards better nanotherapeutics for pancreatic cancer treatment. *Scientific Reports*. 2020;10,260.
170. Belgorodsky B, Fadeev L, Ittah V, Benyamini H, Zelner S, Huppert D, et al. (2005) Formation and Characterization of Stable Human Serum Albumin−Tris-malonic Acid [C60]Fullerene Complex. *Bioconjugate Chemistry*. 2005;16,1058-1062.
171. Sigwalt D, Holler M, Iehl J, Nierengarten J-F, Nothisen M, Morin E, et al. (2011) Gene delivery with polycationic fullerene hexakis-adducts. *Chemical Communications*. 2011;47,4640-4642.
172. Rudzinski WE, Palacios A, Ahmed A, Lane MA, Aminabhavi TM. (2016) Targeted delivery of small interfering RNA to colon cancer cells using chitosan and PEGylated chitosan nanoparticles. *Carbohydr Polym*. 2016;147,323-332.
173. Tekade RK, Sun X. (2017) The Warburg effect and glucose-derived cancer theranostics. *Drug Discov Today*. 2017;22,1637-1653.
174. Kataoka H, Nishie H, Tanaka M, Sasaki M, Nomoto A, Osaki T, et al. (2021) Potential of Photodynamic Therapy Based on Sugar-Conjugated Photosensitizers. *Journal of Clinical Medicine*. 2021;10,841.
175. Serda M, Ware MJ, Newton JM, Sachdeva S, Krzykawska-Serda M, Nguyen L, et al. (2018) Development of photoactive Sweet-C(60) for pancreatic cancer stellate cell therapy. *Nanomedicine (Lond)*. 2018;13,2981-2993.
176. Otake E, Sakuma S, Torii K, Maeda A, Ohi H, Yano S, et al. (2010) Effect and mechanism of a new photodynamic therapy with glycoconjugated fullerene. *Photochem Photobiol*. 2010;86,1356-63.
177. Serda M, Ware MJ, Newton JM, Sachdeva S, Krzykawska-Serda M, Nguyen L, et al. (2018) Development of Photoactive Sweet-C60 for Pancreatic Cancer Stellate Cell Therapy. *Nanomedicine*. 2018;13,2981-2993.
178. Raoof M, Mackeyev Y, Cheney MA, Wilson LJ, Curley SA. (2012) Internalization of C60 fullerenes into cancer cells with accumulation in the nucleus via the nuclear pore complex. *Biomaterials*. 2012;33,2952-2960.
179. Blazkova I, Viet Nguyen H, Kominkova M, Konecna R, Chudobova D, Krejcova L, et al. (2014) Fullerene as a transporter for doxorubicin investigated by analytical methods and in vivo imaging. *ELECTROPHORESIS*. 2014;35,1040-1049.
180. Li J, Yang W, Cui R, Wang D, Chang Y, Gu W, et al. (2016) Metabolizer in vivo of fullerenes and metallofullerenes by positron emission tomography. *Nanotechnology*. 2016;27,155101.
181. Li W, Chen C, Ye C, Wei T, Zhao Y, Lao F, et al. (2008) The translocation of fullerenic nanoparticles into lysosome via the pathway of clathrin-mediated endocytosis. *Nanotechnology*. 2008;19,145102.
182. Di Giosia M, Soldà A, Seeger M, Cantelli A, Arnesano F, Nardella MI, et al. (2021) A Bio-Conjugated Fullerene as a Subcellular-Targeted and Multifaceted Phototheranostic Agent. *Advanced Functional Materials*. 2021;31,2101527.
183. Bashiri G, Padilla MS, Swingle KL, Shepherd SJ, Mitchell MJ, Wang K. (2023) Nanoparticle protein corona: from structure and function to therapeutic targeting. *Lab on a Chip*. 2023;23,1432-1466.
184. Zhang Y, Wu JLY, Lazarovits J, Chan WCW. (2020) An Analysis of the Binding Function and Structural Organization of the Protein Corona. *Journal of the American Chemical Society*. 2020;142,8827-8836.

185. Singh N, Marets C, Boudon J, Millot N, Saviot L, Maurizi L. (2021) In vivo protein corona on nanoparticles: does the control of all material parameters orient the biological behavior? *Nanoscale Advances*. 2021;3,1209-1229.

186. Mosquera J, García I, Henriksen-Lacey M, Martínez-Calvo M, Dhanjani M, Mascareñas JL, et al. (2020) Reversible Control of Protein Corona Formation on Gold Nanoparticles Using Host–Guest Interactions. *ACS Nano*. 2020;14,5382-5391.

187. de Castro CE, Panico K, Stangherlin LM, Ribeiro CAS, da Silva MCC, Carneiro-Ramos MS, et al. (2020) The Protein Corona Conundrum: Exploring the Advantages and Drawbacks of its Presence around Amphiphilic Nanoparticles. *Bioconjugate Chemistry*. 2020;31,2638-2647.

188. Wu L, Fu F, Wang W, Wang W, Huang Z, Huang Y, et al. (2023) Plasma protein corona forming upon fullerene nanocomplex: Impact on both counterparts. *Particuology*. 2023;73,26-36.

189. Di Giosia M, Bomans PHH, Bottoni A, Cantelli A, Falini G, Franchi P, et al. (2018) Proteins as supramolecular hosts for C60: a true solution of C60 in water. *Nanoscale*. 2018;10,9908-9916.

190. Calvaresi M, Zerbetto F. (2010) Baiting Proteins with C60. *ACS Nano*. 2010;4,2283-2299.

191. Di Giosia M, Zerbetto F, Calvaresi M. (2021) Incorporation of Molecular Nanoparticles Inside Proteins: The Trojan Horse Approach in Theranostics. *Accounts of Materials Research*. 2021;2,594-605.

192. Kang S-g, Araya-Secchi R, Wang D, Wang B, Huynh T, Zhou R. (2014) Dual Inhibitory Pathways of Metallofullerenol Gd@C82(OH)22 on Matrix Metalloproteinase-2: Molecular insight into drug-like nanomedicine. *Scientific Reports*. 2014;4,4775.

193. Yang Z, Kang S-g, Zhou R. (2014) Nanomedicine: de novo design of nanodrugs. *Nanoscale*. 2014;6,663-677.

194. Zhou W, Huo J, Yang Y, Zhang X, Li S, Zhao C, et al. (2020) Aminated Fullerene Abrogates Cancer Cell Migration by Directly Targeting Myosin Heavy Chain 9. *ACS Applied Materials & Interfaces*. 2020;12,56862-56873.

195. Pan Y, Wang L, Kang SG, Lu Y, Yang Z, Huynh T, et al. (2015) Gd-Metallofullerenol Nanomaterial Suppresses Pancreatic Cancer Metastasis by Inhibiting the Interaction of Histone Deacetylase 1 and Metastasis-Associated Protein 1. *ACS Nano*. 2015;9,6826-36.

196. Qin Y, Chen K, Gu W, Dong X, Lei R, Chang Y, et al. (2018) Small size fullerenol nanoparticles suppress lung metastasis of breast cancer cell by disrupting actin dynamics. *Journal of Nanobiotechnology*. 2018;16,54.

197. Gu W, Bai X, Ren K, Zhao X, Xia S, Zhang J, et al. (2018) Mono-fullerenols modulating cell stiffness by perturbing actin bundling. *Nanoscale*. 2018;10,1750-1758.

198. Song Y, Zhang M, Zhao L, Yin X, Zhao J, Li J, et al. (2014) Regulation on mechanical properties of collagen: Enhanced bioactivities of metallofullerol. *Nanomedicine: Nanotechnology, Biology and Medicine*. 2014;10,783-793.

199. Liu J, Kang S-g, Wang P, Wang Y, Lv X, Liu Y, et al. (2018) Molecular mechanism of Gd@C82(OH)22 increasing collagen expression: Implication for encaging tumor. *Biomaterials*. 2018;152,24-36.

200. Li J, Chen L, Su H, Yan L, Gu Z, Chen Z, et al. (2019) The pharmaceutical multi-activity of metallofullerenol invigorates cancer therapy. *Nanoscale*. 2019;11,14528-14539.

201. Li L, Zhen M, Wang H, Sun Z, Jia W, Zhao Z, et al. (2020) Functional Gadofullerene Nanoparticles Trigger Robust Cancer Immunotherapy Based on Rebuilding an Immunosuppressive Tumor Microenvironment. *Nano Letters*. 2020;20,4487-4496.

202. Li X, Zhen M, Deng R, Yu T, Li J, Zhang Y, et al. (2018) RF-assisted gadofullerene nanoparticles induces rapid tumor vascular disruption by down-expression of tumor vascular endothelial cadherin. *Biomaterials*. 2018;163,142-153.

203. Guan M, Zhou Y, Liu S, Chen D, Ge J, Deng R, et al. (2019) Photo-triggered gadofullerene: enhanced cancer therapy by combining tumor vascular disruption and stimulation of anti-tumor immune responses. *Biomaterials*. 2019;213,119218.
204. Ye L, Kollie L, Liu X, Guo W, Ying X, Zhu J, et al. (2021) Antitumor Activity and Potential Mechanism of Novel Fullerene Derivative Nanoparticles. *Molecules*. 2021;26,3252.
205. Matysiak-Kucharek M, Czajka M, Sawicki K, Kruszewski M, Kapka-Skrzypczak L. (2018) Effect of nanoparticles on the expression and activity of matrix metalloproteinases. *Nanotechnology Reviews*. 2018;7,541-553.
206. Mustafa S, Koran S, AlOmair L. (2022) Insights Into the Role of Matrix Metalloproteinases in Cancer and its Various Therapeutic Aspects: A Review. *Frontiers in Molecular Biosciences*. 2022;9,
207. Li J, Chen L, Yan L, Gu Z, Chen Z, Zhang A, et al. (2019) A Novel Drug Design Strategy: An Inspiration from Encaging Tumor by Metallofullerenol Gd@C82(OH)22. *Molecules*. 2019;24,2387.

ACS Biomaterials SCIENCE & ENGINEERING

pubs.acs.org/journal/abseba Article

Developing [60]Fullerene Nanomaterials for Better Photodynamic Treatment of Non-Melanoma Skin Cancers

Maciej Serda,* Grzegorz Szewczyk, Olga Krzysztyńska-Kuleta, Julia Korzuch, Mateusz Dulski, Robert Musioł, and Tadeusz Sarna

Cite This: *ACS Biomater. Sci. Eng.* 2020, 6, 5930−5940

Read Online

ACCESS | Metrics & More | Article Recommendations | Supporting Information

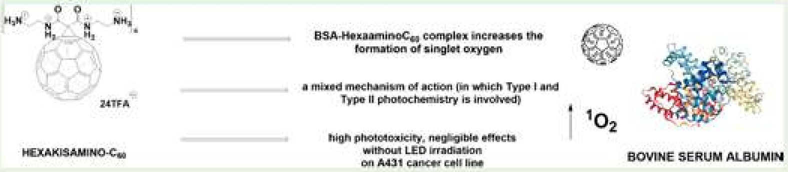

ABSTRACT: Skin cancer is the most common cancer in the U.S.A. and Europe. Its subtype, squamous skin carcinoma (SCC), if allowed to grow, has the potential to metastasize and can become deadly. Currently, carbon nanomaterials are being developed to treat cancer due to their attractive physicochemical and biological properties such as an enhanced permeability effect and their ability to produce reactive oxygen species. Here, we describe the synthesis of two water-soluble aminofullerenes (MonoaminoC$_{60}$ and HexakisaminoC$_{60}$), which were evaluated as novel [60]fullerene based photosentizers exhibiting anticancer properties. Moreover, the previously described neutral glycofullerene GF1 and its peracetylated lipophilic precursor MMS48 were compared with the aminofullerenes for their ability to generate reactive oxygen species and oxidize lipids. Remarkably, the generation of singlet oxygen and a superoxide radical by HexakisaminoC$_{60}$ was found to be markedly elevated in the presence of bovine serum albumin and NADH, respectively. Mechanistic studies of lipid peroxidation using cholesterol as a unique reporter molecule revealed that although all four fullerene nanomaterials primarily generated singlet oxygen, superoxide anion was also formed, which suggest a mixed mechanism of action (in which Type I and Type II photochemistry is involved). The [60]fullerene derivative HexakisaminoC$_{60}$ was also studied for its phototoxicity in squamous skin cancer cell line (A431) using the MTT test and propidium iodide staining.

KEYWORDS: *[60]fullerene, non-melanoma skin cancer, photodynamic therapy, singlet oxygen, EPR spin trapping, lipid peroxidation*

■ INTRODUCTION

Non-melanoma skin cancer (NMSC) is a serious malignant disease, which frequently occurs in older Caucasian patients and is categorized into two subgroups: basal cell carcinoma (BCC) and squamous cell carcinoma (SCC).[1,2] While metastatic BCC is rarely diagnosed,[3,4] metastatic SCC is characterized by a specific proliferation of invasive squamous cells and has an annual incidence of approximately 4%. Despite its statistically low mortality, this malignancy causes considerable problems in the healthcare systems in Europe, the U.S.A., and Australia. A plethora of risk factors are involved in melanoma and NMSC pathogenesis including UV and ionizing radiation, and the occurrence of alterations in the oncogenes/tumor suppressor genes such as BRAF, PTEN, and TP53.[5] The metastatic potential, mortality rates, and reoccurrence are higher for SCC than for BSC, and the current clinical treatment options include surgical excision, radiation therapy, chemotherapy, and any combination of the above.[6] Photodynamic therapy has been used as a successful treatment method in clinical practice with the topical use of 5-aminolevulinic acid methyl ester (MAL-PDT) in patients suffering from basal cell carcinoma.[7] Some novel chemotherapeutic strategies are also under development for the treatment of skin cancer including the use of the inhibitors of the protein tyrosine kinases such as EGFR and non-receptor Src kinases.[8,9]

The use of nanomedical approaches has been extensively explored for both diagnosing and treating skin cancers, including EGFR-targeted immunoliposomes, 5-ALA nanoconjugates with polylactic acid and engineered gold nanoparticles.[10−12] Engineered carbon nanomaterials are promising new approaches, mainly for their cancer photodynamic therapy (PDT) and antimicrobial photodynamic inactivation (PDI) applications.[13,14] The water-soluble fullerene derivatives tend

Received: June 23, 2020
Accepted: September 3, 2020
Published: September 3, 2020

to be great candidates for photosensitizers because of the high triplet yields and the long triplet lifetime of the C_{60} cage, which facilitate their interaction with molecular oxygen.[15] The pioneering studies performed by the Hamblin and Wilson groups, which were mainly focused on the Bingel–Hirsch monoadducts and functionalized pyrrolidinofullerenes, demonstrated the utility of water-soluble aminofullerenes in PDT.[16−19] An interesting addition to the traditional C_{60}-based photosensitizers are the Gadolinium-containing endohedral fullerenes and the derivatives of Gd@C_{82}, which are also used as MRI-contrast agents and to stimulate immunological responses followed by modulating the tumor microenvironment.[20,21] Despite weak absorption of [60]fullerenes in the deep-penetrating NIR region of the spectrum (above 700 nm), they are able to perform the *Type 1* and *Type 2* photochemical reactions and are highly resistant to photobleaching, which make them an attractive option as photosensitizers for most PDT applications.[17] Application of low-penetrating blue light illuminations can be overcome by using femtosecond lasers in two-photon excitation experiments or upconverting nanoparticles such as $NaYF_4$ with Yb^{3+}/ Er^{3+} dopants *via* covalent conjugation/coating absorption to the photosensitizer scaffold.[22]

Previous studies, performed by our group, demonstrated that the water-soluble glycofullerenes were photoactive and they localized inside the nuclear envelope of the pancreatic stellate cells (PSCs).[23] Moreover, the results that were obtained from the cited studies revealed that glycofullerenes could effectively inhibit the nonreceptor tyrosine kinases, with a selectivity toward the FYN A protein, which is an important potential target for skin cancers, even in the presence of the FBS proteins.[24] This observation could be of use in combinational therapies because tyrosine kinase inhibitors are also being investigated in the treatment of skin cancers.[25] At the same time, several reports have demonstrated interactions between the albumin proteins and the photosensitizers, which played an important role in their biodistribution within the tumor tissues.[26] The water-soluble fullerenes are well-known for their interactions with human serum albumin, which forms a stable complex with the [60]fullerene *tris*-malonic acid (C_3 isomer called CF)[27] or PCBM fullerene.[28] Interestingly, although no effects on the quantum yield of $^1O_2$ production was observed for a bovine serum albumin (BSA) complex with [60]fullerene *tris*-malonic acid, the triplet lifetime of HSA-CF was significantly shortened, compared to the noncomplexed fullerene.[29]

On the basis of our previous studies, we wanted to evaluate the possibility of treating non-melanoma skin cancers using the [60]fullerene derivatives. Although our previous studies on pancreatic stellate cells using a water-soluble glycofullerene (*Sweet-C$_{60}$*) demonstrated that it was photoactive, no biophysical studies were performed and therefore its photochemistry remains unknown.[23] Here, the physicochemical properties of the neutral glycofullerene GF1 (a water-soluble analog of *Sweet-C$_{60}$*) and its peracetylated lipophilic analog MMS48 were compared with those of two cationic aminofullerenes— MomoaminoC_{60} and HexakisaminoC_{60} (Figure 1). The formation of singlet oxygen was confirmed by measuring its phosphorescence at 1270 nm in the presence and absence of albumin (BSA). Using EPR spin trapping and HPLC with electrochemical detection, we monitored cholesterol peroxidation and protein oxidation, which revealed that the synthesized fullerene nanomaterials were promising photosensitizers that could be used in anticancer photodynamic therapy. Both singlet oxygen and oxygen radicals can cause oxidative damage to vital targets in cells by starting chain reactions of peroxidation in the cell membranes and disrupting the enzymatic or structural functions of proteins. Lipid and protein peroxides can also damage other important targets in cells.[30,31] The ability to cause photooxidized damage to cellular targets was confirmed using phototoxicity assays in a cellular model of squamous skin cancer.

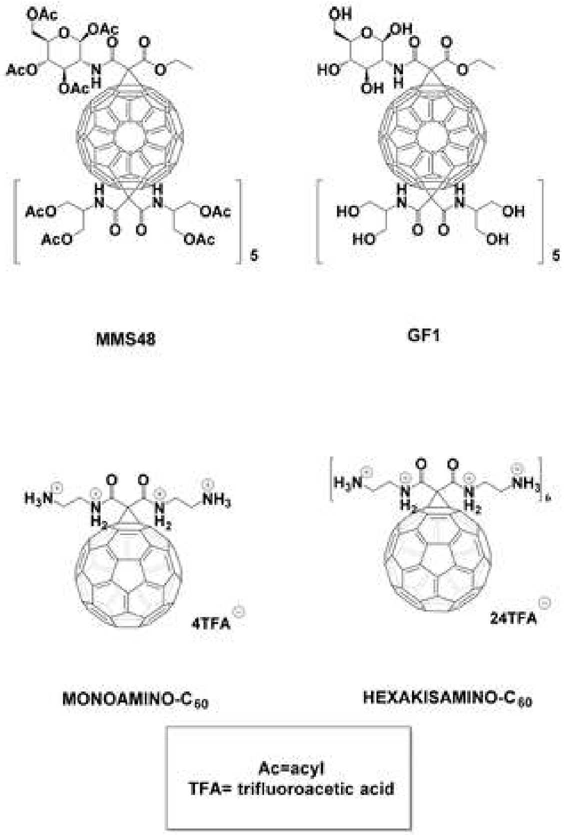

Figure 1. Chemical structures of the fullerenes GF1, MMS48, MONOAMINOC_{60}, and HEXAKISAMINOC_{60}.

EXPERIMENTAL SECTION

Materials. All of the compounds that were used were reagent grade or better and the solvents were used as-received, unless otherwise specified. The following reagents were used as-received: C_{60} (99.5%, SES RESEARCH, U.S.A.), 2-amino-1,3-propanediol (AK Scientific), DBU (1,8-diaza-bicyclo [5.4.0]undec-7-ene, Sigma-Aldrich), acetic anhydride (Acros Organics), malonic acid methyl ester (Acros Organics), CBr_4 (Sigma-Aldrich), EDCI hydrochloride [*N*-ethyl-*N*′-(3-(dimethylamino)propyl)carbodiimide hydrochloride, Acros Organics], *N*-hydroxysuccinimide (Sigma-Aldrich), potassium carbonate (Sigma-Aldrich), trifluoroacetic acid (Acros Organics), and trityl chloride (Acros Organics). All of the solvents that were used to prepare the fullerene nanomaterials were prepared according to the procedures in the literature by distilling them with calcium hydride and were used immediately. The nuclear magnetic resonance spectra were measured on a Bruker Avance III 500 MHz NMR Spectrometer with TMS as the internal standard. The MS spectra for the water-insoluble fullerenes were collected using an Autoflex II MALDI-TOF

https://dx.doi.org/10.1021/acsbiomaterials.0c00932
ACS Biomater. Sci. Eng. 2020, 6, 5930−5940

mass spectrometer, and for the water-soluble [60]fullerene derivatives, an MS electrospray ionization time-of-flight (ESI-microTOF) mass spectrometer was used; both instruments were from Bruker Daltonics Inc. (Fremont, CA, U.S.A.). The final dialysis purification of the water-soluble fullerene nanomaterials was performed on Pall Microsep centrifugal membranes with the molecular cutoffs at 1 and 3 kDa. The purity of all of the compounds was assessed using an Agilent1260, which was equipped with a DAAD detector at 260 nm and an RP-column: Eclipse plus C18 (3.5 μm); flow 0.5 mL/min. The Fourier transform infrared (FTIR) measurements were carried out using an Agilent Cary 640 FTIR spectrometer, which was equipped with a standard source and a DTGS Peltier-cooled detector. The aminofullerene powders were mixed with KBr and measured in the transmittance mode in the 400−4000 cm^{-1} range. The spectrum was recorded at 32 accumulations and a spectral resolution of 4 cm^{-1}. The obtained data were analyzed using the baseline, water and carbon dioxide corrections.

Synthesis of the [60]Fullerene Derivatives. The glycofullerenes MMS48 and GF1 were synthesized according to a previously described methodology.[24] The synthetic protocol for preparing the aminofullerenes (Monoamino-C_{60} and Hexakisamino-C_{60}) is depicted in Scheme S1 of the Supporting Information (SI), which presents the detailed NMR and mass spectrometry analyses, DLS, and zeta potential measurements (see SI).

N^1-Tritylethane-1,2-Diamine (1). Ethylenediamine (24.96 mmol; 1.5 g) was dissolved in 40 mL of dichloromethane, and then anhydrous potassium carbonate (24.96 mmol; 3.45 g) was added to the solution. Next, a trityl chloride solution (12.48 mmol 3.48 g) in DCM was added to the reaction mixture over 40 min and was stirred at room temperature for 3 days. After this time, the white solid was filtered off, and the obtained filtrate was extracted three times by adding 3 × 50 mL of deionized water. The organic phase was dried over magnesium sulfate and purified using column chromatography (DCM: MeOH, 10/1, v/v; $R_f = 0.16$). The final product was obtained as a white solid with a yield of 82% and mp as 93 °C.[32]

N^1,N^3-Bis(2-(tritylamino)ethyl)malonamide (2). Tritylethane-1,2-diamine (3.08 mmol; 0.93 g) was dissolved in 100 mL of methanol and then dimethyl malonate (1.5 mmol; 0.2 g) was added dropwise for 10 min. The obtained reaction mixture was refluxed for 3 h and then stirred at room temperature for 2 days to obtain a reddish solution of the desired malonate. After that time, the reaction mixture was evaporated, and the obtained brownish oil was dissolved in 50 mL methylene chloride and extracted three times with 50 mL of deionized water. The organic phase was evaporated, which produced the desired bismalonamide as a brown, oily product with a final yield of 69%, which was used for the further Bingel−Hirsch cyclopropanation reactions with no additional purifications (the high resolution mass spectrometry of malonate **2** is depicted in Figure S2 of the SI).

MonoaminoC_{60}. The fullerene C_{60} (0.5 mmol; 360 mg) was added to the freshly distilled toluene (450 mL), mixed for 5 min using a magnetic stirrer, which was followed by an additional suspension using an ultrasonic bath for 15 min (the temperature of the C_{60} solution did not exceed 50 °C). Then, a dichloromethane solution (10 mL) of bismalonamide **2** (0.5 mmol; 333.6 mg) and CBr_4 (1 mmol; 331.63 mg) was added to the solution of C_{60}, which was followed by the dropwise addition of a solution of DBU (0.625 mmol; 95.1 mg) in 5 mL of DCM; the reaction was allowed to stir for 2 h at room temperature. After that time, the fullerene monoadduct (3) was isolated using the two-step flash chromatography procedure. For this purpose, the reaction mixture was first purified on a precolumn using toluene as the mobile phase—the biggest fraction was from the unreacted fullerene. Then, the final product was eluted from the column using a mixture of CH_2Cl_2/MeOH 5:1 to 2:1. The brown filtrate was evaporated in vacuo to form a brown solid with a 28% yield and the structure of fullerene monoadduct (3), which was confirmed by NMR spectroscopy (see SI) as well as MALDI-TOF spectrometry (Figure S1). The final hydrolysis of trityl-protected fullerene monoadduct (3) was performed using a 20% dichloromethane solution of trifluoroacetic acid. Briefly, 200 mg of the fullerene monoadduct (3) was dissolved in a 20 mL mixture of DCM and 20% trifluoroacetic acid (1/1, v/v). The solution was stirred at room temperature for 7 days, during which the changes in the color of the aqueous layer from transparent to red-orange were observed. Next, 50 mL of water was added to the solution, and the phases were separated in a separatory funnel and the aqueous phase was collected and evaporated. The MonoaminoC_{60} was purified on centrifugal membranes using a 1 kDa filter membrane (Pall Corporation, U.S.A.), and the upper layer of the membrane was washed four times with 15 mL of distilled water. Then, the desired fullerene nanomaterial (4) was passed through syringe filters (0.2 μm) to sterilize it and to remove any larger agglomerates. The sample was then freeze-dried in a lyophilizer, which resulted in a reddish mesh powder that was stored at −20 °C. The desired MonoaminoC_{60} was characterized using NMR, infrared spectroscopy, and ESI−MS (see the SI).

HexakisaminoC_{60}. A fullerene monoadduct (4) (0.2 mmol; 278 mg) was dissolved in 10 mL of DCM and then 100 mL of toluene was added under intensive stirring at room temperature. In a separate 25 mL vial, 15 mL of a chloroform solution of malonate (2) (2 mmol; 1350 mg) and carbon tetrabromide (4 mmol; 1324 mg) was prepared. The contents of the vial were added to the solution of MonoaminoC_{60} for 5 min, after which, a 3 mL chloroform solution of DBU was prepared (362 mg; 2.4 mmol) to which 0.5 mL DBU solution was added every 60 min. Next, the reaction mixture was stirred at room temperature for 48 h, during which the color of the solution changed to orange. A [60]fullerene Hexakis adduct (5) was purified from the organic impurities using a flash column, first using methylene chloride and then eluting the final [60]fullerene derivative with an eluent that consisted of a mixture of DCM: MeOH (9:1, v/v) and then the final T_h symmetrical Hexakis adduct of [60]fullerene was concentrated on a rotary evaporator. The fullerene derivative (5) was characterized using NMR spectroscopy (See Supporting Information and Figure S1). In order to remove the trityl-protecting group from the fullerene nanomaterial (5), the compound was hydrolyzed using 20% trifluoroacetic acid. Briefly, a sample of the compound (5) was dissolved in a mixture of 10 mL DCM and 10 mL 20% TFA. The solution was stirred at room temperature for 7 days, during which the color of the aqueous layer changed from transparent to orange. Next, 25 mL of water was added to the fullerene solution, extracted and then the aqueous phase was collected and evaporated. The HexakisaminoC_{60} was purified on centrifugal membranes using a 1 kDa filter membrane (Pall Corporation, U.S.A.), the top layer of the membrane was washed four times with 15 mL of distilled water and passed through syringe filters (0.2 μm) to sterilize it and to remove any larger agglomerates. The [60]fullerene nanomaterial was then frozen at −20 °C and freeze-dried, which resulted in a red powder that was then stored in a laboratory freezer at −20 °C. The HexakisaminoC_{60} was characterized using NMR and infrared spectroscopy and was confirmed using ESI−MS.

Singlet Oxygen Phosphorescence and EPR Spin Trapping. The near-infrared luminescence (1270 nm) was measured perpendicular to the excitation beam in the photon-counting mode using a thermoelectric-cooled NIR PMT module (H10330−45; Hamamatsu, Japan), which was equipped with a 1100 nm cutoff filter and an additional dichroic narrow-band NBP filter, selectable from the spectral range of 1150−1355 nm (NDC Infrared Engineering Ltd., Essex, U.K.). The data were collected using a computer-mounted PCI-board multichannel scaler (NanoHarp 250; PicoQuant GmbH, Berlin, Germany). Data analysis, including the first-order luminescence decay, which was fitted using the Levenberg−Marquardt algorithm, was performed using custom-written software. The acquisition time for obtaining the singlet oxygen phosphorescence signals was 20 s. The EPR measurements were performed using a Bruker EMX-AA EPR spectrometer (Bruker BioSpin, Rheinstetten, Germany). The EPR samples were run using a microwave power of 10.6 mW, a modulation amplitude of 0.05 mT, center field 339.0 mT, scan width 8 mT, and scan time 21 s.

The phosphate-buffered (pD 7.4, 10 mmol) D_2O solutions of the fullerene nanomaterials and TMPyP were excited in a 1 cm-optical path quartz fluorescence cuvette (QA-1000; Hellma, Mullheim, Germany) using the monochromatic light pulses that were generated

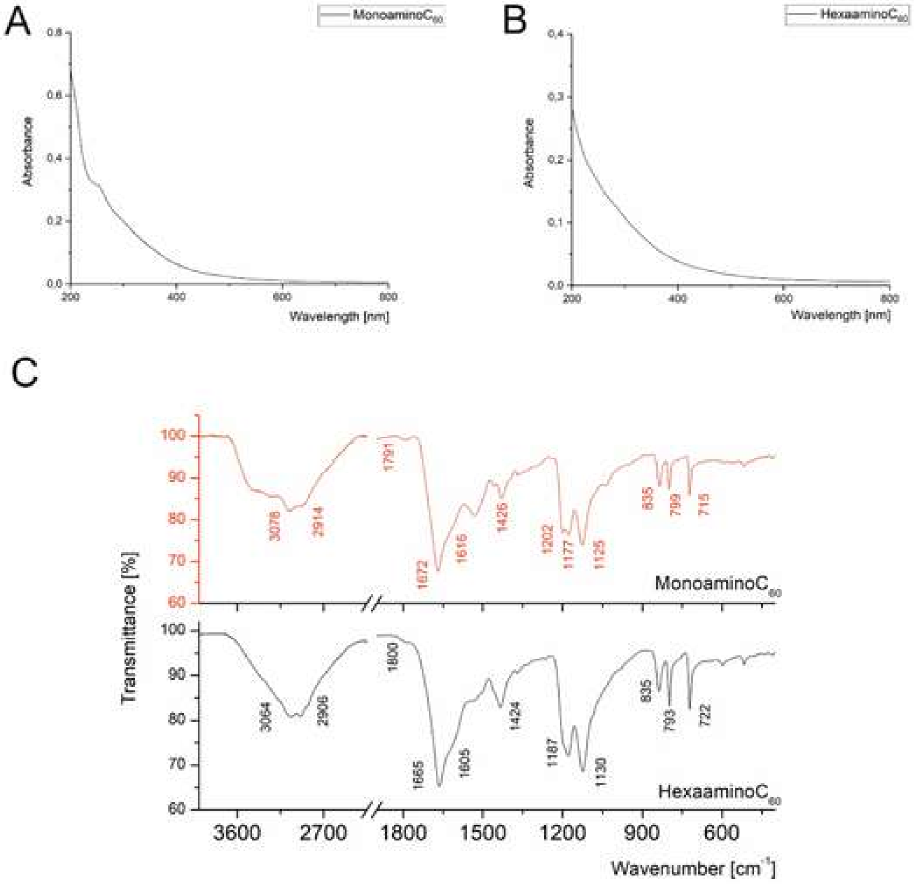

Figure 2. UV–vis and IR spectra of water-soluble [60]fullerenes MonoaminoC_{60} and HexakisaminoC_{60}.

by an integrated nanosecond DSS Nd/YAG laser system, which was equipped with a narrow bandwidth optical parametric oscillator (NT242–1k-SH/SFG; Ekspla, Vilnius, Lithuania). The laser system delivered pulses at a 1-kHz repetition rate and had a pulse energy up to several hundred microjoules in the visible region and up to several tens of microjoules in the UVA–UVB region. The [60]fullerene photosensitizers were photoexcited using a 429 nm wavelength. The absorbance of the samples was set to 0.27 in that wavelength. In order to adjust the photoexcitation energy in the experiments, a laser beam was attenuated with three pieces of wire mesh (light transmission 40% each). The quantum yield of singlet oxygen formation was obtained using 5,10,15,20-tetrakis(1-methyl-4-pyridinio) porphyrin) *tetra*(*p*-toluenesulfonate) (TMPyP) as the reference compound ($\varphi = 0.75$).[33] For detection of radicals photogenerated by the studied [60]fullerens, EPR-spin trapping was employed, using DMPO as the spin trap at a concentration of 100 mM. Samples containing 0.1 mg/mL of appropriate fullerene nanomaterials in 80% DMSO were irradiated in EPR quartz flat cells in the resonant cavity with 402–508 nm (24 mW/cm^2) light, which was derived from a 300 W high-pressure compact arc xenon lamp (Cermax, PE300CE13FM/Module300W; PerkinElmer Optoelectronics, GmbH, Wiesbaden, Germany). To control spectral irradiance, the system was equipped with a water filter, heat reflecting hot mirror, cutoff filter that blocked light below 390 nm and a blue additive dichroic filter 505FD64–25 (Andover Corporation, Salem, NH, U.S.A.).

Photobleaching of HexakisaminoC_{60}. Stability of HexakisaminoC_{60} was checked in PBS solution. Concentration was set to 0.05 mg/mL and absorbance spectra was recorded. The sample was irradiated with blue light from the same source and the same power flux as used for cell phototoxicity (445 nm, 20 mW/cm^2). Absorbance was measured in 5 min intervals to check if any changes occurred.

HPLC Monitored Cholesterol and Liposomes Peroxidation. The HPLC analysis and electrochemical detection on a mercury drop was employed for cholesterol hydroperoxides detection. This method enables identification and quantification of cholesterol hydroperoxides of different origin, thus allowing us to determine the major mechanisms of lipids oxidation.[34] 7$\alpha\beta$-OOH cholesterol hydroperoxides form as a result of cholesterol reaction with oxidizing radicals, while 5α-OOH and 6$\alpha\beta$-OOH hydroperoxides are generated *via* the reaction with singlet oxygen. In brief, multilayered liposomes were prepared from a mixture of DMPC/cholesterol in 3:1 molar ratio. Liposomes were enriched with [60]fullerenes in PBS solution during the creation from dry lipid layers, with one exception—fullerene nanomaterial MMS48 was added to chloroform solution of lipids, as it is totally water-insoluble, due to the presence of acetyl protecting groups. Liposomes were light-treated with 10 mW/cm^2 of blue light (445 nm), then lipids were extracted using modified Folch procedure, dried under nitrogen stream and frozen in −20 °C. For HPLC analysis the samples were dissolved in isopropanol and separated on RP-C_{18} column. The mobile phase consisted of 72% methanol, 11% acetonitrile, 9% ultrapure H_2O (containing 1 mM of $NaClO_4$), and 8% of isopropanol. To determine retention times for cholesterol hydroperoxides (7α-OOH and 5α-OOH) analytical standards were used.

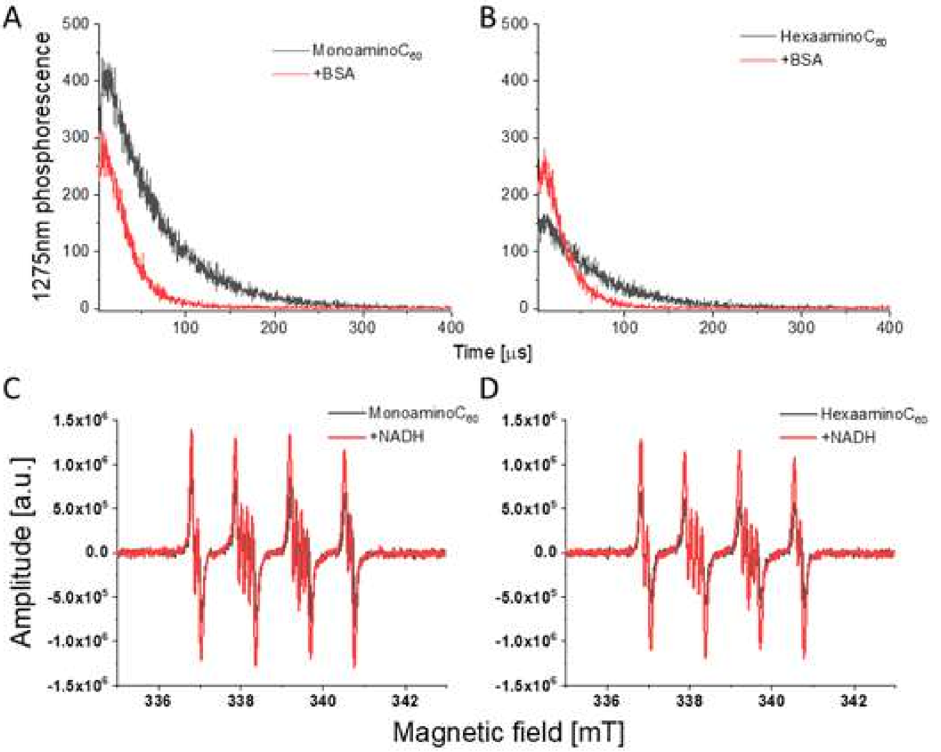

Figure 3. Singlet oxygen luminescence signals (A and B) after 429 nm laser pulse excitation observed in D_2O solutions of MonoaminoC$_{60}$ and HexakisaminoC$_{60}$ in absence (black lines) or with an addition of 35 µM of BSA (red line). DMPO spin trapping of respective C$_{60}$ in 80% of DMSO (C and D) without (black trace) or with addition of NADH (red trace).

Bovine Serum Albumin Oxidation Using CBA Test. Coumarin boronic acid (CBA) reacts with protein hydroperoxides forming fluorescent product 7-hydroxycoumarin (COH). This reaction can be used for quantification of protein oxidation.[35] Stock solution (2.5 mM) of bovine serum albumin (LabEmpire) was prepared in PBS directly before experiment and diluted to final concentration of 100 µM. HexakisaminoC$_{60}$ was added to samples to achieve desire concentrations of 50, 10, and 5 µg/mL. Protein hydroperoxide scavenger ebselen in concentration of 100 µM was added to one of the control samples.[36] Samples were placed in a 96-well plate (black, with bottom transparent) and irradiated with 20 mW/cm^2 blue light (blue COB led light, 445 nm) for 20 min. Just after irradiation 200 U of catalase was added for 5 min to all the samples to remove any hydrogen peroxide. CBA (final concentration 0.4 mM) in 10 times diluted PBS was added. Formation of fluorescent COH was monitored in 10 min intervals for 5 h using 360 (±15 nm) as excitation and 465 (±20 nm) as emission wavelength.

MTT Photocytotoxicity. Human squamous carcinoma A431 was obtained from the American Type Culture Collection (ATCC). The A431 cells were plated in 24-well plates at density of 35 000/well. Twenty-four hours after plating, the cells were incubated with high-glucose DMEM that contained HexakisaminoC$_{60}$ at different concentrations. Feeding was repeated two more times, at 24 h intervals. The day after the final feeding the cells were washed twice with PBS that contained calcium and magnesium ions, then irradiated for 15 min using a blue led light (440 nm) at a fluence rate of 20 mW/cm^2. Dark control cells were kept in the same conditions except for light exposure. After irradiation, the cells were provided by DMEM with 10% FBS. The cytotoxic effect of the photodynamic treatment was quantified 24 h after irradiation, using an MTT assay for the mitochondrial redox function. The MTT solution in DMEM with 10% FBS was added to the treated and control culture wells (final concentration of 0.5 mg/mL). After incubation for 30 min at 37 °C, the culture medium was removed, and the remaining blue precipitate was solubilized in DMSO, followed by reading the absorbance at 560 nm in a plate reader (GENios Plus, Tecan Austria GmbH). The results are reported as the percentage of the paired untreated controls. The experiments were repeated a minimum of three times.

Cellular PI Staining after PDT. To estimate the apoptotic effect of light induced HexakisaminoC$_{60}$, A431 cells were stained using fluorescent dye propidium iodide (PI) 24 h after irradiation, as described in a previously described protocol.[37] In brief, propidium iodide (final concentration 100 µM) was added to the control and treated cells, and fluorescence images (510–560 nm excitation/580 nm emission) were taken to detect PI-positive nuclei. Then, Triton X-100 was added (final concentration 0.1%), and fluorescence images were captured to quantify the total cell number in each field. The number of viable cells and the total number of cells per field were quantified using the ImageJ software with the Huang method[38] for cell finding using a custom-written script by Dr. Łukasz Bujnowicz (Jagiellonian University, Poland).

■ RESULTS AND DISCUSSION

Chemistry. *Synthesis and Physicochemical Properties of Aminofullerenes MonoaminoC$_{60}$ and HexakisaminoC$_{60}$.* On the basis of previously reported literature findings describing the use of fullerene nanomaterials in photodynamic therapy, we aimed to synthesize water-soluble [60]fullerene photosensitizers possessing multiamino groups, which are easily assessable utilizing a trityl function protection/deprotection approach. The fullerene scaffold has great potential to be chemically modified, enhancing its water-solubility, therefore

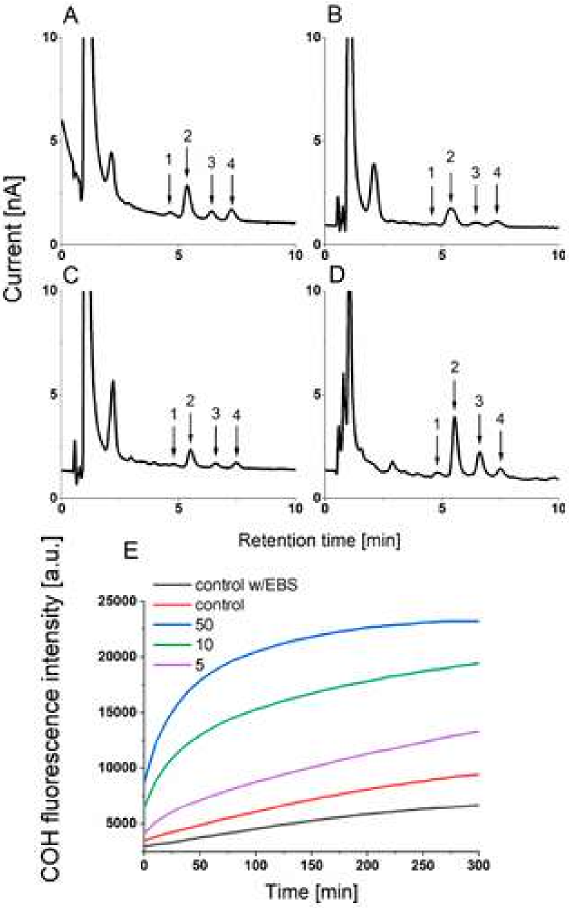

Figure 4. HPLC chromatograms of DMPC/cholesterol liposomes with four [60]fullerene derivatives (A, HexakisaminoC$_{60}$; B, MonoaminoC$_{60}$; C, GF1; D, MMS48). The arrows indicate the cholesterol hydroperoxides with their characteristic retention times (1, 4.7 min—7$\alpha\beta$-OOH; 2, 5.5 min—5α-OOH; and 3 and 4, 6.6 and 7.5 min—6$\alpha\beta$-OOH), respectively. Panel E shows the formation of the protein hydroperoxides that were determined using COH.

the Bingel–Hirsh approach gives a possibility to modify its structure with specially designed malonates, thanks to the ability to control the cyclopropanation reaction and obtaining selected regioisomers, especially [60]fullerene monoadducts and Hexakisadducts with T_h symmetry. This phenomenon was especially important for our biophysical comparative studies, because less substituted fullerenes seem to be more effective photosensitizers based on the studies performed by Hamblin et al.[17,39] However, tailored designed [60]fullerene derivatives might be hard to accomplish, due to variations of the degree of malonate additions and complex addition patterns. To address these problems, we propose the use of malonamide (**2**) in the double Bingel-Hirsh protocol.[23] The molecular ion peak of compound (**2**) was observed in the high resolution ESI mass spectrum at 673.3536 Da (calculated for $C_{45}H_{45}N_4O_2$, 673.35425 Da, Figure S3). The time-controlled reaction is stopped after 2 h to prevent formation on bisadduct regioisomers or used further for creation of highly symmetrical Hexakisadducts from more reactive monoadducts. An overview of whole synthetic strategy is depicted in Scheme S1 (see SI), starting with ethylenediamine core, we aimed to obtain trityl based symmetrical malonamide (**2**), but without using additional coupling agents, only by a gentle refluxing with dimethyl malonate. For all water-soluble fullerene nanomaterials ESI-spectrometry was used for detection of molecular peaks, but trityl-protected [60]fullerenes were measured by MALDI-TOF technique using DCTB matrix. The formation of [60]fullerene monoadduct (**3**) was confirmed by ^{13}C NMR spectroscopy based on its molecular symmetry (Figure S1, characteristic C$_{60}$ signals from 2 × 15 sp^2 carbon atoms between 145 and 139 ppm and one sp^3 carbon at 70.4 ppm) and MALDI-TOF mass spectrometry with a molecular ion peak at 1436.309 Da (M−H+2Na, Figure S4, M−H+2Na). The desired MonoaminoC$_{60}$ was obtained by deprotection of trityl groups in 20% TFA, followed by membrane dialysis with 1 kDa cutoff. It was further characterized by NMR spectroscopy and positively ionization ESI−MS with observed molecular ion peak 478.86 Da $[M + H]^{2+}$ (Figure S5). Next, a highly symmetrical [60]fullerene Hexakisadduct (**5**) was created using fullerene monoadduct (**3**) as a starting material, in a second Bingel−Hirsh reaction with an 10-fold excess of malonate (**2**) and CBr$_4$ and controlled addition of DBU during 6 h. This double Bingel−Hirsh synthetic approach to [60]fullerene Hexakisadducts was described by our group earlier and generates increased yields of final products as well as reduced presence of different regioisomers in the reaction mixture (mainly tris- and tetrakisadducts as byproducts). The T_h symmetry of [60]fullerene Hexakisadduct (**5**) was confirmed by ^{13}C NMR spectroscopy, which is expressed by a reduction of fullerene sp^2 signals in the carbon spectrum. Only two signals (143.97 and 142.62 ppm) of fullerene sp^2 carbons and one sp^3 carbon of cyclopropane ring (70.4 ppm) could be observed in the carbon spectrum of Hexakisadduct (**5**) (Figure S2). The aforementioned hydrolysis protocol was carried out to obtain HexakisaminoC$_{60}$ from a corresponding trityl protected fullerene derivative (**5**) and the desired water-soluble [60]fullerene (**6**) was characterized by NMR spectroscopy and ESI mass spectrometry with detected molecular ion peak at 1839.3 Da (positive mode, 50 mV, $[M+2H]^+$, Figure S6A). The change of experimental setup during electrospray spectrometry measurements (to 300 mV voltage), resulted in a rapid fragmentation of HexakisaminoC$_{60}$, with observed molecular ion peak of a parent MonoaminoC$_{60}$ disodium fragment $[M+2Na+H_2O]^+$.

The UV−vis spectra of two water-soluble aminofullerenes are presented in the Figure 2A,B. This experimental observation could be also partially explained by higher water solubility of HexakisaminoC$_{60}$ (above 250 mg/mL) in comparison to MonoaminoC$_{60}$ (around 30 mg/mL).

In the case of MonoaminoC$_{60}$, one characteristic absorption peak could be observed at 270 nm. This local maximum is similar to the UV absorption spectra of pristine C$_{60}$ fullerene in a toluene solution (maxima observed at 269 nm), with only minimal absorption below 550 nm and negligible fluorescence. In electron spectrum of Hexakisadduct (**6**) no clear maxima was observed, which was also described for water-soluble glycofullerenes and other aminofullerenes.[23,40] Additionally, for the same concentrations of aminofullerenes, the HexakisaminoC$_{60}$ spectrum was hypochromized for a given absorbance on the order of 45%, which may be explained by formation of [60]fullerene aggregates. The DLS measurements performed on a Malvern Zetasizer illustrate that both aminofullerenes

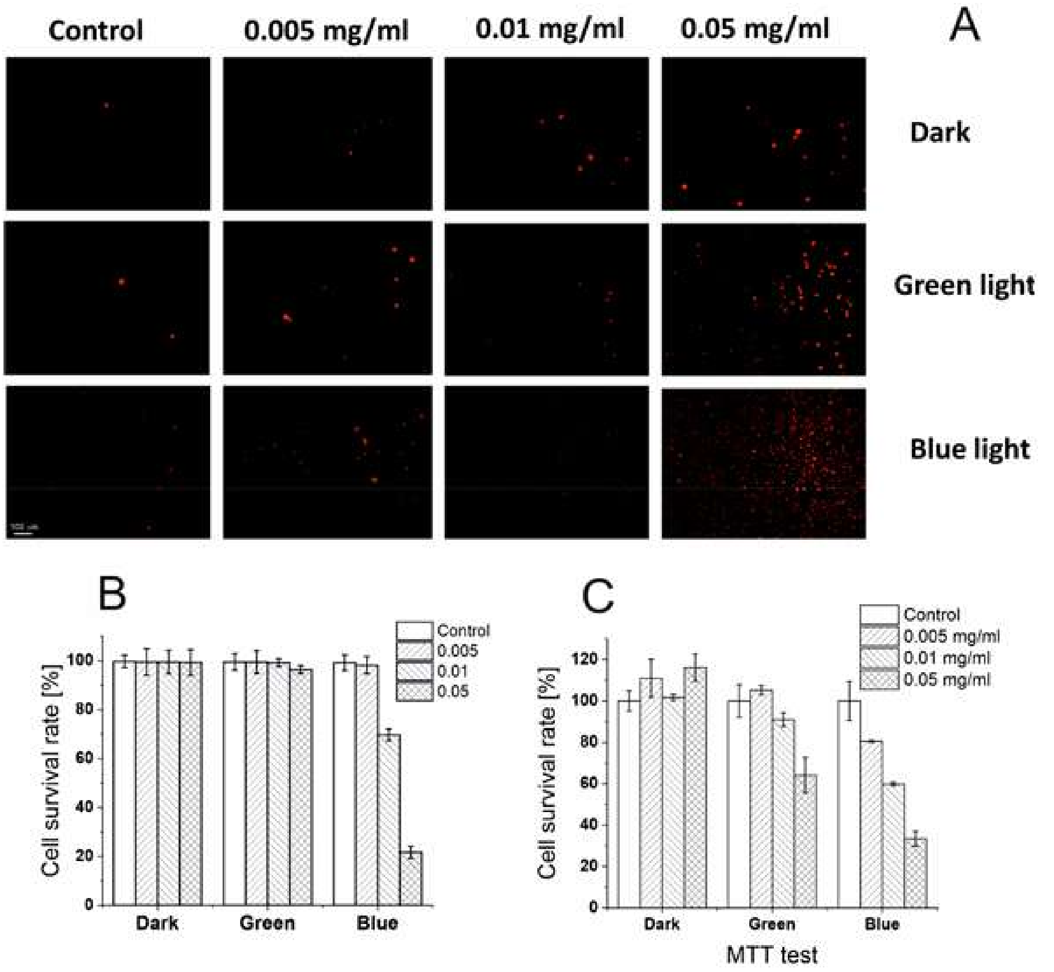

Figure 5. Microscopic images of the phototreated A431 cells that had been stained with propidium iodide (A); the results that were obtained after a mathematic picture analysis (B) of the same experiment, which was recalculated for cell survivability. The result of the MTT assay of the A431 cells after irradiation (C); and different bars show the different HexakisaminoC_{60} concentrations.

form aggregates, which are in a dynamic equilibrium as described previously for fullerene Hexakisadduct C_{60} ser.[41] The MonoaminoC_{60} forms larger aggregates around 354 nm with observed zeta potential at +31 mV; in contrast HexakisaminoC_{60} seems to predominantly aggregate around 99 nm, indicating a surface of charge of +29 mV. Both aminofullerenes present a relatively good degree of stability, and the smaller aggregates and possibly a different morphology of Hexakisadduct aggregates may be partially explained by a different critical packing parameter p.[42]

The infrared spectra of engineered water-soluble fullerenes (MonoaminoC_{60} and HexakisaminoC_{60}) have been analyzed considering two spectral regions: (1) 2250−3800 cm^{-1} and (2) 400−1900 cm^{-1} (Figure 2C). The bands arrangement found in relation to the HexakisaminoC_{60} and MonoaminoC_{60} are quite similar, wherein small differences as for the number of bands, their intensity, or positions result from the number of functional groups anchored to the fullerene scaffold. Looking more precisely on the spectrum of Hexakisamino derivative of C_{60}, region 1 is linked mainly to the overlapping signals originating from the symmetric and asymmetric stretching modes of $\nu(CH_2)$ and $\nu(NH_x)$ (x = 2,3). The band positions of amine groups (3064 and 2906 cm^{-1}) relating to the band position of the typical amine result probably from the presence of inter- or intramolecular interactions.[43] Similarly affected seems to be the position of the methylene bands which may be shifted toward higher wavenumbers due to the presence of positive charge located on the amine groups, in relation to a typical position of the methylene group within the alkene chain.[44,45]

An interesting phenomenon is also observed for the whole band arrangement of region 1, where bands are characterized by the high full width at half-maximum and high intensity, indicating a huge distribution and high number of H-bonds with different donor−acceptor bonds lengths. According to this assumption, weak, medium, and strong hydrogen bonds are present, probably due to the high dynamicity of the system as well as the presence of TFA counterion, enforcing formation of the highly dynamic systems maintained by the H-bonding system. A slightly different situation appeared in the case of aminofullerene monoadduct. Here, the position of two additional bands found at higher wavenumbers is closely related to the symmetric and asymmetric stretching modes of amine groups, typically reported in the literature for free or weakly involved in the hydrogen bonding scheme, NH_2 groups. The other two bands observed in this region are slightly shifted toward higher wavenumbers in relation to the Hexakis aminofullerene, wherein its interpretation is similar like previously. As a result of such observations, the band arrangement of monoamino C_{60} may result from a much smaller number of functional units anchored to the fullerene core and their weaker influence in formation of the H-bonding.

The fingerprint (1) region of HexakisaminoC_{60} fullerene, especially at high wavenumbers is characterized by one maximum, strong in the intensity centered at 1665 cm^{-1}, as well as a shoulder at 1605 cm^{-1} and one band low in the intensity located at 1800 cm^{-1}. All of those bands are linked to the stretching vibration of carbonyl moieties, whereby their positions are indicated on the primary amides located within the organic chain (Figure 2).[46] The position of low lying carbonyl bands may be explained two ways, as a result of the presence of hydrogen bonds or due to the occurrence of the β-diketone structure.[47,48]

In turn, the low intensity band centered at 1800 cm^{-1} might explain taking into account counterion in which the halogen atoms are directly bonded to a carbonyl group that according to the theory absorb strongly at the presence of fluorine. Other bands with the maxima at 1424, 1187, and 1130 cm^{-1} may respectively be linked to the symmetric deformational modes of ethylenediamine groups, as well as skeletal vibration of alkane chain and deformational modes of methylene groups. In turn, the group of bands centered at 835, 793, 722 cm^{-1} are difficult in the interpretation, because of the overlapping character of various modes which may be activated at those wavenumbers. However, those bands may try to interpret as the asymmetric deformation modes of tertiary amides at 835 cm^{-1}, the deformational mode within straight-chain alkanes at 793 cm^{-1} and CF at 726 cm^{-1}. A lower number of functional units anchored to the fullerene core, resulted in some shift of bands toward lower or higher wavenumbers, i.e., a shift of carbonyl moieties, strongly involved in the formation of the H-bonding scheme is correlated with the weakening of mutual interaction between donor−acceptor units. One can conclude that the smaller number of functional units anchored to the fullerene core, the weaker interaction between them could be observed. In addition, the position of bands linked to the modes corresponding to the ethylenediamine or the alkane chain is only slightly changed relating to the HexakisaminoC_{60} but reveal the spatial rearrangement of this kind of functional groups.

Biophysics. The ability to cause photoinduced damage is a primary function of traditional as well as nanomaterial-based photosensitizers. In this study, we have shown that all four [60]fullerenes are able to produce reactive oxygen species (ROS). As depicted in Figure 3CD, the EPR spectra of spin adducts characteristic to spin trapping of superoxide anion by DMPO are being presented[49] (for a simulated spectrum of DMPO−OOH adduct see SI Figure S21). Efficiency of that process was markedly increased by the presence of an external electron donor like NADH (Figures 3CD, red traces). Although superoxide anion is not a very reactive compound, it can travel long distances inside cells and secondary reactions may oxidize targets far from its generation site. Singlet oxygen O_2 ($^1\Delta_g$), however, is much more reactive and in cellular environment could react in close vicinity to its point of formation. Singlet oxygen formation was detected by a direct observation of a characteristic phosphorescence of $O_2(^1\Delta_g)$ at 1275 nm in photon-counting mode (Figure 3AB). Experiments were conducted in phosphate D_2O buffer to increase the lifetime of the generated singlet oxygen and to enhance the detection sensitivity.[50] The quantum yield of singlet oxygen photogeneration for both aminofullerenes was obtained using TMAP as a standard and it was determined to be around 0.1 and 0.062 (HexakisaminoC_{60} *vs* MonoaminoC_{60}, Figures S12 and S18); in the case of MMS48, the tetraphenylporphirine (TPP) was used as a standard, in a chloroform solution (Figure S20). Although it is not a high yield for HexakisaminoC_{60}, in the presence of serum albumin the formation of singlet oxygen was markedly increased (Figure 3B), what was also measured quantitively (Figure S22). As expected, lifetime of singlet oxygen decreased in the presence of albumin, due to reaction with the protein (the corresponding rate constant being around 7×10^8).[51] The elevated efficiency of singlet oxygen photogeneration observed for HexakisaminoC_{60}−BSA complex, compared to HexakisaminoC_{60} alone is noteworthy. Typically, complexation of a photosensitizer molecule by albumin is accompanied by substantial reduction in the photosensitizer efficiency to photogenerate singlet oxygen. Such a phenomenon has been observed for WST-11 and WST-19 photosensitizers.[52,53] The increased efficiency of photogeneration of singlet oxygen by HexakiskisaminoC_{60}−BSA, compared to MonaminoC_{60}−BSA remains rather puzzling, suggesting different mechanism of BSA binding. This may be caused by a different mode of binding affinities of synthesized aminofullerenes to IIA and IIIA subdomains of BSA. The larger and more substituted and T_h symmetrical HexakisaminoC_{60} could be easier to bind to hydrophobic pockets of BSA. Moreover, the computational studies performed by the group of Papadopoulos indicated that positively charged aminofullerens and fullerene carboxylic acids that negatively charged groups attached to the fullerene core may be necessary to enhance ligand−HAS interactions.[54] Only a limited number of cationic compounds have been reported to exempt this rule—this observation may be true for fullerene nanomaterial HexakisaminoC_{60}, but further computational studies should be performed. Moreover, a recent studies by Di Giosia *et al.* have also reported the shielding effects of proteins in the case of C_{60}@lysozyme hybrid, which was visualized by the increase in singlet oxygen generation and reduction of quenching by water molecules.[55,56] In our case, HexakisaminoC_{60} is forming smaller aggregates than MonoaminoC_{60} (99 nm *vs* 354 nm), which may also favor its better ability to produce $^1O_2$ after binding with BSA.

The analysis of cholesterol peroxidation products induced by the studied [60]fullerenes reveal that at least in liposomes, the main oxidizing species is singlet oxygen (Figure 4ABCD). The peak from 7ab-OOH (depicted in Figure 4 as **1**, with a retention time of 4.7 min) is barely visible and could come from internal rearrangements of singlet oxygen-related hydroperoxides.[34] It would suggest that in a lipid microenvironment, the excited triplet states of fullerene nanomaterials are much more prone to energy transfer, resulting in singlet oxygen production. This effect is especially pronounced for the water insoluble form—MMS48 (Figure 4D). From three tested water-soluble fullerene derivatives, HexakisaminoC_{60} was found to be most effective in the photooxidation of cholesterol

(Figure 4A). Additionally, HexakisaminoC$_{60}$ nanomaterial, as well as other tested fullerene nanomaterials were found to be quite resistant to photobleaching in conditions used for photodynamic treatment (Figures S14−S17). As for cellular and tissue applications, the presence of serum albumin is inevitable, we have chosen HexakisaminoC$_{60}$ derivative for further studies in cell phototoxicity experiments using squamous skin carcinoma model. The ability to photooxidize proteins by Hexakis derivative of C$_{60}$ was further investigated using coumarin boronic acid assay (Figure 4E). The obtained results clearly show a dose-dependent increase in the amount of fluorescent COH, which is a product of reaction of nonfluorescent CBA and bovine serum albumin hydroperoxides. This observation confirms that during blue LED light irradiation, HexakisaminoC$_{60}$ is able to also oxidize proteins.

Photodynamic Therapy. To determine cell phototoxicity, the A431 cell line of a non-melanoma skin cancer was used. The cells were fed with HexakisaminoC$_{60}$ fullerene for three consecutive days. During that time, no dark toxicity in the range of the concentrations that were used in the experiment was observed (Figure 5). Phototoxicity was pronounced for the cells that were irradiated with blue light (445 nm), while a significantly weaker effect was observed when the cells were irradiated with green light (500−580 nm). This observation is consistent with the relative absorbance of the C$_{60}$ derivatives. Two methods were used to detect phototoxicity—determining the mitochondrial activity (MTT assay, Figure 5C) and cell membrane permeability (propidium iodide test, Figure 5AB). Although the observed effects for both tests were photosensitizer-dose dependent, the MTT test produced more pronounced results that showed photodynamic damage, which may suggest that the photoinduced damage primarily occurs in the cell mitochondria and cytosol. This observation is in agreement with previous studies on glycofullerenes as well as with the fluorescently labeled fullerene derivative C$_{60}$ serPF, which have demonstrated that water-soluble [60]fullerene derivatives tend to accumulate mainly in the nuclear envelope and cytosol of cancer cells.[23,57] The green light exposure caused negligible effects in the membrane permeability assay even at the highest concentration of the nanophotosensitizer that was used, while for the same conditions, the cell viability that was measured by the MTT test was reduced to 60% (Figure 5). In both of those experiments, the blue LED light irradiation resulted in a substantial increase in cell death with a 0.05 mg/mL concentration of HexakisaminoC$_{60}$ reducing the cell survival rate to around 20%. It was expected that there would be a lower efficiency under green light irradiation compared to the effective absorbance of HexakisaminoC$_{60}$ in the corresponding regions of the absorbance spectrum. Although blue light has a low tissue penetration, in potential *in vivo* application, it can enable very precise targeting, which would reduce the damage to non-malignant tissues.[58] The results that were obtained using blue light irradiation clearly showed that this compound has the properties of a promising photosensitizer that could be used in topical applications.

■ CONCLUSIONS

We synthesized two novel aminofullerenes—MonoaminoC$_{60}$ and HexakisaminoC$_{60}$ and compared their biophysical properties based on studies of ROS formation, and lipid and protein peroxidation. On the basis of the observation that BSA−HexakisaminoC$_{60}$ complex increased the formation of singlet oxygen, we selected HexakisaminoC$_{60}$ for further cellular studies, which confirmed its high phototoxicity, which had negligible effects without LED irradiation. Additionally, we do believe that further molecular docking studies should also be performed to visualize differences of BSA binding to a different [60]fullerene derivatives. The future 3D-spheroid or *in ovo* experiments should be performed to evaluate it as a photosensitizer in the photodynamic therapy of skin cancer, especially using a higher concentration of the [60]fullerene derivative and green LED irradiation due to its higher tissue penetration properties.

■ ASSOCIATED CONTENT

Supporting Information

The Supporting Information is available free of charge at https://pubs.acs.org/doi/10.1021/acsbiomaterials.0c00932.

> Chemistry: Synthetic protocol for obtaining monoaminoC$_{60}$ and hexakisaminoC$_{60}$; NMR of substrates and fullerene derivatives; high resolution ESI mass spectrometry of malonate (2); MALDI-TOF mass spectrometry of water insoluble fullerene (3); ESI mass spectrometry of water-soluble aminofullerenes (4) and (6); DLS studies of water-soluble aminofullerenes (4) and (6); Zeta potential measurements of water-soluble aminofullerenes (4) and (6); HPLC chromatogram of peroxides standards used for lipid peroxidation studies; Biophysics: quantum yield of singlet oxygen formation of hexakisaminoC$_{60}$ (6); EPR spin trapping and singlet oxygen phosphorescence measurements for GF1; and photobleaching of HexakisaminoC$_{60}$ (PDF)

■ AUTHOR INFORMATION

Corresponding Author

Maciej Serda − *Institute of Chemistry, University of Silesia in Katowice, Katowice 40-007, Poland;* orcid.org/0000-0003-4926-5782; Email: maciej.serda@us.edu.pl

Authors

Grzegorz Szewczyk − *Faculty of Biochemistry, Biophysics, and Biotechnology, Jagiellonian University, Kraków 30-387, Poland*
Olga Krzysztyńska-Kuleta − *Faculty of Biochemistry, Biophysics, and Biotechnology, Jagiellonian University, Kraków 30-387, Poland*
Julia Korzuch − *Institute of Chemistry, University of Silesia in Katowice, Katowice 40-007, Poland*
Mateusz Dulski − *Institute of Materials Engineering and Silesian Center for Education and Interdisciplinary Research, University of Silesia in Katowice, Chorzów 41-500, Poland*
Robert Musioł − *Institute of Chemistry, University of Silesia in Katowice, Katowice 40-007, Poland*
Tadeusz Sarna − *Faculty of Biochemistry, Biophysics, and Biotechnology, Jagiellonian University, Kraków 30-387, Poland*

Complete contact information is available at: https://pubs.acs.org/10.1021/acsbiomaterials.0c00932

Author Contributions

Design, conceptualization, and methodology: M.S., G.S.; chemical synthesis and characterization: M.S., J.K., and M.D.; Biophysical measurements: G.S.; Cellular experiments: O.K.K.; Writing and editing: M.S., G.S., R.M., and T.S.

Notes

The authors declare no competing financial interest.

■ ACKNOWLEDGMENTS

M.S. thanks the National Science Center (Poland) for its support (Grant SONATA UMO-2016/23/D/NZ7/00912). M.D. is thankful for financial support from the National Science Center that was based on decision 2017/26/D/ST8/01117. Additionally, the authors want to thank Dr. Bujnowcz for his custom-written script for cell image analysis and Institute of Applied Radiation Chemistry from Lodz University of Technology (Poland) for providing us CBA probe.

■ REFERENCES

(1) Apalla, Z.; Lallas, A.; Sotiriou, E.; Lazaridou, E.; Ioannides, D. Epidemiological trends in skin cancer. *Dermatology practical & conceptual* **2017**, *7* (2), 1.

(2) Didona, D.; Paolino, G.; Bottoni, U.; Cantisani, C. Non melanoma skin cancer pathogenesis overview. *Biomedicines* **2018**, *6* (1), 6.

(3) Ting, P. T.; Kasper, R.; Arlette, J. P. Metastatic basal cell carcinoma: report of two cases and literature review. *J. Cutaneous Med. Surg.* **2005**, *9* (1), 10−15.

(4) Toll, A.; Margalef, P.; Masferrer, E.; Ferrándiz-Pulido, C.; Gimeno, J.; Pujol, R. M.; Bigas, A.; Espinosa, L. Active nuclear IKK correlates with metastatic risk in cutaneous squamous cell carcinoma. *Arch. Dermatol. Res.* **2015**, *307* (8), 721−729.

(5) Bastian, B. C. The molecular pathology of melanoma: an integrated taxonomy of melanocytic neoplasia. *Annu. Rev. Pathol.: Mech. Dis.* **2014**, *9* (1), 239−271.

(6) Apalla, Z.; Nashan, D.; Weller, R. B.; Castellsague, X. Skin cancer: epidemiology, disease burden, pathophysiology, diagnosis, and therapeutic approaches. *Dermatology and therapy* **2017**, *7* (1), 5−19.

(7) Christensen, E.; Warloe, T.; Kroon, S.; Funk, J.; Helsing, P.; Soler, A.; Stang, H.; Vatne, Ø.; Mørk, C. Guidelines for practical use of MAL-PDT in non-melanoma skin cancer. *J. Eur. Acad. Dermatol. Venereol.* **2010**, *24* (5), 505−512.

(8) Jung, S. K.; Lee, K. W.; Byun, S.; Kang, N. J.; Lim, S. H.; Heo, Y.-S.; Bode, A. M.; Bowden, G. T.; Lee, H. J.; Dong, Z. Myricetin suppresses UVB-induced skin cancer by targeting Fyn. *Cancer Res.* **2008**, *68* (14), 6021−6029.

(9) Cranmer, L. D.; Engelhardt, C.; Morgan, S. S. Treatment of unresectable and metastatic cutaneous squamous cell carcinoma. *Oncologist* **2010**, *15* (12), 1320.

(10) Safwat, M. A.; Soliman, G. M.; Sayed, D.; Attia, M. A. Fluorouracil-loaded gold nanoparticles for the treatment of skin cancer: development, in vitro characterization, and in vivo evaluation in a mouse skin cancer xenograft model. *Mol. Pharmaceutics* **2018**, *15* (6), 2194−2205.

(11) Petrilli, R.; Eloy, J. O.; Saggioro, F. P.; Chesca, D. L.; de Souza, M. C.; Dias, M. V.S.; daSilva, L. L.P.; Lee, R. J.; Lopez, R. F.V. Skin cancer treatment effectiveness is improved by iontophoresis of EGFR-targeted liposomes containing 5-FU compared with subcutaneous injection. *J. Controlled Release* **2018**, *283*, 151−162.

(12) Shi, L.; Wang, X.; Tu, Q.; Wang, H.; Zhang, H.; Wang, P.; Zhang, L.; Huang, Z.; Wang, X.; Zhao, F.; Luan, H. Treating cutaneous squamous cell carcinoma using 5-aminolevulinic acid polylactic-co-glycolic acid nanoparticle-mediated photodynamic therapy in a mouse model. *Int. J. Nanomed.* **2015**, *10*, 347.

(13) Huang, P.; Xu, C.; Lin, J.; Wang, C.; Wang, X.; Zhang, C.; Zhou, X.; Guo, S.; Cui, D. Folic acid-conjugated graphene oxide loaded with photosensitizers for targeting photodynamic therapy. *Theranostics* **2011**, *1*, 240.

(14) Zhu, Z.; Tang, Z.; Phillips, J. A.; Yang, R.; Wang, H.; Tan, W. Regulation of singlet oxygen generation using single-walled carbon nanotubes. *J. Am. Chem. Soc.* **2008**, *130* (33), 10856−10857.

(15) Mroz, P.; Pawlak, A.; Satti, M.; Lee, H.; Wharton, T.; Gali, H.; Sarna, T.; Hamblin, M. R. Functionalized fullerenes mediate photodynamic killing of cancer cells: Type I versus Type II photochemical mechanism. *Free Radical Biol. Med.* **2007**, *43* (5), 711−719.

(16) Mroz, P.; Tegos, G. P.; Gali, H.; Wharton, T.; Sarna, T.; Hamblin, M. R. Photodynamic therapy with fullerenes. *Photochemical & Photobiological Sciences* **2007**, *6* (11), 1139−1149.

(17) Hamblin, M. R. Fullerenes as photosensitizers in photodynamic therapy: pros and cons. *Photochemical & Photobiological Sciences* **2018**, *17* (11), 1515−1533.

(18) Lee, J.; Mackeyev, Y.; Cho, M.; Li, D.; Kim, J.-H.; Wilson, L. J.; Alvarez, P. J. Photochemical and antimicrobial properties of novel C60 derivatives in aqueous systems. *Environ. Sci. Technol.* **2009**, *43* (17), 6604−6610.

(19) Cho, M.; Lee, J.; Mackeyev, Y.; Wilson, L. J.; Alvarez, P. J.; Hughes, J. B.; Kim, J.-H. Visible light sensitized inactivation of MS-2 bacteriophage by a cationic amine-functionalized C60 derivative. *Environ. Sci. Technol.* **2010**, *44* (17), 6685−6691.

(20) Liu, Y.; Jiao, F.; Qiu, Y.; Li, W.; Lao, F.; Zhou, G.; Sun, B.; Xing, G.; Dong, J.; Zhao, Y.; et al. The effect of Gd@ C82 (OH) 22 nanoparticles on the release of Th1/Th2 cytokines and induction of TNF-α mediated cellular immunity. *Biomaterials* **2009**, *30* (23−24), 3934−3945.

(21) Guan, M.; Zhou, Y.; Liu, S.; Chen, D.; Ge, J.; Deng, R.; Li, X.; Yu, T.; Xu, H.; Sun, D.; et al. Photo-triggered gadofullerene: enhanced cancer therapy by combining tumor vascular disruption and stimulation of anti-tumor immune responses. *Biomaterials* **2019**, *213*, 119218.

(22) Hamblin, M. R. Upconversion in photodynamic therapy: plumbing the depths. *Dalton Transactions* **2018**, *47* (26), 8571−8580.

(23) Serda, M.; Ware, M. J.; Newton, J. M.; Sachdeva, S.; Krzykawska-Serda, M.; Nguyen, L.; Law, J.; Anderson, A. O.; Curley, S. A.; Wilson, L. J.; Corr, S. J. Development of photoactive Sweet-C60 for pancreatic cancer stellate cell therapy. *Nanomedicine (London, U. K.)* **2018**, *13* (23), 2981−2993.

(24) Serda, M.; Malarz, K.; Mrozek-Wilczkiewicz, A.; Wojtyniak, M.; Musiol, R.; Curley, S. A. Glycofullerenes as non-receptor tyrosine kinase inhibitors-towards better nanotherapeutics for pancreatic cancer treatment. *Sci. Rep.* **2020**, *10* (1), 1−11.

(25) Simões, M. F.; Sousa, J. S.; Pais, A. C. Skin cancer and new treatment perspectives: A review. *Cancer Lett.* **2015**, *357* (1), 8−42.

(26) Chen, Y.; Miclea, R.; Srikrishnan, T.; Balasubramanian, S.; Dougherty, T. J.; Pandey, R. K. Investigation of human serum albumin (HSA) binding specificity of certain photosensitizers related to pyropheophorbide-a and bacteriopurpurinimide by circular dichroism spectroscopy and its correlation with in vivo photosensitizing efficacy. *Bioorg. Med. Chem. Lett.* **2005**, *15* (13), 3189−3192.

(27) Belgorodsky, B.; Fadeev, L.; Ittah, V.; Benyamini, H.; Zelner, S.; Huppert, D.; Kotlyar, A. B.; Gozin, M. Formation and Characterization of Stable Human Serum Albumin- Tris-malonic Acid [C60] Fullerene Complex. *Bioconjugate Chem.* **2005**, *16* (5), 1058−1062.

(28) Krumkacheva, O. A.; Timofeev, I. O.; Politanskaya, L. V.; Polienko, Y. F.; Tretyakov, E. V.; Rogozhnikova, O. Y.; Trukhin, D. V.; Tormyshev, V. M.; Chubarov, A. S.; Bagryanskaya, E. G.; et al. Triplet Fullerenes as Prospective Spin Labels for Nanoscale Distance Measurements by Pulsed Dipolar EPR Spectroscopy. *Angew. Chem.* **2019**, *131* (38), 13405−13409.

(29) Qu, X.; Komatsu, T.; Sato, T.; Glatter, O.; Horinouchi, H.; Kobayashi, K.; Tsuchida, E. Structure, photophysical property, and cytotoxicity of human serum albumin complexed with tris (dicarboxymethylene)[60] fullerene. *Bioconjugate Chem.* **2008**, *19* (8), 1556−1560.

(30) Gebicki, J. M. Oxidative stress, free radicals and protein peroxides. *Arch. Biochem. Biophys.* **2016**, *595*, 33−39.

(31) Gutteridge, J. Lipid peroxidation and antioxidants as biomarkers of tissue damage. *Clin. Chem.* **1995**, *41* (12), 1819−1828.

(32) Wang, F.; Good, J. A.; Rath, O.; Kaan, H. Y. K.; Sutcliffe, O. B.; Mackay, S. P.; Kozielski, F. Triphenylbutanamines: kinesin spindle protein inhibitors with in vivo antitumor activity. *J. Med. Chem.* **2012**, *55* (4), 1511−1525.

(33) Snyder, J. W.; Lambert, J. D.; Ogilby, P. R. 5, 10, 15, 20-Tetrakis (N-Methyl-4-Pyridyl)-21 H, 23H-Porphine (TMPyP) as a Sensitizer for Singlet Oxygen Imaging in Cells: Characterizing the Irradiation-dependent Behavior of TMPyP in a Single Cell. *Photochem. Photobiol.* **2006**, *82* (1), 177−184.

(34) Korytowski, W.; Bachowski, G. J.; Girotti, A. W. Analysis of cholesterol and phospholipid hydroperoxides by high-performance liquid chromatography with mercury drop electrochemical detection. *Anal. Biochem.* **1993**, *213* (1), 111−119.

(35) Michalski, R.; Zielonka, J.; Gapys, E.; Marcinek, A.; Joseph, J.; Kalyanaraman, B. Real-time measurements of amino acid and protein hydroperoxides using coumarin boronic acid. *J. Biol. Chem.* **2014**, *289* (32), 22536−22553.

(36) Sies, H. Ebselen, a selenoorganic compound as glutathione peroxidase mimic. *Free Radical Biol. Med.* **1993**, *14* (3), 313−323.

(37) Olchawa, M.; Krzysztynska-Kuleta, O.; Duda, M.; Pawlak, A.; Pabisz, P.; Czuba-Pelech, B.; Sarna, T. In vitro phototoxicity of rhodopsin photobleaching products in the retinal pigment epithelium (RPE). *Free Radical Res.* **2019**, *53* (4), 456−471.

(38) Huang, L.-K.; Wang, M.-J. J. Image thresholding by minimizing the measures of fuzziness. *Pattern recognition* **1995**, *28* (1), 41−51.

(39) Sharma, S. K.; Chiang, L. Y.; Hamblin, M. R. Photodynamic therapy with fullerenes in vivo: reality or a dream? *Nanomedicine (London, U. K.)* **2011**, *6* (10), 1813−1825.

(40) Ashcroft, J. M.; Tsyboulski, D. A.; Hartman, K. B.; Zakharian, T. Y.; Marks, J. W.; Weisman, R. B.; Rosenblum, M. G.; Wilson, L. J. Fullerene (C60) immunoconjugates: interaction of water-soluble C60 derivatives with the murine anti-gp240 melanoma antibody. *Chem. Commun.* **2006**, No. 28, 3004−3006.

(41) Lapin, N. A.; Vergara, L. A.; Mackeyev, Y.; Newton, J. M.; Dilliard, S. A.; Wilson, L. J.; Curley, S. A.; Serda, R. E. Biotransport kinetics and intratumoral biodistribution of malonodiserinolamide-derivatized [60] fullerene in a murine model of breast adenocarcinoma. *Int. J. Nanomed.* **2017**, *12*, 8289.

(42) Chen, M.; Zhou, S.; Guo, L.; Wang, L.; Yao, F.; Hu, Y.; Li, H.; Hao, J. Aggregation Behavior and Antioxidant Properties of Amphiphilic Fullerene C60 Derivatives Cofunctionalized with Cationic and Nonionic Hydrophilic Groups. *Langmuir* **2019**, *35* (21), 6939−6949.

(43) Krueger, P. J.; Jan, J. Infrared spectra and the molecular conformations of some aliphatic amines. *Can. J. Chem.* **1970**, *48* (20), 3229−3235.

(44) McKean, D.; Duncan, J.; Batt, L. CH stretching frequencies, bond lengths and dissociation energies. *Spectrochimica Acta Part A: Molecular Spectroscopy* **1973**, *29* (6), 1037−1049.

(45) Socrates, G. *Infrared and Raman Characteristic Group Frequencies: Tables and Charts*; John Wiley & Sons: New York, 2004.

(46) Craig, N. C.; Evans, D. A. Infrared and Raman Spectra of cis-and trans-1,2-Dichloro-1,2-difluoroethylene. *J. Am. Chem. Soc.* **1965**, *87* (19), 4223−4230.

(47) Long, F.; Bakule, R. Keto-Enol Transformation of 1, 2-Cyclohexanedione. II. Acid Catalysis in Strongly Acidic Media 1−3. *J. Am. Chem. Soc.* **1963**, *85* (15), 2313−2318.

(48) Campbell, R.; Gilow, H. β-Diketones. III. 1, 2 The Effect of Ring Size and Conjugation on Tautomerism. *J. Am. Chem. Soc.* **1962**, *84* (8), 1440−1443.

(49) Buettner, G. R.; Mason, R. P. Spin-trapping methods for detecting superoxide and hydroxyl free radicals in vitro and in vivo. *Critical reviews of oxidative stress and aging: advances in basic science, diagnostics and intervention* **2002**, *1*, 27−38.

(50) Nonell, S.; Redmond, R. On the determination of quantum yields for singlet molecular oxygen photosensitization. *J. Photochem. Photobiol., B* **1994**, *22* (2), 171−172.

(51) Gimenez, R. E.; Vargova, V.; Rey, V.; Turbay, M. B. E.; Abatedaga, I.; Moran Vieyra, F. E.; Paz Zanini, V. I.; Mecchia Ortiz, J. H.; Katz, N. E.; Ostatna, V.; et al. Interaction of singlet oxygen with bovine serum albumin and the role of the protein nano-compartmentalization. *Free Radical Biol. Med.* **2016**, *94*, 99−109.

(52) Vakrat-Haglili, Y.; Weiner, L.; Brumfeld, V.; Brandis, A.; Salomon, Y.; McIlroy, B.; Wilson, B. C.; Pawlak, A.; Rozanowska, M.; Sarna, T.; et al. The microenvironment effect on the generation of reactive oxygen species by Pd- bacteriopheophorbide. *J. Am. Chem. Soc.* **2005**, *127* (17), 6487−6497.

(53) Ashur, I.; Goldschmidt, R.; Pinkas, I.; Salomon, Y.; Szewczyk, G.; Sarna, T.; Scherz, A. Photocatalytic generation of oxygen radicals by the water-soluble bacteriochlorophyll derivative WST11, non-covalently bound to serum albumin. *J. Phys. Chem. A* **2009**, *113* (28), 8027−8037.

(54) Leonis, G.; Avramopoulos, A.; Papavasileiou, K. D.; Reis, H.; Steinbrecher, T.; Papadopoulos, M. G. A comprehensive computational study of the interaction between human serum albumin and fullerenes. *J. Phys. Chem. B* **2015**, *119* (48), 14971−14985.

(55) Di Giosia, M.; Bomans, P. H.; Bottoni, A.; Cantelli, A.; Falini, G.; Franchi, P.; Guarracino, G.; Friedrich, H.; Lucarini, M.; Paolucci, F.; et al. Proteins as supramolecular hosts for C 60: a true solution of C 60 in water. *Nanoscale* **2018**, *10* (21), 9908−9916.

(56) Soldà, A.; Cantelli, A.; Di Giosia, M.; Montalti, M.; Zerbetto, F.; Rapino, S.; Calvaresi, M. C 60@ lysozyme: a new photosensitizing agent for photodynamic therapy. *J. Mater. Chem. B* **2017**, *5* (32), 6608−6615.

(57) Raoof, M.; Mackeyev, Y.; Cheney, M. A.; Wilson, L. J.; Curley, S. A. Internalization of C60 fullerenes into cancer cells with accumulation in the nucleus via the nuclear pore complex. *Biomaterials* **2012**, *33* (10), 2952−2960.

(58) Zhao, Z.; Fairchild, P. W. In *Dependence of Light Transmission through Human Skin on Incident Beam Diameter at Different Wavelengths, Laser-Tissue Interaction IX*; International Society for Optics and Photonics: 1998; pp 354−360.

scientific reports

OPEN

Towards water-soluble [60] fullerenes for the delivery of siRNA in a prostate cancer model

Julia Korzuch[1,6], Monika Rak[2,6], Katarzyna Balin[3], Maciej Zubko[4,5], Olga Głowacka[2], Mateusz Dulski[4], Robert Musioł[1], Zbigniew Madeja[2] & Maciej Serda[1]✉

This paper presents two water-soluble fullerene nanomaterials (HexakisaminoC$_{60}$ and monoglucosamineC$_{60}$, which is called here JK39) that were developed and synthesized as non-viral siRNA transfection nanosystems. The developed two-step Bingel–Hirsch reaction enables the chemical modification of the fullerene scaffold with the desired bioactive fragments such as D-glucosamine while keeping the crucial positive charged ethylenediamine based malonate. The ESI–MS and ^{13}C-NMR analyses of JK39 confirmed its high T$_h$ symmetry, while X-ray photoelectron spectroscopy revealed the presence of nitrogen and oxygen-containing C–O or C–N bonds. The efficiency of both fullerenes as siRNA vehicles was tested in vitro using the prostate cancer cell line DU145 expressing the GFP protein. The HexakisaminoC$_{60}$ fullerene was an efficient siRNA transfection agent, and decreased the GFP fluorescence signal significantly in the DU145 cells. Surprisingly, the glycofullerene JK39 was inactive in the transfection experiments, probably due to its high zeta potential and the formation of an extremely stable complex with siRNA.

Nanotechnology has changed traditional medicinal chemistry, by enabling the development of small molecular drugs with targeted nanotherapeutics[1]. The central premise of medical chemistry is that a specific small molecule can bind to the desired enzyme or receptor, which results in a specific therapeutic effect. The aforementioned inhibition process can also be achieved using nucleic acid therapies including a technique called RNA interference (Nobel Prize 2006) in the presence of engineered nanomaterials used as transfection agents[2,3]. An efficient transfection agent must deliver the targeted siRNA into the cytoplasm where it degrades the targeted mRNA after binding to the argonaute proteins (AGO) and the further formation of the RNA-induced silencing complex (RISC)[4]. Recently, the FDA has approved an siRNA-based drug (lipid nanoparticles, patisiran) to treat transthyretin-mediated amyloidosis[5]. Due to increased interest in the nanomedical approaches in molecular biology, the interactions of nucleic acids and carbon nanomaterials have been thoroughly studied and discussed, mainly focusing on the interactions of the DNA-carbon nanotubes/cationic fullerenes[6,7]. The use of [60]fullerene hexakisadducts as DNA transfection agents was previously described in case of multivalent cationic fullerenes and polycationic fullerenes, which formed a stable complexes with DNA plasmids with minimal cytotoxicity in mammalian cells[8–10]. Although the interaction of the cationic fullerenes with DNA is well presented even in murine models, the siRNA transfection techniques have mainly been developed for only one derivative, TPFE (*tetra*-piperazino-[60]fullerene epoxide)[11], which forms a stable 7 nm micelle, but has limited options for its further chemical functionalization or the addition of targeting groups or ligands for biorthogonal/click chemistry. Furthermore, the main advantages of fullerene-based transfection agents over cationic lipids are the high water-solubility, the ability to cross biological membranes, low cytotoxicity and a high synthetic accessibility allowing additional options for bioconjugation with desired drugs in engineered nanomaterials. Moreover, it has been proven that TPFE is non-toxic and is effective for lung-targeted in vivo siRNA delivery, which is based on the formation of the micrometer-sized TPFE–siRNA–serum protein complexes, which could be a stabilization factor for relatively unstable siRNA under physiological conditions[12]. Studies performed by Wang et al. described a fullerene-ethylenediamine modified dextran hybrid (C$_{60}$-Dex-NH$_2$) as an efficient siRNA transfection agent when they evaluated it in the human breast cancer cell line MDA-MB-231, which could be photo-activated and could

[1]Institute of Chemistry, University of Silesia in Katowice, 40-006 Katowice, Poland. [2]Faculty of Biochemistry, Biophysics and Biotechnology, Jagiellonian University, 30-387 Kraków, Poland. [3]Institute of Physics and Silesian Center for Education and Interdisciplinary Research, University of Silesia in Katowice, 41-500 Chorzów, Poland. [4]Institute of Materials Engineering, University of Silesia in Katowice, 41-500 Chorzów, Poland. [5]Department of Physics, Faculty of Science, University of Hradec Králové, 500-03 Hradec Králové, Czech Republic. [6]These authors contributed equally: Julia Korzuch and Monika Rak. ✉email: maciej.serda@us.edu.pl

destroy the endo-lysosomal membranes via a controllable generation of ROS[13]. Simultaneously, the interactions of carbon nanomaterials with biological fluids are crucial factors that determine their cellular fate and further tissue targeting[14,15]. Experimental and computational studies have been performed to describe the formation of complexes between the water-soluble carboxylated fullerenes and serum albumins and other proteins such as lysosome and the serine proteinases[16,17]. Our previous studies showed that the protein corona is formed on the surface of glycofullerenes and modulates their inhibitory activity, however its detailed composition is still unknown[18]. Due to nanoparticle zeta-potentials influence on the formation and composition of the protein corona, it was observed that in positively charged nanoparticles after their complexation with the plasma proteins, the complex's final zeta potential decreases[19].

Herein a facile methodology for the synthesis of highly water-soluble [60]fullerene hexakisadducts is presented using the Bingel-Hirsch synthetic approach to modify the buckyball scaffold. Our robust protocol was used to create two highly functionalized T_h symmetrical fullerene nanomaterials including monoglucosamineC_{60} which is called here a JK39 compound with a D-glucosamine's fragment. The rationale behind this approach was to increase the interactions of the nucleic acids with a sugar fragment as has been described for the chitosan-based transfection agents[20]. The additional advantage of fullerene hexakisadducts is that they limit the occurrence of several regioisomers, simplify of the purification process and increase water-solubility in contrast to the fullerene monoadducts, which is particularly useful in biological experiments[21,22]. During the designing step, we kept in mind that the glycofullerenes that we previously reported on, could localize in the nuclear envelope- which could be a beneficial property for the transfection process[23]. We previously described HexakisaminoC_{60} as being a non-toxic photosensitizer that could be used to generate reactive oxygen species as described for the treatment non-melanoma skin cancer[24]. The engineered water-soluble aminofullerenes HexakisaminoC_{60} and JK39 were designed as dual-acting nanotherapeutics, which degrade a targeted mRNA in a sequence-specific manner that might have a potential additional photodynamic activity. Considering the interactions of fullerenes with serum albumins, the transfection experiments were conducted in a FBS-containing medium to test the ability of the synthesized carbon nanomaterials to transfect the desired siRNA. We selected Lipofectamine 3000 because it is a modern transfection agent that is commonly used in molecular biological experiments[25].

Methods

Materials. All of the compounds that were used reagent grade or better, and the solvents were used as they were received unless otherwise specified. The following reagents were used as received: C_{60} (99.5 + %, SES Research, U.S.A.), D-glucosamine hydrochloride (Sigma Aldrich), DBU (1,8-diaza-bicyclo[5.4.0]undec-7-ene, Sigma Aldrich), ethyl hydrogen malonate (Sigma Aldrich), CBr_4 (Sigma Aldrich) and DIC. The following reagents: acetic anhydride (Fisher), pyridine (Sigma Aldrich), and DMF (Sigma Aldrich) were prepared according to the procedures in the literature, distilling them with calcium hydride and were then used immediately. The Lipofectamine 3000, which was used as the control siRNA transfection agent, was obtained from Thermo Fisher Scientific (U.S.A.). For the in vitro experiments we have used the human prostate cancer (DU145) cell line (American Type Culture Collection, Rockville, U.S.A.), 24-well plates (Corning; Falcon®), a DMEM F12 Ham medium (Sigma-Aldrich, St.Louis, MO, USA), fetal bovine serum (FBS; Gibco), Penicillin–Streptomycin (Sigma-Aldrich, St.Louis, MO, USA), PTAI-11 (trimethyl undecaprenyl ammonium iodide; Collection of Polyprenols, Institute of Biochemistry and Biophysics PAS, Warsaw, Poland; PTAI-11 is patented (No. 231158, Polish Patent Office 2019; No. 230096, Polish Patent Office 2018, No. 211824, Polish Patent Office 2012) and there is a patent application pending (No. PCT/PL2015/000093, WO/2016/032348, Polish Patent Office, European Patent Office), DOPE (1,2-dioleoyl-*sn*-glycero-3-phosphoethanolamine; Sigma-Aldrich, St.Louis, MO, USA), DC-cholesterol (3ß-[*N*-(*N*',*N*'-dimethylaminoethane)-carbamoyl]cholesterol hydrochloride; Sigma-Aldrich, St.Louis, MO, USA).

The nuclear magnetic resonance spectra were measured on a *Bruker Avance III 500 MHz NMR Spectrometer* with TMS as the internal standard. The MS spectra were collected using an electrospray ionization time-of-flight (ESI-microTOF) mass spectrometer from Bruker Daltonics Inc (U.S.A.). The high-resolution mass spectrometry was carried out on the ESI-Q-TOF maXis impact (Bruker Daltonics Inc, U.S.A.). The purity of all the compounds was assessed using an Agilent1260 HPLC equipped with a DAAD detector at 260 nm, RP-column: Eclipse plus C_{18} (3.5 µm); flow 0.5 mL/min. The Fourier transform infrared (FTIR) measurements were taken using an Agilent Cary 640 FTIR spectrometer, that was equipped with a common source and a DTGS Peltier-cooled detector. The fullerene powders were measured using ATR diamond accessory in the 400–4000 cm^{-1} range. The spectrum was recorded at 32 accumulations and at a spectral resolution of 4 cm^{-1}. The dynamic light scattering and zeta potentials for the fullerene nanomaterials and their complexes with siRNA were measured using Zetasizer Nano (Malvern Panalytical Ltd, UK). The transmission electron microscopy (TEM) observations were performed using a JEOL high resolution (HR-TEM) JEM 3010 microscope operating at a 300 kV accelerating voltage, that was equipped with a Gatan 2 k × 2 k Orius™ 833SC200D CCD camera. The chemical analysis of the surface of fullerenes was performed using the X-ray photoelectron spectroscopy (XPS) technique. The X-ray Photoelectron Spectroscopy measurements were taken using a Physical Electronic XPS spectrometer (Physical Electronics PHI 5700, Chanhassen, MN, U.S.A.). Monochromatic Al Kα radiation (1486 eV) was used to excite the photoelectrons from the surface of fullerenes. The photoemission spectra were collected in a wide binding energy range (− 2 to 1400 eV) and in the characteristic photoemission lines binding energy ranges of carbon, oxygen, nitrogen, and fluorine which was detected on samples' surface. The analysis was carried out using PHI MultiPak (v.9.6.0.1, ULVAC PHI, Chigasaki, Japan) software. The EGFP silencing efficiency was evaluated with an OLYMPUS IX81 (Olympus) fluorescence microscope and a Guava® easyCyte 8 flow cytometer (Luminex, Austin, TX, USA), at a 488 nm laser excitation. The percentage of GFP-positive cells was analyzed using InCyte software ver. 3.3 (Luminex, Austin, TX, USA).

Synthesis of fullerene JK39 and malonic acid ligands for Bingel–Hirsch reaction. Our group previously described the HexakisaminoC_{60} synthetic protocol[24]. The robust approach for obtaining fullerene nanomaterial JK39 is depicted in Scheme S1 in the Supporting Information, and includes additional spectroscopic data. The synthesis of the [60]fullerene monoadduct (**5**), as well as its malonic acid precursor that contains the D-Glucosamine unit (4), were also previously described by our group[23].

Ethylenediamine (15 mL; 0.25 mol) was dissolved in chloroform and cooled to 0 °C followed by the dropwise addition of 125 mL of a chloroform solution of di-*tert*-butyl bicarbonate (5.46 g; 0.025 mol) over three hours. Then, the reaction mixture was allowed to reach room temperature after which it was stirred for an additional 16 h. After that time, the solution was washed six times, with 200 mL of DI water and four times with 200 mL of brine. The organic phases were dried over $MgSO_4$ and evaporated under reduced pressure. The final product was obtained as a colorless oil of *N*-Boc-protected ethylenediamine (**1**) with a 45% yield. The *N*-Boc-1,2-diaminoethane (1 g; 6.2 mmol) was dissolved in 50 mL of methanol, and then dimethylmalonate (0.39 g; 2.95 mmol) was added dropwise. The reaction mixture was refluxed for three hours and then stirred for an additional 72 h at room temperature. After that time, the methanol was evaporated in vacuo. The final product was purified by the initial extraction (DCM/H_2O) followed by column chromatography (DCM:MeOH, 20:1). The final product (**2**) was obtained as a sticky off-white gum with13% yield.

The glycofullerene monoadduct (**5**) (45.2 mg; 0.0365 mmol) was dissolved in 10 mL of dichloromethane and 100 mL of toluene. The mixture was stirring for 15 min. Then the *N*-Boc-diethylamine malonate (142 mg; 0.365 mmol) and CBr_4 (241.6 mg; 0.73 mmol) were dissolved in 10 mL of DCM that had been added to the fullerene solution. In the next step, DBU (66.7 mg; 0.438 mmol) was dissolved in 3 mL of dichloromethane, and 0.5 mL of the base was added to the solution for six hours. After all of the DBU was added, the reaction mixture was stirred at room temperature, for an additional 48 h, during which the color of the solution changed from red-brown to orange. The product was purified using a flash column in the gradient conditions (DCM, DCM: MeOH 10:1 to 5:1). The C_{60} hexakisadduct (**6**) structure which had a T_h symmetry was confirmed using ^{13}C-NMR spectroscopy and mass spectrometry. To obtain a water-soluble fullerene derivative (**7**), the hexakisadduct was dissolved in 10 mL of DCM, and 20% trifluoroacetic acid was added. The reaction was stirred at room temperature for 10 days, during which two phases appeared in the solution. The water phase was collected, evaporated in vacuo and purified on centrifugal membranes using a 1 kDa filter membrane (Pall Corporation, U.S.A.). The top layer of the membrane was washed five times, with 15 mL of distilled water. Subsequently, the [60]fullerene nanomaterial was frozen at − 20 °C and freeze-dried. The final product was obtained as a brown solid with a 30% yield and was stored in a laboratory freezer at − 20 °C. The hexakisadduct (**7**) was characterized using NMR spectroscopy and infrared spectroscopy, and the structure was confirmed using ESI mass spectrometry.

Imaging the siRNA-aminofullerene complexes using transmission electron microscopy. The TEM measurements that are presented in Figs. 3A,B and S8 were obtained using a JEOL high resolution (HR-TEM) JEM 3010 microscope operating at a 300 kV accelerating voltage. The samples of the fullerene–siRNA complexes (20 µL of a desired solutions in nuclease free water, R = 70; 0.45 µg siRNA GFP and 37.5 µg of fullerene nanomaterial) were deposited on a copper grid with a holey carbon amorphous film under air and then dried at room temperature for 24 h.

siRNA transfection using the fullerene nanomaterials. The human prostate cancer (DU145) cell line was obtained from the American Type Culture Collection (Rockville, U.S.A.), nr HTB-81. The DU145 cells were seeded into the wells of a 24-well plate at a density of 5×10^4 and cultivated for 24 h in a DMEM F12 Ham medium with 10% FBS without antibiotics. The [60]fullerene nanomaterials and siRNA were suspended in nuclease-free water at pH 7. Next, they were mixed at a 1:1 (*v:v*) ratio and incubated for 30 min at room temperature. After incubation, the mixture was added to the wells with the cells that contained the FBS-supplemented medium (final FBS concentration—5%). A 0.45 µg/well of siRNA GFP (Sigma Aldrich) was used with 37.5 µg of HeksakisaminoC_{60}, 37.5 µg of JK39, or 1.5 µL of Lipofectamine® 3000. After five hour incubation 300 µL of the medium that had been supplemented with 20% of FBS and antibiotics (Penicillin–Streptomycin [200U–0.2 mg/mL]). The mixture of PTAI-11 (trimethylundekaprenylammonium iodide; Collection of Polyprenols, Institute of Biochemistry and Biophysics PAS, Warsaw, Poland) + DOPE (1,2-dioleoyl-*sn*-glycero-3-phosphoethanolamine; Sigma Aldrich) + DC-cholesterol (3ß-[*N*-(*N*′,*N*′-dimethylaminoethane)-carbamoyl]cholesterol hydrochloride; Sigma Aldrich) at a 1:1:1 molar ratio in 3 µg of lipids was used 24 h after the siRNA had been introduced into the transfected cells with 2.7 µg of pEGFP-C1 plasmid as was previously described[26,27]. To summarize, the experimental steps were: day 1—plating cells; day 2—transfection with siRNA using fullerenes or Lipofectamine® 3000; day 3—transfection with the pEGFP-C1 plasmid using PTAI-11 + DOPE + DC-cholesterol and day 4—evaluating the efficiency of EGFP silencing.

Results and discussion

The procedure for synthesizing HexakisaminoC_{60} as well as its biophysical properties were published earlier, when investigating its photodynamic activity in the non-melanoma skin cancer model[24]. The fullerene nanomaterial JK39 was obtained in a time-controlled two-step Bingel–Hirsch reaction (for the synthetic protocol, see the Supporting Information Scheme S1), in which a peracyleted D-glucosamine fullerene monoadduct (5) was further modified in a second Bingel-Hirsch reaction with Boc-protected malonate (2) its high-resolution ESI spectrum is presented in Fig. S4. In general, the Boc protection on aminomalonate was more useful in the Bingel-Hirsch reaction in terms of the general yields and purification procedure than a previously used trityl function. As a result, T_h-symmetrical hexakisadduct (6) was created, whose structure was confirmed by the presence of two fullerene sp^2 signals at $\delta = 146$ and 141 ppm along with an sp^3 signal at $\delta = 69$ ppm in the ^{13}C-NMR spectrum of

(6) (Fig. S2). Additionally, one could also observe three characteristic signals for different types of NH groups, which are presented between 8.20 and 7.30 ppm in ^{1}H-NMR spectrum (Fig. S1) of fullerene nanomaterial (6). After the hydrolysis of [60]fullerene derivative (6) a highly water-soluble fullerene nanomaterial (7) was created, and its structure was studied using ^{13}C-NMR spectroscopy. The strongest signals in ^{13}C-NMR of fullerene nanomaterial (7) are those connected with TFA counter anion signals (both quartets are located around 162 and 115 ppm, Fig. S3) as well as the methylene groups in ethylenediamine fragments ($NH–CH_2CH_2NH$), located at 38 and 37 ppm, which are depicted in Fig. S3. Due to the limits of our ESI–MS detector (3000 Da), we were not able to measure the molecular peak of the protected fullerene nanomaterial (6) which had a molecular mass at 3109 Da; however, it was possible to detect signals from its fragmentation (Fig. S5). The peak at 2685 Da resulted from the fragmentation of *D*-glucosamine malonate (M = 459 Da) from the parent structure with the addition of two water molecules. In contrast, the peak at 2297 Da corresponded to the fragmental structure without an acetylated D-glucosamine malonate unit, and one Boc-protected aminomalonate (M = 388 Da), which was presented as an adduct with two water molecules. In the next step in our synthetic protocol, the acetyl and Boc protection were removed from the fullerene nanomaterial (6) via a TFA hydrolysis, which was followed by further membrane dialysis, to form the final water-soluble JK39, which was further characterized using the NMR, FTIR, and XPS techniques with additional measurements of its size (DLS) and zeta potential.

The ESI-mass spectrum of a water-soluble fullerene is depicted in Fig. 2B. We were not able to directly detect its molecular peak (M = 1941 Da) due to its polycationic nature, although the spectrum did show a huge signal at 1038 Da, which corresponded to the double-charged cationic form of fullerene (7) $[M + 3Na]^{2+}$.

The analysis of the infrared spectrum of JK39 is very similar to previously published HexakisaminoC_{60} and should be performed by considering two spectral regions, firstly (1) 2250–3800 cm^{-1} and secondly, (2) 400–1900 cm^{-1} (Fig. 2A)[24]. According to this division, for both compounds region 1 is determined by the presence of the overlapping signals that had originated from the symmetric and asymmetric stretching modes of $\nu(CH_x)$, and the ammonium cations containing $\nu(-CH_2NH_x^+)$ (x = 2, 3)[28]. As a result of the introduction of the D-glucosamine fragment, an additional band at 3246 cm^{-1} can be explained by the presence of amine ν(NH), and it is worth noting that its position is linked to the presence of intra- or intermolecular interactions with hydroxyl groups[29]. It is also interesting that the character of the band arrangement within region 1 in both compounds indicated a considerable distribution and high number of *H*-bonds with different donor–acceptor bond lengths. Unfortunately, it was not easy to interpret and analyze the signal of the hydroxyl groups due to the high complexity of the spectrum, e.g. there was an increase in the intensity of the signal of JK39 above 3300 cm^{-1}, which may indicate the presence of the hydroxyl groups as a result of the introduction of the glucosamine fragment. In turn, interpreting of the bands from region 2 was much more complicated due to the higher complexity of the molecular vibration. However, two bands at around 1665 cm^{-1} and 1527 cm^{-1} referred to the asymmetric and symmetric deformation vibration of ammonium cation, while the shoulders that were observed close to those two maxima but that were located at lower wavenumbers, are related to the vibration of the ammonium cation. The literature and previously reported data for HexakisaminoC_{60} that suggested that the position of the band at 1665 cm^{-1} might also be explained by taking into account the stretching vibration of carbonyl modes due to the occurrence of the β-diketone structure[24,30], or due to the high dynamicity of the system through the formation of hydrogen bonds which shifted the carbonyl band maximum into lower wavenumbers. In turn, the presence of a less intense band around 1800 cm^{-1} might be explained through the presence of *N*-protonated amide moiety, which is unusual due to well-known favorable *O*-protonation process. However, it was previously discussed in the literature that some amides and peptides are *N*-protonated, especially in case of strained amides, but also for peptides with electron donating groups and alfa-effects[31–33]. Other bands at the maxima around 1430, 1180, and 1120 cm^{-1} might respectively be linked to the deformational modes of the ethylenediamine groups, the rocking vibration of the ammonium cation or the skeletal vibration of the alkane chain and deformational modes of the methylene groups. The presence of sugar-based malonate was also reflected in the occurrence of low intense bands at 1369, 1285, and 1039 cm^{-1} due to the C–O–C vibration within the pyranose ring and the deformational modes of $-CH_2CH_3$ chain.

The local environment detected on the fullerene surface elements was examined using the XPS technique. Based on the analysis of the XPS survey spectra, several elements were detected on the surface of both fullerene nanomaterials. The chemical composition and calculated atomic and weight concentrations are combined for both fullerenes in Table S1 (see Supporting Information). Elements with an atomic concentration below one atomic percentage, such as Si, S, Na, Cl, and Br can be treated as contaminants. An analysis of the main components of the examined samples (C, O, N, F) indicated some variations in the atomic concentration and, consequently, in the relative ratio of the individual components. The most pronounced differences are presented in the amount of the detected carbon and nitrogen as both of the fullerene nanomaterials have the same ethylenediamine core with the main difference in the D-glucosamine unit (Fig. 1). The chemical state for carbon, oxygen, nitrogen, and fluorine was determined by analyzing the high-resolution spectra of the C1s, O1s, F1s, and N1s photoemission lines. It was revealed that for a particular element, the presence of several different chemical states was related to the specific chemical bonding with the surrounding elements. The analysis of the main component of the both samples—carbon indicated that carbon existed in several different chemical states (see deconvoluted C1s line in Fig. 2C). The chemical state with the lowest binding energy (282.42 eV for sample JK39 and 282.58 eV for the HexakisaminoC_{60}) was related to the occurrence of silicone contamination. The most pronounced peak in the spectra of both samples was located at 284.82 eV and was related to the presence of C–H or C–C bonds[34]. Interestingly, oxygen and nitrogen containing groups C–O or C–N (at 287.10 eV) were detected for both samples[35,36], whereas the presence of typical carbonyl group (C=O) (288.18 eV) was only detected for fullerene JK39[37,38]. For the HexakisaminoC_{60} fullerene, the peak at 288.5 eV was assigned to the O=C–OH bond, which could be also correlated to the presence of CF_3COO^- counterion[38]. The C–F (286.3 for JK39, and 286.6 eV for HexakisaminoC_{60}) bond and $-CF_3$ fragment of trifluoroacetic acid (687.8 eV for JK39 and 687.9 eV for

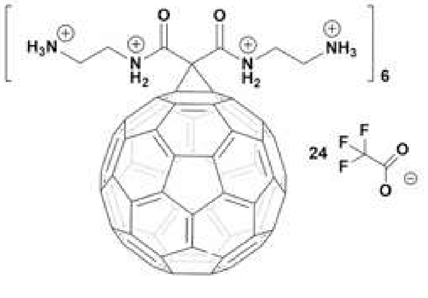

HEXAKISAMINOC_{60}

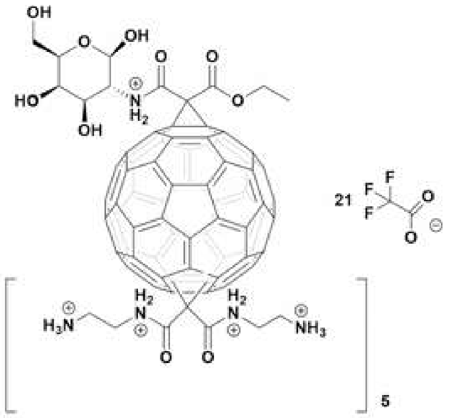

JK39

Figure 1. The non-viral cationic fullerene nanomaterials HexakisaminoC_{60} and JK39 that were used for the siRNA transfection.

HexakisaminoC_{60}) were identified through the F1s deconvolution presented in Fig. S9[39]. The O1s line (Supporting Information, Fig. S9) that indicated a carbon–oxygen bond; weakly adsorbed oxygen (O_2/OH^-) were detected at ~ 530.3 eV, C=O (carbonyl slightly below 532 eV), and O–C=O at around 533.3 eV[40,41]. The deconvoluted N1s line (see Fig. 2C) indicated the presence of four components; the most pronounced component at 399.6 eV was assigned to the C–N[36] or N–(C=O)– bonds[42], the one at 398.0 eV to basic nitrogen(pyridinic type), and the chemical state at 401.4 eV to quaternary N[43]. Assuming that some of the nitrogen in the 398 eV bonding energy state could come from *N*-protonated amide fragment, the increased amount that was observed for sample JK39 (see the green line in Fig. 2C, for sample JK39, it was 22% of all of the nitrogen, for HexakisaminoC_{60}—13%) could confirm the structure of sample JK39 with nitrogen attached to pyranose ring. We also calculated pKa values of all nitrogen atoms in our malonate substrates which are depicted in Fig. S10. In case of D-glucosamine containing malonate pK_a of the nitrogen is 19.3, while the ethylenediamine-based malonate has to pKa one for amine (10.2) and amide 19.5.

Based on our previous studies with water-soluble fullerenes and kinetic experiments on fullerene C_{60}ser that were conducted Wilson's group, we postulated that the synthesized fullerene nanomaterials would form smaller and larger aggregates in a water solution, that are in constant equilibrium[18,44]. They can disaggregate when they are exposed to a higher ionic strength (salt addition), organic solvents, and the adsorption of the protein corona on the surface of fullerene[18]. At a concentration of 0.1 mg/mL, HexakisaminoC_{60} forms aggregated at 100 nm (PDI = 0.2) with a zeta potential at + 28.6 mV[24], while the fullerene derivative JK39 formed two subpopulations of aggregates at 134 and 599 nm (PDI = 0.365) also with two different values of the zeta potential at + 54 and + 90 mV (Figs. S6, S7, Supporting Information). The presence of two signals in the zeta potential measurement of JK39 might be caused by the considerable polydispersity of the fullerene nanomaterial and could confirm its lower stability. Additionally, the studies performed by Deryabin et al. on ten different fullerene derivatives demonstrated an obvious relationship between the zeta potentials of the functionalized [60]fullerene aggregates and their size in salt-free aqueous[45]. Besides, nanoparticles with a positive zeta potential have a long-circulating half-life due to the absorption of the protein corona and can form electrostatic complexes with RNA which is crucial when developing siRNA transfection agents[46]. When developing efficient fullerene nanomaterial transfection agents, certain conditions must be met. Firstly, the engineered fullerene nanomaterials should be able to form a stable complex with the desired sequence of siRNA, and that complex must deliver the RNA to the cytosol, thus protecting it from being degraded by nucleases[47]. On the other hand, the complex that is formed between the RNA and cationic fullerene should not be too stable—the desired siRNA has to cleave from the complex and perform an endosomal escape and intracellular release to form the RNA-induced silencing complex (RISC)[48]. The endosomal escape process and triggering the intracellular release tend to be the most important factors when developing effective siRNA delivery tools and are still not well understood for engineered nanomaterials[49]. Here, we decided to test the ability of our fullerene nanomaterials to silence the GFP fluorescence signal using a prostate cancer cell line (DU145) due to the simplicity of the model[26]. To better mimic in vivo conditions, we conducted all of the siRNA transfection experiments in the presence of FBS.

The R value (70) that used in the transfection experiments was calculated by dividing the nitrogen-to-phosphorus (N/P) ratio by two. Interestingly, due to the many positive charges placed at the nitrogen atoms in our two fullerene nanomaterials HexakisaminoC_{60} and JK39 (24 and 20, respectively), the R number was also high—the experimental values of the R parameter that were used for the siRNA transfection with the TPFE fullerene was between 20 and 50. Interestingly, in the transfection experiments carried out using the TPFE fullerene, it was dissolved in a potassium chloride solution (pH 2) to ensure the complete protonation of the aminofullerene

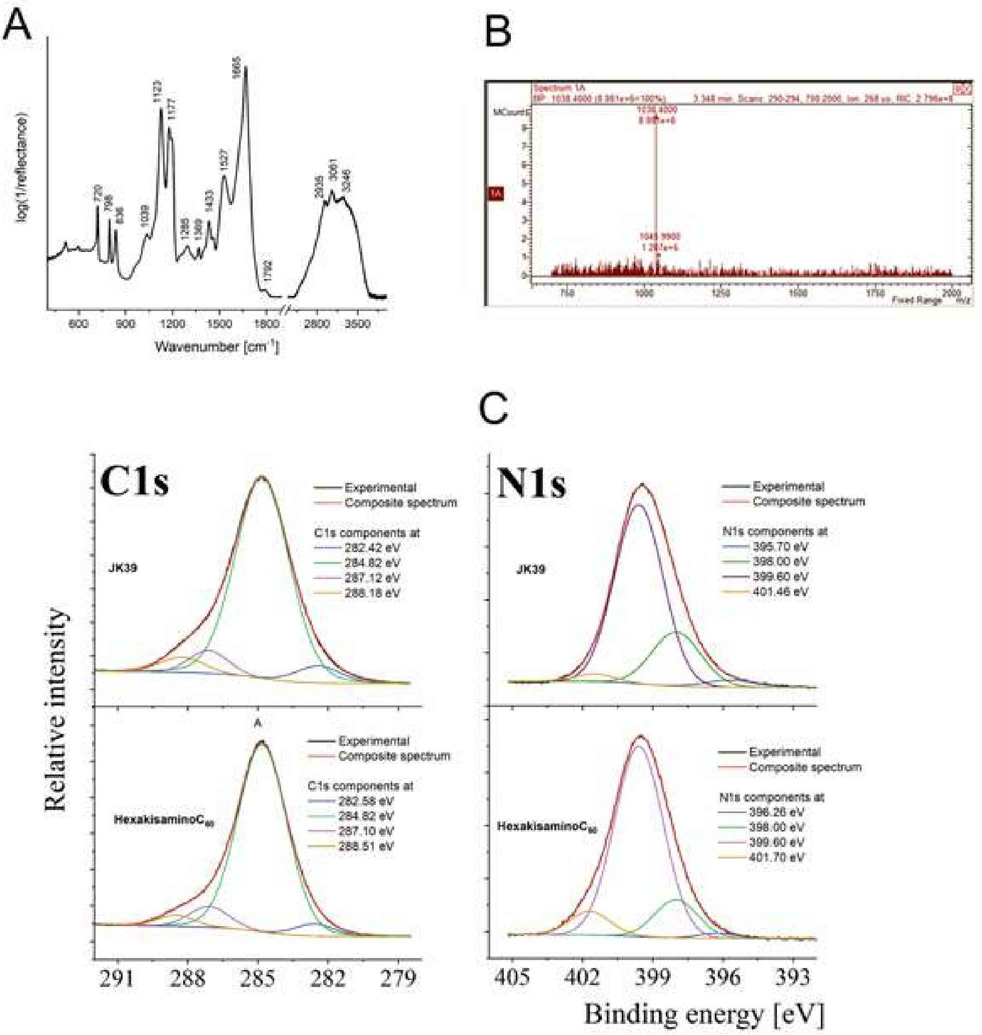

Figure 2. (**A**) Infrared spectrum of fullerene JK39; (**B**) ESI-mass spectrum of water-soluble fullerene JK39 (positive mode, 100 mV); (**C**) A high-resolution photoemission spectra of carbon and nitrogen measured in the fullerene nanomaterials JK39 and HexakisaminoC$_{60}$.

core before the formation of complex with desired siRNA. In our experiments two fullerene nanomaterials were dissolved in nuclease free water (pH 7) without adding any buffers—the low pH of that solution could have cytotoxic effects on the cells.

Our next step was the physicochemical characterization of the fullerene-siRNA complexes. Firstly, we studied the changes in the zeta potential of the formed complexes, assuming that it would decrease due to the anionic character of the RNA phosphate groups. As is depicted in Fig. 3C, the zeta potential of the HexakisaminoC$_{60}$-siRNA complex was + 19.1 mV (a change from + 28.6 mV), while the JK39-siRNA complex also had a higher zeta potential, measured at + 32.7 mV—a change from + 54 and + 90 mV (Fig. 3D). Simultaneously, the HexakisaminoC$_{60}$-siRNA complex formed monodisperse aggregates (PDI = 0.29) around 361 nm, whereas the JK39-siRNA complex had a polydisperse mixture of aggregates around 110, 604, and 4230 nm with PDI > 0.6. The observations mentioned above regarding the size of the siRNA complexes were further investigated with TEM morphology measurements, which revealed that was a fluffy-like structure (Fig. 3A) and polydispersity for the JK39-siRNA complex (Fig. 3B) and an image of the HexakisaminoC$_{60}$-siRNA complex which is presented in Fig. S8. The previously published reports by Nakamura et al. that described the TPFE-siRNA–plasma protein complex interactions revealed that it can disintegrate on a solid substrate, which suggests that it would also be unstable in vivo for releasing siRNA[11].

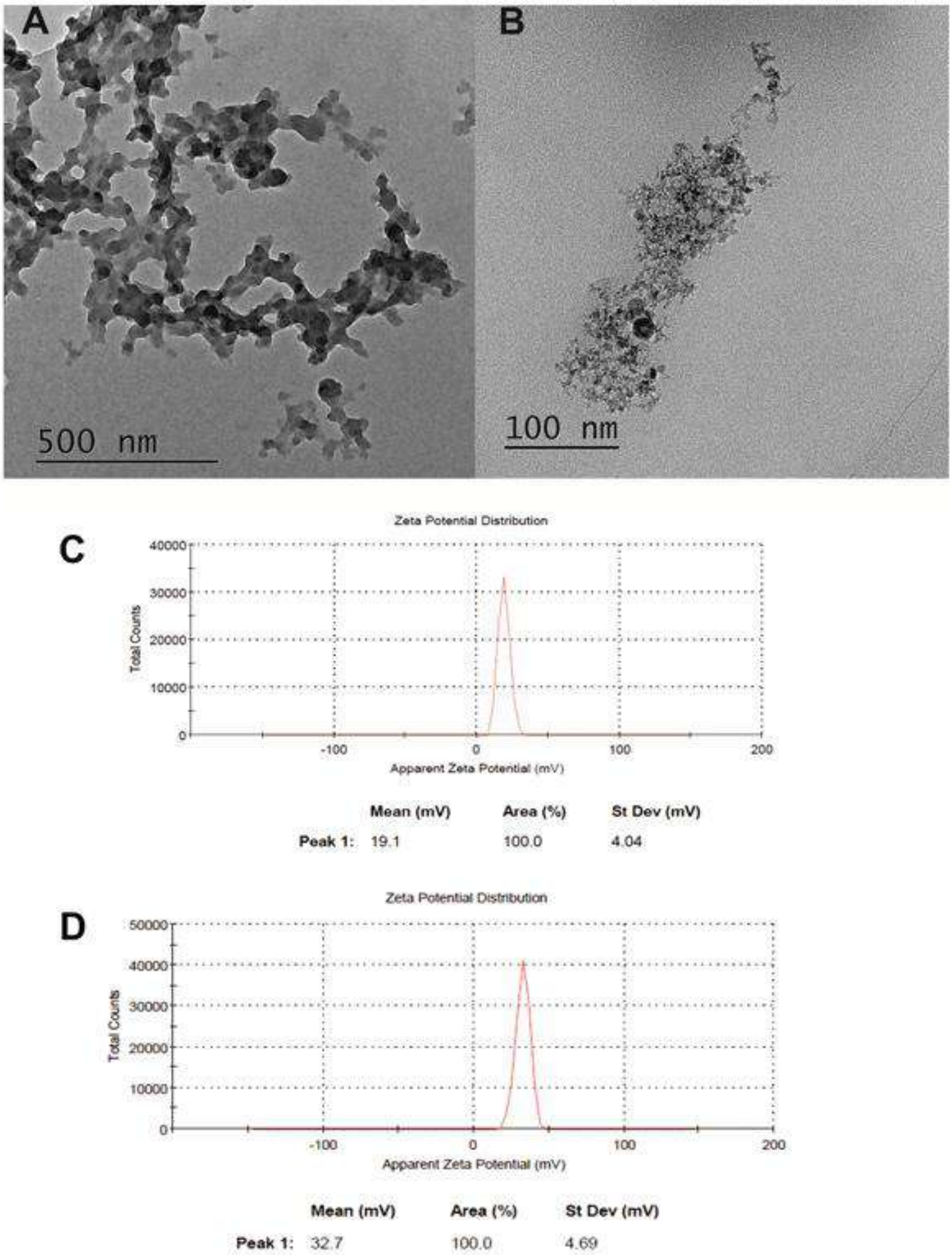

Figure 3. The TEM images of the siRNA-fullerene complexes that were measured for (**A**) HexakisaminoC_{60} and (**B**) JK39 carbon nanomaterials; (**C,D**) zeta potentials of the siRNA-fullerene complexes that were measured for C-HexakisaminoC_{60} and D-JK39 carbon nanomaterials.

Our final experiment was to test the siRNA transfection efficacy of the created highly water-soluble fullerene nanomaterials on prostate cancer cells that had been transfected with the EGFP-encoding plasmid and to compare their transfection properties in the presence of a serum with lipid-based Lipofectamine 3000 being used as a positive control. The results are depicted in Fig. 4, which shows a significant decrease in the fluorescence signal (to around 50%) when the cells were treated with the HexakisaminoC_{60}-siRNA complex. Notably, the fullerene nanomaterial JK39 had quite a low transfections efficacy. Based on the zeta potential measurements and TEM

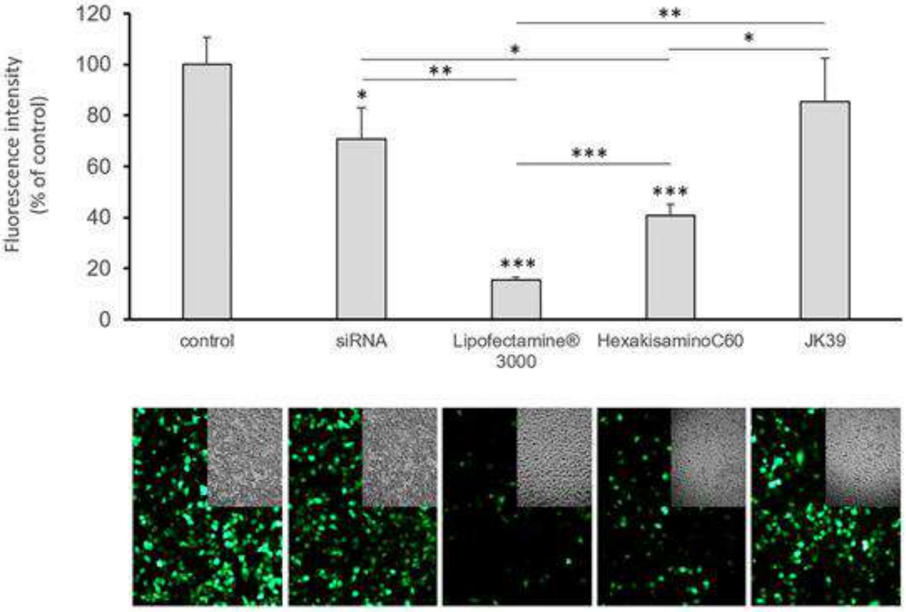

Figure 4. The efficiency of the siRNA transfer in vitro with the engineered fullerene nanomaterials HexakisaminoC$_{60}$ and JK39 and the resulting EGFP silencing in a prostate cancer model (DU145 cells that had been transfected with the plasmid encoding EGFP). Each value represents the mean ± SD (n = 3). Statistical significance was determined using the t-test ($^{*}p < 0.05$; $^{**}p < 0.01$; $^{***}p < 0.001$).

analysis, we suspect that JK39 forms an extremely stable complex with siRNA delivering it to the cytosol but that it cannot cleave it in cellular conditions. These effects could also be caused by the D-glucosamine moiety, which has an additional nitrogen connected at C2 position of glucosamine, which could be additionally protonated (as TFA salt) and that the differences in protein corona adsorbed on the surface of fullerene nanomaterials-JK39 possess additional sugar based hydroxyl groups. This explanation complies with the higher zeta potential of sugar-based JK39 complex and thus its higher stability within cells. Moreover siRNA, when used without adding of any transfection agent, works better; it decreases the GFP fluorescence signal to 75 percent of the starting signal, which further confirms our hypothesis. An attractive option for future biological studies of the JK39 fullerene nanomaterial could be to test the photocleavage of the JK39-siRNA stable complex based on the irradiation of cells with blue/green light (glycofullerenes are photosensitizers) and the generation of ROS, which led to good results for the C$_{60}$-Dex-NH$_2$ fullerene and the upconversion nanomaterials that were used as the siRNA transfection agents[13,50].

Conclusions

In summary, inspired by a previously developed TPFE cationic fullerene transfection agent, we developed two cationic fullerenes HexakisaminoC$_{60}$ and monoglucosamine JK39, which had a T$_h$ symmetry that is characteristic for Bingel–Hirsch hexakisadducts. To the best of our knowledge, this is the first example of [60]fullerene hexakisadduct being ready to transfect siRNA. We postulate that the inactivity of JK39 fullerene in transfection experiments is caused by its high initial zeta potential and polydispersity. Future biological experiments should also determine how JK39 protects siRNA against enzymatic degradation, mainly by analyzing the adsorbed serum proteins (protein corona) on its surface. The cationic water-soluble fullerene nanomaterials to which adding interesting groups and tags (as sugars, azides or triple bonds for biorthogonal chemistry) can be attached, might hold considerable promise for in vivo siRNA delivery in the future.

Received: 7 March 2021; Accepted: 4 May 2021
Published online: 19 May 2021

References

1. Farjadian, F. *et al.* Nanopharmaceuticals and nanomedicines currently on the market: Challenges and opportunities. *Nanomedicine* **14**, 93–126. https://doi.org/10.2217/nnm-2018-0120 (2019).
2. Mei, Y. *et al.* Recent progress in nanomaterials for nucleic acid delivery in cancer immunotherapy. *Biomater. Sci.* **7**, 2640–2651 (2019).
3. Dammes, N. & Peer, D. Paving the road for RNA therapeutics. *Trends Pharmacol. Sci.* **41**, 755 (2020).

4. Dykxhoorn, D. M. & Lieberman, J. Running interference: Prospects and obstacles to using small interfering RNAs as small molecule drugs. *Annu. Rev. Biomed. Eng.* **8**, 377–402 (2006).
5. Garber, K. Alnylam launches era of RNAi drugs. *Nat Biotechnol.* **36**, 777–778 https://doi.org/10.1038/nbt0918-777 (2018).
6. Kam, N. W. S., Liu, Z. & Dai, H. Functionalization of carbon nanotubes via cleavable disulfide bonds for efficient intracellular delivery of siRNA and potent gene silencing. *J. Am. Chem. Soc.* **127**, 12492–12493 (2005).
7. Nakamura, E. *et al.* Functionalized fullerene as an artificial vector for transfection. *Angew. Chem.* **112**, 4424–4427 (2000).
8. Sitharaman, B. *et al.* Water-soluble fullerene (C(60)) derivatives as nonviral gene-delivery vectors. *Mol. Pharm.* **5**, 567–578. https://doi.org/10.1021/mp700106w (2008).
9. Sigwalt, D. *et al.* Gene delivery with polycationic fullerene hexakis-adducts. *Chem. Commun.* **47**, 4640–4642 (2011).
10. Illescas, B. M. *et al.* Multivalent cationic dendrofullerenes for gene transfer: Synthesis and DNA complexation. *J. Mater. Chem. B* **8**, 4505–4515 (2020).
11. Minami, K. *et al.* siRNA delivery targeting to the lung via agglutination-induced accumulation and clearance of cationic tetraamino fullerene. *Sci. Rep.* **4**, 4916 (2014).
12. Minami, K., Okamoto, K., Harano, K., Noiri, E. & Nakamura, E. Hierarchical assembly of siRNA with tetraamino fullerene in physiological conditions for efficient internalization into cells and knockdown. *ACS Appl. Mater. Interfaces* **10**, 19347–19354 (2018).
13. Wang, J. *et al.* Visible light-switched cytosol release of siRNA by amphiphilic fullerene derivative to enhance RNAi efficacy in vitro and in vivo. *Acta Biomater.* **59**, 158–169 (2017).
14. Corbo, C. *et al.* The impact of nanoparticle protein corona on cytotoxicity, immunotoxicity and target drug delivery. *Nanomedicine* **11**, 81–100 (2016).
15. Cai, X. *et al.* Characterization of carbon nanotube protein corona by using quantitative proteomics. *Nanomed. Nanotechnol. Biol. Med.* **9**, 583–593 (2013).
16. Belgorodsky, B. *et al.* Formation and characterization of stable human serum albumin–Tris-malonic Acid [C60] fullerene complex. *Bioconjug. Chem.* **16**, 1058–1062 (2005).
17. Calvaresi, M. & Zerbetto, F. Baiting proteins with C60. *ACS Nano* **4**, 2283–2299. https://doi.org/10.1021/nn901809b (2010).
18. Serda, M. *et al.* Glycofullerenes as non-receptor tyrosine kinase inhibitors-towards better nanotherapeutics for pancreatic cancer treatment. *Sci. Rep.* **10**, 1–11 (2020).
19. Gräfe, C. *et al.* Intentional formation of a protein corona on nanoparticles: serum concentration affects protein corona mass, surface charge, and nanoparticle–cell interaction. *Int. J. Biochem. Cell Biol.* **75**, 196–202 (2016).
20. Rudzinski, W. E., Palacios, A., Ahmed, A., Lane, M. A. & Aminabhavi, T. M. Targeted delivery of small interfering RNA to colon cancer cells using chitosan and PEGylated chitosan nanoparticles. *Carbohyd. Polym.* **147**, 323–332 (2016).
21. Hirsch, A., Lamparth, I., Grösser, T. & Karfunkel, H. R. Regiochemistry of multiple additions to the fullerene core: Synthesis of a Th-symmetric hexakis adduct of C60 with Bis (ethoxycarbonyl) methylene. *J. Am. Chem. Soc.* **116**, 9385–9386 (1994).
22. Campisciano, V., La Parola, V., Liotta, L. F., Giacalone, F. & Gruttadauria, M. Fullerene–Ionic-liquid conjugates: A new class of hybrid materials with unprecedented properties. *Chem. A Eur. J.* **21**, 3327–3334 (2015).
23. Serda, M. *et al.* Development of photoactive Sweet-C60 for pancreatic cancer stellate cell therapy. *Nanomedicine (Lond.)* **13**, 2981–2993. https://doi.org/10.2217/nnm-2018-0239 (2018).
24. Serda, M. *et al.* Developing [60] fullerene nanomaterials for better photodynamic treatment of non-melanoma skin cancers. *ACS Biomater. Sci. Eng.* **6**, 5930 (2020).
25. Wang, T., Larcher, L. M., Ma, L. & Veedu, R. N. Systematic screening of commonly used commercial transfection reagents towards efficient transfection of single-stranded oligonucleotides. *Molecules* **23**, 2564 (2018).
26. Rak, M. *et al.* Boost of serum resistance and storage stability in cationic polyprenyl-based lipofection by helper lipids compositions. *Eur. J. Pharm. Biopharm.* **155**, 199–209 (2020).
27. Rak, M. *et al.* Efficient and non-toxic gene delivery by anionic lipoplexes based on polyprenyl ammonium salts and their effects on cell physiology. *J. Gene Med.* **18**, 331–342 (2016).
28. Chenon, B. & Sandorfy, C. Hydrogen bonding in the amine hydrohalides: I. General aspects. *Can. J. Chem.* **36**, 1181–1206 (1958).
29. Stewart, J. E. Vibrational spectra of primary and secondary aliphatic amines. *J. Chem. Phys.* **30**, 1259–1265 (1959).
30. Long, F. & Bakule, R. Keto-enol transformation of 1, 2-cyclohexanedione. II. Acid catalysis in strongly acidic media 1–3. *J. Am. Chem. Soc.* **85**, 2313–2318 (1963).
31. Perrin, C. L. Proton exchange in amides: Surprises from simple systems. *Acc. Chem. Res.* **22**, 268–275. https://doi.org/10.1021/ar00164a002 (1989).
32. Cho, S. J. *et al.* N-protonation vs O-protonation in strained amides: Ab initio study. *J. Org. Chem.* **62**, 4068–4071. https://doi.org/10.1021/jo962063z (1997).
33. Cook, D. The infrared spectra of N-acyltrialkylammonium halides, in relation to those of amide salts. *Can. J. Chem.* **40**, 2362–2368 (1962).
34. Watts, J. F. High resolution XPS of organic polymers: The Scienta ESCA 300 database. G. Beamson and D. Briggs. 280pp.,£ 65. John Wiley & Sons, Chichester, ISBN 0471 935921 (1992). *Surf. Interface Anal.* **20**, 267–267 (1993).
35. Yu, J. *et al.* Effects of fullerene derivatives on bioluminescence and application for protease detection. *Chem. Commun.* **48**, 11011–11013. https://doi.org/10.1039/C2CC36099C (2012).
36. Yan, X. *et al.* Preparation and characterization of electrochemically deposited carbon nitride films on silicon substrate. *J. Phys. D Appl. Phys.* **37**, 907 (2004).
37. Chi, K. *et al.* Freestanding graphene paper supported three-dimensional porous graphene–polyaniline nanocomposite synthesized by inkjet printing and in flexible all-solid-state supercapacitor. *ACS Appl. Mater. Interfaces* **6**, 16312–16319 (2014).
38. Veerapandian, M., Zhang, L., Krishnamoorthy, K. & Yun, K. Surface activation of graphene oxide nanosheets by ultraviolet irradiation for highly efficient anti-bacterials. *Nanotechnology* **24**, 395706 (2013).
39. Bon, S. B. *et al.* Plasma fluorination of chemically derived graphene sheets and subsequent modification with butylamine. *Chem. Mater.* **21**, 3433–3438 (2009).
40. Yu, B. *et al.* Functionalized graphene oxide/phosphoramide oligomer hybrids flame retardant prepared via in situ polymerization for improving the fire safety of polypropylene. *RSC Adv.* **4**, 31782–31794 (2014).
41. Sadri, R. *et al.* A bio-based, facile approach for the preparation of covalently functionalized carbon nanotubes aqueous suspensions and their potential as heat transfer fluids. *J. Colloid Interface Sci.* **504**, 115–123 (2017).
42. Nishimura, O., Yabe, K. & Iwaki, M. X-ray photoelectron spectroscopy studies of high-dose nitrogen ion implanted-chromium: A possibility of a standard material for chemical state analysis. *J. Electron Spectrosc. Relat. Phenom.* **49**, 335–342 (1989).
43. Daems, N., Sheng, X., Vankelecom, I. F. & Pescarmona, P. P. Metal-free doped carbon materials as electrocatalysts for the oxygen reduction reaction. *J. Mater. Chem. A* **2**, 4085–4110 (2014).
44. Lapin, N. A. *et al.* Biotransport kinetics and intratumoral biodistribution of malonodiserinolamide-derivatized [60] fullerene in a murine model of breast adenocarcinoma. *Int. J. Nanomed.* **12**, 8289 (2017).
45. Deryabin, D. G. *et al.* A zeta potential value determines the aggregate's size of penta-substituted [60] fullerene derivatives in aqueous suspension whereas positive charge is required for toxicity against bacterial cells. *J. Nanobiotechnol.* **13**, 1–13 (2015).
46. Molinaro, R. *et al.* Polyethylenimine and chitosan carriers for the delivery of RNA interference effectors. *Expert Opin. Drug Deliv.* **10**, 1653–1668 (2013).
47. Sioud, M. On the delivery of small interfering RNAs into mammalian cells. *Expert Opin. Drug Deliv.* **2**, 639–651 (2005).

48. Wittrup, A. *et al.* Visualizing lipid-formulated siRNA release from endosomes and target gene knockdown. *Nat. Biotechnol.* **33**, 870–876 (2015).
49. Wang, J. *et al.* Far-red light-mediated programmable anti-cancer gene delivery in cooperation with photodynamic therapy. *Biomaterials* **171**, 72–82 (2018).
50. Zhang, Y. *et al.* Photo-tearable tape close-wrapped upconversion nanocapsules for near-infrared modulated efficient siRNA delivery and therapy. *Biomaterials* **163**, 55–66 (2018).

Acknowledgements

This work was supported by National Science Centre (Poland) Grant OPUS (UMO-2019/35/B/NZ7/02459) awarded to Dr. Maciej Serda. Dr. Mateusz Dulski acknowledges the financial support from the National Science Center based on decision 2017/26/D/ST8/01117. Additionally, we would like to thank Professor Ewa Swiezewska and Dr. Marek Masnyk of the Institute of Biochemistry and Biophysics Polish Academy of Sciences (PAS) in Warsaw for supplying PTAI-11. We would like also to thank Professor Ewa Zuba-Surma of the Department of Cell Biology, Faculty of Biochemistry, Biophysics and Biotechnology, Jagiellonian University for the possibility to use Guava® easyCyte 8 flow cytometer. We would also thank Mr Richard Visser from Advanced Chemistry Development UK Ltd (ACD/Labs) for his help in pK_a parameters calculation for selected malonic acid derivatives using the ACD Percepta Software.

Author contributions

Conception and design: M.S. and M.R. Acquisition of data: J.K., M.R., K.B., M.Z., O.G., M.D. and M.S. Analysis and interpretation of the data: M.R., K.B., M.Z., M.D., R.M., Z.M. and M.S. Manuscript preparation: M.S., M.R., M.D. and K.B. wrote the manuscript. All authors read and approved the final manuscript.

Competing interests

The authors declare no competing interests.

Additional information

Supplementary Information The online version contains supplementary material available at https://doi.org/10.1038/s41598-021-89943-5.

Correspondence and requests for materials should be addressed to M.S.

Reprints and permissions information is available at www.nature.com/reprints.

ACS Biomaterials SCIENCE & ENGINEERING

In Situ Cellular Localization of Nonfluorescent [60]Fullerene Nanomaterial in MCF-7 Breast Cancer Cells

Maciej Serda,* Katarzyna Malarz, Julia Korzuch, Magdalena Szubka, Maciej Zubko, and Robert Musioł

Cite This: *ACS Biomater. Sci. Eng.* 2022, 8, 3450−3462 Read Online

ACCESS | Metrics & More | Article Recommendations | Supporting Information

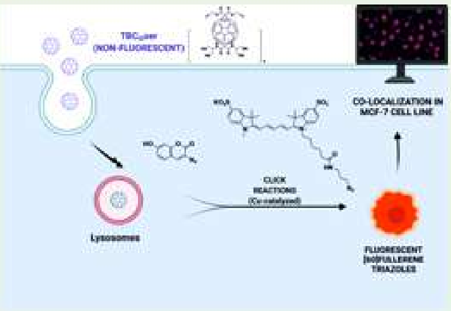

ABSTRACT: Cellular localization of carbon nanomaterials in cancer cells is essential information for better understanding their interaction with biological targets and a crucial factor for further evaluating their biological properties as nanovehicles or nanotherapeutics. Recently, increasing efforts to develop promising fullerene nanotherapeutics for cancer nanotechnology have been made. However, the main challenge regarding studying their cellular effects is the lack of effective methods for their visualization and determining their cellular fate due to the limited fluorescence of buckyball scaffolds. Herein, we developed a method for cellular localization of nonfluorescent and water-soluble fullerene nanomaterials using the *in vitro* click chemistry approach. First, we synthesized a triple-bonded fullerene probe (TBC$_{60}$ser), which was further used as a starting material for 1,3-dipolar cycloaddition using 3-azido-7-hydroxycoumarin and sulfo-cyanine5 azide fluorophores to create fluorescent fullerene triazoles. In this work, we characterized the structurally triple-bonded [60]fullerene derivative and confirmed its high symmetry (T_h) and the successful formation of fullerene triazoles by spectroscopic techniques (i.e., ultraviolet−visible, fluorescence, and Fourier transform infrared spectroscopies) and mass spectrometry. The created fluorescent fullerene triazoles were successfully localized in the MCF-7 breast cancer cell line using fluorescent microscopy. Overall, our findings demonstrate that TBC$_{60}$ser localizes in the lysosomes of MCF-7 cells, with only a small affinity to mitochondria.

KEYWORDS: *[60]fullerenes, click reactions, cellular colocalization, breast cancer, lysosomes, triazoles*

INTRODUCTION

At present, nanomedicine is entering clinical trials, and some nanotherapeutics have already been approved by the FDA and EMA to treat several lethal diseases, including cancer and microbial infections.[1,2] Compared with traditional treatment modalities, engineered nanoparticles offer new therapeutic options, especially for breast cancer, where nanotherapeutics such as Doxil and Abraxane have already been used in adjuvant therapies.[3] Breast tumors are heterogeneous and complex pathogenic entities, and those that do not express crucial hormone receptors (e.g., triple-negative breast cancer) are significantly more invasive and apt to metastasize.[4] Carbon nanomaterials have attracted significant interest in cancer nanotechnology, especially as drug delivery vehicles and theranostic pharmaceuticals on a nanometric scale.[5−7] Some examples of nanotherapeutics include a multifunctional drug delivery system with transferrin/hyaluronic acid-functionalized multiwalled carbon nanotubes (HA-MWCNTs/Tf@ART) for *in vitro* treatment of breast cancer cells as well as [60]fullerene nanoconjugate with docetaxel, which significantly improve its bioavailability.[8,9]

Biological uptake and cellular and organ localization of engineered nanoparticles are crucial information when developing novel carbon nanomaterials for cancer nanotechnology and beyond.[10] Several analytical techniques have been developed to study the localization of nanomaterials in biological samples, including fluorescent, intravital, and transmission electron microscopies.[11,12] These techniques have been used to study biodistribution and uptake/clearance of carbon nanomaterials in cancer tissues in living organisms and traditional two-dimensional cellular cultures, especially for fluorescent carbon dots, near-infrared absorbing carbon nanotubes, and fluophore-labeled fullerenes.[13−15] Fullerene derivatives have been studied extensively in the last 30 years, as there are several synthetic approaches to make them water-soluble. This includes reactions with strong bases in the presence of quaternary ammonium salts, interactions with polyhydroxylated sugars, as well as Bingel−Hirsch/Prato reactions with substrates possessing a large number of amine, hydroxyl, or carboxylic functional groups.[16,17] After the formation of fully water-soluble [60]fullerene nanomaterials,

Received: May 9, 2022
Accepted: July 8, 2022
Published: July 20, 2022

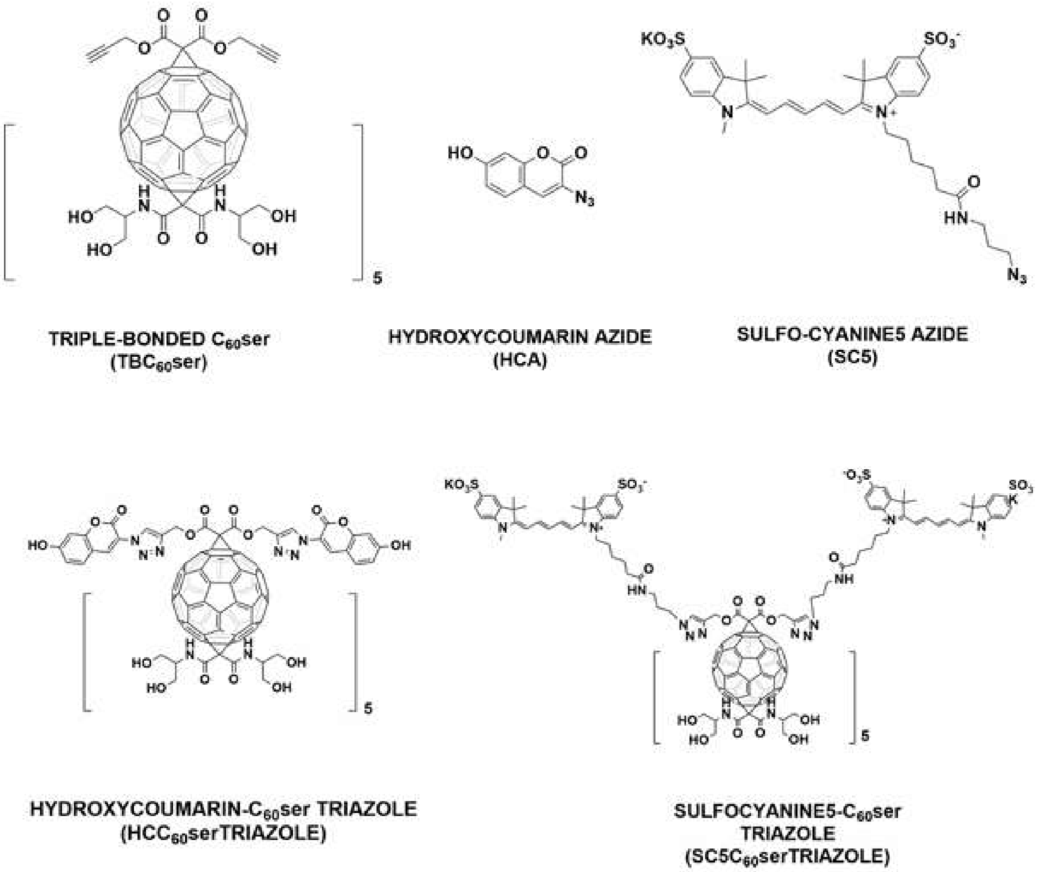

Figure 1. Chemical structures of triple-bonded[60]fullerene nanomaterial C_{60}ser (TBC_{60}ser) and fluorescent probes (HCA and SC5) that were used for its visualization and formation of fullerene triazoles.

they were intensively explored in terms of their cytotoxicity profiles and cell uptake models.[18,19] Nevertheless, detection of fullerene derivatives in cells is limited due to their drastically weak fluorescence in polar solvents.[20] Some of the literature methods reported to overcome this inconvenience rely on nonspecific complexation with fluorophores, synthesizing fluorescently labeled fullerene derivatives, or visualization of fullerene nanomaterials using a special fullerene antibody.[19,21] Another approach was proposed by Di Giosia and co-workers, who synthesized a water-soluble C_{70}@lysozyme complex and confirmed its localization in lysosomes using photoacoustic and third-harmonic generation (THG) imaging techniques.[22] Most of the above-mentioned methods share an important drawback related to substantial changes in the properties of the nanomaterial. Particularly, covalent binding of the fluorophore to the buckyball may drastically alter not only physicochemical parameters but also essentially the affinity of the latter toward biological targets and its fate in the cellular environment. Fullerene-specific antibodies are apparently free from these drawbacks but introduce others related to the chemical nature of the monoclonal antibody as well as unacceptable specificity at times, especially to fullerene derivatives.

The development of "click chemistry" changed the fields of organic synthesis and nanotechnology, opening novel possibilities for drug development and bioconjugation;[23,24] its methodology is mainly based on copper(I)-catalyzed 1,3-dipolar cycloadditions between organic azides and alkynes, resulting in 1,4-disubstituted 1,2,3-triazoles as variously functionalized molecular scaffolds. These click reactions have been successfully used to efficiently functionalize engineered carbon nanomaterials, including CNTs, graphene oxide, and fullerenes.[25−27] Classical works by groups led by Nierengarten and Martin described the formation of very complex fullerene nanomaterials using various copper catalysts (e.g., $CuSO_4 \cdot 5H_2O$ and sodium ascorbate), often with fascinating supramolecular and biological properties, such as Ebola virus inhibition or liquid crystal formation.[28,29] However, to the best of our knowledge, there are no reports describing the use of *in situ* copper(I)-catalyzed click reactions in cancer cells to confirm the cellular localization of nonfluorescent fullerene nanomaterials. Our observation is of great practical importance to all cancer nanotechnology scientists working with water-soluble fullerenes and studying their biodistribution. Owing to previous works on concentration-dependent cytotoxicity of copper(I) salts in cellular conditions,[30,31] novel synthetic approaches were developed. These include famous works by Bertozzi and co-workers describing "biorthogonal reactions", which could be performed even in living organisms (including humans) using a plethora of cyclooctyne derivatives and appropriate organic azides in copper-free conditions.[32] More-

Scheme 1. 1,3-Dipolar Cycloaddition Reactions between TBC$_{60}$ser and Selected Probes Creating Fluorescent Fullerene Triazoles

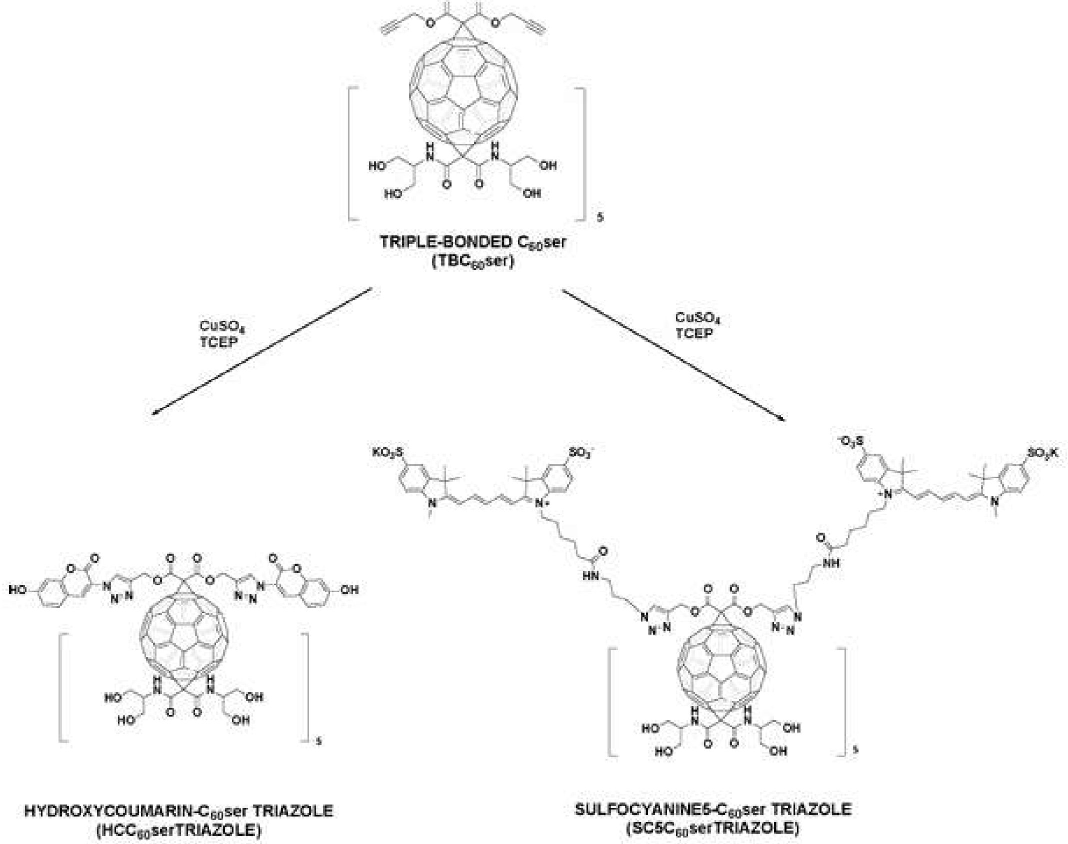

over, novel cyclooctyne derivatives of [60]fullerene were also created for bioorthogonal reactions, but they are not soluble in water, and no reports have been published describing their direct translation for *in vivo* experiments.[33]

Here, we developed a facile method for *in situ* visualization of a water-soluble fullerene nanomaterial, TBC$_{60}$ser, in breast cancer cells MCF 7 (Figure 1). We used the C$_{60}$ser scaffold as a nontoxic and fully water-soluble buckyball, which was previously reported to penetrate through cellular membranes in cancer cells.[19,34] Therefore, to investigate TBC$_{60}$ser cellular localization, we used two different approaches. First, 7-hydroxy-coumarin azide (HCA) was used as a nonfluorescent precursor that was activated fluorescently only after the formation of [60]fullerene triazole. Second, the bright and photostable sulfo-cyanine 5 (SC5) azide acted as a double control dye, attached to the fullerene scaffold via copper-catalyzed cycloaddition in water (Scheme 1) to doubly confirm the cellular localization of the fullerene nanomaterial. In fact, it was demonstrated here that appropriate *in situ* cellular tagging of [60]fullerene with a triple-bond tag allowed us to visualize engineered fullerene nanostructures in lysosomes of breast cancer cells. Interestingly, during our survey for cellular visualization of nonfluorescent buckyballs, we also synthesized an azide analog of TBC$_{60}$ser, which could be used for biorthogonal approaches with cyclooctyne-derived dyes convenient for copper-free, strain-promoted click reactions. However, our cellular experiments demonstrated that, regardless of the desirable solubility, C$_{60}$ser azide did not pass through the cell membranes and remained in the culture medium (data not shown); thus it did not meet the essential experimental criterion and cannot be used in further investigations. However, it is reasonable to underline the unpredictable issues of altering the pharmacokinetic and physicochemical properties of the nanomaterial during transformation to molecular probes.

■ MATERIALS AND METHODS

Materials. All of the chemicals used were of reagent-grade quality or better, and the solvents were dried according to literature procedures. The following reagents were used as received: C$_{60}$ (99.5+%, SES Research, USA), propargyl alcohol (Acros Organics), *p*-toluenesulfonic acid monohydrate (Sigma-Aldrich), 1,8-diazabicyclo[5.4.0]undec-7-ene (DBU, Sigma-Aldrich), malonic acid (Sigma-Aldrich), CBr$_4$ (Sigma-Aldrich), 2-amino-1,3-propanediol (AK Scientific), acetic anhydride (Fisher), *N*-acetylglycine (Acros Organics), 2,4-dihydroxybenzaldehyde (Acros Organics), anhydrous sodium acetate (Sigma-Aldrich), sodium nitrite (Avantor), sodium azide (Sigma-Aldrich), copper sulfate pentahydrate (Avantor), tris(2-carboxyethyl)phosphine (Sigma-Aldrich), and sulfo-cyanine5 azide (Lumiprobe).

Methods. Nuclear magnetic resonance (NMR) spectra were obtained using a Bruker Advance III 500 MHz NMR spectrometer with tetramethylsilane as the internal standard. Mass spectroscopy

(MS) spectra were collected using an electrospray single quad Agilent InfinityLab LC/MSD XT mass spectrometer in the range of 100−3000 Da, equipped with an Agilent HPLC 1260 Infinity II system and SBC18 column (1.8 μm, 2.1 × 50 mm); additional electrospray ionization (ESI) MS measurements were carried out using a Varian 320-MS ESI mass spectrometer. Both ESI-MS measurements were conducted in an acetonitrile/H_2O/TFA mixture (70/29.9/0.1, v/v). A water-insoluble fullerene monoadduct (**2**) mass measurement was conducted using a Bruker Autoflex II MALDI-TOF mass spectrometer. Attenuated total reflectance Fourier transform infrared (ATR-FT-IR) measurements were taken using a JASCO FT/IR-4600 spectrophotometer equipped with a JASCO ATR PRO ONE kit. Fullerene powders were measured using an ATR ZnSe accessory in the 700−4000 cm^{-1} range. The spectra were recorded using 64 accumulations and at a spectral resolution of 1 cm^{-1}. Ultraviolet−visible (UV−vis) and fluorescence spectra were measured on JACSO spectrometers (V-700 and FP 8500 models). Dynamic light scattering and ζ potentials of the fullerene nanomaterial TBC_{60}ser were measured using a Zetasizer Nano Instrument (Malvern Panalytical Ltd., UK). High-resolution transmission electron microscopy (HRTEM) observations were performed using a JEOL JEM 3010 microscope operating at a 300 kV accelerating voltage, which was equipped with a Gatan 2k × 2k Orius 833SC200D CCD camera. Chemical analyses of the surface of the fullerenes were performed via X-ray photoelectron spectroscopy (XPS) using a PHI 5700/660 Physical Electronics photoelectron spectrometer with monochromatic Al $K\alpha$ X-ray radiation (1486.6 eV). The energy of the electrons was measured with a hemispherical analyzer at a resolution of approximately 0.3 eV. Measurements of the photoelectron emission were taken from a surface area with a diameter of 800 μm and at a takeoff angle of 45°. Quantification of the XPS spectra, utilizing peak area and the peak height sensitivity factor, was used for Multipak Physical Electronics analysis. The XPS core-level spectra were fitted using the Doniach−Sunjic method. The final dialysis purification of the water-soluble fullerene nanomaterials was performed on Pall Microsep centrifugal membranes with molecular cut-offs at 1 and 3 kDa (Pall Corporation).

Synthesis. *Synthesis of Dipropargyl Malonate.* Malonic acid (20 mmol; 2000 mg), *para*-toluenesulfonic acid (*p*-TSA; 0.3 mmol; 60 mg), and 50 mL of toluene were added to a round-bottom flask equipped with a magnetic stirrer and a reflux condenser. Next, a solution of propargyl alcohol (95 mmol; 5380 mg) in 3 mL of toluene was added to the reaction mixture, followed by heating for 48 h at 120 °C. After that time, a brown solution was obtained, which was further extracted with a saturated solution of sodium bicarbonate; organic phases were combined dried over magnesium sulfate, then evaporated on a rotary evaporator to obtain a lightly yellowish, oily dipropargyl malonate. The final product was characterized by NMR spectroscopy (see Supporting Information and Figures S2 and S3).

Synthesis of 3-Azido-7-hydroxycoumarin. The nonfluorescent coumarin derivative was synthesized using a modified procedure.[35] In brief, 2,4-dihydroxy benzaldehyde (20 mmol; 2.76 g), *N*-acetylglycine (20 mmol; 2.34 g), and anhydrous sodium acetate (60 mmol; 4.92 g) were dissolved in 100 mL of acetic anhydride and heated under reflux for 4 h. After this time, the reaction mixture was poured into an ice container, and the resulting yellow solid of peracetylated 3-amino-7 hydroxycoumarin was filtered under reduced pressure. The intermediate was used for further reactions without additional purification. In order to hydrolyze the acetyl protecting groups from 3-amino-7 hydroxycoumarin and introduce the azide group in the 3-position of the coumarin, a hydrolysis reaction followed by the formation of diazonium salt was performed. For this purpose, the previously obtained intermediate was heated under reflux in a solution of concentrated HCl and ethanol at a 2:1 volume ratio (20 mL of 35% HCl and 10 mL of 95% C_2H_5OH) for 1 h. The reaction mixture was allowed to cool, and 20 mL of cold water was added to dilute the solution. The reaction mixture was then cooled in an ice bath, and sodium nitrite (40 mmol; 2.760 g) was gradually added before stirring for another 5−10 min. Then, sodium azide (60 mmol; 3.900 g) was added in small portions. After stirring for 15 min at room temperature, the resulting precipitate was filtered, washed with water, and then dried *in vacuo* to give the final azide as a brown solid, with a melting point of 121 °C (lit: 118−120 °C).[35] The final compound was characterized by NMR and UV−vis spectroscopies, and its lack of fluorescence properties was confirmed in cellular experiments.

*[60]Fullerene Monoadduct (**2**).* The [60]fullerene (0.5 mmol; 360 mg) was dissolved in 400 mL of dry, degassed toluene using an ultrasonic bath (20 min). To obtain a purple solution of C_{60}, dipropargyl malonate (0.44 mmol; 80 mg) and CBr_4 (0.63 mmol; 210 mg) were added with intense stirring. Next, a DBU solution (0.625 mmol; 95 mg) in 7 mL of toluene was added dropwise to the reaction mixture. The reaction mixture was stirred for 3 h at room temperature and monitored by the thin-layer chromatography (TLC) technique. Upon completion of the reaction, a brown solution of [60]fullerene monoadduct was obtained, which was first purified by pouring the reaction mixture through a silica plug to remove mostly unreacted [60]fullerene, and then a brownish monoadduct fraction was further purified on a column using a toluene/dichloromethane 1/1 (v/v) eluent, followed by evaporation on a rotary evaporator. A lightly brownish solid was obtained (102 mg, 22% yield), which was further characterized by NMR and FT-IR spectroscopies and MALDI-TOF spectrometry. The [60]fullerene monoadduct (**2**) spectral characterization was in accordance with literature describing triple-bonded [60]fullerene derivatives (with 3-butynyl fragments).[36] The spectral characterization and MALDI-TOF mass spectrometry of compound (**2**) can be found in the Supporting Information (Figures S8 and S9).

*The [60]Fullerene Hexakisadduct (**3**) and Its Water-Soluble Analog (**4**).* A large-scale synthesis of peracetylated diserinol malonate was published by our group previously.[37] The [60]fullerene monoadduct (**2**) (0.2 mmol; 144 mg) was dissolved in a mixture of 10 mL of dry methylene chloride and 100 mL of dry toluene while stirring vigorously at room temperature in a nitrogen atmosphere. The peracetylated diserinol malonate was added to a fullerene solution (2 mmol; 836 mg) with an excess of carbon tetrabromide (4 mmol; 1324 mg). Next, a solution of DBU in chloroform was prepared by dissolving 1,8-diazabicyclo[5.4.0]undec-7-ene (2.4 mmol; 362 mg) in 3 mL of chloroform, which was added in 0.5 mL portions every 60 min, and the reaction mixture was stirred at room temperature for 72 h, observing a color change of the solution to brown-reddish. The final fullerene hexakisadduct (**3**) was purified using gradient flash column chromatography with dichloromethane and methanol as eluents (starting from 99:1 and finishing with 50:50 v/v), resulting in the formation of a brownish, oily liquid in 27% yield. The water-insoluble fullerene nanomaterial (**3**) was subsequently deprotected from acetyl protecting groups using the HCl-1,4-dioxane methodology developed earlier.[37] In brief, the peracetylated [60]fullerene derivative (**3**) was dissolved in 18 mL of 1,4-dioxane, and 3 mL of concentrated HCl was added to the brownish solution of fullerene nanomaterial and stirred for 7 days at room temperature. After that time, the final product was purified by three cycles of dialysis of an aqueous solution of (**4**) using a centrifugal membrane (molecular weight exclusion limit = 1.0 kDa; Nanosept, Pall Corporation, USA), which was then lyophilized and stored at −20 °C.

In Vitro Cu-Catalyzed Click Reactions using TBC_{60}ser and Organic Azides (HCA and SC5). Before the cellular experiments, all novel fullerene triazoles were synthesized using copper(I)-catalyzed click reactions. In general, 5 mg of TBC_{60}ser was dissolved in 10 mL of DI water (and 5 mL of DMSO in the case of HCA reaction), and 1 mg of the appropriate organic azide was added to the fullerene solution with the addition of 0.1 mmol $CuSO_4 \cdot 5H_2O$ and 0.1 mmol tris(2-carboxyethyl)phosphine (TCEP) as a reducing agent; the reaction mixture was further stirred at room temperature for 6 h. After that time, fullerene triazoles were purified using centrifugal membranes with 1-kDa cut-offs (Pall Corporation, USA) and characterized using ESI-MS, UV−vis, and FT-IR spectroscopy.

Biological Studies. *Cell Culture and Cytotoxicity.* The human breast carcinoma cell line (MCF-7) was purchased from ATCC. The normal human dermal fibroblasts cell line (NHDF) was obtained from PromoCell. MCF-7 was cultured in Dulbecco's modified Eagle's

Scheme 2. Synthetic Strategy for Obtaining Water-Soluble Fullerene Nanomaterial TBC$_{60}$ser and Nonfluorescent Dye 3-Azido-7-hydroxycoumarin

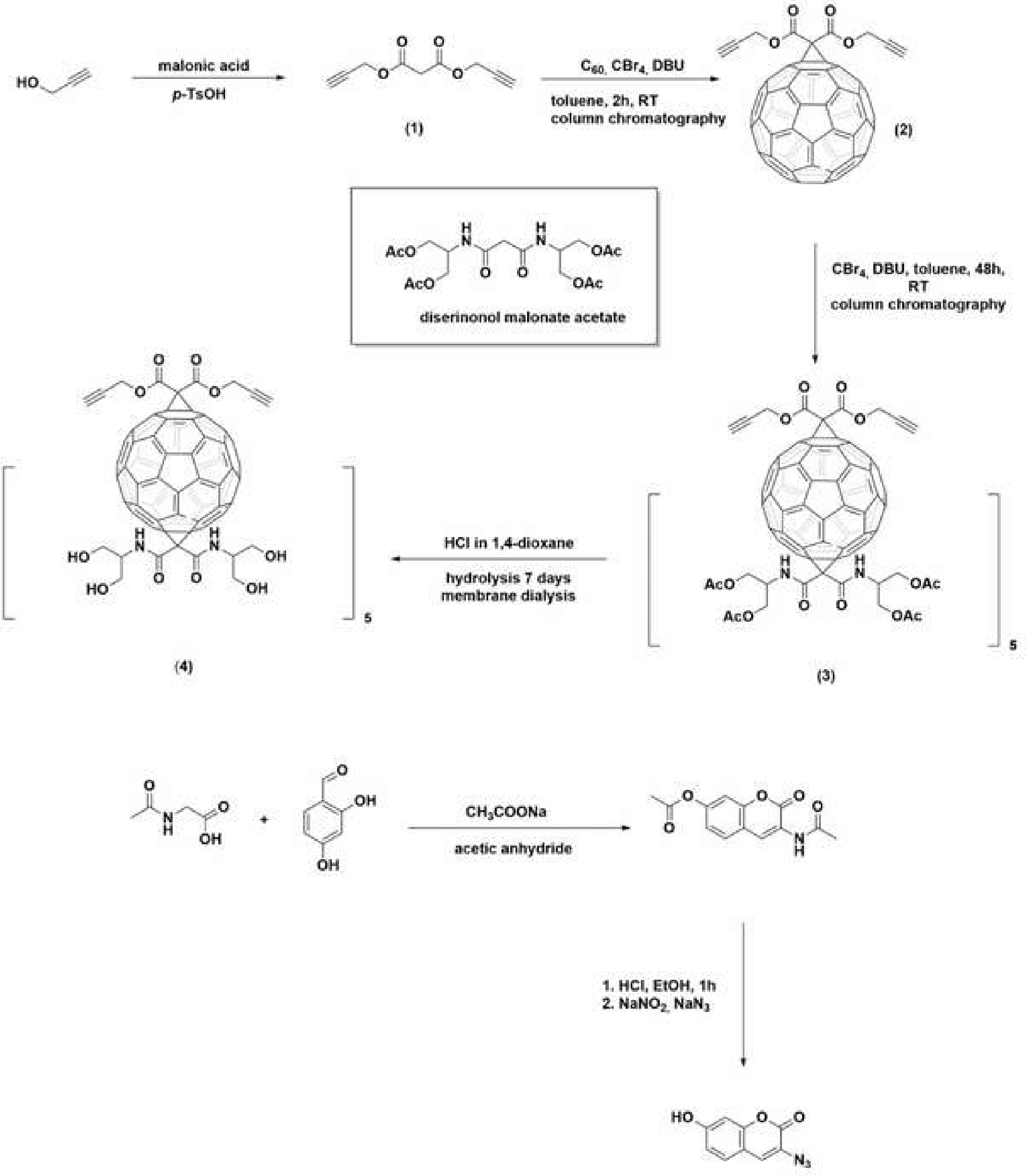

medium (DMEM) supplemented with 10% heat-inactivated fetal bovine serum (FBS, all from Sigma-Aldrich) containing a 1% v/v mixture of antibiotics (i.e., penicillin/streptomycin, Gibco). The DMEM for the NHDF were supplemented with 15% noninactivated FBS and antibiotics. The cells were grown under standard conditions at 37 °C with a 5% CO_2 humidified atmosphere.

The MCF-7 and NHDF cells were seeded into 96-well plates (Nunc) at a density of 5000 cells per well and incubated at 37 °C for 24 h for cytotoxicity experiments. The next day, the complete DMEM was replaced with solutions of tested fullerene nanomaterials, azides, or copper(II) sulfate pentahydrate at various concentrations. A cytotoxicity assay was performed after 72 h of incubation using CellTiter 96AQueous One Solution-MTS (Promega) according to the supplier's protocol. In short, the solutions of tested compounds were removed, and 100 μL of DMEM (without FBS or phenol red) with 20 μL of the MTS reagent were added to each well and incubated at 37 °C for 1 h. Then, the samples' absorbance was measured at 490 nm using a multiplate reader (Synergy 4, BioTek). The results were calculated as the percentage of the control (untreated cells) and estimated as the inhibitory concentration (IC_{50}) values (using GraphPad Prism 9). Each experiment was performed three times.

Cellular Staining. Before cellular staining experiments, MCF-7 cells were seeded onto coverslips at a density of 120,000 cells per slide and incubated at 37 °C for 48 h. Then, the DMEM was removed, and solutions of the fullerene nanomaterial (TBC$_{60}$ser, 468 μM = 1 mg/

https://doi.org/10.1021/acsbiomaterials.2c00542
ACS Biomater. Sci. Eng. 2022, 8, 3450−3462

mL), SC5 (25 μM), and HCA (25 μM) were added and further incubated for 2 h. Additionally, nuclei were stained with Hoechst 33342 (Invitrogen). Then, the cells were washed three times with PBS and mounted with DMEM without FBS or phenol red. The cellular staining results were immediately observed after excitation at 386 nm/438 and 650 nm (Cy5 filter) using the CellInsight CX7 High Content Analysis Platform (ThermoFisher).

In Situ Click Reactions and Cellular Colocalization Studies. MCF-7 cells were seeded in the same manner as described in Cellular Staining section. Then, the DMEM was removed, and the solution of fullerene TBC$_{60}$ser (468 μM) was added and further incubated overnight. After this time, the cells were washed twice with PBS and incubated with click reaction reagents SC5 (25 μM) or HCA (25 μM), $CuSO_4$ (1 mM), and TCEP (1 mM) for 2 h at 37 °C. Additionally, nuclei were stained with Hoechst 33342 (Invitrogen), mitochondria with MitoTracker Green or Orange, and lysosomes with LysoTracker Yellow HCK-123 according to previously described protocols.[38] The MCF-7 cells were washed three times with PBS and mounted with DMEM without FBS or phenol red. Cellular imaging was performed using the CellInsight CX7 High Content Analysis Platform under an appropriate filter for the click reaction or dyes used and a 40× objective. The fluorescence images were processed using ImageJ software 1.41 (Wayne Rasband, National Institutes of Health, Bethesda, MD, USA). The Manders' and Pearson's coefficients, which were used to show the colocalization triazole derivatives of TBC$_{60}$ser with specific-organelle trackers, were calculated using the ImageJ plugin "JACoP."

■ RESULTS AND DISCUSSION

The synthetic approach to [60]fullerene derivatives is mainly based on two synthetic approaches, which rely on classical Bingel−Hirsch cyclopropanations and Prato cycloadditions. The aforementioned methodology provides an opportunity to create fully water-soluble fullerene nanotherapeutics that are decorated with solubilizing addends.[39] In the case of the Bingel−Hirsch reaction, only two regioisomers are in the purview of the medicinal chemist: [60]fullerene monoadducts and corresponding hexakisadducts, which can exist only as one regioisomer and can be easily recognized by ^{13}C NMR measurements.[40] A plethora of isomers of fullerene derivatives could be formed in the case of other regioisomers (bis-, tris-, tetrakis-, and pentakis-adducts), observed in their purified form only when complicated and laborious separation techniques are applied. An example of such strenuous procedures is the work of Shi and co-workers, who separated 19 structural isomers of bisPCBM [60]fullerene.[41]

Here, we developed a robust methodology to create a fully water-soluble [60]fullerene hexakisadduct containing two different malonate addends: one containing the triple bonds and one with diserinol malonate units as a solubilizing scaffold (see the synthetic protocol depicted in Scheme 2). The dipropargyl malonate was synthesized using a simple esterification procedure, and its spectroscopic characteristics are presented in the Supporting Information (Figures S2−S5). The fullerene monoadduct (2) was obtained by mixing the buckyball (C_{60}) with dipropargyl malonate in the presence of CBr_4 and DBU, using time-controlled (3 h) Bingel−Hirsch cyclopropanation to avoid the formation of bis- and trisadducts. The ^1H NMR spectra showed characteristic signals of methine protons close to 2.49 ppm, whereas symmetry was confirmed by ^{13}C NMR, with 15 signals of fullerene sp^2 carbons and one sp^3 carbon appearing close to 70 ppm (Supporting Information, Figure S8). The structure of the created fullerene derivative (2) was additionally confirmed by MALDI-MS, which confirmed that the mass of the fullerene monoadduct was 897 Da (Figure S9), where the observed molecular ion peak had an m/z value matching that of the calculated monoisotopic mass. Further functionalization of the triple-bonded monoadduct to the water-soluble T_h symmetrical hexakis-adduct was carried out in a second cyclopropanation reaction with peracetylated diserinol malonate as a water-solubilizing scaffold. By monitoring the progress of the reaction (72 h) using TLC and the slow addition of DBU over 6 h, we were able to obtain the peracetylated [60]fullerene hexakisadduct (3). This was purified using column chromatography and immediately hydrolyzed to obtain the highly water-soluble fullerene nanomaterial (4), which was further characterized using NMR, IR, and XPS spectroscopies, and its mass was confirmed by ESI-MS. The ^{13}C NMR spectrum of T_h-symmetrical [60]fullerene derivative (4) is shown in Figure S1, and signal contributions from two C_{60}-sp^2 carbons (144 and 141 ppm) and one C_{60}-sp^3 carbon (69 ppm) were clearly observed. Two different signals from the carbonyl groups that are present in the fullerene nanomaterial (4) were also noticeable between 165 and 170 ppm as well as two characteristic signals of triple-bonded carbons at 78 and 77 ppm. As depicted in Figure S10, a molecular ion peak at 2141 Da was observed for a water-soluble hexakis-fullerene derivative (4), which corresponds to a $[M + 2H]^+$ cation that could be formed in eluent containing 0.1% TFA (calculated mass for fullerene [4]: 2139 Da) in fullerene decorated with hydroxyl groups; thus, the spectroscopic data, in combination with mass spectrometry, clearly confirmed the creation of the symmetrical [60]fullerene derivative (4).

FT-IR spectroscopy is a convenient method to confirm the presence of functional groups that are attached to engineered carbon nanomaterials. When studying the formation of fullerene triazoles, FT-IR could also be helpful to confirm that no unreacted terminal alkyne residues (signals around 2100 cm^{-1}) remain in the final products. In the case of fullerene nanomaterial (4), two different types of carbonyl groups are present in the molecule due to two different types of malonate addends connected to the buckyball scaffold: dipropargyl malonate (ester) and diserinol malonate (secondary amide). Here, the characteristic absorbance of two different carbonyl groups present in fullerene hexakisadduct (4) was observed at 1649 and 1719 cm^{-1} (Figure 2), which

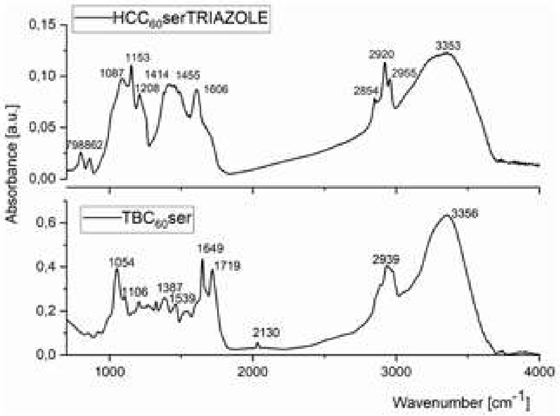

Figure 2. FT-IR spectrum of TBC$_{60}$ser and its fluorescent triazole derivative HCC$_{60}$serTRIAZOLE.

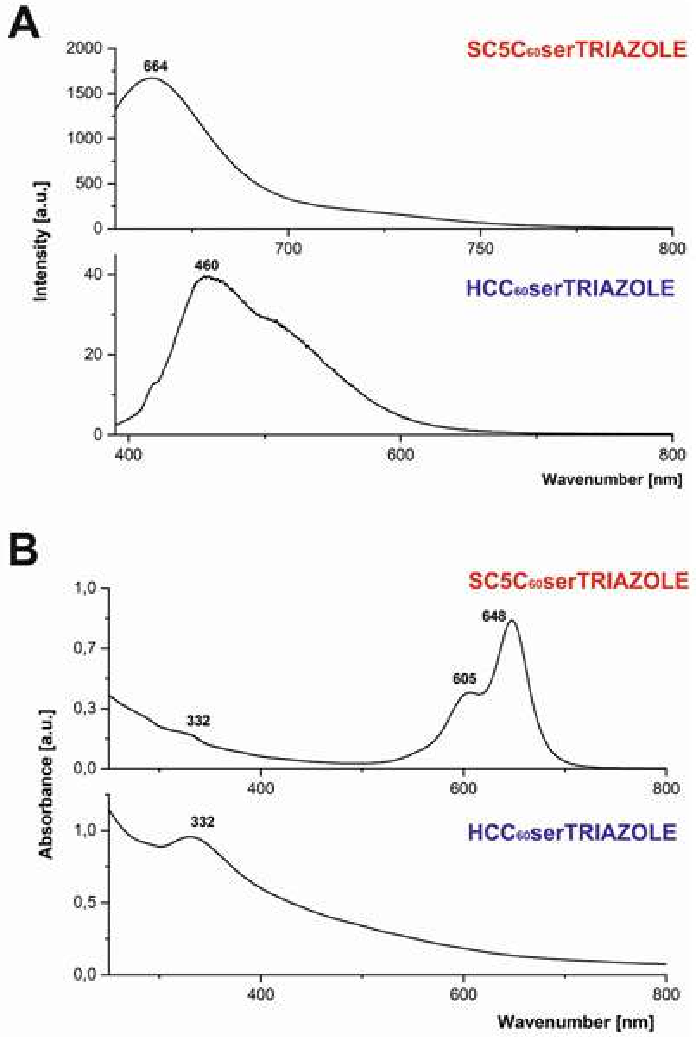

Figure 3. Fluorescence (A) and UV−vis (B) spectra of fullerene-based fluorescent triazoles HCC$_{60}$serTRIAZOLE and SC5C$_{60}$serTRIAZOLE (DI water, $c = 0.01$ mg/mL).

correspond to stretching vibrations of carbonyl moieties ν(C═O). The strong intensity band at 1649 cm^{-1} is linked to stretching vibrations of the carbonyl group present in the secondary amide, whereas a band near 1539 cm^{-1} is characteristic of the in-plane N−H bends of the secondary amide group.[42] On the other hand, an intense band near 1719 cm^{-1} is caused by unsaturated ester fragments in the structure of TBC$_{60}$ser, namely, dipropargyl malonate units (see Figure S5). Diagnostic signals from the terminal bond present in TBC$_{60}$ser are easily found as weak bands close to 2130 cm^{-1} (C≡C); however, C−H stretch signals (3330−3270 cm^{-1}) are not easily observed in functionalized fullerene derivatives with many OH groups and in the presence of hydrogen bonds. Intense and vast bands near 3300 cm^{-1} confirm the presence of OH stretching vibrations with additional bending modes (δC−OH and δOH near 1380 cm^{-1}).

Before performing the cellular 1,3-dipolar cycloadditions, we confirmed the formation of two different fullerene triazoles (HCC$_{60}$serTRIAZOLE and SC5C$_{60}$serTRIAZOLE, Scheme 1) using spectroscopic techniques (i.e., FT-IR and UV−vis) as well as ESI-MS. The FT-IR spectrum of HCC$_{60}$serTRIAZOLE is presented in Figure 2 and compared to the parent structure-TBC$_{60}$ser. The analysis of this spectrum provides evidence for the changes in the structure of starting fullerene nanomaterial, TBC$_{60}$ser, with an apparent absence of characteristic signals from the triple-bond function (near 2130 cm^{-1}), indicating a successful 1,3-dipolar cycloaddition and the formation of triazole. The broad- and medium-range signal at 1606 cm^{-1} could also be identified as a N═N stretching mode from the triazole ring in combination with stretching vibrations of secondary amide ν(C═O); however, additional weak IR stretches from the C═CH groups of the triazole ring are not visible due to strong and broad OH signals in the 3000−3500 cm^{-1} range. Additional confirmation of the formation of coumarin-based triazole came from MS analysis. As depicted in Figure S11, one can observe a characteristic molecular ion peak

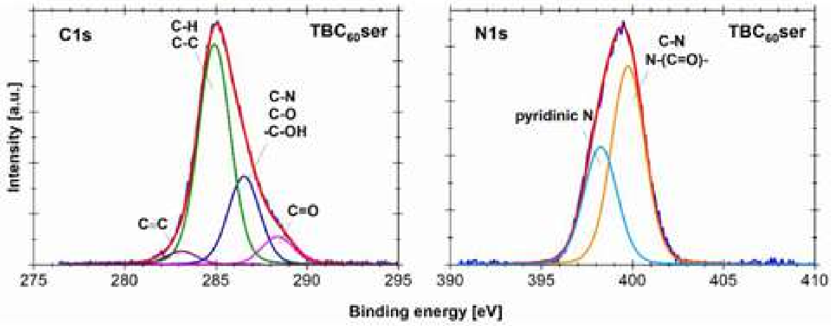

Figure 4. XPS profiles (C 1s and N 1s) of fullerene nanomaterial TBC$_{60}$ser.

at 2542 Da, which could be associated with our [60]fullerene derivative HCC$_{60}$serTRIAZOLE (calculated theoretical mass = 2543 Da). Additional ESI-MS experiments performed using a higher voltage (300 mV) revealed a fragmentation ion at 2325 Da $[M + Na]^{+}$, which could be associated with a fragment with only one triazole attached to the fullerene scaffold (calculated mass for $M + H]^{+}$ ion = 2302 Da, Figure S12). The more challenging structure of fullerene nanomaterial SC5C$_{60}$serTRIAZOLE was also successfully confirmed using spectroscopic methods (i.e., UV−vis and FT-IR), supplemented by EIS. As in the case of terminal alkynes, the infrared spectrum of organic azides has a diagnostic range close to 2100 cm^{-1}, which is presented in the case of the second substrate for click reaction: sulfo-cyanine5 azide dye (Figure S6, band near 2097 cm^{-1}). In the FT-IR spectrum of SC5C$_{60}$serTRIAZOLE (Figure S7), the strongest and broad stretches located at 1615 cm^{-1} corresponded to the plethora of secondary amide groups presented within the engineered structures of the fullerene nanomaterial, with an absence of azide groups. The presence of the sulfo group in the structure of fullerene triazole could be also correlated with signals at 1040 and 1100 cm^{-1} (S═O), whereas the hydroxyl groups from several diserinol fragments are shown as an extensive band near 3300 cm^{-1}, making it impossible to observe triazole stretches. The molecular peak of our fullerene nanomaterial, SC5C$_{60}$serTRIAZOLE, was not detected at 3663 Da, $[M + H]^{+}$ due to the limits of our ESI detector (3000 Da); however, additional fragmentation analyses confirmed the successful 1,3-dipolar cycloaddition and formation of triazole. As depicted in Figure S13 for a higher applied voltage (300 V), one could observe a fragmentation ion at 2826 Da, corresponding to the formation of a specific one-armed sulfo-cyanine5 cation with cleaved fragment sulfo-cyanine5 connected via an ester bond. Interestingly, the mass observed at 2137 Da was derived from the parent structure by cleaving two sulfo-cyanine5 units and the formation of a malonic acid ethyl ester derivative (Figure S12).

According to our theoretical assumptions, after the *in situ* click reactions, the formed fullerene triazoles should be fluorescent and easily visualized in the cellular environment. The UV−vis and fluorescent spectra of organic azides SC5 and HCA are presented in Supporting Information (Figures S16−S19). As shown in Figure 3A, the electronic spectra of fullerene triazoles are presented with a characteristic maximum from a fullerene fragment at 332 nm and strong sulfo-cyanine fragments observed at 605 and 648 nm. The emission spectra of the desired fullerene-based triazoles in water are depicted in Figure 3B, confirming the formation of blue-emitting HCC$_{60}$serTRIAZOLE (460 nm) and red-emitting SC5C$_{60}$serTRIAZOLE (664 nm). In this context, a crucial question should be asked—whether the presence of albumin proteins and protein corona formation on the surface of fullerene nanomaterials in the cellular milieu would quench their fluorescence. Further cellular *in situ* click reactions of water-soluble TBC$_{60}$ser were carried out to address this relevant question.

The photoelectron spectroscopy technique (XPS) was used to examine the electronic structure and composition of TBC$_{60}$ser. Atomic concentration calculations were made based on the ratio of each of the compounds to the sum of all the compositional elements. The photoemission lines of C 1s, O 1s, and N 1s were deconvoluted after background subtraction to determine possible chemical bonds in the examined sample (Figures 4 and S15). Table S1 shows the chemical composition, atomic concentration, and percentage contributions of chemical state for a particular element. The C 1s peak can be deconvoluted into four lines, corresponding to carbon atoms existing in different functional groups. The most intensive line at 248.9 eV was characteristic for graphitic carbon (i.e., C−C or C−H). The second line at 286.5 eV was related to oxygen- and nitrogen-containing groups (i.e., C−O, C−N, or −C−OH), while carbonyl groups C═O were represented by the third line at 288.3 eV.[43] The O 1s spectrum revealed three compositional lines that were assigned to carbonyl groups (C═O) at 531.9 eV, carboxyl groups (O−C═O) at 533.2 eV, and quinones at 530.5 eV.[44] The N 1s spectrum consisted of two components: The peak located at 399.8 eV was ascribed to C−N and N−(C═O)− bonds, while the peak located at 398.3 eV was ascribed to basic nitrogen (pyridinic type).[45,46]

Further studies were conducted to determine the occurrence of carbon−carbon triple bonds within the TBC$_{60}$ser fullerene nanomaterial. The reported literature data indicated the presence of a C 1s line at a binding energy of 283 ± 0.2 eV, where carbyne bonds (triple bond between carbon and the transition metal) were detected.[47] Additionally, the C≡C alkynic bond for methylacetylide (CH_3−C≡C−Ag) was revealed at binding energies of 283.3 and 283.6 eV in a study of the electronic structure of unsaturated C_3H_3 groups adsorbed on a silver surface.[48] For acetylide species (H−C≡C−), the binding energy assigned to the C≡C bond was measured at 283.1 eV.[49] Because the carbon−carbon triple bond occurs in the structure of TBC$_{60}$ser fullerene in small amounts, the intensity of the photoemission line assigned to

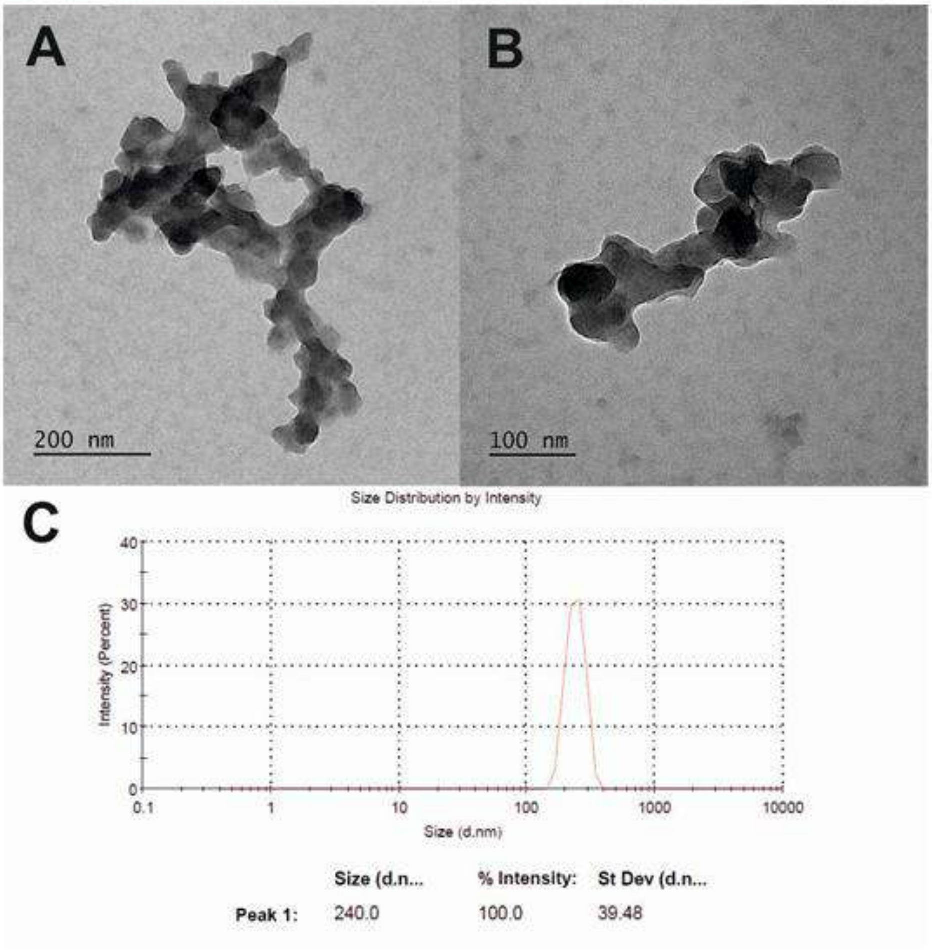

	Size (d.n...	% Intensity:	St Dev (d.n...
Peak 1:	240.0	100.0	39.48

Figure 5. (A, B) Images of fullerene nanomaterial TBC$_{60}$ser visualized using TEM. (C) DLS measurement of TBC$_{60}$ser.

this state should be relatively low. Moreover, based on the above-mentioned literature data, this line should be located at a relatively low binding energy, and its detection may be difficult due to its proximity to the most intense C 1s line of the compound (C−C/C−H). We observed a chemical state with a binding energy at 283.1 eV, which should be related to the presence of a carbon−carbon triple bond. The atomic concentration calculations and deconvoluted C 1s line indicated that 2.8% of carbon atoms formed triple bonds. These results correlated well with the number of bonds present in the examined structure, where the estimated concentration of carbon in a triple bond should be approximately 3.7 at%. The slightly lower value of detected triple-bonded carbons might be the result of the presence of surface contamination.

Further characterization of TBC$_{60}$ser was performed using TEM microscopy and dynamic light scattering (DLS) measurements, as depicted in Figure 5. As previously reported by Wilson et al., the malonodiserinolamide [60]fullerene derivative (C$_{60}$ser) formed aggregates in water, which were in dynamic equilibrium with a small percentage of single C$_{60}$ser molecules.[34] During the analysis of TEM images of TBC$_{60}$ser, it was revealed that it formed fluffy-like aggregates ranging from 100−500 nm, but smaller aggregates were also observed (Figures 5A,B). A similar observation was reported by Wilson when studying C$_{60}$ser but using scanning electron microscopy.[34] For the DLS of TBC$_{60}$ser, the peaks were concentration dependent; upon increasing the concentration, larger aggregates were also observed (for a concentration above 1 mg/mL, peaks above 1 μm were <1% of the detected fullerene aggregates). Furthermore, the average size of [60]fullerene derivative TBC$_{60}$ser agreed with the hydrodynamic diameter determined by DLS in DI water (240 nm, Figure 5C). To better understand the interactions of the triple-bonded buckyball in the cellular milieu, its ζ potential was measured, showing a stable negative charge (−34.8 mV, Figure S14), which confirmed that it was stable in water solutions (ζ potential higher than ±30 mV). It should also be mentioned that charged nanoparticles have higher cell internalization and faster opsonization rates than electrically neutral particles; however, negatively charged nanoparticles are slowly incorporated by cells.[50]

In the final stages of our research, we performed biological studies to verify the possibility of forming adducts of triazole derivatives of fullerene with dyes hydroxycoumarin azide (called HCC$_{60}$serTRIAZOLE) and sulfo-cyanine azide5 (called SC5C$_{60}$serTRIAZOLE) in the cellular environment

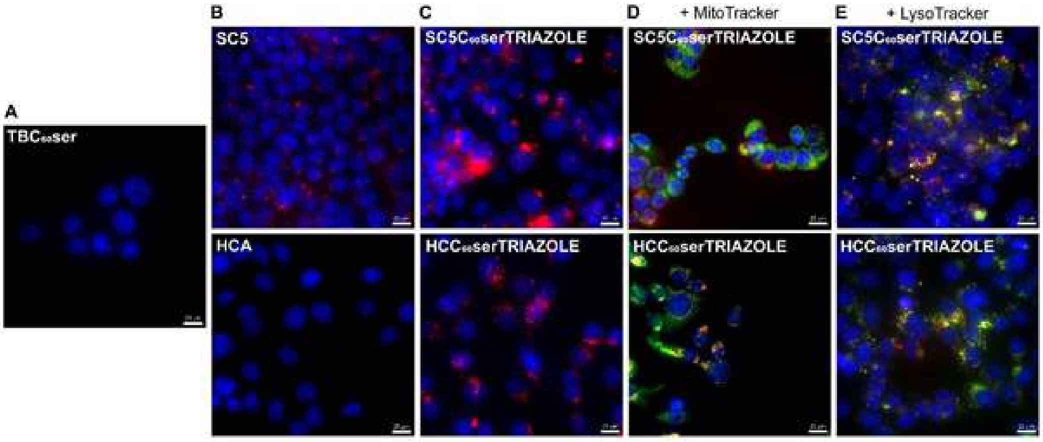

Figure 6. Cellular colocalization study of fullerene nanomaterial TBC$_{60}$ser (A), dyes: SC5 and HCA (B), and its triazole derivatives (C−E) in breast cancer (MCF-7) cell line. Cell nuclei are colored blue, mitochondria/lysosomes in green, and SC5 and fullerene adducts (SC5C$_{60}$serTRIAZOLE and HCC$_{60}$serTRIAZOLE) in red. HCC$_{60}$serTRIAZOLE is labeled red in ImageJ, whereas it is green in the live image. Scale bars = 25 μm.

using a copper-catalyzed click reaction. The basis of using all these components for cell labeling by click chemistry was their low toxicity. Because of this, we first investigated the cytotoxicity of the investigated fullerene nanomaterial (TBC$_{60}$ser), hydroxycoumarin azide (HCA), sulfo-cyanine azide5 (SC5), and copper sulfate (CuSO$_4$) on a human breast cancer cell line (MCF-7). The cells were treated with a wide range of concentrations of compounds that were tested for 72 h. After this time, the cytotoxicity was determined using the colorimetric method (i.e., an MTS assay based on tetrazolium salt). As presented in Table S2 in the Supporting Information, TBC$_{60}$ser at a concentration of 468 μM (1 mg/mL) did not affect cell viability or cell number during the long-term assay. We report similar results for both tested dyes, where the concentration (25 μM) used for the click reaction did not induce a cytotoxic effect. TBC$_{60}$ser was also nontoxic on normal cells.

To evaluate the behavior of TBC$_{60}$ser, HCA, and SC5 ligands in the cellular environment, we performed a series of live-cell imaging experiments. The results are shown in Figure 6A,B. As expected, fullerene and hydroxycoumarin azide did not show any fluorescence after excitation at 386 and 438 nm, respectively. Indeed, according to our assumption, the hydroxycoumarin azide should be activated only after attachment to TBC$_{60}$ser. On the other hand, for sulfo-cyanine azide5, after excitation at 650 nm, we recorded a red fluorescence signal in the area adjacent to the cell nucleus. Next, we optimized our two approaches for a cellular copper(I)-catalyzed click reaction by testing different variants of doses and incubation times of the components used to label the cells (approaches are presented in Scheme 1). Finally, we performed experiments in which we incubated the MCF-7 cells with 468-μM TBC$_{60}$ser for 24 h, followed by another 2 h incubation with 25 μM HCA or SC5 dye. The cell images were acquired immediately after labeling, and the fluorescence signals were registered after excitation at 386 nm/438 or 650 nm (Cy5 filter), depending on the visualization approach used. As shown in Figure 6C, the cells were successfully labeled through the copper-catalyzed reaction between the non-fluorescent fullerene (TBC$_{60}$ser) and SC5 or HCA azides, which resulted in highly fluorescent triazole derivatives: SC5C$_{60}$serTRIAZOLE and HCC$_{60}$serTRIAZOLE. The formed HCC$_{60}$serTRIAZOLE adduct provided a green fluorescent signal in the real live image. However, it is marked with red in Figure 6 for better clarity. The localization of fullerene triazoles in cells was determined by costaining with cell-trackers binding to mitochondria and lysosomes (Figure 6D,E). As a result of this staining, it was observed that both compounds SC5C$_{60}$serTRIAZOLE and HCC$_{60}$serTRIAZOLE had a higher tendency to accumulate in lysosomes (Figure 6E). The images generated from the combined channels of the tested compounds and the LysoTracker clearly show multiple overlapping areas of localization (indicated in yellow). These results appear to be consistent with a previous report on the cellular uptake of fullerene nanomaterials into cells via the clathrin-dependent endocytic pathway and their distribution in lysosomes.[51]

Similarly, studies using high-contrast optoacoustic and THG imaging techniques confirmed the localization of the C$_{70}$@lysozyme complex inside lysosomes of HeLa cells.[22] In addition, the subcellular localization and tendency of C$_{60}$ fullerenes to accumulate in lysosomes may be explained by their surface charge. Recently, Ma et al.[52] revealed that anionic C$_{60}$-(EDA-EA) with a ζ potential of −15 mV was preferentially transported into lysosomes. In contrast, cationic C$_{60}$-EDA (+13 mV), under the influence of a negative membrane potential in the cell, was able to enter cells more rapidly and enrich mitochondria.[52] On the other hand, some reports indicated that C$_{60}$ fullerenes with high electronegativity may have a higher affinity for mitochondria due to a protonated pool in the intermembrane space.[53] Interestingly, our tested compounds may also bind to mitochondria to a much lesser extent (Figure 6D).

We performed a quantitative evaluation to validate our observations by calculating the Pearson correlation coefficient (PCC) and Mander's overlap coefficient (MOC) for all obtained merged images using ImageJ software.[54] For SC5C$_{60}$serTRIAZOLE, lysosomal colocalization was characterized by very high PCCs and MOCs (above 0.83, Table S3). On the other hand, both coefficients indicated a low affinity of

SC5C$_{60}$serTRIAZOLE toward mitochondria (PCC = 0.55 and MOC = 0.31). For the second triazole, the calculated correlation coefficients were above 0.74 for lysosomes and in the range of 0.5−0.67 for mitochondria. Additionally, control experiments that stained with SC5 dye alone showed that the dye had no affinity toward lysosomes (Figure S20). In this case, PCC and MOC were 0.413 and 0.293, respectively.

CONCLUSIONS

In summary, we synthesized triple-bonded symmetrical (T_h) fullerene hexakisadduct TBC$_{60}$ser, which was characterized spectrally (NMR, FT-IR, XPS measurements), followed by mass spectrometry and TEM/DLS studies. The ^{13}C NMR spectra confirmed its high symmetry (two fullerene sp^2 and one sp^3 carbon), whereas triple bonds were confirmed by FT-IR and XPS. The obtained [60]fullerene nanomaterial was further used as a probe for cellular visualization of non-fluorescent buckyballs in a breast cancer model. Interestingly, the described protocol allowed the detection of [60]fullerene derivatives in the presence of FBS proteins. This observation is of practical importance due to the formation of protein coronas on the buckyball surface, which did not disturb the method's efficacy. Interestingly, colocalization studies revealed that TBC$_{60}$ser localized in lysosomes of the MCF-7 cells with a low affinity to mitochondria. Further studies should be performed for finding appropriate azidofullerenes that are water-soluble and penetrate cell membranes, which could be used as a partner for strain-promoted click reactions in animals.

ASSOCIATED CONTENT

Supporting Information

The Supporting Information is available free of charge at https://pubs.acs.org/doi/10.1021/acsbiomaterials.2c00542.

> Synthetic procedures; NMR and FT-IR spectroscopies; mass spectrometry (MALDI, ESI); UV−vis spectroscopy; DLS and ζ measurements; XPS spectroscopy; biological properities of TBC$_{60}$ser and fullerene triazoles (PDF)

AUTHOR INFORMATION

Corresponding Author

Maciej Serda − *Institute of Chemistry, University of Silesia in Katowice, Katowice 40-006, Poland;* orcid.org/0000-0003-4926-5782; Email: maciej.serda@us.edu.pl

Authors

Katarzyna Malarz − *Silesian Center for Education and Interdisciplinary Research, 41-500 Chorzow, Poland; Chełkowski Institute of Physics, University of Silesia in Katowice, 41-500 Chorzow, Poland;* orcid.org/0000-0003-4283-3126

Julia Korzuch − *Institute of Chemistry, University of Silesia in Katowice, Katowice 40-006, Poland*

Magdalena Szubka − *Silesian Center for Education and Interdisciplinary Research, 41-500 Chorzow, Poland; Chełkowski Institute of Physics, University of Silesia in Katowice, 41-500 Chorzow, Poland*

Maciej Zubko − *Institute of Materials Engineering, University of Silesia in Katowice, 41-500 Chorzow, Poland; Department of Physics, Faculty of Science, University of Hradec Králové, 500 03 Hradec Králové, Czech Republic*

Robert Musiol − *Institute of Chemistry, University of Silesia in Katowice, Katowice 40-006, Poland*

Complete contact information is available at: https://pubs.acs.org/10.1021/acsbiomaterials.2c00542

Notes

The authors declare no competing financial interest.

ACKNOWLEDGMENTS

This work was supported by National Science Centre (Poland) grant SONATA (UMO-2016/23/D/NZ7/00912) awarded to Dr. Maciej Serda.

REFERENCES

(1) de Lázaro, I.; Mooney, D. J. Obstacles and opportunities in a forward vision for cancer nanomedicine. *Nat. Mater.* **2021**, *20*, 1469−1479.

(2) Bobo, D.; Robinson, K. J.; Islam, J.; Thurecht, K. J.; Corrie, S. R. Nanoparticle-Based Medicines: A Review of FDA-Approved Materials and Clinical Trials to Date. *Pharm. Res.* **2016**, 33 (10), 2373−2387.

(3) Wu, D.; Si, M.; Xue, H.-Y.; Wong, H. L. Nanomedicine applications in the treatment of breast cancer: current state of the art. *International journal of nanomedicine* **2017**, *12*, 5879.

(4) Arpino, G.; Milano, M.; De Placido, S. Features of aggressive breast cancer. *Breast* **2015**, *24* (5), 594−600.

(5) Zakharian, T. Y.; Seryshev, A.; Sitharaman, B.; Gilbert, B. E.; Knight, V.; Wilson, L. J. A Fullerene-Paclitaxel Chemotherapeutic: Synthesis, Characterization, and Study of Biological Activity in Tissue Culture. *J. Am. Chem. Soc.* **2005**, *127* (36), 12508−12509.

(6) Chen, D.; Dougherty, C. A.; Zhu, K.; Hong, H. Theranostic applications of carbon nanomaterials in cancer: Focus on imaging and cargo delivery. *J. Controlled Release* **2015**, *210*, 230−245.

(7) Nalepa, P.; Gawecki, R.; Szewczyk, G.; Balin, K.; Dulski, M.; Sajewicz, M.; Mrozek-Wilczkiewicz, A.; Musioł, R.; Polanski, J.; Serda, M. A [60] fullerene nanoconjugate with gemcitabine: synthesis, biophysical properties and biological evaluation for treating pancreatic cancer. *Cancer Nanotechnology* **2020**, *11* (1), 2.

(8) Zhang, H.; Ji, Y.; Chen, Q.; Jiao, X.; Hou, L.; Zhu, X.; Zhang, Z. Enhancement of cytotoxicity of artemisinin toward cancer cells by transferrin-mediated carbon nanotubes nanoparticles. *J. Drug Targeting* **2015**, *23* (6), 552−567.

(9) Raza, K.; Thotakura, N.; Kumar, P.; Joshi, M.; Bhushan, S.; Bhatia, A.; Kumar, V.; Malik, R.; Sharma, G.; Guru, S. K.; et al. C60-fullerenes for delivery of docetaxel to breast cancer cells: a promising approach for enhanced efficacy and better pharmacokinetic profile. *International journal of pharmaceutics* **2015**, *495* (1), 551−559.

(10) Mehra, N. K.; Jain, A. K.; Nahar, M. Carbon nanomaterials in oncology: an expanding horizon. *Drug discovery today* **2018**, *23* (5), 1016−1025.

(11) Lapin, N. A.; Krzykawska-Serda, M.; Ware, M. J.; Curley, S. A.; Corr, S. J. Intravital microscopy for evaluating tumor perfusion of nanoparticles exposed to non-invasive radiofrequency electric fields. *Cancer nanotechnology* **2016**, *7* (1), 5.

(12) Xie, X.; Liao, J.; Shao, X.; Li, Q.; Lin, Y. The effect of shape on cellular uptake of gold nanoparticles in the forms of stars, rods, and triangles. *Sci. Rep.* **2017**, *7* (1), 3827.

(13) Moon, H. K.; Lee, S. H.; Choi, H. C. In vivo near-infrared mediated tumor destruction by photothermal effect of carbon nanotubes. *ACS Nano* **2009**, *3* (11), 3707−3713.

(14) Li, Y.; Bai, G.; Zeng, S.; Hao, J. Theranostic carbon dots with innovative NIR-II emission for in vivo renal-excreted optical imaging and photothermal therapy. *ACS Appl. Mater. Interfaces* **2019**, *11* (5), 4737−4744.

(15) Lapin, N. A.; Krzykawska-Serda, M.; Dilliard, S.; Mackeyev, Y.; Serda, M.; Wilson, L. J.; Curley, S. A.; Corr, S. J. The effects of non-invasive radiofrequency electric field hyperthermia on biotransport and biodistribution of fluorescent [60]fullerene derivative in a murine

orthotopic model of breast adenocarcinoma. *J. Controlled Release* **2017**, *260*, 92−99.

(16) Rašović, I. Water-soluble fullerenes for medical applications. *Materials science and technology* **2017**, *33* (7), 777−794.

(17) Kwag, D. S.; Park, K.; Oh, K. T.; Lee, E. S. Hyaluronated fullerenes with photoluminescent and antitumoral activity. *Chem. Commun.* **2013**, *49* (3), 282−284.

(18) Sayes, C. M.; Fortner, J. D.; Guo, W.; Lyon, D.; Boyd, A. M.; Ausman, K. D.; Tao, Y. J.; Sitharaman, B.; Wilson, L. J.; Hughes, J. B.; et al. The Differential Cytotoxicity of Water-Soluble Fullerenes. *Nano Lett.* **2004**, *4* (10), 1881−1887.

(19) Raoof, M.; Mackeyev, Y.; Cheney, M. A.; Wilson, L. J.; Curley, S. A. Internalization of C60 fullerenes into cancer cells with accumulation in the nucleus via the nuclear pore complex. *Biomaterials* **2012**, *33* (10), 2952−2960.

(20) Lin, S.-K.; Shiu, L.-L.; Chien, K.-M.; Luh, T.-Y.; Lin, T.-I. Fluorescence of fullerene derivatives at room temperature. *J. Phys. Chem.* **1995**, *99* (1), 105−111.

(21) Serda, M.; Ware, M. J.; Newton, J. M.; Sachdeva, S.; Krzykawska-Serda, M.; Nguyen, L.; Law, J.; Anderson, A. O.; Curley, S. A.; Wilson, L. J.; et al. Development of photoactive Sweet-C60 for pancreatic cancer stellate cell therapy. *Nanomedicine (Lond)* **2018**, *13* (23), 2981−2993.

(22) Di Giosia, M.; Soldà, A.; Seeger, M.; Cantelli, A.; Arnesano, F.; Nardella, M. I.; Mangini, V.; Valle, F.; Montalti, M.; Zerbetto, F.; et al. A Bio-Conjugated Fullerene as a Subcellular-Targeted and Multifaceted Phototheranostic Agent. *Adv. Funct. Mater.* **2021**, *31* (20), 2101527.

(23) Kolb, H. C.; Sharpless, K. B. The growing impact of click chemistry on drug discovery. *Drug discovery today* **2003**, *8* (24), 1128−1137.

(24) Kumar, G. S.; Lin, Q. Light-triggered click chemistry. *Chem. Rev.* **2021**, *121*, 6991−7031.

(25) Li, H.; Cheng, F.; Duft, A. M.; Adronov, A. Functionalization of single-walled carbon nanotubes with well-defined polystyrene by "click" coupling. *J. Am. Chem. Soc.* **2005**, *127* (41), 14518−14524.

(26) Kou, L.; He, H.; Gao, C. Click chemistry approach to functionalize two-dimensional macromolecules of graphene oxide nanosheets. *Nano-Micro Letters* **2010**, *2* (3), 177−183.

(27) Iehl, J.; de Freitas, R. P.; Nierengarten, J.-F. Click chemistry with fullerene derivatives. *Tetrahedron Lett.* **2008**, *49* (25), 4063−4066.

(28) Muñoz, A.; Sigwalt, D.; Illescas, B. M.; Luczkowiak, J.; Rodríguez-Pérez, L.; Nierengarten, I.; Holler, M.; Remy, J.-S.; Buffet, K.; Vincent, S. P.; et al. Synthesis of giant globular multivalent glycofullerenes as potent inhibitors in a model of Ebola virus infection. *Nat. Chem.* **2016**, *8*, 50.

(29) Iehl, J.; Nguyen, T. L. A.; Frein, S.; Hahn, U.; Barberá, J.; Nierengarten, J.-F.; Deschenaux, R. Designing liquid-crystalline dendronised hexa-adducts of [60] fullerene via click chemistry. *Liq. Cryst.* **2017**, *44* (12−13), 1852−1860.

(30) Speers, A. E.; Cravatt, B. F. Profiling enzyme activities in vivo using click chemistry methods. *Chemistry & biology* **2004**, *11* (4), 535−546.

(31) Kennedy, D. C.; McKay, C. S.; Legault, M. C.; Danielson, D. C.; Blake, J. A.; Pegoraro, A. F.; Stolow, A.; Mester, Z.; Pezacki, J. P. Cellular consequences of copper complexes used to catalyze bioorthogonal click reactions. *J. Am. Chem. Soc.* **2011**, *133* (44), 17993−18001.

(32) Sletten, E. M.; Bertozzi, C. R. From mechanism to mouse: a tale of two bioorthogonal reactions. *Accounts of chemical research* **2011**, *44* (9), 666−676.

(33) Ramos-Soriano, J.; Reina, J. J.; Illescas, B. M.; Rojo, J.; Martín, N. Maleimide and Cyclooctyne-Based Hexakis-Adducts of Fullerene: Multivalent Scaffolds for Copper-Free Click Chemistry on Fullerenes. *Journal of organic chemistry* **2018**, *83* (4), 1727−1736.

(34) Lapin, N. A.; Vergara, L. A.; Mackeyev, Y.; Newton, J. M.; Dilliard, S. A.; Wilson, L. J.; Curley, S. A.; Serda, R. E. Biotransport kinetics and intratumoral biodistribution of malonodiserinolamide-derivatized [60]fullerene in a murine model of breast adenocarcinoma. *Int. J. Nanomed.* **2017**, *12*, 8289−8307.

(35) Hems, E. S.; Wagstaff, B. A.; Saalbach, G.; Field, R. A. CuAAC click chemistry for the enhanced detection of novel alkyne-based natural product toxins. *Chem. Commun.* **2018**, *54* (86), 12234−12237.

(36) Teng, F.-A.; Guo, Y.; He, J.; Zhang, Y.; Han, Z.; Li, H. Convenient syntheses of fullerynes for 'clicking'into fullerene polymers. *Designed monomers and polymers* **2017**, *20* (1), 283−292.

(37) Serda, M.; Malarz, K.; Mrozek-Wilczkiewicz, A.; Wojtyniak, M.; Musiol, R.; Curley, S. A. Glycofullerenes as non-receptor tyrosine kinase inhibitors-towards better nanotherapeutics for pancreatic cancer treatment. *Sci. Rep.* **2020**, *10* (1), 260.

(38) Czaplińska, B.; Malarz, K.; Mrozek-Wilczkiewicz, A.; Musiol, R. Acid selective pro-dye for cellular compartments. *Sci. Rep.* **2019**, *9* (1), 15304.

(39) Nakamura, E.; Isobe, H. Functionalized Fullerenes in Water. The First 10 Years of Their Chemistry, Biology, and Nanoscience. *Acc. Chem. Res.* **2003**, *36* (11), 807−815.

(40) Hirsch, A.; Lamparth, I.; Grösser, T.; Karfunkel, H. R. Regiochemistry of multiple additions to the fullerene core: synthesis of a Th-symmetric hexakis adduct of C60 with Bis (ethoxycarbonyl) methylene. *J. Am. Chem. Soc.* **1994**, *116* (20), 9385−9386.

(41) Shi, W.; Salerno, F.; Ward, M. D.; Santana-Bonilla, A.; Wade, J.; Hou, X.; Liu, T.; Dennis, T. J. S.; Campbell, A. J.; Jelfs, K. E.; et al. Fullerene Desymmetrization as a Means to Achieve Single-Enantiomer Electron Acceptors with Maximized Chiroptical Responsiveness. *Adv. Mater.* **2021**, *33* (1), 2004115.

(42) Miyazawa, T.; Shimanouchi, T.; Mizushima, S. i. Normal vibrations of N-methylacetamide. *J. Chem. Phys.* **1958**, *29* (3), 611−616.

(43) Yu, J.; Guan, M.; Li, F.; Zhang, Z.; Wang, C.; Shu, C.; Wei, H.; Zhang, X.-E. Effects of fullerene derivatives on bioluminescence and application for protease detection. *Chem. Commun.* **2012**, *48* (89), 11011−11013.

(44) Yu, B.; Wang, X.; Qian, X.; Xing, W.; Yang, H.; Ma, L.; Lin, Y.; Jiang, S.; Song, L.; Hu, Y.; et al. Functionalized graphene oxide/phosphoramide oligomer hybrids flame retardant prepared via in situ polymerization for improving the fire safety of polypropylene. *Rsc Advances* **2014**, *4* (60), 31782−31794.

(45) Korzuch, J.; Rak, M.; Balin, K.; Zubko, M.; Glowacka, O.; Dulski, M.; Musiol, R.; Madeja, Z.; Serda, M. Towards water-soluble [60] fullerenes for the delivery of siRNA in a prostate cancer model. *Sci. Rep.* **2021**, *11* (1), 10565.

(46) Serda, M.; Gawecki, R.; Dulski, M.; Sajewicz, M.; Talik, E.; Szubka, M.; Zubko, M.; Malarz, K.; Mrozek-Wilczkiewicz, A.; Musioł, R. Synthesis and applications of [60] fullerene nanoconjugate with 5-aminolevulinic acid and its glycoconjugate as drug delivery vehicles. *RSC Adv.* **2022**, *12* (11), 6377−6388.

(47) Dement'ev, V.; Haghi, A.; Kodolov, V. Selected Communications, Short Notes, and Abstracts. In *Nanoscience and Nanoengineering*; Apple Academic Press: Palm Bay, FL, 2018; pp 301−352.

(48) Kung, H.; Wu, S.-M.; Wu, Y.-J.; Yang, Y.-W.; Chiang, C.-M. Tracking the Chemistry of Unsaturated C3H3 Groups Adsorbed on a Silver Surface: Propargyl- Allenyl- Acetylide Triple Bond Migration, Self-Hydrogenation, and Carbon- Carbon Bond Formation. *J. Am. Chem. Soc.* **2008**, *130* (31), 10263−10273.

(49) Vohs, J.; Carney, B.; Barteau, M. Selectivity of proton abstraction from propyne on the silver (110) surface. *J. Am. Chem. Soc.* **1985**, *107* (26), 7841−7848.

(50) Hühn, D.; Kantner, K.; Geidel, C.; Brandholt, S.; De Cock, I.; Soenen, S. J.; Rivera Gil, P.; Montenegro, J.-M.; Braeckmans, K.; Müllen, K.; et al. Polymer-coated nanoparticles interacting with proteins and cells: focusing on the sign of the net charge. *ACS Nano* **2013**, *7* (4), 3253−3263.

(51) Li, W.; Chen, C.; Ye, C.; Wei, T.; Zhao, Y.; Lao, F.; Chen, Z.; Meng, H.; Gao, Y.; Yuan, H.; et al. The translocation of fullerenic nanoparticles into lysosome via the pathway of clathrin-mediated endocytosis. *Nanotechnology* **2008**, *19* (14), 145102.

(52) Ma, H.; Zhang, X.; Yang, Y.; Li, S.; Huo, J.; Liu, Y.; Guan, M.; Zhen, M.; Shu, C.; Li, J.; et al. Cellular uptake, organelle enrichment, and in vitro antioxidation of fullerene derivatives, mediated by surface charge. *Langmuir* **2021**, 37 (8), 2740−2748.

(53) Santos, S. M.; Dinis, A. M.; Peixoto, F.; Ferreira, L.; Jurado, A. S.; Videira, R. A. Interaction of fullerene nanoparticles with biomembranes: from the partition in lipid membranes to effects on mitochondrial bioenergetics. *toxicological sciences* **2014**, *138* (1), 117−129.

(54) Collins, T. J. ImageJ for microscopy. *Biotechniques* **2007**, *43* (S1), S25−S30.

International Journal of Nanomedicine
Dovepress
open access to scientific and medical research

Open Access Full Text Article

ORIGINAL RESEARCH

Identification and Biological Evaluation of a Water-Soluble Fullerene Nanomaterial as BTK Kinase Inhibitor

Katarzyna Malarz[1,*], Julia Korzuch[2,*], Tainah Dorina Marforio[3], Katarzyna Balin[1], Matteo Calvaresi[3], Anna Mrozek-Wilczkiewicz[1], Robert Musiol[2], Maciej Serda[2]

[1]A. Chełkowski Institute of Physics, University of Silesia in Katowice, Chorzów, Poland; [2]Institute of Chemistry, University of Silesia in Katowice, Katowice, Poland; [3]Department of Chemistry "Giacomo Ciamician", University of Bologna, Bologna, Italy

*These authors contributed equally to this work

Correspondence: Maciej Serda; Katarzyna Malarz, Email maciej.serda@us.edu.pl; katarzyna.malarz@us.edu.pl

Introduction: Thanks to recent advances in synthetic methodology, water-soluble fullerene nanomaterials that interfere with biomolecules, especially DNA/RNA and selected proteins, have been found with tremendous potential for applications in nanomedicine. Herein, we describe the synthesis and evaluation of a water-soluble glycine-derived [60]fullerene hexakisadduct (HDGF) with T_h symmetry, which is a first-in-class BTK protein inhibitor.

Methods: We synthesized and characterized glycine derived [60]fullerene using NMR, ESI-MS, and ATR-FT-IR. DLS and zeta potential were measured and high-resolution transmission electron microscopy (HRTEM) observations were performed. The chemical composition of the water-soluble fullerene nanomaterial was examined by X-ray photoelectron spectrometry. To observe aggregate formation, the cryo-TEM analysis was carried out. The docking studies and molecular dynamic simulations were performed to determine interactions between HDGF and BTK. The in vitro cytotoxicity was evaluated on RAJI and K562 blood cancer cell lines. Subsequently, we examined the induction of cell death by autophagy and apoptosis by determining the expression levels of crucial genes and caspases. We investigated the direct association of HDGF on inhibition of the BTK signalling pathway by examining changes in the calcium levels in RAJI cells after treatment. The inhibitory potential of HDGF against non-receptor tyrosine kinases was evaluated. Finally, we assessed the effects of HDGF and ibrutinib on the expression of the BTK protein and downstream signal transduction in RAJI cells following anti-IgM stimulation.

Results: Computational studies revealed that the inhibitory activity of the obtained [60]fullerene derivative is multifaceted: it hampers the BTK active site, interacting directly with the catalytic residues, rendering it inaccessible to phosphorylation, and binds to residues that form the ATP binding pocket. The anticancer activity of produced carbon nanomaterial revealed that it inhibited the BTK protein and its downstream pathways, including PLC and Akt proteins, at the cellular level. The mechanistic studies suggested the formation of autophagosomes (increased gene expression of *LC3* and *p62*) and two caspases (caspase-3 and −9) were responsible for the activation and progression of apoptosis.

Conclusion: These data illustrate the potential of fullerene-based BTK protein inhibitors as nanotherapeutics for blood cancer and provide helpful information to support the future development of fullerene nanomaterials as a novel class of enzyme inhibitors.

Keywords: fullerenes, BTK inhibitor, anticancer agent, autophagy, apoptosis

Introduction

Since their discovery in 1985, fullerenes have emerged as an object of interest for synthetic chemists based on their unique structure and physical properties.[1] These observations supported the exploration of the biological activity of fullerenes, which was first started by the case of HIV-1 protease inhibition reported by Sijbesma et al.[2] However, the first breakthrough for nanomedical applications of the engineered buckyballs was possible thanks to the development of chemical methods enhancing their water-solubility, mainly using Bingel–Hirsch cyclopropanations and Prato

Received: 11 January 2023
Accepted: 14 March 2023
Published: 31 March 2023

Graphical Abstract

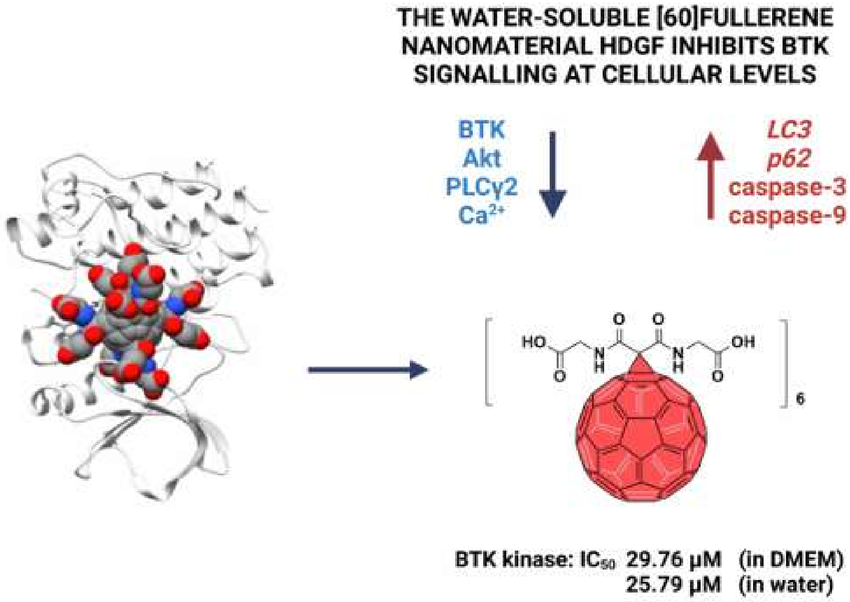

cycloadditions.[3,4] Under appropriate conditions, Bingel–Hirsch reactions lead to the formation of T_h symmetrical hexakisadducts that are present only in the form of one regioisomer, which is essential for biological applications.[5–7] Currently, there is rapid development of appropriately engineered fullerene nanomaterials, mainly for drug delivery systems, antioxidants, and MRI contrast agents.[8] The interactions between proteins and carbon nanomaterials, especially the protein corona formation, are believed to play a crucial role in the biological effects of carbon nanomaterials.[9,10] The observation of fullerene–protein complexation has been investigated for the past 20 years, from the initial experiments describing the creation of fullerene complexes with bovine serum albumin to further exploration using computational methods.[11,12] Interestingly, the strong adsorption of lysozyme protein can be used as a method to solubilize fullerenes, enabling the formation of lysosomal trafficking phototheranostic agents.[13] The BTK protein is a non-receptor tyrosine kinase that has an essential role in signal transduction of the B-cell antigen receptor, with crucial applications in treating chronic lymphocytic leukemia (CLL) and mantle cell lymphoma (MCL).[14] Many novel BTK inhibitors have been developed in the past decade, including the small molecules ibrutinib and evobrutinib, which have high selectivity over other kinases and pronounced activity at nanomolar concentrations.[15] In general, the BTK inhibitors can be divided into two subgroups, reversible and irreversible; the latter shows strong binding to the Cys481 residue of BTK protein.[16] Interestingly, BTK activation is initiated by the phosphorylation of Tyr551 in the kinase domain, which can occur in the cellular environment using spleen tyrosine kinase (SYK) or SRC-type kinases.[17] The Tyr551 position is crucial for modulation of BTK protein activity—some active inhibitors such as CGI1746 bind BTK in a modified, inactive conformation in which the regulatory Tyr551 is rotated and forms a new binding pocket (H3 pocket).[18] However, up to now, no carbon nanomaterials have been designed that can successfully inhibit BTK kinase activity at the cellular level.

We have recently begun to explore the use of fullerene nanomaterials as first-in-class carbon nanomaterial inhibitors of non-receptor tyrosine kinases, namely Fyn A kinase.[19] Previously developed glycofullerene-based inhibitors were non-toxic and had no effect on the cell cycle of pancreatic cancer cells, but induced autophagy and disrupted redox balance. The formation of a protein corona on the surface of glycofullerenes modulated their inhibition effectiveness and

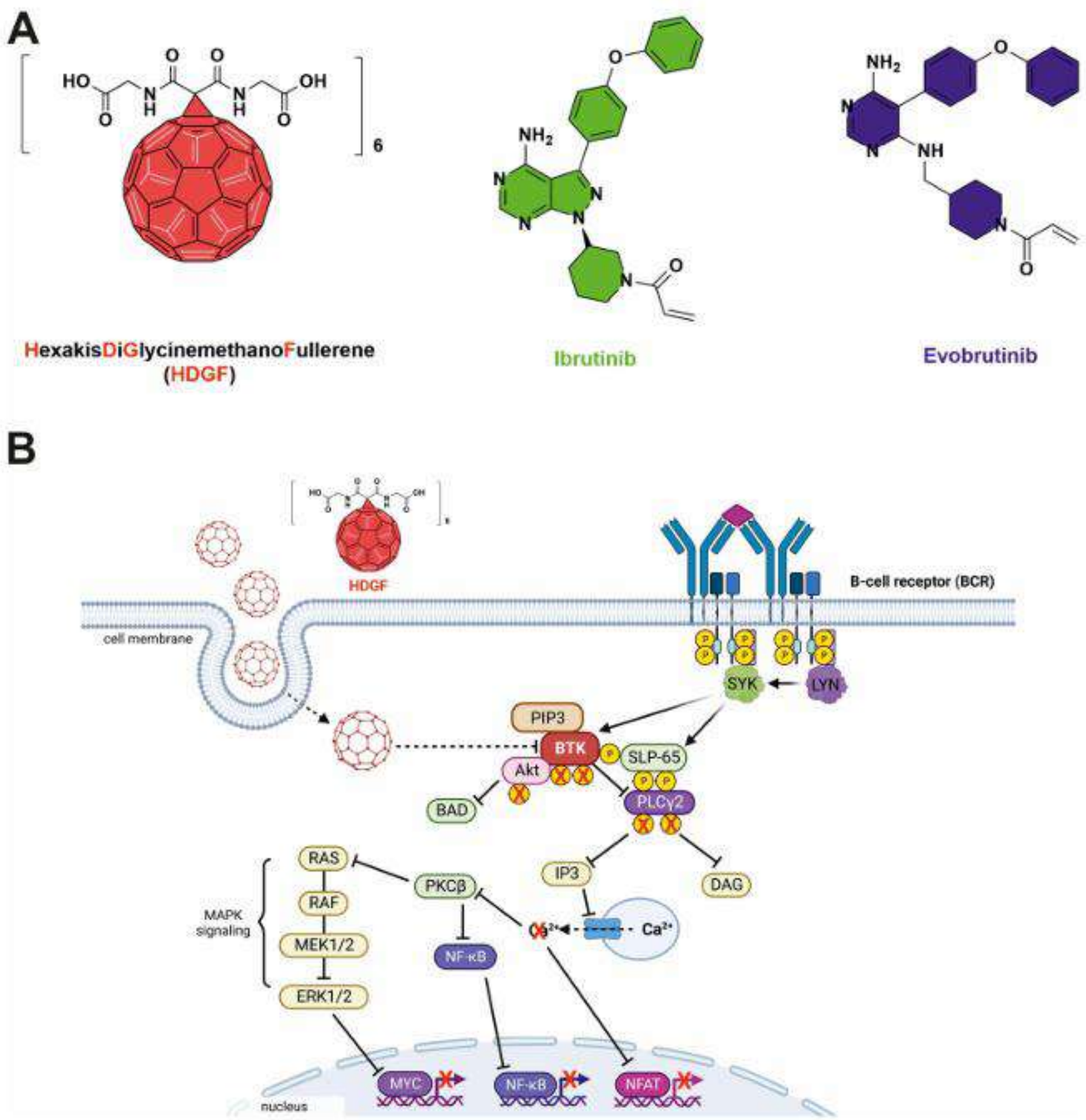

Figure 1 Structure of HDGF and FDA-approved BTK inhibitors (**A**). Proposed mechanism of action of HDGF in RAJI cells. Image created with BioRender.com (**B**).

remodeled their selectivity, impairing the ability to reduce protein levels at a cellular scale. In the present study, we demonstrate that the modification of the buckyball scaffold using diglycine malonate via Bingel–Hirsch cyclopropanation is an easy and robust approach to forming a hexakis diglycinemethanofullerene (HDGF) nanomaterial (Figure 1) with the ability to block the formation of the BTK protein, thereby inhibiting its downstream molecular pathway in RAJI cells. Our initial studies of anticancer activity were carried out on two blood cancer cells – K562 and RAJI. HDGF exhibits good anticancer properties only against RAJI cells, so further its molecular mechanism of action was characterized on this cellular model.

Materials and Methods

Materials

All chemicals used were of reagent-grade quality or better. Solvents were dried in accordance with standard literature procedures. The following reagents were used as received: C_{60} (99.5+%, SES Research, USA), glycine tert-butyl hydrochloride (Sigma Aldrich, USA), malonic acid (Sigma Aldrich, USA), DBU (1,8-diazabicyclo[5.4.0]undec-7-ene, Sigma Aldrich, USA), triethylamine (Fisher, Belgium), CBr_4 (Sigma Aldrich, USA), 1,4-dioxane (Acros Organics, Belgium), thionyl chloride (Fisher, UK), dichloromethane (Chempur, Poland), anhydrous sodium sulfate (POCH, Poland), diethyl ether (Eurochem, Poland), ethyl acetate (POCH, Poland), toluene (Chempur, Poland), methanol (Chempur), and concentrated hydrogen chloride (POCH, Poland).

Methods

Nuclear magnetic resonance (NMR) spectra were obtained using a Bruker Avance III 500 MHz NMR spectrometer with tetramethylsilane as the internal standard. Mass spectroscopy (MS) was performed using a single electrospray quad Agilent InfinityLab LC/MSD XT mass spectrometer, equipped with an Agilent HPLC 1260 Infinity II system and SBC18 column (1.8 µm, 2.1×50 mm). Spectra were collected in the range 100–3000 Da. Additional electrospray ionization (ESI) MS measurements were performed using a Varian 320-MS ESI mass spectrometer and high-resolution spectra were collected on Agilent 6224 TOF spectrometer. All ESI-MS measurements were conducted in an acetonitrile/H_2O mixture. Attenuated total reflectance Fourier transform infrared (ATR-FT-IR) measurements were collected using a JASCO FT/IR-4600 spectrophotometer equipped with a JASCO ATR PRO ONE kit. Fullerene powders were measured using an ATR ZnSe accessory in the range 700–4000 cm^{-1}. The spectra were recorded using 64 accumulations at a spectral resolution of 1 cm^{-1}. Dynamic light scattering and zeta potentials of the fullerene nanomaterial 4 were measured using a Zetasizer Nano Instrument (Malvern Panalytical Ltd., UK). High-resolution transmission electron microscopy (HRTEM) observations were performed using a JEOL JEM 3010 microscope operating at a 300 kV accelerating voltage, which was equipped with a Gatan 2k × 2k Orius^{TM} 833SC200D CCD camera. The chemical composition of the water-soluble fullerene nanomaterial 4 was examined by X-ray photoelectron spectrometry (Physical Electronics PHI 5700, Chanhassen, MN, USA) using monochromatic Al Kα radiation (1486 eV). The analysis area was 800 µm in diameter. The spectra were collected from the surface of the powdered sample placed onto carbon conductive tape. The survey spectrum was collected with a pass energy of 187.85eV, with a pass energy of 23.50 eV for the O1s, C1s, and N1s core levels. PHI MultiPak (v.9.6.0.1, ULVAC PHI, Chigasaki, Japan) software was used to calculate the atomic concentrations and curve fitting. As the sample was air-exposed, the adventitious carbon located at 284.8 eV (assigned to C–C hydrocarbon bonds) was used to calibrate the spectra. To deconvolute the O1s, C1s, and N1s peaks, Shirley-type background subtraction and the Gauss–Lorentz line shape were applied. Cryo-electron microscopy, as well as room-temperature measurements, were performed on the Titan Krios 3Gi (Thermo Scientific) and Tecnai G2 F30 electron microscope at the University of Chicago Advanced Electron Microscopy Core Facility (RRID:SCR_019198). Cryo-EM was conducted on copper grids (Lacey carbon, EMS LC200-Cu) which were plasma-cleaned (Gatan Solarus) for 30s. Then, 3.5 µL of fullerene solution in DI water (c = 1 mg/mL) was applied to the grid, blotted for 2s, and plunge-frozen using the Thermo Scientific Vitrobot (Mark IV). The grids were stored in liquid nitrogen until imaging. Then, they were clipped in autogrids (Thermo Scientific) and placed into the cassette for loading onto the Titan Krios 3Gi (Thermo Scientific). The grids were imaged using EPU (Thermo Scientific). For room-temperature EM of fullerene nanomaterials (negative staining) carbon-coated copper grids (EMS CF200-Cu) were plasma cleaned (Gatan Solarus). The 3.5 µL of fullerene sample dissolved in DI water (c = 1 mg/mL) was applied to the grid for 1 minute and then blotted away. The grid was rinsed with two drops of uranyl formate stain (0.75%) and then stained with a third drop of uranyl formate for 45s. The stain was then blotted away. The grid was imaged on a Tecnai G2 F30 electron microscope FEI). The final dialysis purification of the water-soluble fullerene nanomaterial was performed using Pall Microsep™ centrifugal membranes with molecular cut-offs at 1 and 3 kDa (Pall Corporation).

Synthetic Procedures

Synthesis of malonyl dichloride. Malonyl dichloride was prepared according to previously reported references.[20] Briefly, malonic acid (0.9 g; 8.65 mmol) was dissolved in 30 mL of thionyl chloride. The reaction was stirred for 48 hours at 50°C. Then, the solvent was removed, and the obtained liquid was used in the next step without further purification.

Synthesis of Di-*tert*-Butyl-Diglycinyl Malonate (1)

Under argon protection, glycine *tert*-butyl ester hydrochloride (3301 mg, 10 mmol), dried triethylamine (2020 mg, 50 mmol), and dried dichloromethane (200 mL) were mixed in a round-bottomed flask at −10°C. A solution of malonyl dichloride (564 mg, 20 mmol) in dried dichloromethane was added for 0.5 h. After the mixture was stirred for 1 hour at −10°C, it was left to reach room temperature and stirred for another 12 hours. After water (300 mL) was added, and the organic phase was extracted with dichloromethane (3 × 300 mL). The organic phase was dried over anhydrous Na_2SO_4. After the solvent was removed, the residue was purified on a silica gel column with a mixture of petroleum ether and ethyl acetate (10:2) as the eluent to give the pure product (1.5 g, 25%) as a brown, viscous liquid.

Synthesis of the [60]Fullerene Monoadduct (2)

The [60]fullerene (1 mmol; 720 mg) was dissolved in 700 mL of dry toluene using an ultrasonic bath (20 minutes). To the solution of C60, glycine malonate (1.25 mmol; 330 mg) and CBr_4 (2 mmol; 662 mg) were added. The DBU solution (1 mmol; 152 mg) in 6 mL of DCM was added dropwise to the reaction mixture. The reaction mixture was stirred for 3 hours at room temperature and monitored by TLC. Subsequently, the unreacted [60]fullerene was removed by pouring the reaction mixture through a silica plug. The [60]fullerene was flushed out with toluene. The residual brownish monoadduct fraction was purified on a column using a dichloromethane/methanol eluent (50:1 v/v), followed by evaporation on a rotary evaporator. A light-brown solid was obtained (192.7 mg, 18% yield) and characterized by NMR and FT-IR spectroscopy and MALDI-TOF spectrometry.

Synthesis of Water-Soluble [60]Fullerene Hexakisadduct (4)

The [60]fullerene monoadduct (2) (0.178 mmol; 187 mg) was dissolved in a mixture of 30 mL of dry methylene chloride and 100 mL of dry toluene. Glycine malonate (1.78 mmol; 587.7 mg) and excess CBr_4 (3.56 mmol; 1178 mg) were added to the fullerene solution and stirred vigorously at room temperature. Next, a solution of DBU (2.14 mmol; 324 mg) in 3 mL of dichloromethane was added dropwise in aliquots (0.5 mL per hour). The reaction mixture was stirred at room temperature for 48 hours, and the solution changed color to reddish brown. The final product (3) was purified using column chromatography with a dichloromethane/methanol gradient as the eluent (starting from dichloromethane and finishing with 50:50 v/v), which resulted in the formation of a brown solid with a 19% yield. The water-insoluble fullerene nanomaterial (3) was deprotected from *tert*-butyl ester groups using the HCl-1,4-dioxane methodology. The [60]fullerene derivative (3) was dissolved in 18 mL of 1,4-dioxane and 3 mL of concentrated HCl. The fullerene nanomaterial was stirred for 7 days at room temperature. Subsequently, the final product was purified by dialysis of an aqueous solution of (4) using a centrifugal membrane (molecular weight exclusion limit 1.0 kDa; Nanosept, Pall Corporation, USA) in three cycles, lyophilized, and stored at −20°C.

Molecular Docking and MD Simulations

System Setup

The crystal structure of the BTK (PDB ID: 5P9J) was downloaded from the Protein Data Bank (PDB). The structure of the covalent inhibitor (ibrutinib) was removed from the PDB structure, and the protonation of the native cysteine (Cys481) was restored. The Amber ff14SB force field was used to model the BTK protein.[21] The GAFF force field was used to model HDGF using the antechamber module implemented in Amber16. The partial atomic charges of HDGF were calculated using the restraint electrostatic potential method (RESP) at the HF/6-31G* level of theory.

Docking

Docking models were generated using the PatchDock algorithm: 1276 poses were obtained.[22] The docking poses were clustered to avoid the generation of redundant solutions, and five possible complexes were identified (Figure S1).

MD Simulations

The five poses were minimized by 5000 steps of steepest descent minimization, followed by 5000 steps of the conjugate gradient algorithm. The minimized structures underwent an equilibration step of 1 ns and were heated from 0 to 300 K (Langevin thermostat). Periodic boundary conditions (PBC) and particle mesh Ewald summation were used throughout (with a cut-off radius of 10 Å for the direct space sum). The MD simulations were performed using an explicit solvent (TIP3P water model). Sodium counterions were included to exactly neutralize the charge of the system. After the equilibration, a production MD simulation of 100 ns was performed for every system at 300 K. Amber 16 was used to run all the simulations. Only the simulation obtained from Pose 1 generated a stable complex in water.

Molecular Mechanics/Generalized Born Surface Area (MM/GBSA) Analysis

In total, 5000 frames were extracted from MD simulations and used for the MM-GBSA analysis. An infinite cut-off was used for all the interactions. The electrostatic contribution to the solvation free energy was calculated with the Generalized Born (GB) model, as implemented in MMPBSA.py.[23] The nonpolar contribution to the solvation-free energy was determined with solvent-accessible surface area-dependent terms. To obtain an estimate of the binding entropy, the normal modes for the complex, receptor, and ligand were calculated, and the results were averaged using the PTRAJ program (Normal Mode Analysis) via MMPBSA.py.[23] The analysis of the molecular structures/MD trajectories and creation of images was performed using Chimera.

Biological Studies

Cell Cultures

The human suspension chronic myelogenous leukemia cell line K562 and human suspension Burkitt's lymphoma cell line RAJI were purchased from Sigma Aldrich. Cell lines were cultured in RPMI-1640 medium (Merck) containing 10% heat-inactivated FBS and a mix of two antibiotics (penicillin/streptomycin, 1% v/v; Gibco). Cell lines were cultured at 37°C with a humidified atmosphere containing 5% CO_2.

Cytotoxicity Studies

The cells were seeded in 96-well plates (Nunc) at a density of 8,000 cells per well and incubated under standard conditions at 37°C for 24 h. The assay was performed following incubation for 72 h with various concentrations of HDGF and ibrutinib. Then, DMEM without phenol red with CellTiter 96®AQueous One Solution-MTS (Promega) solution was added to each well and incubated for 1 h at 37°C. The optical density of the samples was measured at 490 nm using a multi-plate reader (Varioskan LUX, Thermo Scientific). The obtained results were presented relative to the control and were estimated as the inhibitory concentration (IC_{50}) values (using GraphPad Prism 9). Each individual compound was tested in triplicate in a single experiment; each experiment was performed three or four times.

Tyrosine Kinase Assay

Assays using the Kinase Selectivity TK-2 profiling systems and ADP-Glo Kinase Assay (both from Promega) were performed to determine the inhibition of the non-receptor tyrosine kinases. The reagents were prepared in accordance with the manufacturer's instructions and the protocol for nanomaterials established by our group.[19] Briefly, 95 μL of 2.5× Kinase Reaction Buffer was added to each of the kinases (ABL1; BRK; BTK; CSK; Fyn A; Lck; Lyn B; Src) from an eight-well strip. Then, 15 μL of freshly prepared solution of ATP (100 μM) was added to the eight-well substrate/co-factor strip. The HDGF was dissolved in water or DMEM with 12% FBS to a concentration of 40 mg/mL, which was then used as the stock solution to prepare the 0.05–2 mg/mL concentrations in 1× Kinase Reaction Buffer (40 mM Tris, pH 7.5; 20 mM $MgCl_2$; 0.1 mg/mL BSA; 50 μM DTT). First, 1 μL of prepared solutions of the HDGF was transferred into 384-well white plate. Then, 2 μL of kinases from the eight-well strip were added to each well, and the plate was incubated for 10 min at room temperature. Then, 2 μL of the substrates from the eight-well substrate/co-factor strip were added to each well, and the plate was incubated for one h at room temperature. Solutions of 1× Kinase Reaction Buffer with 5% vehicle (water or DMEM with 12% FBS) were used as the negative controls without inhibitors or enzymes. To stop the reaction, 5 μL of ADP-Glo reagent was added to each well, and the plate was incubated for 40 min at room temperature. After this time, 10 μL of the Kinase Detection Reagent was added to each well, and the luminescence was measured in a Varioskan LUX multi-plate reader following 30 min incubation at room temperature. The obtained results were compared with the control (without inhibitor) and the inhibitory concentration (IC_{50}) values were estimated using GraphPad Prism 9.

Calcium Assay

RAJI cells were seeded in a 96-well black plate at a density of 40,000 cells per well and incubated under the standard conditions of 37°C for 24 h. The following day, the medium was removed, and solutions of the tested nanomaterial HDGF (347 and 174 μM) and ibrutinib (30 and 15 μM) were added. After incubation for 24 h, the Fluo-4 AM assay (Invitrogen) was performed in accordance with the manufacturer's instructions. Briefly, the cells were centrifuged and washed with cold PBS, and the cells were resuspended in a solution of Fluo-4 AM (5 μM) and incubated for 30 min at 37°C. After staining, the lymphoma cells were washed with cold PBS and resuspended in DMEM without serum and phenol red. The fluorescence intensity was measured in a Varioskan LUX multi-plate reader with a 485 nm excitation and a 520 nm emission filter. The experiments were performed at least three times.

Analysis of the mRNA Expression

RAJI cells were exposed to the tested nanomaterial HDGF (347, 174, and 84 μM) and ibrutinib (30 and 15 μM) for 24 h. Then, total RNA was isolated using TRIzol Reagent (Ambion). Reverse transcription was performed on 1 μg of total RNA using a ProtoScript M-MuLV First Strand cDNA Synthesis Kit (New England BioLabs). RT-qPCR was performed using a QuantStudio 5 Real-Time PCR System (Thermo Scientific) in a 10 μL reaction volume containing Luna Universal qPCR Master Mix (New England BioLabs), specific primer pair mix, and cDNA. The PCR reaction was performed as follows: initial denaturation at 95°C for 60s; followed by 40 denaturation cycles of 95°C and 15 sec; annealing (primer-specific temperature for 30s); and extension at 72°C for 30s. Melting curve analysis was used to determine the specific PCR products. The results were analyzed based on a comparison of the expression of the target genes to the reference gene, *HPRT1*, using the $2^{-\Delta\Delta CT}$ method. The experiments were performed at least four times. All primer pair sequences were purchased from Merck and are listed in Table S2.

Immunoblotting

Before the experiment, RAJI cells were seeded onto 3 cm Petri dishes (Nunc) at a density of 500,000 cells per well. The following day, the cells were stimulated with anti-human IgM (12 μg/mL, 10 min) and the medium was replaced with the solution of HDGF (347 and 174 μM) and ibrutinib (20 μM). After exposure for 24 h, the cells were collected, centrifuged, and lysed on ice in complete RIPA buffer containing Halt Protease Inhibitor Cocktail, Halt Phosphatase Inhibitor Cocktail, and 0.5 M EDTA (all from Thermo Scientific). The protein quantification was measured using a BCA Protein Assay Kit (Thermo Scientific) in accordance with the manufacturer's protocol. Equal amounts of the proteins were separated by SDS-PAGE and transferred onto nitrocellulose membranes. After nonspecific binding was blocked by incubation of the membrane in 5% non-fat milk prepared in TTBS (Tris-buffered saline with Tween 20), the membranes were incubated with specific primary antibodies (all from Cell Signaling) at 1:1000 dilution (for BTK, phospho-BTK, PLCγ2, phospho-PLCγ2, Akt, phospho-Akt, caspase-9, caspase-3, and c-Myc) and at 1:2000 dilution for the reference proteins (vinculin, β-actin, and GAPDH) overnight at 4°C. On the next day, the membranes were washed and incubated with horseradish peroxidase (HRP)-conjugated secondary antibodies for 1 h at room temperature. The chemiluminescence signals were recorded after staining with a SuperSignal™ West Pico Chemiluminescent Substrate (Thermo Scientific) using the ChemiDoc™ XRS+ System (BioRad). The experiments were performed at least four of five times. The densitometric analysis was conducted using ImageJ software (Wayne Rasband, National Institutes of Health, USA).

Statistical Analysis

The results are presented as the mean ± standard deviation (SD) of all independent experiments performed. The statistical analysis for calcium assay and mRNA analysis was performed using one- or two-way ANOVA with Dunnett's post-hoc test. A p-value of 0.05 or less was considered to be statistically significant.

Results and Discussion

To avoid formation of a plethora of [60]fullerene regioisomers, a water-soluble fullerene nanomaterial was prepared in a two-step Bingel–Hirsch reaction; first, a more reactive fullerene monoadduct (2) was formed, which was further reacted with the same malonate to create the protected fullerene hexakisadduct (Scheme 1). The formed carbon nanomaterial was

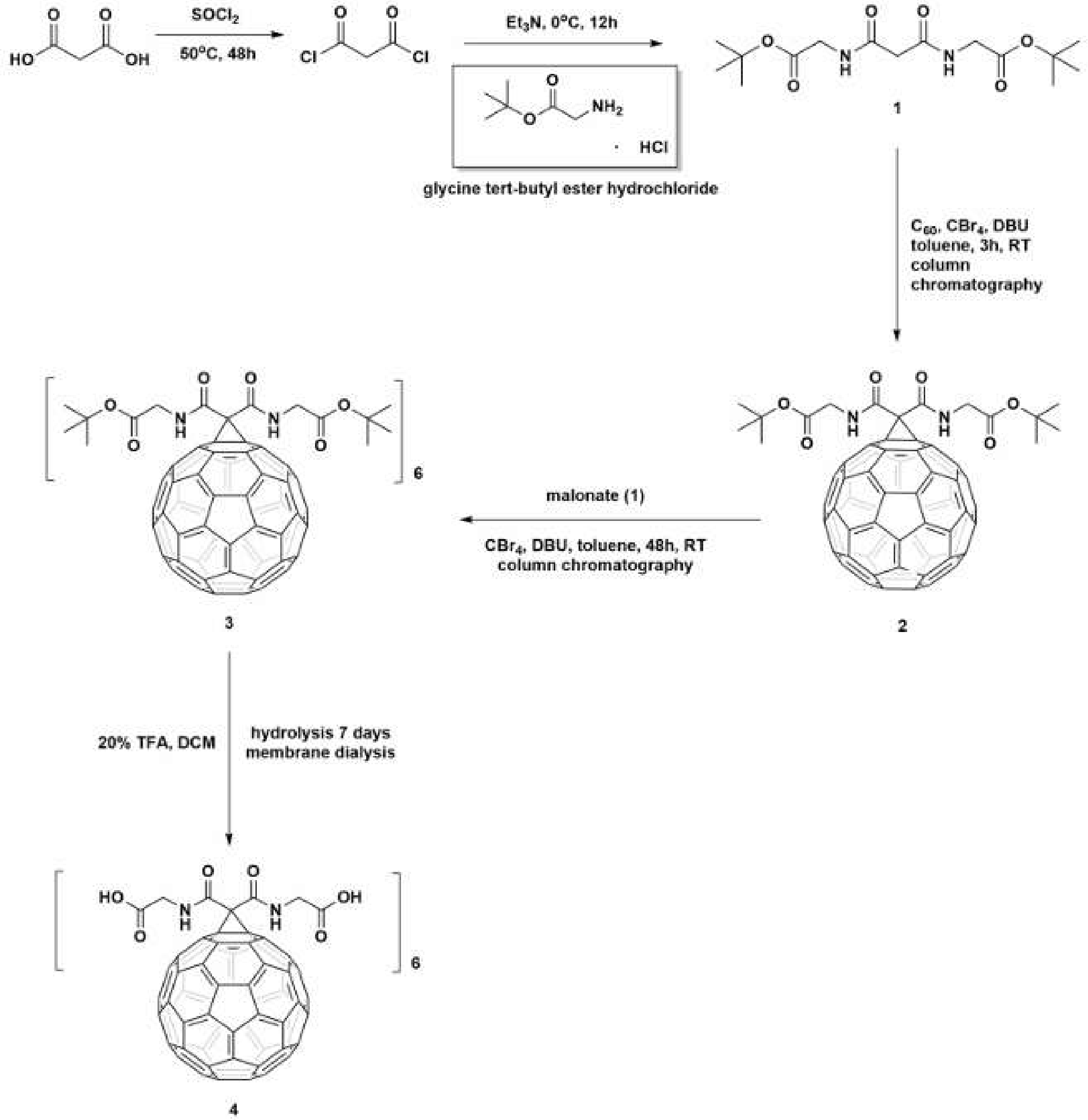

Scheme 1 Synthetic protocol for obtaining fullerene nanomaterial 4.

hydrolyzed and purified by membrane dialysis to form the described water-soluble fullerene nanomaterial, HDGF. The ^{1}H and ^{13}C NMR spectra of malonate 1 and its fullerene derivatives are shown in Figures S2–S5 (SI). The reaction conditions for the studied cyclopropanations were initially optimized, to obtain in the first step only, the [60]fullerene monoadduct (malonate/DBU/CBr_4 ratio 1.25/1/2). For the second Bingel–Hirsch reaction, the reaction conditions used were previously developed to graft the second malonate groups to fullerene derivative 2 and were successfully applied to produce compound 3, which was deprotected in acid conditions to the form pure water-soluble nanomaterial 4 (HDGF) after purification by membrane dialysis.[24] The chemical structure of compound 2 was easily confirmed by its ^{1}H- and ^{13}C-NMR spectra (Figures S4 and S5) as well as by mass spectrometry (Figures S6 and S7). The ^{13}C-NMR fullerene monoadduct displayed 15 characteristic signals of fullerene sp^2 carbons (in the 145–139 ppm range, Figure S5), as well as one sp^3 carbon at approximately 70 ppm, with no additional peaks from bis- and trisadducts. In the case of the [60] fullerene hexakisadduct, its symmetry (T_h) was confirmed by a characteristic ^{13}C-NMR spectrum in which three fullerene signals were observed (two sp^2 carbons between 145 and 139 ppm and one sp^3 signal at approximately 70 ppm, Figure 2A).

Additionally, ESI-TOF mass spectra of compounds 2 and 3 confirmed the molecular ion peaks for fullerene monoadduct and the protected hexakisadduct, for which masses were observed at 1048.1519 Da $[(M+3Na)+3H_2O]^+$ and 2841.0877 Da, respectively (Figures S7 and S8).

The analysis of the survey spectrum of HDGF indicates that the main constituents of the examined samples were carbon, oxygen, and nitrogen. The analysis of the C1s line (Figure 2B) indicates that carbon occurs in four different chemical environments. In the deconvoluted C1s range, the most intense line, with a binding energy of 284.8 eV, indicates the presence of the C–C and C–H bonds in the sample.[25] The second chemical state, observed at a binding energy of 286.6 eV, can be assigned to C–O and C–N bonds (similar to those observed in fullerene derivatives) and to –C–OH bonds.[26] The line at 288 eV represents the carbonyl group and the double carbon bond with oxygen (C=O).[27] The analysis of the chemical state of nitrogen indicated that it existed in only two chemical surroundings (see Figure 2B). The peak localized at 399.8 eV can be assigned to C–N and N–(C=O)– bonds, whereas the N1s component at 398.4 eV can be assigned to pyridinic type nitrogen.[28] The deconvolution of the O1s spectrum, shown in the Supporting Information (Figure S9), revealed the presence of three compositional lines at 529.2 eV, 530.6 eV, and 532.5 eV. The chemical state of oxygen detected at 529.2 eV has been observed in graphene oxide films and can be linked to atomic oxygen.[29,30] The chemical composition, atomic concentration, and percentage contributions of HDGF obtained from the XPS studies are presented in Table S1.

The final fullerene nanomaterial 4 was also characterized using FT-IR spectroscopy (Figure 2C). Characteristic signals of carbonyl group were present at approximately 1725 cm^{-1} and a there was a broad signal for OH groups with a maximum at approximately 3335 cm^{-1}, suggesting possible H-bonding. DLS analysis revealed the formation of [60] fullerene aggregates at approximately 235 nm with an observed zeta potential of −40.7 mV (Figure 2F and G), but with a relatively high polydispersity index (PDI = 0.27). As water-soluble fullerene is able to form a wide range of aggregates that are in stable equilibrium, we also studied this phenomenon using cryo- and room temperature electron microscopy. The cryo-TEM analysis (Figure 2D) revealed that HDGF formed smaller spherical aggregates (15–35 nm in diameter) as well as the larger, "fluffy" type of aggregates (200–300 nm in diameter, Figure 2E), which were also previously observed for aminofullerenes.[28] Additionally, we have checked the behavior of synthesized fullerene nanomaterial in a different pH conditions, as well as in medium containing FBS (Figures S10–S14). In general, we observed formation of larger aggregates (400 nm) at lower pH values (pH = 3) and almost the same behavior at pH = 6 and pH = 7. In contrast, at higher pH values, the formation of two subtypes of fullerene aggregates was clearly detected – around 40 nm and 250 nm. The further studies on fullerene aggregation in cellular medium containing FBS confirmed its stability-almost the same pattern of aggregates was observed after 3 days.

To evaluate the inhibitory potential of HDGF against non-receptor tyrosine kinases, including ABL, BRK, BTK, and Src family kinases, we performed the ADP Glo Kinase assay. As shown in Table 1, HDGF dissolved in water exhibited strong inhibitory activity, with inhibition at micromolar concentrations, for BTK and Fyn kinases. The calculated IC_{50} values were 25.79 μM and 11.90 μM, respectively. Interestingly, for HDGF dissolved in DMEM with 12% FBS, we observed that the high-level BTK kinase inhibition was maintained (IC_{50} = 29.76 μM). In our previous work, we

https://doi.org/10.2147/IJN.S401058

hydrolyzed and purified by membrane dialysis to form the described water-soluble fullerene nanomaterial, HDGF. The ^{1}H and ^{13}C NMR spectra of malonate 1 and its fullerene derivatives are shown in Figures S2–S5 (SI). The reaction conditions for the studied cyclopropanations were initially optimized, to obtain in the first step only, the [60]fullerene monoadduct (malonate/DBU/CBr_4 ratio 1.25/1/2). For the second Bingel–Hirsch reaction, the reaction conditions used were previously developed to graft the second malonate groups to fullerene derivative 2 and were successfully applied to produce compound 3, which was deprotected in acid conditions to the form pure water-soluble nanomaterial 4 (HDGF) after purification by membrane dialysis.[24] The chemical structure of compound 2 was easily confirmed by its ^{1}H- and ^{13}C-NMR spectra (Figures S4 and S5) as well as by mass spectrometry (Figures S6 and S7). The ^{13}C-NMR fullerene monoadduct displayed 15 characteristic signals of fullerene sp^2 carbons (in the 145–139 ppm range, Figure S5), as well as one sp^3 carbon at approximately 70 ppm, with no additional peaks from bis- and trisadducts. In the case of the [60] fullerene hexakisadduct, its symmetry (T_h) was confirmed by a characteristic ^{13}C-NMR spectrum in which three fullerene signals were observed (two sp^2 carbons between 145 and 139 ppm and one sp^3 signal at approximately 70 ppm, Figure 2A).

Additionally, ESI-TOF mass spectra of compounds 2 and 3 confirmed the molecular ion peaks for fullerene monoadduct and the protected hexakisadduct, for which masses were observed at 1048.1519 Da $[(M+3Na)+3H_2O]^+$ and 2841.0877 Da, respectively (Figures S7 and S8).

The analysis of the survey spectrum of HDGF indicates that the main constituents of the examined samples were carbon, oxygen, and nitrogen. The analysis of the C1s line (Figure 2B) indicates that carbon occurs in four different chemical environments. In the deconvoluted C1s range, the most intense line, with a binding energy of 284.8 eV, indicates the presence of the C–C and C–H bonds in the sample.[25] The second chemical state, observed at a binding energy of 286.6 eV, can be assigned to C–O and C–N bonds (similar to those observed in fullerene derivatives) and to –C–OH bonds.[26] The line at 288 eV represents the carbonyl group and the double carbon bond with oxygen (C=O).[27] The analysis of the chemical state of nitrogen indicated that it existed in only two chemical surroundings (see Figure 2B). The peak localized at 399.8 eV can be assigned to C–N and N–(C=O)– bonds, whereas the N1s component at 398.4 eV can be assigned to pyridinic type nitrogen.[28] The deconvolution of the O1s spectrum, shown in the Supporting Information (Figure S9), revealed the presence of three compositional lines at 529.2 eV, 530.6 eV, and 532.5 eV. The chemical state of oxygen detected at 529.2 eV has been observed in graphene oxide films and can be linked to atomic oxygen.[29,30] The chemical composition, atomic concentration, and percentage contributions of HDGF obtained from the XPS studies are presented in Table S1.

The final fullerene nanomaterial 4 was also characterized using FT-IR spectroscopy (Figure 2C). Characteristic signals of carbonyl group were present at approximately 1725 cm^{-1} and a there was a broad signal for OH groups with a maximum at approximately 3335 cm^{-1}, suggesting possible H-bonding. DLS analysis revealed the formation of [60] fullerene aggregates at approximately 235 nm with an observed zeta potential of −40.7 mV (Figure 2F and G), but with a relatively high polydispersity index (PDI = 0.27). As water-soluble fullerene is able to form a wide range of aggregates that are in stable equilibrium, we also studied this phenomenon using cryo- and room temperature electron microscopy. The cryo-TEM analysis (Figure 2D) revealed that HDGF formed smaller spherical aggregates (15–35 nm in diameter) as well as the larger, "fluffy" type of aggregates (200–300 nm in diameter, Figure 2E), which were also previously observed for aminofullerenes.[28] Additionally, we have checked the behavior of synthesized fullerene nanomaterial in a different pH conditions, as well as in medium containing FBS (Figures S10–S14). In general, we observed formation of larger aggregates (400 nm) at lower pH values (pH = 3) and almost the same behavior at pH = 6 and pH = 7. In contrast, at higher pH values, the formation of two subtypes of fullerene aggregates was clearly detected – around 40 nm and 250 nm. The further studies on fullerene aggregation in cellular medium containing FBS confirmed its stability-almost the same pattern of aggregates was observed after 3 days.

To evaluate the inhibitory potential of HDGF against non-receptor tyrosine kinases, including ABL, BRK, BTK, and Src family kinases, we performed the ADP Glo Kinase assay. As shown in Table 1, HDGF dissolved in water exhibited strong inhibitory activity, with inhibition at micromolar concentrations, for BTK and Fyn kinases. The calculated IC_{50} values were 25.79 μM and 11.90 μM, respectively. Interestingly, for HDGF dissolved in DMEM with 12% FBS, we observed that the high-level BTK kinase inhibition was maintained (IC_{50} = 29.76 μM). In our previous work, we

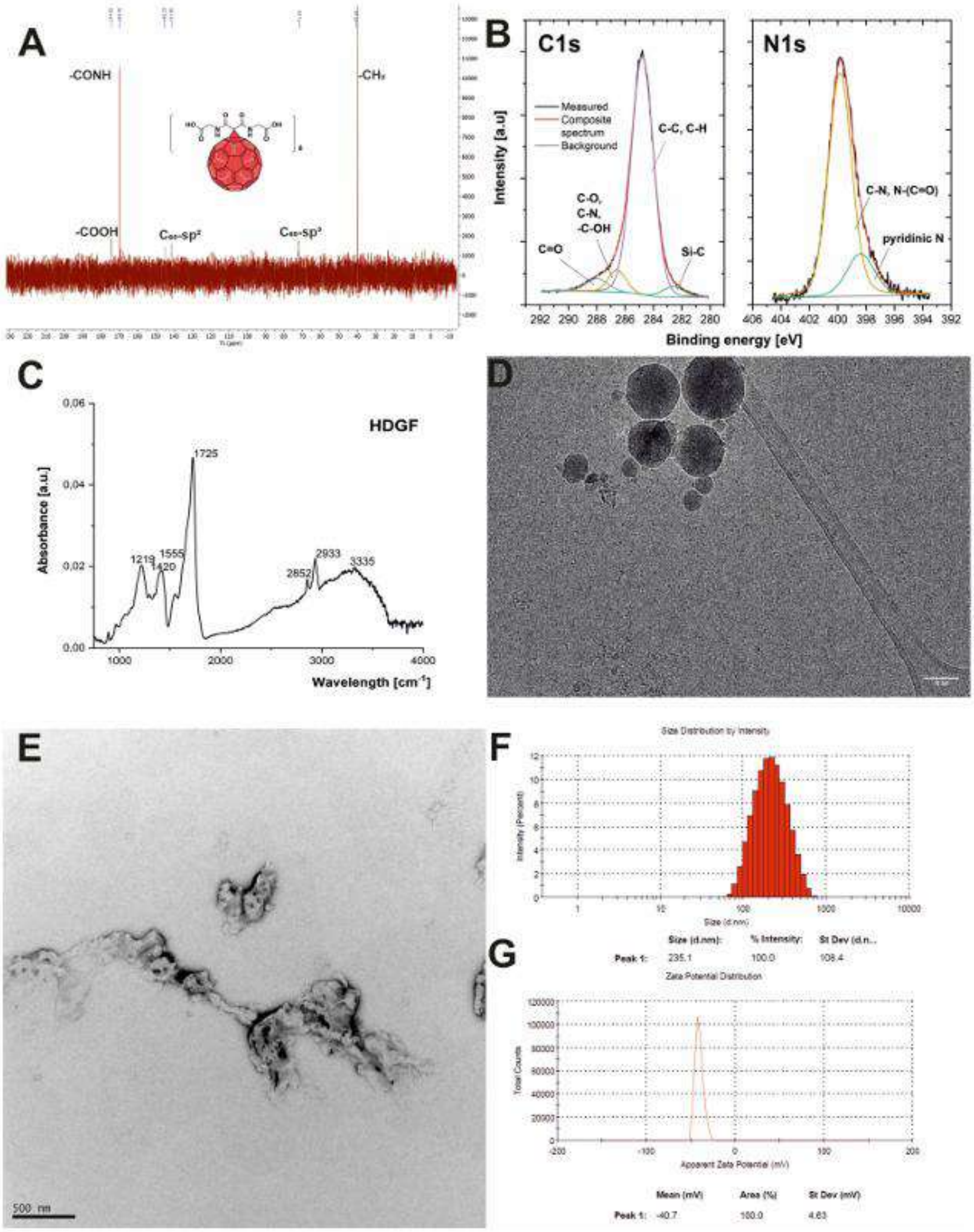

Figure 2 Physico-chemical characterization of fullerene nanomaterial HDGF: (**A**) The ^{13}C-NMR spectrum; (**B**) A high-resolution XPS spectra of C1s and N1s; (**C**) The FT-IR spectrum; (**D**) Cryo-transmission electron microscopy; (**E**) Transmission electron microscopy; (**F**) Dynamic light scattering measurements; (**G**) Zeta potential measurements.

Table 1 Inhibitory Activity of Tested HDFG Against a Panel of Tyrosine Kinases

Nanomaterial	Inhibitory Activity - IC$_{50}$ [μM] on Kinases							
	ABL1	**BRK**	**BTK**	**CSK**	**Fyn A**	**Lck**	**Lyn B**	**Src**
HDGF in DMEM*	>922.1	471.73 ± 27.28	29.76 ± 5.41	152.78 ± 25.30	44.15 ± 8.43	359.62 ± 80.36	864.1 ± 143.1	195.44 ± 45.14
HDGF in water*	>99.21	>99.21	25.79 ± 2.48	>99.21	11.90 ± 3.47	>99.21	72.42 ± 23.81	>99.21

Notes: *HDGF was dissolved in DMEM with 12% FBS or water. The final concentration of solvents was 5%.

observed an attenuation of the inhibitory potential of glycofullerenes in culture medium.[19] The reason for this phenomenon was the interaction of nanomaterials with serum and the formation of a protein corona on their surface. The presence of a protein corona can lead to the aggregation of nanoparticles, modifying their surface properties by reducing stability, which affects their interaction with cells and inhibits their ability to bind to specific target receptors.[31] For the other kinases tested, we noted significant differences in the inhibitory activity of HDGF dissolved in water or medium. In the case of the Fyn kinase, we observed an almost four-fold weaker effect for the tested nanomaterial in DMEM (IC$_{50}$ = 44.15 μM). In turn, we observed a more significant difference in inhibition for the Lyn kinase. The calculated IC$_{50}$ values were 72.42 μM and 864.1 μM for HDGF dissolved in water and medium, respectively. Additionally, we observed the weak affinity of HDGF for ABL, BRK, CSK, Lck, and Src kinases.

To understand the atomistic details of the interaction between HDGF and BTK, we used a docking procedure able to determine the fullerene binding site in proteins. HDGF binds in the active site of BTK, interacting directly with Cys481, Arg525, and Tyr551, which are crucial residues for the activity of BTK (Figure 3A). These interactions may explain the inhibitory effect of HDGF on the BTK protein.

HDGF shows strong shape and electrostatic complementarity with the BTK active site (Figure 3B). In particular, the negatively charged HDGF interacts favorably with the positively charged region of the active site that can physiologically bind a molecule that is negatively charged, such as ATP. The phosphorylation of Tyr551 is essential for BTK function, and HDGF obscures Tyr551, strongly reducing its accessibility (Figure 3C). Starting from the docking pose, an MD simulation for 100 ns was performed. MM/GBSA analysis of the MD trajectory estimated a favorable binding energy for HDGF with BTK, of −43.8 kcal mol^{-1} (Figure 3D). Fingerprint analysis provided the contribution to the binding of each amino acid with HDGF. The most strongly interacting amino acids were positively charged residues,

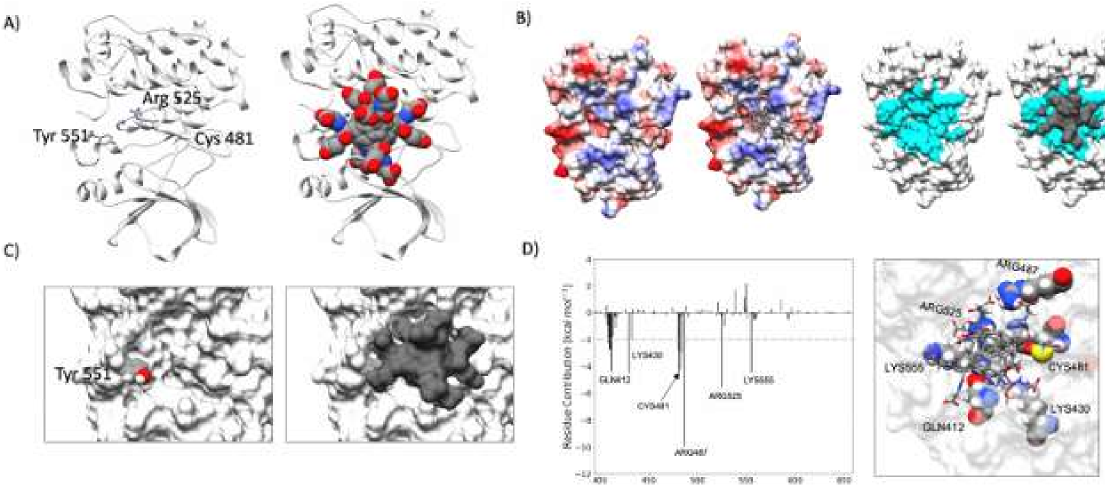

Figure 3 (**A**) Identification of the HDGF binding pocket in the BTK three-dimensional structure. (**B**) Electrostatic (on the left) and surface (on the right) complementarity between HDGF and BTK. (**C**) Accessibility of Tyr551 before (on the left) and upon (on the right) HDGF binding. (**D**) $\Delta G_{binding}$ between HDGF and BTK broken down by residue.

such as Lys430, Arg487, Arg525, and Lys555. Notably, HDGF strongly interacts with: i) the ATP binding pocket of BTK (Gln412 and Lys430); ii) the catalytic residue Arg525; and iii) Cys481, which represents the site of covalent binding of the most commonly studied covalent inhibitors of BTK, such as ibrutinib, acalabrutinib, or zanubrutinib. The inhibitory activity of HDGF is multifaceted: it hampers the BTK active site, interacting directly with the catalytic residues Arg525, obscures Tyr551, rendering it inaccessible to phosphorylation, and binds to residues that form the ATP binding pocket.

In subsequent experimental studies, we focused on exploring the mechanism of action of HDGF at the cellular level. First, we assayed the cytotoxicity of HDGF in two suspension-culture human cell lines: K562 (leukemia) cells and RAJI (lymphoma) cells. We chose these two cell lines because of their characteristics, including high levels of BTK expression, as reported previously.[32,33] The tested nanomaterial resulted in good antiproliferative activity against RAJI cells. The calculated IC_{50} parameter was 350 µM (Figure 4A). In contrast, the leukemia cells were resistant to HDGF. The reference small-molecule BTK inhibitor, ibrutinib, has a high level of activity against K562 cells (IC_{50} = 0.85 µM) and moderate activity against RAJI cells (IC_{50} = 20.88 µM).[34] Subsequently, we examined the induction of cell death by autophagy and apoptosis in RAJI cells treated with HDGF. For this purpose, we determined the expression of two essential genes (*LC3* and *p62*) related to the autophagy process by qRT-PCR (Figure 4B), as well as two caspases (caspase-3 and −9) responsible for the activation and progression of apoptosis by Western blotting (Figure 4C). Our results showed that 347 µM HDGF caused a significant increase in the mRNA expression of *LC3*, which is a marker of autophagosomes formation.

Additionally, we observed an almost three-fold increase in the expression of *p62* after exposure to HDGF (174 µM) and ibrutinib (15 µM). However, protein expression analysis showed that HDGF caused a marked increase in the cleavage product of caspases −3 and −9. These proteins are among the activators and effectors of the apoptosis process, and an increase in their expression is a hallmark of this form of cell death.[35] Subsequently, we began to investigate the direct association of HDGF on inhibition of the BTK signaling pathway by examining changes in the calcium levels in

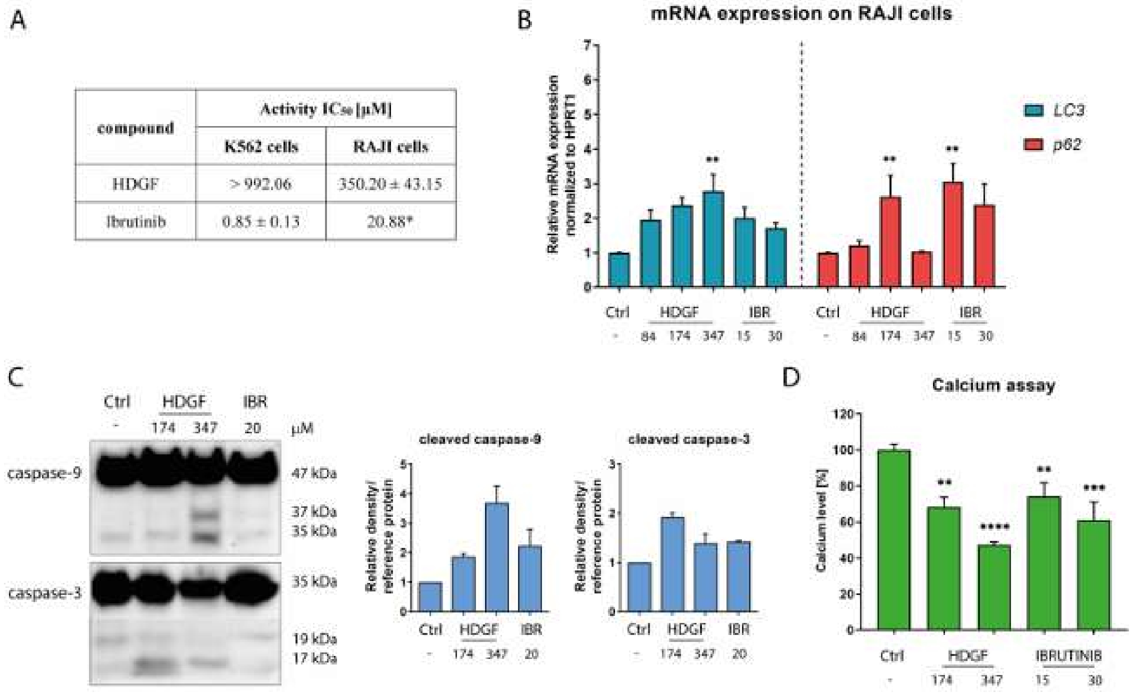

compound	Activity IC_{50} [µM]	
	K562 cells	RAJI cells
HDGF	> 992.06	350.20 ± 43.15
Ibrutinib	0.85 ± 0.13	20.88*

Figure 4 Antiproliferative activity of HDGF and ibrutinib against K562 and RAJI cells (*value for lymphoma taken from ref.) (**A**). The effects of the tested compounds on the expression of genes associated with autophagy (**B**) and the expression of proteins related to the apoptosis process (**C**). The calcium levels after exposure to the tested compounds in RAJI cells (**D**). Statistical significances were calculated using one- or two-way ANOVA with Dunnett's post hoc test: $^{**}p < 0.01$, $^{***}p < 0.001$, $^{****}p < 0.0001$ compared with the untreated cells (control).

RAJI cells after treatment. Several reports indicate that BTK kinase is involved in B-cell antigen receptor signal transduction, which triggers a cascade of events leading to the activation of phospholipase C-γ2 (PLCγ2) phosphorylation, calcium mobilization in cells, stimulation of ERK, JNK, and MAPK kinases, in addition to NF-κB activation.[36–38] Our analyses showed that cellular calcium levels drop dramatically following incubation with HDGF and the BTK inhibitor ibrutinib. In addition, the downward trend in calcium levels in RAJI cells is dependent on the drug and dose used (Figure 4D).

Next, we explored the effect of HDGF on the expression of the BTK kinase and its downstream targets in the signaling pathway at the cellular level. As mentioned above, the BTK kinase is responsible for the activation of PLCγ2,

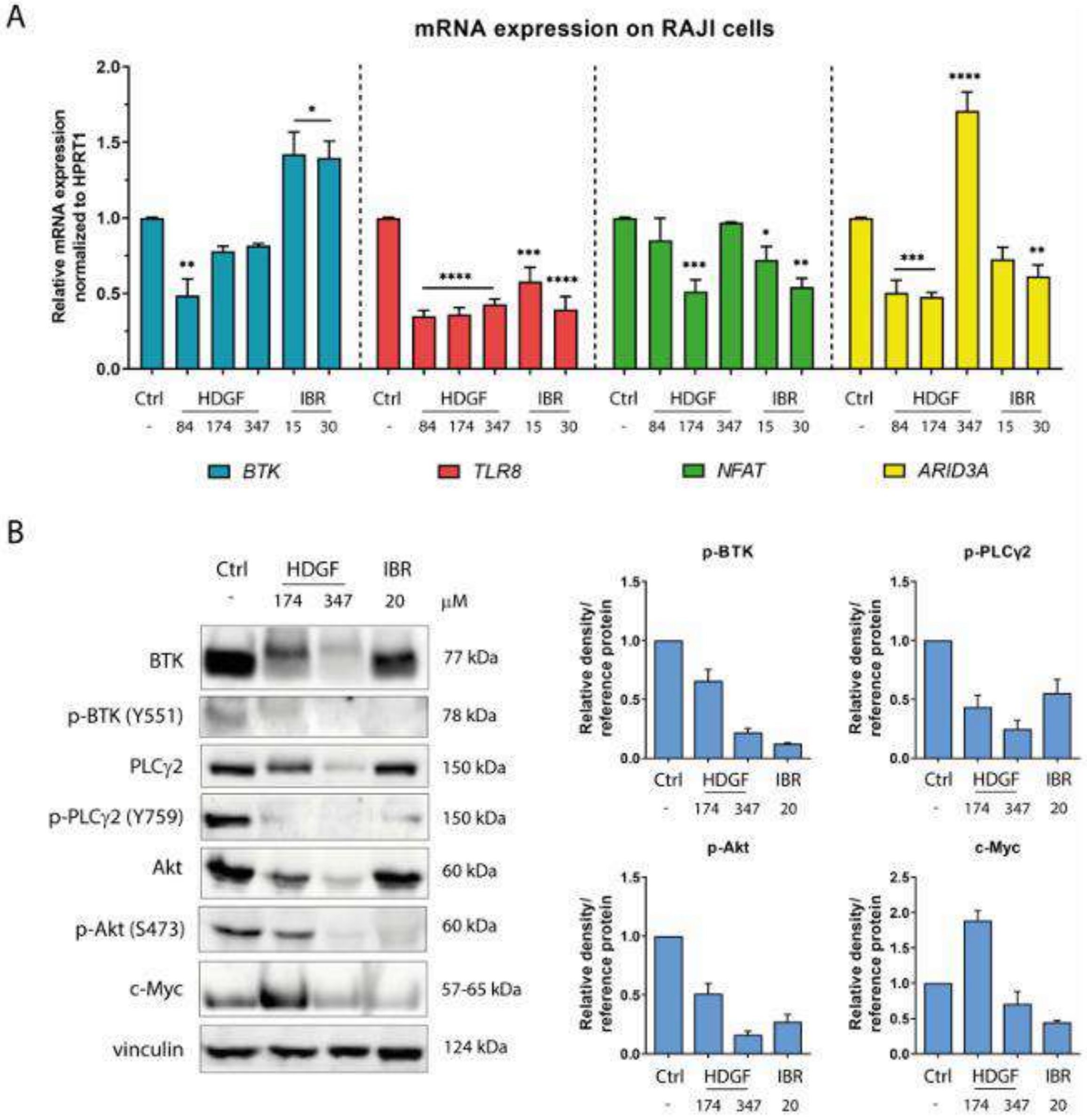

Figure 5 Impact of the tested compounds on the expression of selected genes (**A**) and proteins (**B**) associated with the BTK signaling pathway in RAJI cells. The statistical significances were calculated using one- or two-way ANOVA with Dunnett's post hoc test: $^{*}p < 0.05$, $^{**}p < 0.01$, $^{***}p < 0.001$, $^{****}p < 0.0001$ compared with the untreated cells (control).

which then boosts the influx of calcium ions into the cellular environment, and subsequently stimulates transcriptional factors, including the nuclear factor of activated T-cells (NFAT) or NF-κB.[39,40] Moreover, in B-cells, this kinase functions as a transcriptional regulator that can interact with proteins such as Arid3a or BAM11. Additionally, BTK participates in the immune response by interacting with the TIR domains of TLR8 and TLR9, which mediate TNF induction and NF-κB recruitment.[41] Consequently, we examined the influence of HDGF and ibrutinib on changes in the mRNA expression of *BTK*, *TLR8*, *NFAT*, and *ARID3A* in RAJI cells. As shown in Figure 5A, 84 μM HDGF caused a significant, almost two-fold decrease in *BTK* gene expression. Additionally, we observed a slight downregulation of this gene after exposure to higher concentrations of HDGF. Surprisingly, *BTK* expression increased after exposure to ibrutinib. The explanation for this phenomenon may be that gene production is enhanced to compensate for the low protein expression of BTK following inhibition by ibrutinib. Moreover, we observed a significant decrease in the expression of *TLR8* and *NFAT* after incubation with both the tested compounds. In the case of *ARID3A*, we noticed a significant, almost two-fold downregulation after exposure to 84 and 174 μM HDGF and 30 μM ibrutinib.

Finally, we assessed changes in the BTK protein expression and downstream signaling transduction after exposure of RAJI cells to HDGF and ibrutinib following anti-IgM stimulation. Notably, the stimulation of RAJI cells could initiate the full activation of BTK kinase through Bcr receptor signaling and subsequently induce PLCγ2 phosphorylation and activation of downstream signaling cascade pathways, including MAPK or Akt. The results are presented in Figure 5B. In general, we noticed significant inhibition of the phosphorylation of the BTK protein and downstream targets, including PLCγ2 and Akt. At 347 μM, HDGF caused an almost five-fold decrease in the level of phosphorylation of BTK at Tyr551.

Changes in the total BTK protein expression also was noted. Similar results were also observed for treatment with an FDA-approved BTK inhibitor. In turn, we noticed significant inhibition of phosphorylation of PLCγ2 at the Tyr759 site after exposure to 174 and 347 μM HDGF. Interestingly, the observed effects were more significant than with ibrutinib. In the case of c-Myc protein, a downstream target of the MAPK pathway, we observed a slight downregulation after treatment with 374 μM HDGF and 20 μM ibrutinib. From a therapeutic perspective, the suppression of c-Myc expression may be crucial to overcome resistance mechanisms and to sensitize cells to ibrutinib treatment.[42] The HDGF also blocked the phosphorylation of Akt at the Ser473 residue, which can be activated without calcium release events. Thus, the tested [60]fullerene derivative may contribute to the inhibition of pro-survival processes, cell migration, and cell adhesion, which are driven by the activation of the Akt pathway.

Conclusions

To the best of our knowledge, our study is the first to describe the inhibition of the BTK protein using a water-soluble fullerene nanomaterial. Our data show the controlled synthesis of a highly water-soluble and T_h symmetrical diglycinyl [60]fullerene hexakisadduct, which was confirmed by ^{13}C-NMR spectroscopy and mass spectroscopy. The created fullerene nanomaterial formed spherical aggregates visualized by cryo-TEM with a negative zeta potential of approximately −40 mV. The enzymatic and cellular studies revealed strong inhibition of the BTK protein with an IC_{50} of approximately 25 μM, with only a slight influence of adsorbed protein corona. The cytotoxicity and mechanistic studies in RAJI and K562 cells revealed the increased gene expression of *LC3* and *p62* with an additional increase in the cleavage product of caspase−3 and −9, suggesting the cell death occurred by mixed mechanisms. Moreover, the cellular calcium levels dropped dramatically after cells were treated with HDGF. To better understand the molecular mechanism of BTK inactivation by HDGF, we performed computational studies, which predicted that HDGF binds in the active site of BTK, interacting directly with Cys481, Arg525, and Tyr551, the residues that are crucial for the activity of BTK. Our data provide helpful information for the development of fullerene-based inhibitors of non-receptor kinases.

Acknowledgments

This work was supported by National Science Centre (Poland) grant 2019/35/B/NZ5/04208 awarded to Dr Katarzyna Malarz. The publication was co-financed by the funds granted under the Research Excellence Initiative of the University of Silesia in Katowice (KM). Dr Maciej Serda thanks for National Science Centre (Poland) for grant funding (UMO-2016/23/D/NZ7/00912).

Disclosure

The authors declare no competing financial interest.

References

1. Steve FA, Acquah AVP, Markelov DA, Semisalov AS, Leonhardt BE, Magi JM. The beautiful molecule: 30 years of C60 and its derivatives. *ECS J Solid State Sci Technol*. 2017;6(6):M3155–M3162. doi:10.1149/2.0271706jss
2. Sijbesma R, Srdanov G, Wudl F, et al. Synthesis of a fullerene derivative for the inhibition of HIV enzymes. *J Am Chem Soc*. 1993;115(15):6510–6512. doi:10.1021/ja00068a006
3. Nakamura E, Isobe H. Functionalized fullerenes in water. The first 10 years of their chemistry, biology, and nanoscience. *Acc Chem Res*. 2003;36(11):807–815. doi:10.1021/ar030027y
4. Rašović I. Water-soluble fullerenes for medical applications. *Mater Sci Technol*. 2017;33(7):777–794. doi:10.1080/02670836.2016.1198114
5. Hirsch A, Lamparth I, Grösser T, Karfunkel HR. Regiochemistry of multiple additions to the fullerene core: synthesis of a Th-symmetric hexakis adduct of C60 with bis (ethoxycarbonyl) methylene. *J Am Chem Soc*. 1994;116(20):9385–9386. doi:10.1021/ja00099a088
6. Muñoz A, Sigwalt D, Illescas BM, et al. Synthesis of giant globular multivalent glycofullerenes as potent inhibitors in a model of Ebola virus infection. *Nat Chem*. 2015;8:50. doi:10.1038/nchem.2387
7. Dhiman S, Kaur A, Sharma M. Fullerenes for anticancer drug targeting: teaching an old dog a new trick. *Mini Rev Med Chem*. 2022;22(22):2864–2880. doi:10.2174/1389557522666220317145544
8. Kazemzadeh H, Mozafari M. Fullerene-based delivery systems. *Drug Discov Today*. 2019;24(3):898–905. doi:10.1016/j.drudis.2019.01.013
9. Ge C, Du J, Zhao L, et al. Binding of blood proteins to carbon nanotubes reduces cytotoxicity. *Proc Natl Acad Sci U S A*. 2011;108(41):16968–16973. doi:10.1073/pnas.1105270108
10. Pinals RL, Yang D, Rosenberg DJ, et al. Quantitative protein corona composition and dynamics on carbon nanotubes in biological environments. *Angew Chem Int Ed*. 2020;59(52):23668–23677. doi:10.1002/anie.202008175
11. Belgorodsky B, Fadeev L, Ittah V, et al. Formation and characterization of stable human serum albumin− tris-malonic acid [C60] fullerene complex. *Bioconjug Chem*. 2005;16(5):1058–1062.
12. Calvaresi M, Zerbetto F. Baiting proteins with C60. *ACS Nano*. 2010;4(4):2283–2299. doi:10.1021/nn901809b
13. Di Giosia M, Soldà A, Seeger M, et al. A bio-conjugated fullerene as a subcellular-targeted and multifaceted phototheranostic agent. *Adv Funct Mater*. 2021;31(20):2101527. doi:10.1002/adfm.202101527
14. Burger JA. BTK inhibitors: present and future. *Cancer J*. 2019;25(6):386.
15. Liang C, Tian D, Ren X, et al. The development of Bruton's Tyrosine Kinase (BTK) inhibitors from 2012 to 2017: a mini-review. *Eur J Med Chem*. 2018;151:315–326.
16. Molina-Cerrillo J, Alonso-Gordoa T, Gajate P, Grande E. Bruton's Tyrosine Kinase (BTK) as a promising target in solid tumors. *Cancer Treat Rev*. 2017;58:41–50. doi:10.1016/j.ctrv.2017.06.001
17. Lin L, Czerwinski R, Kelleher K, et al. Activation loop phosphorylation modulates Bruton's Tyrosine Kinase (Btk) kinase domain activity. *Biochemistry*. 2009;48(9):2021–2032. doi:10.1021/bi8019756
18. Di Paolo JA, Huang T, Balazs M, et al. Specific Btk inhibition suppresses B cell–and myeloid cell–mediated arthritis. *Nat Chem Biol*. 2011;7(1):41–50. doi:10.1038/nchembio.481
19. Serda M, Malarz K, Mrozek-Wilczkiewicz A, Wojtyniak M, Musiol R, Curley SA. Glycofullerenes as non-receptor tyrosine kinase inhibitors-towards better nanotherapeutics for pancreatic cancer treatment. *Sci Rep*. 2020;10(1):1–11. doi:10.1038/s41598-019-57155-7
20. Wu J-C, Wang D-X, Huang Z-T, Wang M-X. Synthesis of diverse N, O-bridged calix [1] arene [4] pyridine-C60 dyads and triads and formation of intramolecular self-inclusion complexes. *J Org Chem*. 2010;75(24):8604–8614. doi:10.1021/jo1019267
21. Maier JA, Martinez C, Kasavajhala K, Wickstrom L, Hauser KE, Simmerling C. Ff14SB: improving the accuracy of protein side chain and backbone parameters from Ff99SB. *J Chem Theory Comput*. 2015;11(8):3696–3713. doi:10.1021/acs.jctc.5b00255
22. Schneidman-Duhovny D, Inbar Y, Nussinov R, Wolfson HJ. PatchDock and SymmDock: servers for rigid and symmetric docking. *Nucleic Acids Res*. 2005;33(suppl_2):W363–W367. doi:10.1093/nar/gki481
23. Miller BR, McGee TD, Swails JM, Homeyer N, Gohlke H, Roitberg AE. MMPBSA. py: an efficient program for end-state free energy calculations. *J Chem Theory Comput*. 2012;8(9):3314–3321. doi:10.1021/ct300418h
24. Serda M, Ware MJ, Newton JM, et al. Development of photoactive sweet-C60 for pancreatic cancer stellate cell therapy. *Nanomedicine*. 2018;13(23):2981–2993. doi:10.2217/nnm-2018-0239
25. Watts JF. High resolution XPS of organic polymers: the scienta ESCA 300 database. *Surf Interface Anal*. 1993;20(3):267. doi:10.1002/sia.740200310
26. Yu J, Guan M, Li F, et al. Effects of fullerene derivatives on bioluminescence and application for protease detection. *Chem Comm*. 2012;48(89):11011–11013. doi:10.1039/C2CC36099C
27. Chen X, Wang X, Fang D, Review A. On C1s XPS-spectra for some kinds of carbon materials. *Fuller Nanotub Carbon Nanostructures*. 2020;28(12):1048–1058. doi:10.1080/1536383X.2020.1794851
28. Korzuch J, Rak M, Balin K, et al. Towards water-soluble [60] fullerenes for the delivery of SiRNA in a prostate cancer model. *Sci Rep*. 2021;11(1):1–10. doi:10.1038/s41598-021-89943-5
29. Yang D, Velamakanni A, Bozoklu G, et al. Chemical analysis of graphene oxide films after heat and chemical treatments by X-ray photoelectron and micro-raman spectroscopy. *Carbon*. 2009;47(1):145–152. doi:10.1016/j.carbon.2008.09.045
30. Gladys M, El Zein A, Mikkelsen A, Andersen JN, Held G. Chemical composition and reactivity of water on clean and oxygen-covered Pd surface science. *Surf Sci*. 2008;602(22):3540–3549.
31. Wu LJ, Fu FQ, Wang WH, et al. Plasma protein corona forming upon fullerene nanocomplex: impact on both counterparts. *Particuology*. 2023;73:26–36. doi:10.1016/j.partic.2022.04.0061674-2001
32. Malarz K, Mularski J, Pacholczyk M, Musiol R. The landscape of the anti-kinase activity of the IDH1 inhibitors. *Cancers*. 2020;12(3):536. doi:10.3390/cancers12030536

33. Chu Y, Lee S, Shah T, et al. Ibrutinib significantly inhibited Bruton's Tyrosine Kinase (BTK) phosphorylation, in-vitro proliferation and enhanced overall survival in a preclinical Burkitt Lymphoma (BL) model. *Oncoimmunology*. 2019;8(1):e1512455. doi:10.1080/2162402X.2018.1512455
34. Ge Y, Wang C, Song S, et al. identification of highly potent BTK and JAK3 dual inhibitors with improved activity for the treatment of B-cell lymphoma. *Eur J Med Chem*. 2018;143:1847–1857. doi:10.1016/j.ejmech.2017.10.080
35. Li J, Yuan J. Caspases in apoptosis and beyond. *Oncogene*. 2008;27(48):6194–6206. doi:10.1038/onc.2008.297
36. Bajpai UD, Zhang K, Teutsch M, Sen R, Wortis HH. Bruton's tyrosine kinase links the B cell receptor to nuclear factor κB activation. *J Exp Med*. 2000;191(10):1735–1744. doi:10.1084/jem.191.10.1735
37. Pal Singh S, Dammeijer F, Hendriks RW. Role of bruton's tyrosine kinase in B cells and malignancies. *Mol Cancer*. 2018;17(1):1–23. doi:10.1186/s12943-017-0753-1
38. Tomlinson MG, Woods DB, McMahon M, et al. A conditional form of bruton's tyrosine kinase is sufficient to activate multiple downstream signaling pathways via PLC gamma 2 in B cells. *BMC Immunol*. 2001;2(1):1–12. doi:10.1186/1471-2172-2-4
39. Hendriks RW, Yuvaraj S, Kil LP. Targeting bruton's tyrosine kinase in B cell malignancies. *Nat Rev Cancer*. 2014;14(4):219–232. doi:10.1038/nrc3702
40. Antony P, Petro JB, Carlesso G, et al. Directs the activation of NFAT and NF-κB via distinct molecular mechanisms. *Exp Cell Res*. 2003;291(1):11–24. doi:10.1016/S0014-4827(03)00338-0
41. Hayakawa K, Li Y-S, Shinton SA, et al. Crucial role of increased Arid3a at the pre-B and immature B cell stages for B1a cell generation. *Front Immunol*. 2019;10:457. doi:10.3389/fimmu.2019.00457
42. Moyo TK, Wilson CS, Moore DJ, Eischen CM, Enhances M. B-cell receptor signaling in precancerous B cells and confers resistance to Btk inhibition. *Oncogene*. 2017;36(32):4653–4661. doi:10.1038/onc.2017.95

Feature

Interactions between modified fullerenes and proteins in cancer nanotechnology

Maciej Serda [1,*], **Julia Korzuch** [1], **Dominik Dreszer** [1], **Martyna Krzykawska-Serda** [2], **Robert Musioł** [1]

[1] Institute of Chemistry, University of Silesia in Katowice, Katowice, Poland
[2] Faculty of Biochemistry, Biophysics and Biotechnology, Jagiellonian University, Kraków, Poland

Fullerenes have numerous properties that fill the gap between small molecules and nanomaterials. Several types of chemical reaction allow their surface to be ornamented with functional groups designed to change them into 'ideal' nanodelivery systems. Improved stability, and bioavailability are important, but chemical modifications can render them practically soluble in water. 'Buckyball' fullerene scaffolds can interact with many biological targets and inhibit several proteins essential for tumorigeneses. Herein, we focus on the inhibitory properties of fullerene nanomaterials against essential proteins in cancer nanotechnology, as well as the use of dedicated proteins to improve the bioavailability of these promising nanomaterials.

Keywords: fullerene; protein interactions; protein corona; enzyme inhibitors; cancer nanotechnology; nanomedicine

Introduction

Development of the derivatization reactions of fullerenes heralded a new era in medicinal chemistry. Specific functionalization allows greater effectiveness in creating designed fullerene nanomaterials (DFNs) with excellent water solubility, biocompatibility, and potential for applications as nanodelivery systems for drugs.[1] The three main types of modification of buckyballs can be classified as: the formation of hydroxyfullerenes; Bingel–Hirsch cyclopropanations forming mono- and hexakisadducts; and Prato reaction products (i.e., pyrrolidinofullerenes).[2]

Several interactions of DFNs with biomolecules have been described and verified *in vitro* and *in vivo*. For example, the interactions of buckyballs with nucleic acids (DNA and several types of RNA) rely on the formation of complexes between positively charged fullerenes and negatively charged phosphonic groups, and have led to applications in transfection protocols studied in rodent models.[3] The specific interactions of fullerene nanomaterials with proteins were observed in early biomedical studies (using HIV-1 protease,[4] human serum albumin,[5] and lysozymes[6] as the main targets). An extraordinary proof of concept for interactions was the discovery of a specific antifullerene monoclonal antibody.[7] More importantly, it allowed for extended investigation of the cellular fate, and the targets of those nanoparticles (NPs) opened a route to a more direct approach. Interestingly, current reports reveal several diverse applications of fullerene derivatives in nanomedicine, which can be categorized as: (i) photodynamic therapy of cancer/ photoinactivation of microbes; (ii) small molecule/nucleic acid delivery; (iv)

https://doi.org/10.1016/j.drudis.2023.103704

antioxidants/neurodegenerative disease; and (iv) MRI/PET contrast agents.[8–14] However, no drug candidate based on a fullerene scaffold has entered clinical trials, apart from dermatological studies to test the anti-wrinkle property of fullerene-C$_{60}$ in humans.[15]

One of the biggest challenges is to understand the nature of interactions between DFNs and proteins. Complex interactions between fullerenes and proteins can be categorized into three main subgroups: π–π stacking (between fullerene sp^2 carbons and aromatic residues of proteins); van der Waals (between the C$_{60}$ cage and protein surface); and hydrophobic (i.e., nonpolar solvation).[16] Interestingly, the larger structure of C$_{70}$ fullerene enables stronger interactions with more amino acids, which create its binding pocket.[17] Calvaresi and coworkers designed an algorithm that quantitatively investigates the interaction of C$_{60}$ and the surface of each protein from the desired test set from the Protein Database (PDB), which led to identification of new protein targets that could interact with C$_{60}$.[18]

Here, we focus on the interactions between DFNs and proteins from the perspective of cancer nanotechnology. The interactions of fullerene derivatives with DNA/RNA are based on cationic complex formation (i.e., aminofullerenes–anionic nucleic acids) and, hence, are not discussed further here.[11] A more detailed target-related approach to interactions is necessary because many reports have shown only the cytotoxic effect of fullerene nanomaterials. In addition, determining the exact protein targets and mechanisms of action has not yet been described in detail. It has been postulated that the biological effects of DFNs are dependent upon the interaction between fullerene and the protein upon administration and their intratumoral levels (Figure 1). DFNs can be incorporated with proteins (e.g., lysozymes and/or albumin) *ex vivo* before administration to reach the desired solubility. Alternatively, DFNs can interact with serum proteins so that a protein corona is formed around the fullerene NPs. Each mechanism can lead to a different (or identical) interaction with cancer-related proteins. Moreover, direct inhibition of cancer-related enzymes is also possible. These possibilities highlight several questions: how is the mechanism of action of DFNs related to the delivery method? Is it possible to have protein-unbound DFNs in tissues? Which protein-based delivery results in optimal anticancer effects?

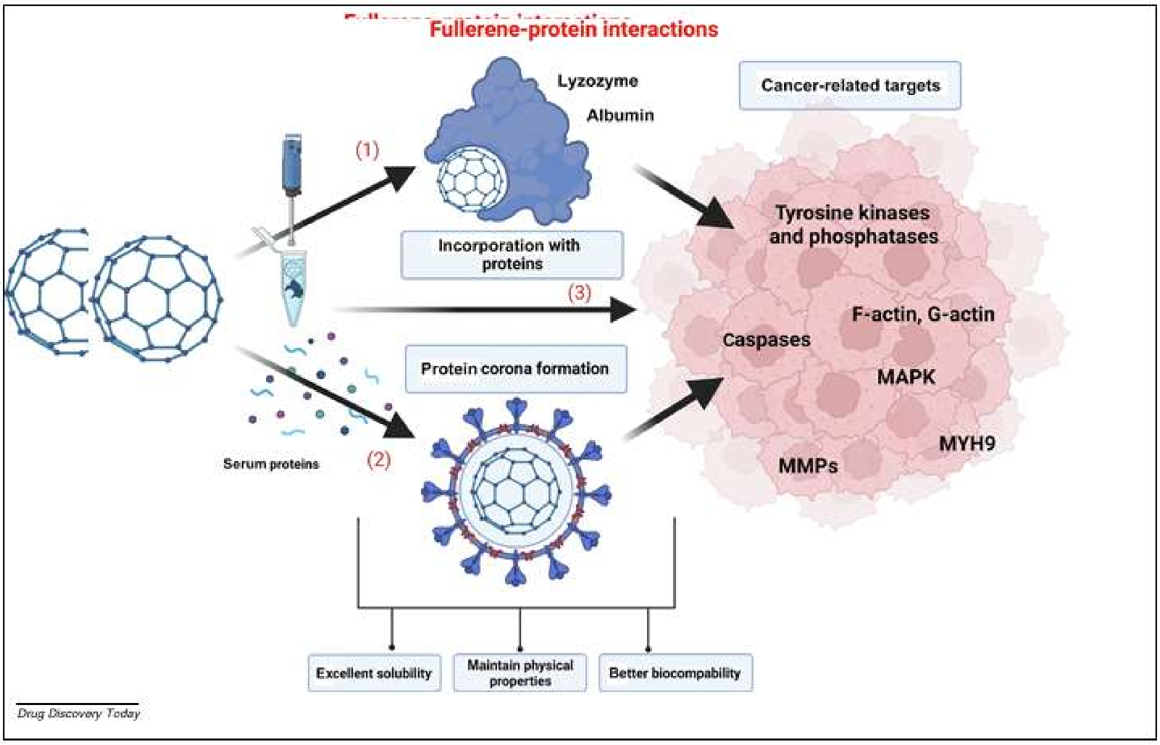

FIGURE 1

Schematic of fullerene–protein interactions. Possible interactions of fullerene nanomaterials with proteins: (1) solubilization through interaction between a designed fullerene nanomaterial (DFN) and protein (lysozyme or albumin); (2) formation of a protein corona adsorbed on the surface of buckyballs as a result of interactions with serum proteins; and (3) direct interaction between the DFN and cancer-related proteins. Created with BioRender (BioRender.com). Abbreviations: MAP, mitogen-activated protein kinase; MMP, matrix metalloproteinase; MYH9, myosin heavy chain 9.

Complexes between fullerenes and proteins

The interactions of fullerenes with peptides can be viewed from the perspective of creating a specific complex between a fullerene cage and a specific fragment of a protein (pockets, gaps, or even crevices), which can bind fullerene derivatives of different sizes and shapes. This can be a controlled or uncontrolled process. In a controlled process, selected proteins (albumin or lysozymes) are used to dissolve the carbon nanomaterial in an aqueous environment, resulting in a fullerene–protein complex with improved pharmacological features. Conversely, if modified fullerene nanomaterials are administered to cell cultures or directly to a living organism, a protein corona (hard or soft) is formed, the composition of which cannot be fully predicted.

Pristine fullerenes are highly hydrophobic in that their bulk form is almost insoluble in biologically relevant environments. Derivatization is not always helpful in overcoming this problem, but it can increase protein-binding properties considerably. Calvaresi and colleagues described a method for improving fullerene solubility by forming complexes with selected proteins (mainly serum albumin and lysozymes) and these complexes were used as a novel type of photosensitizer in anti-cancer therapies.[19] The fullerene scaffold interact with proteins via guest–host interactions whereby the binding pocket of the protein binds the hydrophobic fullerene scaffold via interactions (π–π stacking, hydrophobic, surfactant-like, or charge–π). In general, the advantage of this bioconjugation approach is the monodispersed nature of the formed complex, which prevents deactivation of excited electronic states by surrounding fullerene particles.[16] Their study with lysozymes demonstrated that fullerene particles interacted with lysozymes in a 1:1 ratio, which prevents the formation of undesirable aggregates (Figure 2).[20] Additionally, Figure 3 provides a schematic of the interactions between fullerenes and proteins.

The affinity of a fullerene for a protein is the driving force for most of the activities mentioned above. The formation of a protein corona is not a new concept in NPs but, in the case of fullerenes, cannot be controlled and designed via specific chemical functionalization. In biological environments (e.g., extracellular liquids or blood), NPs make contact with various proteins to form a corona on their surface.[21] Notably, this is not restricted to animal models, and permits investigation in simplified *in vitro* environments. The corona determines the biological activity of the engineered nanomaterial and, thus, influences its associated biological properties. In addition, formation of a protein corona can influence cellular uptake of the DFN. For instance, internalization of the fluorescently labeled fullerene nanomaterial C_{60}serPF was sensitive to various inhibitors, which suggested multiple pathways of uptake (clathrin-mediated endocytosis, caveolae-mediated endocytosis, and micropinocytosis).[22]

In-depth analysis of the literature revealed detailed proteomic studies of protein coronas for various carbon nanomaterials, including carbon nanotubes and graphene oxide.[23,24] However, proteomic data describing the detailed composition of hard and soft protein coronas in the case of fullerene nanomaterials are lacking. Recently, Wu and coworkers described physicochemical studies of the formation of protein coronas on fullerene nanocomplexes, which induced further aggregation of nanocomplexes and demonstrated that the secondary structure of the studied proteins changed after binding to a C_{60}-nanocomplex.[25] Formation of a protein corona on the surface of glycofullerenes also changed the inhibitory properties of fullerene nanomaterials against non-receptor tyrosine kinases.[26]

The development of synthetic methods has led to a significant development in the preparation of water-soluble fullerene nanomaterials, which can be generally classified as hydroxyfullerenes, (methano)-fullerene acids, and aminofullerenes. The structures of most common anti-cancer fullerenes are depicted in Figure 4 and a tabular summary of the molecular targets for each fullerene class is provided in Table 1.

Enzyme inhibition by fullerene nanomaterials

Tyrosine kinases and phosphatases

Tyrosine kinases and phosphatases are often overexpressed in cancer, and enable the progression and survival of cancer cells.[27] Thus, receptor tyrosine kinases have been major targets for cancer specific drugs for more than two decades. However, such a treatment often is associated with tumor resistance and relapse.[28] The first suggestion of direct inhibition of tyro-

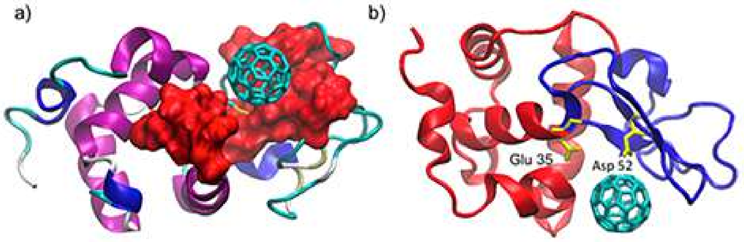

Drug Discovery Today

FIGURE 2

Identification of the C_{60} binding pocket. **(a)** Docking of C_{60} in the lysozyme structure; the red area corresponds to the residues undergoing the largest chemical shift changes according to nuclear magnetic resonance (NMR) measurements; **(b)** lysozyme R (red) and β domains (blue). The active site residues (Glu35 and Asp 52), crucial for the catalytic activity of the enzyme, are shown in yellow. Reproduced, with permission, from[20].

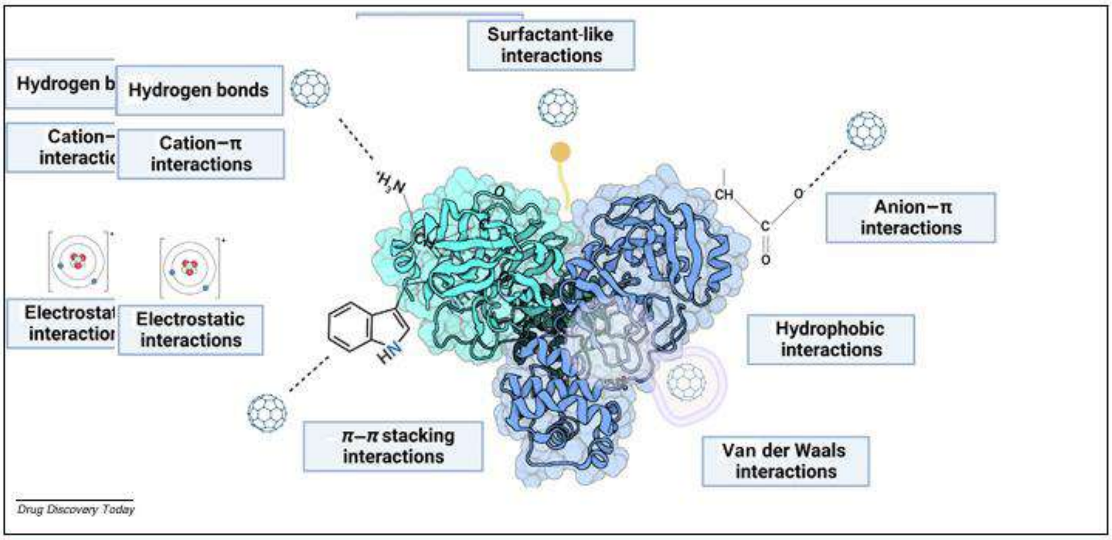

FIGURE 3
Schematic of the different types of interaction between fullerenes and proteins. Created with BioRender (BioRender.com).

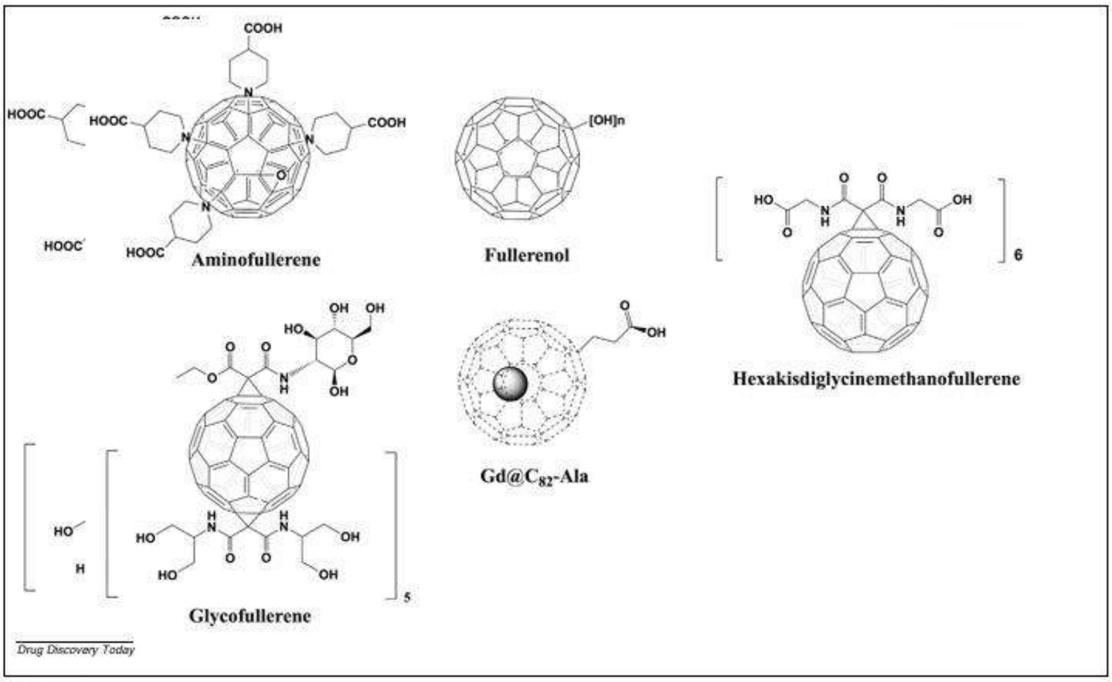

FIGURE 4
Structures of common anti-cancer fullerene nanomaterials.

TABLE 1

Examples of protein targets inhibited by fullerene nanomaterials.

Fullerene class	Therapeutic agent	Target	Refs
Aminofullerenes	C_{70}-EDA	MYH9	36
	Tetra[4-(amino)piperidin-1-yl]C_{60} epoxide TAPC4	Hsp90β, MYH9	37
	$C_{60}(NH_2)_{30}$	CD45	44
	Pyridinium derivatives	Caspase-3/7	39
	Bis-pyridinium fullerene	MEK-ERK	33,34
	1,10,10-tetramethyl [60]fullerenodipyrrolidinium diiodide	Caspase-9	40
Fullerenols	$C_{60}(OH)_{30}$	CD45	44
	$Na_4[C_{60}(OH)_{30}]$	PTP1B	30
	[60/70]fullerenols	F-actin and G-actin	52,54
	Glycofullerenes	FynA, BTK proteins	26
Gadofullerenes	$Gd@C_{82}(OH)_{22}$	MMP-2, MMP-9	50,51
Carboxyfullerenes	Glycine-derived fullerene	BTK proteins	32
	Fulleropyrrolidine derivatives	CD45	30,43
Pristine C_{60}	Oral fullerene tablets	p53, NF-κB, STAT3	47
Miscellaneous	Miscellaneous	p38- and ERK-MAPK, p65 protein	48

sine kinases by DFNs was made in 1998, but relevant research has since been abandoned. In seminal work, Lu and coworkers observed that polyhydroxylated fullerene (considered to be a trapper of free radicals) exerted antiproliferative activity through cytosolic protein kinase.[29] Later, enzymatic studies by Kobzar and colleagues suggested that DFNs be considered a new class of inhibitors of protein tyrosine phosphatases (PTPs).[30] The evaluated compounds were potent inhibitors of cluster of differentiation (CD)45, showing a half-maximal inhibitory concentration in the high-nanomolar range and with inhibitory activity against PTP1B and other phosphatases. A study on Jurkat cells by Ritter and coworkers revealed that inhibition of phosphorylation of protein tyrosine could be one of the photocytotoxic effects of C_{60}.[31] Discovery of selective inhibitors of tyrosine kinases provided several efficacious small molecules for clinical practice and revolutionized the pharmaceutical market. However, inhibitors of these enzymes at the nanometer level have been reported only sporadically. Serda and colleagues described the inhibitory activity of sugar derivatives of glycofullerenes to be similar to that of non-receptor kinase inhibitors that target proto-oncogene tyrosine-protein kinase Fyn (Fyn A) and Bruton's tyrosine kinase (BTK).[26] Interestingly, formation of a fullerene–protein corona was an important factor in inhibition and changing the selectivity of the fullerene. Synthesized DFNs were found to be nontoxic against healthy cells, inducing autophagy and disrupting the redox balance in pancreatic cancer cells. Computational studies on glycine-derived fullerene (HDGF) demonstrated that HDGF could bind the active site of BTK and interact directly with Cys 481, Arg 525, and Tyr 551, residues that are crucial for the activity of BTK.[32] Furthermore, Sumi and collaborators demonstrated that a *bis*-pyridinium fullerene derivative induced the apoptosis of human chronic myelogenous leukemia-derived (K562) cells via downregulation of expression of breakpoint cluster region protein (BCR-ABL) proteins and T315I-mutated BCR-ABL in a reactive oxygen species (ROS)-dependent manner.[33,34]

Myosin heavy chain 9

Myosin heavy chain 9 (MYH9) is a cytoplasmic protein that controls epithelial–mesenchymal transition (EMT) and cell motility. A meta-analysis of large-scale clinical trials showed MYH9 to be overexpressed in various malignancies and to correlate with a poor prognosis. Interestingly, MYH9 can regulate the phenotypes of cancer stem cells, worsening tumor prognosis.[35] In addition, downregulation of MYH9 can be associated with decreased expression of proteins crucial for cancer development, such as Snail, Vimentin, E-Cadherin, SOX, CD44, and OCT4. Recent studies on an ethylenediamine (EDA) derivative of C_{70} have referred to its antineoplastic properties and further impact on metastasis.[36] Those studies demonstrated that C_{70}-EDA binds to the C-terminal part of MYH9. After cell uptake, C_{70}-EDA accumulates in lysosomes and mitochondria, and binds cytoplasmatic MYH9. Blockade of the C terminus prevents protein transport to the cell edge, which indicates that this aminofullerene impacts the cellular distribution of MYH9, but not its protein expression. Huo and coworkers revealed that a synthesized aminofullerene targeted MYH9 and HSP90 directly.[37] They investigated the anti-cancer mechanism of action of their DFN, which revealed that it inhibited expression of cyclin D1, which led to arrest of the cell cycle in G0/G1. The synthesized aminofullerene achieved high efficacy *in vivo*, inhibiting the proliferation and metastasis of melanoma cells.

Caspases

Caspases are specific proteases with a crucial part in programmed cell death. Therefore, modulation/inhibition of their activity could be important for therapy of cancer and neurodegenerative diseases. However, caspases can also regulate cellular proliferation and genomic instability. This broad spectrum of actions highlights the risks of insufficient modulation of caspases and possibility of drug resistance development.[38] Yasuno and colleagues synthesized a series of novel pyridine derivatives of C_{60}-fullerene. Examination of their effect on leukemic (HL60) cells revealed that such derivatives had strong antiproliferative effects, including drug-resistant variants.[39] Interestingly, this DFN activated caspase-3 and caspase-7, causing condensation of nuclear chromatin and inducing apoptosis. Other studies of cationic pyrrolidinium fullerenes reported apoptosis induction resulting from activation of caspase-9 via suppression of protein kinase B in primary effusion lymphoma (PEL) cells.[40]

Tyrosine phosphatase

PTPs have a vital role in the enzymatic dephosphorylation of tyrosine residues in proteins that have undergone phosphorylation, thereby exerting an influence on signaling transduction similar to that of protein tyrosine kinases (PTKs).[41] Tyrosine phosphorylation is controlled by PTPs, which can function as tumor suppressors.[42] Using enzymatic assays, several water-soluble fullerene derivatives have been identified as PTP (e.g., CD45, PTP1B, TC-PTP, and SHP2) inhibitors, and their inhibition mode studied using molecular docking.[30,43,44] Molecular-docking calculations of the pristine C_{60} scaffold and hydroxyfullerene derivatives showed them to be docked into the space between the D1 and D2 domains of CD45.

p38, mitogen-activated protein kinase and nuclear factor-κB pathways

Mitogen-activated protein kinase (MAPK) has important oncogenic roles in a broad spectrum of tumors (including increase of cancer proliferation, survival, and metastasis), and is associated with poor response to treatment. Despite the high impact of MAPK activation, results from clinical trials have not been promising because of the presence of alternative pathways and feedback loops.[45] Nuclear factor (NF-κB) has been identified as one of the links between resistance therapy pathways and anti-cancer treatment failure. Various strategies to inhibit NF-κB have been applied without poor success, possibly beause of multiple upstream and downstream effectors. The hydroxyfullerene $C_{60}(OH)_{22}$ has been reported to influence the metastasis of murine breast cancer (4 T1) cells.[46] This DFN inhibits the EMT by blocking cytokine release and impacting the p38 and MAPK signaling pathways. $C_{60}(OH)_{22}$ blocks the p38 and extracellular signal-regulated kinase (ERK)–MAPK signaling pathways and phosphorylation of p65 protein, which is necessary for activating NF-κB in malignant brown adipose-derived stem cells. However, in normal cells, it influences only the p38–MAPK signaling pathway. Interestingly, oral fullerene tablets can act directly on, and reduce the inflammatory state at, colorectal tumor sites in mice. This newly designed DFN scavenged ROS, prevented mutations of wild-type p53, and inhibited activation of the NF-κB pathway.[47]

Matrix metalloproteinases

Matrix metalloproteinases (MMPs) are zinc-dependent endopeptidases responsible for degradation of extracellular matrix (ECM) proteins (i.e., collagen and laminin). High expression of MMPs in tumor cells aid ECM remodeling and release of membrane-bound growth factors to create the microenvironment for tumorigenesis.[48] Three strategies are popular for MMP activity modulation in cancer: suppression of MMPs translation and/or transcription; inhibition of MMPs enzymatic activity; and blocking of MMPs activation. Despite much research, small molecular and very selective MMP inhibitors are difficult to identify.[49] Gadofullerene ($Gd@C_{82}$) is a type of endohedral DFN that contains a gadolinium atom enclosed in a cage comprising 82 carbon atoms. The hydroxylated version of gadofullerene, $Gd@C_{82}(OH)_{22}$, in the form of NPs has been evaluated as an antineoplastic agent that activates the immune system, remodels the ECM, and influences angiogenesis.[50,51] The main targets for inhibition are MMP-2 and MMP-9 via allosteric modulation exclusively at the ligand site.

F-actin and G-actin proteins

Actin is involved in cytoskeleton formation, cell signaling, cytokinesis, and cell motility. Qin *et al.* reported that fullerenols interfere with the dynamic assembly of actin to inhibit the invasion and migration of cancer cells.[52] One crucial step would be to block the EMT in cancer cells. This transition can be regulated by actin-binding proteins (e.g., CFL1 and SATB1).[53] In a mouse model, a DFN obstructed the spread of breast cancer cells through blood vessels and their ability to establish new colonies in the lung. The reduced capacity of treated cells to adhere to surfaces might result from interference by fullerenols with rearrangement of the actin cytoskeleton and modified intracellular distribution of integrin. This action is achieved as a result of modification of the equilibrium of F-actin and G-actin and remodeling of the actin cytoskeleton.

In addition, hydroxyfullerenes reduced the number of actin fibers as well as the number and length of filopodia. These results show that fullerenes can inhibit the migration and invasiveness of cancer cells by remodeling the actin skeleton of these cells and changing the intracellular distribution of integrins. Other work by Qin *et al.* revealed that fullerenols bind directly to the F-actin surface, thereby inhibiting bundling and relevant cell behaviors.[54]

Receptors

In the case of receptor–fullerene interactions, the amount of published data available is significantly lower compared with that relating to enzymes. In work by Ren *et al.*,[55] possible binding sites and modes of action of fullerene derivatives to β2 adrenergic receptors were presented. However, no results from experiments on isolated receptors or larger systems were provided. The potential interactions of fullerenes with potassium channels have also been explored.[56,57] Interestingly, Kraszewski *et al.* demonstrated that pristine fullerenes or their aggregates can interact with both the extracellular and transmembrane regions of proteins.[57] Furthermore, studies by Calvarezi *et al.* indicated that there might be multiple binding sites for fullerenes on channel proteins.[58] From the perspective of this review, studies of the interaction of fullerenes with toll-like receptors (TLRs) appear to be more significant. Such interactions have been observed for other carbon nanostructures, such as nanotubes, as well as for fullerene derivatives.[59,60] TLRs are a group of receptors associated with innate immunity.[61] Their activity is crucial for nonspecific defense mechanisms against bacterial and viral threats.[62] However, there have been reports suggesting that TLRs and the associated activation of inflammatory states also have a role in tumor development[63] and that blocking them could be an effective anticancer therapeutic approach.[64]

Concluding remarks

Fullerene NPs are biocompatible and have low toxicity. Their stability and easy functionalization make them ideal vehicles for drug delivery. Increasing numbers of studies have shown that DFNs can interact with various proteins. Importantly, these interactions can involve adsorption onto the protein surface, insertion into the hydrophobic pockets of proteins, and modulation of protein conformation. However, crucial features must be established. Theoretical and experimental studies should be undertaken to ascertain the composition of fullerene–protein coronas. Molecular-docking approaches could be used to find other proteins for fullerene solubilization. The mechanism of inhibition must be determined each time an interaction with a specific protein is observed. Regardless of the increasing number of reports on enzyme inhibition, whether a DFN can interact directly with active centers competing with substrates remains unknown. The interaction of fullerenes with proteins is an exciting area of research with potential applications in drug delivery and other fields. However, more research is needed to fully understand the benefits and risks of these interactions, and to develop safe and efficacious fullerene-based technologies.

Declaration of interest

The authors declare no conflict of interest.

Data availability

No data was used for the research described in the article.

Acknowledgment

This work was supported by National Science Centre (Poland) Grant OPUS (UMO-2019/35/B/NZ7/02459) awarded to M.S.

References

1. Kazemzadeh H, Mozafari M. Fullerene-based delivery systems. *Drug Discov Today*. 2019;24:898–905.
2. Acquah SF, Penkova AV, Markelov DA, Semisalova BE, Leonhardt BE, Magi JM. The beautiful molecule: 30 years of C60 and its derivatives. *ECS J Solid State Sci Technol*. 2017;6 M3155.
3. Maeda-Mamiya R et al. In vivo gene delivery by cationic tetraamino fullerene. *Proc Natl Acad Sci U S A*. 2010;107:5339–5344.
4. Sijbesma R et al. Synthesis of a fullerene derivative for the inhibition of HIV enzymes. *J Am Chem Soc*. 1993;115:6510–6512.
5. Belgorodsky B et al. Formation and characterization of stable human serum albumin-tris-malonic acid [C60] fullerene complex. *Bioconjug chem*. 2005;16:1058–1062.
6. Soldà A et al. C 60@ lysozyme: a new photosensitizing agent for photodynamic therapy. *J Mater Chem B*. 2017;5:6608–6615.
7. Braden BC, Goldbaum FA, Chen B-X, Kirschner AN, Wilson SR, Erlanger BF. X-ray crystal structure of an anti-Buckminsterfullerene antibody Fab fragment: biomolecular recognition of C60. *Proc Natl Acad Sci U S A*. 2000;97:12193–12197.
8. Sharma SK, Chiang LY, Hamblin MR. Photodynamic therapy with fullerenes in vivo: reality or a dream? *Nanomedicine (Lond)*. 2011;6:1813–1825.
9. Heredia DA, Durantini AM, Durantini JE, Durantini EN. Fullerene C60 derivatives as antimicrobial photodynamic agents. *J Photochem Photobiol C*. 2022;51 100471.
10. Illescas BM, Pérez-Sánchez A, Mallo A, Martín-Domenech à, Rodríguez-Crespo I, Martín N. Multivalent cationic dendrofullerenes for gene transfer: synthesis and DNA complexation. *J Mater Chem B*. 2020;8:4505–4515.
11. Liu S et al. Fullerene-based nanocomplex assists pulmonary delivery of siRNA for treating metastatic lung cancer. *Nano Today*. 2023;50 101878.
12. Malekzadeh D, Asadi A, Abdolmaleki A, Dehghan G. Neuroprotection of fullerene in improving cognitive–behavioral disruptions and neurobiochemical enzymes activities. *Nanomedicine*. 2023;18:525–539.
13. Han Z, Wu X, Roelle S, Chen C, Schiemann WP, Lu Z-R. Targeted gadofullerene for sensitive magnetic resonance imaging and risk-stratification of breast cancer. *Nat Commun*. 2017;8:692.
14. Zaibaq NG, Pollard AC, Collins MJ, Pisaneschi F, Pagel LJ, Wilson LJ. Evaluation of the biodistribution of serinolamide–derivatized C60 fullerene. *Nanomaterials*. 2020;10:143.
15. Kato S, Taira H, Aoshima H, Saitoh Y, Miwa N. Clinical evaluation of fullerene-C60 dissolved in squalane for anti-wrinkle cosmetics. *J Nanosci Nanotechnol*. 2010;10:6769–6774.
16. Di Giosia M, Zerbetto F, Calvaresi M. Incorporation of molecular nanoparticles inside proteins: the trojan horse approach in theranostics. *Acc Mater Res*. 2021;2:594–605.
17. Marforio TD, Mattioli EJ, Zerbetto F, Calvaresi M. Fullerenes against COVID-19: repurposing C60 and C70 to clog the active site of SARS-CoV-2 protease. *Molecules*. 2022;27:1916.
18. Calvaresi M, Zerbetto F. Baiting proteins with C60. *ACS Nano*. 2010;4:2283–2299.
19. Di Giosia M et al. Proteins as supramolecular hosts for C 60: a true solution of C 60 in water. *Nanoscale*. 2018;10:9908–9916.
20. Calvaresi M et al. C60@ lysozyme: direct observation by nuclear magnetic resonance of a 1: 1 fullerene protein adduct. *ACS Nano*. 2014;8:1871–1877.
21. Corbo C, Molinaro R, Parodi A, Toledano Furman NE, Salvatore F, Tasciotti E. The impact of nanoparticle protein corona on cytotoxicity, immunotoxicity and target drug delivery. *Nanomedicine*. 2016;11:81–100.
22. Raoof M, Mackeyev Y, Cheney MA, Wilson LJ, Curley SA. Internalization of C60 fullerenes into cancer cells with accumulation in the nucleus via the nuclear pore complex. *Biomaterials*. 2012;33:2952–2960.
23. Cai X et al. Characterization of carbon nanotube protein corona by using quantitative proteomics. *Nanomedicine*. 2013;9:583–593.
24. Di Santo R et al. Personalized graphene oxide–protein corona in the human plasma of pancreatic cancer patients. *Front Bioeng Biotechnol*. 2020;8:491.
25. Wu L et al. Plasma protein corona forming upon fullerene nanocomplex: Impact on both counterparts. *Particuology*. 2023;73:26–36.
26. Serda M, Malarz K, Mrozek-Wilczkiewicz A, Wojtyniak R, Musioł R, Curley SA. Glycofullerenes as non-receptor tyrosine kinase inhibitors-towards better nanotherapeutics for pancreatic cancer treatment. *Sci Rep*. 2020;10:1–11.
27. Sivaganesh V et al. Protein tyrosine phosphatases: mechanisms in cancer. *Int J Mol Sci*. 2021;22:12865.
28. Saraon P, Pathmanathan S, Snider J, Lyakisheva A, Wong V, Stagljar I. Receptor tyrosine kinases and cancer: oncogenic mechanisms and therapeutic approaches. *Oncogene*. 2021;40:4079–4093.
29. Lu L-H, Lee Y-T, Chen H-W, Chiang LY, Huang H-C. The possible mechanisms of the antiproliferative effect of fullerenol, polyhydroxylated C60, on vascular smooth muscle cells. *Br J Pharmacol*. 1998;123:1097.
30. Kobzar OL, Trush VV, Tanchuk VY, Zhilenkov AV, Troshin PA, Vovk AI. Fullerene derivatives as a new class of inhibitors of protein tyrosine phosphatases. *Bioorg Med Chem Lett*. 2014;24:3175–3179.
31. Franskevych D et al. Fullerene C 60 penetration into leukemic cells and its photoinduced cytotoxic effects. *Nanoscale Res Lett*. 2017;12:1–9.
32. Malarz K et al. Identification and biological evaluation of a water-soluble fullerene nanomaterial as BTK kinase inhibitor. *Int J Nanomed*. 2023;18:1709–1724.
33. Sumi K et al. A bis-pyridinium fullerene derivative induces apoptosis through the generation of ROS in BCR-ABL-positive leukemia cells. *Eur J Pharmacol*. 2022;916 174714.
34. Sumi K et al. Novel mechanism by a bis-pyridinium fullerene derivative to induce apoptosis by enhancing the MEK-ERK pathway in a reactive oxygen species-independent manner in BCR-ABL-positive chronic myeloid leukemia-derived K562 cells. *Int J Mol Sci*. 2022;23:749.
35. Chen M et al. MYH9 is crucial for stem cell-like properties in non–small cell lung cancer by activating mTOR signaling. *Cell Death Discov*. 2021;7:282.
36. Zhou W et al. Aminated fullerene abrogates cancer cell migration by directly targeting myosin heavy chain 9. *ACS Appl Mater Interfaces*. 2020;12:56862–56873.
37. Huo J et al. Amphiphilic aminated derivatives of [60] fullerene as potent inhibitors of tumor growth and metastasis. *Adv Sci*. 2022;9:2201541.
38. Boice A, Bouchier-Hayes L. Targeting apoptotic caspases in cancer. *Biochim Biophys Acta Mol Cell Res*. 2020;1867 118688.
39. Yasuno T, Ohe T, Ikeda H, Takahashi K, Nakamura S, Mashino T. Synthesis and antitumor activity of novel pyridinium fullerene derivatives. *Int J Nanomed*. 2019;14:6325–6337.
40. Watanabe T et al. Pyrrolidinium fullerene induces apoptosis by activation of procaspase-9 via suppression of Akt in primary effusion lymphoma. *Biochem Biophys Res Commun*. 2014;451:93–100.
41. Song Y, Zhao M, Zhang H, Yu B. Double-edged roles of protein tyrosine phosphatase SHP2 in cancer and its inhibitors in clinical trials. *Pharmacol Ther*. 2022;230 107966.
42. Östman A, Hellberg C, Böhmer FD. Protein-tyrosine phosphatases and cancer. *Nat Rev Cancer*. 2006;6:307–320.
43. Qian M, Shan Y, Guan S, Zhang H, Wang S, Han W. Structural basis of fullerene derivatives as novel potent inhibitors of protein tyrosine phosphatase 1B: insight into the inhibitory mechanism through molecular modeling studies. *J Chem Inf Model*. 2016;56:2024–2034.
44. Yu Y, Sun H, Hou T, Wang S, Li Y. Fullerene derivatives act as inhibitors of leukocyte common antigen based on molecular dynamics simulations. *RSC Adv*. 2018;8:13997–14008.

45. Najafi M, Ahmadi A, Mortezaee K. Extracellular-signal-regulated kinase/mitogen-activated protein kinase signaling as a target for cancer therapy: an updated review. *Cell Biol Int.* 2019;43:1206–1222.
46. Hao T et al. Fullerene mediates proliferation and cardiomyogenic differentiation of adipose-derived stem cells via modulation of MAPK pathway and cardiac protein expression. *Int J Nanomed.* 2016;11:269.
47. Cao X et al. Oral fullerene tablets for colorectal cancer therapy based on modulation of tumor inflammatory microenvironments. *J Mater Chem B.* 2022;10:9457–9465.
48. Mondal S, Adhikari N, Banerjee S, Amin SA, Jha T. Matrix metalloproteinase-9 (MMP-9) and its inhibitors in cancer: a minireview. *Eur J Med Chem.* 2020;194 112260.
49. Alaseem A, Alhazzani K, Dondapati P, Alobid S, Bishayee A, Rathinavelu A. Matrix Metalloproteinases: A challenging paradigm of cancer management. *Semin Cancer Biol.* 2019;56:100–115.
50. Kang S-g et al. Molecular mechanism of pancreatic tumor metastasis inhibition by $Gd@C_{82}(OH)_{22}$ and its implication for de novo design of nanomedicine. *Proc Natl Acad Sci U S A.* 2012;109:15431–15436.
51. Chen SH, Kang S-g, Luo J, Zhou R. Charging nanoparticles: increased binding of Gd@ C 82 (OH) 22 derivatives to human MMP-9. *Nanoscale.* 2018;10:5667–5677.
52. Qin Y et al. Small size fullerenol nanoparticles suppress lung metastasis of breast cancer cell by disrupting actin dynamics. *J Nanobiotechnology.* 2018;16:1–14.
53. Izdebska M, Zielińska W, Grzanka D, Gagat M. The role of actin dynamics and actin-binding proteins expression in epithelial-to-mesenchymal transition and its association with cancer progression and evaluation of possible therapeutic targets. *Biomed Res Int.* 2018;2018. XXX.
54. Gu W et al. Mono-fullerenols modulating cell stiffness by perturbing actin bundling. *Nanoscale.* 2018;10:1750–1758.
55. Ren L, Jing Z, Xia F, Zhang JZ, Li Y. Toxic effect of fullerene and its derivatives upon the transmembrane beta(2)-adrenergic receptors. *Molecules.* 2022;27. XXX.
56. Monticelli L, Barnoud J, Orlowski A, Vattulainen I. Interaction of C70 fullerene with the Kv1.2 potassium channel. *Phys Chem Chem Phys.* 2012;14:12526–12533.
57. Kraszewski S, Tarek M, Treptow W, Ramseyer C. Affinity of C60 neat fullerenes with membrane proteins: a computational study on potassium channels. *ACS Nano.* 2010;4:4158–4164.
58. Calvaresi M, Furini S, Domene C, Bottoni A, Zerbetto F. Blocking the passage: C60 geometrically clogs K(+) channels. *ACS Nano.* 2015;9:4827–4834.
59. Wakimoto T et al. Hydroxylated fullerene: a potential antiinflammatory and antioxidant agent for preventing mouse preterm birth. *Am J Obstet Gynecol.* 2015;213:708.
60. Turabekova M, Rasulev B, Theodore M, Jackman J, Leszczynska D, Leszczynski J. Immunotoxicity of nanoparticles: a computational study suggests that CNTs and C60 fullerenes might be recognized as pathogens by Toll-like receptors. *Nanoscale.* 2014;6:3488–3495.
61. Lim KH, Staudt LM. Toll-like receptor signaling. *Cold Spring Harb Perspect Biol.* 2013;5 a011247.
62. Aluri J, Cooper MA, Schuettpelz LG. Toll-like receptor signaling in the establishment and function of the immune system. *Cells.* 2021;10. XXX.
63. Oblak A, Jerala R. Toll-like receptor 4 activation in cancer progression and therapy. *Clin Dev Immunol.* 2011;2011 609579.
64. Zandi Z et al. The anticancer effect of the TLR4 inhibition using TAK-242 (resatorvid) either as a single agent or in combination with chemotherapy: a novel therapeutic potential for breast cancer. *J Cell Biochem.* 2020;121:1623–1634.

Maciej Serda [1,*], Julia Korzuch [1], Dominik Dreszer [1], Martyna Krzykawska-Serda [2], Robert Musioł [1]

[1] Institute of Chemistry, University of Silesia in Katowice, Katowice, Poland
[2] Faculty of Biochemistry, Biophysics and Biotechnology, Jagiellonian University, Kraków, Poland

* *Corresponding author.*

NANOMEDICINE
2025, VOL. 20, NO. 6, 585–601
https://doi.org/10.1080/17435889.2025.2461985

Taylor & Francis
Taylor & Francis Group

RESEARCH ARTICLE

OPEN ACCESS Check for updates

Aminofullerenes as targeted inhibitors of EGFR: from pancreatic cancer inhibitors to *Drosophila m.* Toxicology

Katarzyna Malarz[a,b], Julia Korzuch[c], Anna Mrozek-Wilczkiewicz[a,b], Magdalena Szubka[b], Patryk Rurka[b], Karol Małota[d], Aitor Herraiz[e], Dominik Dreszer[c], Karina Kocot[c], Fernando Herranz[e], Magdalena Rost-Roszkowska[d], Tao Sun[f], Robert Musioł[c] and Maciej Serda[c]

[a]Department of Systems Biology and Engineering, Silesian University of Technology, Gliwice, Poland; [b]Institute of Physics, Faculty of Science and Technology, University of Silesia in Katowice, Chorzów, Poland; [c]Institute of Chemistry, Faculty of Science and Technology, University of Silesia in Katowice, Katowice, Poland; [d]Institute of Biology, Biotechnology and Environmental Protection, Faculty of Natural Sciences, University of Silesia in Katowice, Katowice, Poland; [e]Instituto de Química Médica, Consejo Superior de Investigaciones Científicas (IQM-CSIC), Madrid, Spain; [f]Key Laboratory of Smart Drug Delivery Ministry of Education, Department of Pharmaceutics, School of Pharmacy, Fudan University, Shanghai, China

ABSTRACT

Aim: Pancreatic ductal adenocarcinoma (PDAC) is recognized as one of the most formidable cancers, largely due to its distinct microenvironment characterized predominantly by extensive desmoplastic stroma. In this study, we synthesized three novel water-soluble fullerene-based nanomaterials targeting EGFR protein.

Methods: The direct amination of fullerene carbon atoms, was followed by conjugation with a modified derivative of the EGFR inhibitor-erlotinib, resulting in the formation of novel water-soluble fullerene derivatives.

Results: Further investigation into PAN02 and AsPC-1 cell lines revealed that these fullerene nanomaterials could induce cell cycle arrest in the G0/G1 phase, corroborated by alterations in the expression levels of the p27 and cyclin E1 proteins. Additionally, mechanisms of cell death were identified as autophagy for C_{60}BUT and C_{70}BUT-ERL, and apoptosis for Gd@C_{82}EDA-ERL nanomaterials.

Conclusions: Crucially, the study uncovered the efficacy of synthesized aminofullerenes in inhibiting the EGFR signaling pathway. The further toxicological studies of Gd@C_{82}EDA-ERL fullerene on *Drosophila melanogaster*, underscored its potential for theranostic applications.

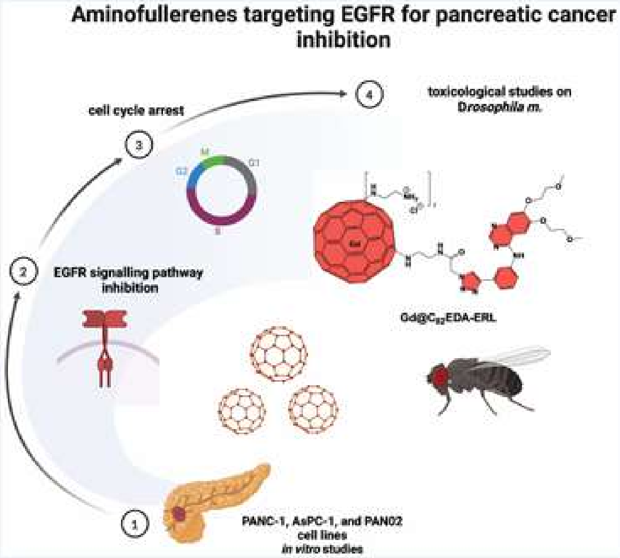

ARTICLE HISTORY
Received 28 August 2024
Accepted 30 January 2025

KEYWORDS
Fullerene; aminofullerene; pancreatic cancer; EGFR inhibitors; drosophila; cancer nanotechnology

CONTACT Maciej Serda maciej.serda@us.edu.pl Institute of Chemistry, Faculty of Science and Technology, University of Silesia in Katowice, 9 Szkolna Street, Katowice 40-006, Poland; Katarzyna Malarz katarzyna.malarz@us.edu.pl Department of Systems Biology and Engineering, Silesian University of Technology, Akademicka 16, Gliwice 44-100, Poland

Supplemental data for this article can be accessed online at https://doi.org/10.1080/17435889.2025.2461985.

1. Background

Pancreatic ductal adenocarcinoma (PDA) is a major contributor to cancer-related deaths worldwide, with a significant number of cases being locally advanced and thus not amenable to surgical excision [1,2]. This malignancy is notoriously resistant to a plethora of therapeutic modalities, including chemotherapy, radiotherapy, and targeted pharmaceuticals [3]. Its resistance can be attributed to factors such as an intricate stromal environment, diminished immunogenicity, and epigenetic modifications of the parenchymal cells [4]. Conventionally, the clinical management of pancreatic cancer involves the surgical excision of the tumor, supplemented with chemoradiotherapy [5]. Chemotherapy frequently involves the usage of multiple small molecules and natural products, such as gemcitabine, paclitaxel, cisplatin, and the epidermal growth factor receptor (EGFR) inhibitor erlotinib [6].

The EGFR belongs to the tyrosine receptor kinase family and plays an instrumental role in orchestrating a myriad of cellular activities [7]. The overexpression of EGFR is a recurrent phenomenon in pancreatic cancer, correlating with the malignancy's aggressive disposition and its resistance to treatment. Erlotinib is a first-generation EGFR kinase inhibitor that was approved by the Food and Drug Administration (FDA) in 2016 for pancreatic cancer treatment. It works by binding to the ATP-binding site of the EGFR kinase domain, thus preventing ATP association [8]. By inhibiting EGFR kinase activity, erlotinib disrupts the signaling networks that promote the growth and survival of cancer cells, thereby potentially slowing down the progression of pancreatic cancer [9].

Interestingly, a range of nanotherapeutic formulations have been specifically engineered for the management of PDA. In recent years, the FDA has approved two notable formulations. In 2013, Abraxane, an albumin-bound nanoformulation of paclitaxel, was approved for use alongside gemcitabine. In 2015, a liposomal version of irinotecan co-administered with 5-fluorouracil was approved for patients with metastatic PDA who exhibit limited responsiveness to gemcitabine [10,11]. Carbon nanomaterials (CNs) have garnered significant interest within the scientific community because of their exceptional optical, photothermal, and mechanical properties, alongside a versatile chemistry for covalent functionalization. The inherent hydrophobic nature of these carbonaceous nanomaterials enables them to effectively load drugs through hydrophobic interactions or π–π stacking, establishing them as efficient platforms for drug delivery [12,13]. The biocompatibility of these CNs has been enhanced through synthetic derivatization, either *via* covalent or non-covalent modifications [14]. Covalent modifications of fullerenes typically involve the addition of hydroxyl, carboxyl, or amino groups to their surface, such as in Bingel-Hirsch/Prato reactions for controlled synthesis of biologically active fullerenes [15–17].

Gadolinium-containing endohedral fullerenes have shown promising applications in various cancer therapies. They act as specific inhibitors of breast cancer stem cells and interact with several matrix metalloproteinases in human pancreatic cancer xenografts [18,19]. Additionally, the immune-related pathways through which $Gd@C_{82}(OH)_{22}$ nanoparticles impede tumor growth not only facilitate the production of *Th1* cytokine but also reduce *Th2* cytokine levels while preserving the integrity of B cells and T cells [20]. The MRI-contrast agent properties of water-soluble gadofullerenes have been extensively studied by the groups of Wilson and Wang [21,22]. The published longitudinal proton relativities for these gadofullerenes were remarkably high and varied based on their chemical modification and fullerene cage structure [23]. Several investigations consistently demonstrated that polyhydroxylated $Gd@C_{82}$ ($Gd@C_{82}(OH)_x$) exhibits significantly elevated r_1 relaxivity levels. Specifically, at magnetic field strengths of 0.5 T, the observed enhancement is in the range of 12–14 times, while at 7.0 T, it reaches six to eight times greater compared to the commercially available Magnevist, as documented in the relevant literature [24,25]. Aminated fullerene derivatives exhibit substantial potential in cancer nanotechnology, largely attributed to their facile and robust synthetic pathways mainly *via* direct (photo)amination, as well as their convenient purification by membrane dialysis to yield water-soluble cationic buckyballs. Their ability to undergo further bioconjugation with carboxylated small-molecular ligands, antibodies, or negatively charged proteins underscores their promise for translational biomedical applications [26,27]. For example, in a recent study, Chunru Wang and colleagues identified myosin heavy chain 9 (MYH9) as a critical molecular target of the aminated fullerene derivative C_{70}EDA and investigated its inhibitory mechanism [28]. The C_{70}EDA fullerene binds to the C-terminal region of MYH9, inducing MYH9 translocation from the cytoplasm to the cellular periphery.

Our previous studies have shown that *D*-glucosamine derivatives of [60]fullerenes had phototoxic effects on pancreatic cancer cells and accumulated mostly in the nucleus of pancreatic stellate cells [29]. Furthermore, our preceding research showed that the studied glycofullerenes were effective inhibitors of non-receptor tyrosine kinases (Fyn A and BTK) with IC_{50} values in the lower micromolar range. Additionally, we have established that the formation of a protein corona on the surface of [60]fullerene derivatives significantly alter their functional profile, thereby refining the specificity of these CNs toward Fyn A and BTK kinases. Utilizing our knowledge of fullerene and gadofullerene scaffolds in relation to their interactions with pancreatic cancer, we developed a series of water-soluble aminofullerenes based on C_{60}, C_{70}, and $Gd@C_{82}$ substrates. These aminofullerenes incorporate ethylenediamine (EDA) and 1,4-diaminobutane (BUT) fragments by direct amination of fullerene core (formation of Csp^2-N bonds). However, some of the obtained derivatives were not stable in water, or their further conjugation with erlotinib derivatives was unsuccessful. We believed that the synthesized aminofullerenes were ideal candidates for further functionalization with small molecules that target pancreatic cancer. Therefore, we modified the erlotinib molecule by performing copper-catalyzed 1,3-dipolar cycloaddition with corresponding azidoacetic acid to form a triazole derivative of erlotinib with a carboxyl function (called here ERL-COOH).

In this report, we examined the effectiveness of two nanoconjugates of fullerenes with erlotinib derivative (referred to as C_{70}BUT-ERL and $Gd@C_{82}$EDA-ERL) and one aminofullerene (referred to as C_{60}BUT) in combating cancer. We focused on

Article highlights

- The successful synthesis of three aminofullerenes was demonstreted (C_{60}BUT, C_{70}BUT, and Gd@C_{82}EDA) as well as their two nanoconjugates (C_{70}BUT-ERL, Gd@C_{82}EDA-ERL). They were obtained *via* straightforward direct amination of buckyball cores, followed by further nanonocjugation and structurally confirmed by multiple spectroscopy techniques (FT-IR, UV-Vis, NMR and XPS).
- It was revealed that C_{60}BUT exhibits significant anti-cancer efficacy against several pancreatic cancer cell lines (PANC-1, AsPC-1, PAN02), with IC_{50} values comparable to, or better than, the FDA-approved inhibitor erlotinib.
- The unique dispersion behaviors of these novel aminofullerenes in aqueous solutions should be higlighted, forming well-defined nanoscale aggregates suitable for biomedical applications.
- It was shown that the fullerene derivatives arrest the cell cycle in G0/G1 phase in both PAN02 and AsPC-1 cell lines, driven by elevated p27 and reduced cyclin E1 expression.
- It was demonstrated that C_{60}BUT and C_{70}BUT-ERL favor autophagy induction, while Gd@C_{82}EDA-ERL triggers apoptosis, underscoring distinct modes of cell death.
- The suppression of EGFR signaling (p-EGFR, p-Akt, PI3K, Ras) in pancreatic cancer cells was confirmed, providing a mechanistic explanation for the robust anticancer effects.
- The safety profile of Gd@C_{82}EDA-ERL was verified *in vivo* using the *Drosophila melanogaster* model, showing no detectable toxicity or detrimental ultrastructural changes in midgut epithelium.
- The translational potential of gadofullerene-based theranostics should be highlighted, demonstrating favorable MRI relaxivity while simultaneously carrying biologically active compounds.

the high anticancer activity of C_{60}BUT on pancreatic cancer cell lines, including PANC-1, AsPC-1, and PAN02. Moreover, we tested the toxicological properties of the gadofullerene nanoconjugate Gd@C_{82}EDA-ERL using the *Drosophila melanogaster* model and found it to be nontoxic while also revealing information about its tissue localization. The roadmap for this study is given in Figure 1.

2. Experimental

2.1. Materials

All chemicals used were of reagent-grade quality or better. Solvents were dried following standard literature procedures. The following reagents were used as received: C_{60}, C_{70} (both 99.5+%, SES Research, USA), Gd@C_{82} (Funano, P.R. China), erlotinib hydrochloride, ethylenediamine and 1,4-diaminobutane (Sigma Aldrich, Germany), toluene (Chempur, Poland), methanol (Chempur, Poland), and concentrated hydrogen chloride (Avantor, Poland). All solvents were prepared according to the corresponding literature procedures, which involved treating them with a dehydrating agent, distilling them, and then using them immediately. Triton X-100 was from Avantor Performance Materials Poland S.A. (Gliwice, Poland). The stock solution of yttrium (1000 µg/mL) was purchased from Merck Millipore (Darmstadt, Germany). The solution of silicon in isopropanol was purchased from SERVA (Heidelberg, Germany). High-purity water from the Milli-Q system (Millipore, Molsheim, France) was used for sample preparation and reagent dilutions. The final dialysis purification of the water-soluble fullerene nanomaterials was performed on MicrosepTM (Pall Corporation, USA) centrifugal membranes with molecular cutoffs of 1 and 3 kDa.

2.2. Characterizations

Nuclear magnetic resonance (NMR) spectra were obtained using a Bruker Avance III 500 MHz NMR spectrometer with tetramethylsilane as the internal standard. The *CHNS* elemental analysis was performed with a FlashSmart thermal analyzer (Thermo Fisher Scientific). Attenuated total reflectance Fourier transform infrared (ATR-FT-IR) measurements were collected using a JASCO FT/IR-4600 spectrophotometer equipped with a JASCO ATR PRO ONE kit. The fullerene powders were measured using an ATR ZnSe accessory in the range 700–4000 cm^{-1}. The spectra were recorded using 64

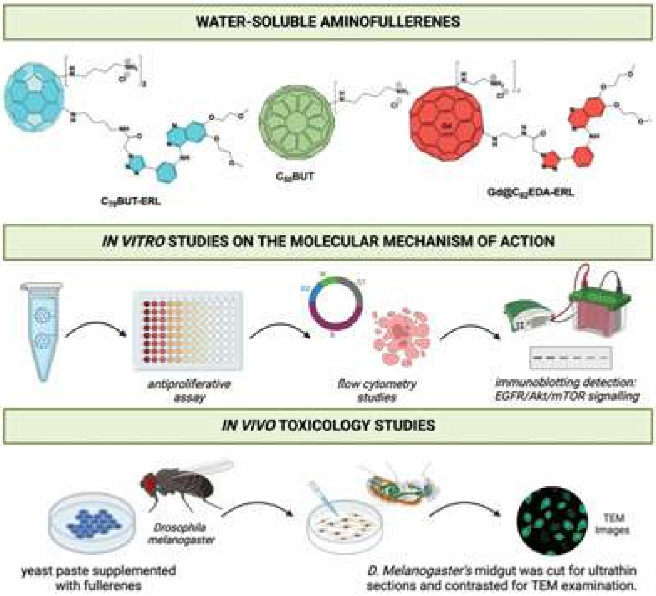

Figure 1. Roadmap of the current study: (A) synthesis of fullerene nanomaterials and their *in vitro* activity with mechanism of action (EGFR signaling inhibition) and *in vivo* toxicology studies. Created with Biorender^{R}.

accumulations at a spectral resolution of 1 cm^{-1}. The dynamic light scattering of the fullerene nanomaterials was measured using a Zetasizer Nano Instrument (Malvern Panalytical Ltd., UK). The high-resolution mass spectrometry was carried out on the ESI-Q-TOF maXis impact (Bruker Daltonics Inc, USA). The X-ray photoelectron spectroscopy (XPS) spectra were collected on a PHI5700/660 Physical Electronics Photoelectron Spectrometer (Physical Electronics PHI 5700, Chanhassen, MN, USA) equipped with monochromatic Al Kα X-ray radiation (1486.6 eV). The energy of the electrons was measured with a hemispherical analyzer and a resolution of approximately 0.3 eV. The measurements of photoelectron emission were taken from a surface area with a diameter of 800 µm and at a take-off angle of 45°. The spectra were calibrated to adventitious carbon located at 284.9 eV because the sample was exposed to air. Quantification of XPS spectra utilizing peak area and peak height sensitivity factor used the Multipak Physical Electronics application (v.9.6.0.1, ULVAC PHI, Chigasaki, Japan). The XPS core level spectra were fitted with the Doniach-Sunjic method. The microstructural observations and the micro-compositional analyses were conducted using the JEOL-7600F scanning electron microscope (SEM) equipped with the Oxford X-ray energy dispersive spectroscopy (EDS) microprobe. The microprobe operated at 15 kV accelerating voltage and 1 nA probe current. High-resolution SEM images were obtained using an extra-lens Everhart-Thornley secondary electron detector. The pictures were acquired at an accelerating voltage of 5–10 kV and probe current of 200 pA. Total reflection X-ray fluorescence (TXRF) was applied to determine Gd concentration in Gd@C$_{82}$EDA and Gd@C$_{82}$EDA-ERL solutions. TXRF measurements were conducted utilizing the S4 T-STAR spectrometer, manufactured by Bruker AXS Microanalysis (Berlin, Germany). The instrument is equipped with a 50 W Mo target X-ray tube, a multilayer monochromator, and an SSD detector. The X-ray tube operated at 50 kV and 1000 µA. The measurements were carried out in an ambient air atmosphere, with a counting time of 1000 s, with Y utilized as an internal standard. The relaxometric properties of Gd@C$_{82}$EDA and Gd@C$_{82}$EDA-ERL were assessed by measuring longitudinal and transverse relaxation times. This evaluation was conducted using a Magritek Spisolve 60 MHz benchtop spectrometer device with a static magnetic field of 1 T. Each sample was diluted in Milli-Q water and measured at four different concentrations (between 0.1 and 1 mm). The r_1 and r_2 values (factors used to evaluate the efficiency of a sample as a contrast agent) were obtained as the slope resulting from the linear fit of the 1/T1/2 (s-1) relaxation time versus the metal concentration (mM). Cryo-EM was conducted on copper grids (Lacey carbon, EMS LC200-Cu) which were plasma-cleaned (Gatan Solarus, USA) for 30 s. Then, 3.5 µL of fullerene solution in DI water (c = 0.5 mg/mL) was applied to the grid, blotted for 2 s, and plunge-frozen using the Thermo Scientific Vitrobot (Mark IV). The grids were stored in liquid nitrogen until imaging, then clipped in autogrids (Thermo Scientific, USA) and placed into the cassette for loading onto the Titan Krios 3Gi (Thermo Scientific, USA). The grids were imaged using EPU (Thermo Scientific, USA).

2.3. Synthesis

The extended spectral data of synthesized small molecules and fullerene nanomaterials can be found in Supporting Information.

2.3.1. Synthesis of 2-azidoacetic acid

We modified the procedure of Dyke for an experimental process [30]. First, we dissolved 1.76 g (12.7 mmol) of 2-bromoacetic acid in 20 mL of distilled water and cooled it to 0 °C. Then, we dissolved 1.46 g (22.5 mmol) of sodium azide (NaN_3) in 5 mL of water and added it dropwise over 10 min. Following a 15-min interval, the ice bath was removed, and the resulting reaction mixture was continuously stirred at ambient temperature for 12 hours. The reaction mixture was acidified gradually using a 2 M HCl solution until the pH level reached 1. Then, the resulting aqueous solution underwent extraction with Et_2O which was performed thrice with 40 mL each time. The combined organic layers were subsequently treated with magnesium sulfate ($MgSO_4$) and filtrated. The final product was obtained as a colorless oil, with a yield of 45% (0.65 g).

2.3.2. Synthesis of (2-(4-(3-((6,7-bis(2-methoxyethoxy)quinazolin-4-yl)amino)phenyl)-1 h–1,2,3-triazol-1-yl)acetic acid, ERL-COOH)

To prepare the desired product, 400 mg (1.02 mol) of erlotinib hydrochloride and 205 mg (1.78 mol) of 2-azidoacetic acid were dissolved in 20 mL of water with the addition of 5 mL of *tert*-butanol. After that, 25.4 mg (101.67 mmol) of copper sulfate and 20.14 mg (101.67 mmol) of sodium ascorbate were added to the solution. The resulting mixture was heated to 60 °C and stirred for 48 h. The reaction was considered complete when the erlotinib signal was no longer observed on the TLC plate. The solvent was then lyophilized, and the resulting yellow powder was purified on the column chromatography (final product $R_f = 0.16$, DCM : MeOH, 50:1, *v/v*). The white solid of the final product was collected with a 91% yield (462 mg, with a melting point of 218 °C).

2.3.3. Synthesis of water-soluble aminofullerenes Gd@C$_{82}$(EDA)$_8$

30 mg (26.29 µmol) of Gd@C$_{82}$ was dissolved in 20 mL of EDA (0.3 mol). The solution was then suspended in an ultrasonic bath for 15 min and then left to stir for 48 h at room temperature. The amine was evaporated, and the remaining brown solid was collected. To improve the solubility of aminofullerene, the transformation to hydrochloride was performed as follows: Gd@C$_{82}$(EDA)$_8$ was dissolved in 10 mL of water and 3 mL of 1 M HCl. After 1 h of stirring at room temperature, the solvent was evaporated. The product was dissolved in deionized water, purified using centrifugal membranes with 1k cutoffs, and lyophilized. The chemical composition was confirmed through elemental analysis and spectroscopic characterization (FT-IR, XPS, TXRF).

2.3.4. C_{60}(BUT)$_3$ and C_{70}(BUT)$_3$

30 mg of pristine C_{60} (41.76 µmol) or C_{70} (35.71 µmol) was dissolved in 10 mL of BUT (99.5 mmol) and suspended using an ultrasonic bath for 15 min. The solution was then left to stir at room temperature for 48 h. The amine was evaporated, and the remaining brown solid was collected. To increase the solubility, the aminofullerene was transformed into hydrochloride. This was done by dissolving the obtained aminofullerene in 10 mL of water and 3 mL of 1 M HCl. After stirring at

room temperature for 1 h, the solvent was evaporated. The product was then dissolved in deionized water and purified using centrifugal membranes with 1K cutoffs.

2.3.5. General procedure for conjugation of aminofullerenes with ERL-COOH

Total of 30 mg of the desired aminofullerene (-NH_2 form) Gd@C_{82}EDA (24.78 µmol) or C_{70}BUT (27.25 µmol) were dissolved in 20 mL of water and 5 mL of DMSO in the presence of NHS (one equivalent) and EDCI (one equivalent). Then, one equivalent of ERL-COOH was added, and the mixture was stirred at room temperature for 24 h. After 24 h, the solution was purified using centrifugal membranes with 1K cutoffs to remove any unreacted small molecular impurities. The aminofullerene synthesis was followed by hydrochloride formation to enhance the solubility in water and medium.

2.4. Determination of Gd concentration using the TXRF technique

To conduct TXRF analysis, we took 50 µL of previously sonicated suspensions of Gd@C_{82}EDA or Gd@C_{82}EDA-ERL and placed them inside a 2-mL Eppendorf tube. We then added 50 µL of 10 mg L^{-1} Y solution (internal standard), and 400 µL of 1% Triton-X-100 (surface active agent). The sample was then vortexed for 5 min and sonicated for 15 min. This ensured that the sample was evenly dispersed and homogeneous. Finally, 10 µL of suspension was carefully pipetted onto a siliconized quartz reflector and dried at 80 °C using a heating plate. The obtained results are summarized in Table S2 and Figure S14 shows the TXRF spectrum of the measured gadofullerenes.

2.5. Cell culture conditions

The PAN02 murine pancreatic carcinoma cell line was obtained from NCI-Frederick Cancer Research Facility, while the AsPC-1 human pancreas adenocarcinoma cell line and PANC-1 human pancreas ductal adenocarcinoma cell line were obtained from Sigma Aldrich. The NHDF normal human dermal fibroblast cell line was acquired from PromoCell. The PANC-1 cells were cultured in Dulbecco's modified Eagle's medium (DMEM) which was supplemented with 10% heat-inactivated fetal bovine serum (FBS) from Merck. The DMEM for the NHDF was supplemented with 15% non-inactivated FBS. PAN02 and AsPC-1 cells were cultured in Roswell Park Memorial Institute (RPMI) 1640 which was supplemented with 10% heat-inactivated FBS from Merck. Each complete medium included a combination of two antibiotics, penicillin, and streptomycin (1% *v/v*; Gibco). All the cell lines were maintained at 37 °C in a 5% CO_2 humidified atmosphere.

2.6. Cytotoxicity measurements

The cells were seeded in 96-well Nunc plates with a density of 5,000 cells/well (cancer cells) or 4,000 cells/well (normal cells), and incubated under standard conditions at 37° C for 24 h. The cells were then incubated for 72 h with varying concentrations of the tested compounds. The next step was adding DMEM without phenol red, along with CellTiter 96®AQueous One Solution-MTS (Promega), to each well, and incubating for either 1 or 3 h at 37 °C. The samples' optical densities were then measured at 490 nm using a multi-plate reader (Varioskan LUX, Thermo Scientific). The results obtained were compared to the control and calculated as inhibitory concentration (IC_{50}) values using GraphPad Prism 9. Each specific compound underwent triplicate testing in a single experiment, and each experiment was replicated three or four times.

2.7. Cell cycle assay

The PAN02 and AsPC-1 cells were seeded in a 3 cm Petri dish at a density of 200,000 cells/dish and incubated at a temperature of 37 °C. After 24 h, we replaced the medium and exposed each cell line to C_{60}BUT, C_{70}BUT-ERL, and Gd@C_{82}EDA-ERL nanomaterials. After another 24 h of incubation, we conducted assays employing the Muse™ Cell Cycle Kit (Millipore) following the supplier's instructions. In brief, the cells were harvested, cold PBS-washed, and centrifuged. The cells were then fixed in ice-cold 70% ethanol and stored at −20 °C overnight and the subsequent day involved washing the cells with cold PBS, centrifuging, and resuspending them in Muse™ Cell Cycle Reagent. After a 30 min incubation at room temperature in the dark, the samples were analyzed for cellular subpopulation values across different cell cycle phases using a Muse Cell Analyzer (Millipore). This experimental protocol was repeated a minimum of three times for reliable results.

2.8. Apoptosis assay

The cells were treated the same as mentioned in the section above. After 48 h of treatment, assays were conducted using the FITC Annexin V Apoptosis Detection kit with 7-AAD (Bio-Legend), following the manufacturer's instructions. The cells were harvested, PBS-washed, and centrifuged. Next, the cells were reconstituted in Annexin V Binding Buffer and incubated for 15 min at room temperature in the dark with FITC Annexin V and 7-AAD Viability Staining Solution. Following staining, the samples were assessed for live, early, and late apoptotic cells using the Muse Cell Analyzer. Each experiment was replicated a minimum of three times to obtain reliable outcomes.

2.9. Western blot measurements

The PAN02 and AsPC-1 cells were seeded in 3 cm Petri dishes at a density of 500,000 cells per well and incubated under standard conditions for 24 h. Next, the cells were incubated with freshly prepared solutions of tested C_{60}BUT, C_{70}BUT-ERL, and Gd@C_{82}EDA-ERL nanomaterials for one day. After that, the pancreatic cells were detached by trypsinization, collected into Eppendorf tubes, and centrifuged. The cell pellets were resuspended in a RIPA buffer containing Halt Protease Inhibitor Cocktail, Halt Phosphatase Inhibitor Cocktail along with 0.5 M EDTA (all from Thermo Scientific) and lysed on ice for 20 min. The obtained lysates were sonicated and centrifuged for 10 min at 4 °C. The supernatants were transferred to new tubes and used in further studies. To determine the protein concentration, a Micro BCA™ Protein Assay Kit (Thermo Scientific) was used as per the manufacturer's instructions. 20 µg of the proteins were electrophoresed on SDS-Page gels and transferred onto nitrocellulose membranes. The membranes were blocked in 5% nonfat milk prepared in TTBS (containing 0.1% Tween-20) for 1 h. After this time, the membranes were incubated with specific primary antibodies at 1:1000 dilution. The following primary antibodies were used: EGFR, phospho-EGFR (Tyr1068), mTOR, phospho-mTOR (Ser2448), Akt, phospho-Akt (Ser473), IDH1, PTEN, PI3K p85, Ras, Src, $p27^{Kip1}$, cyclin E1, PARP, GAPDH, and vinculin. The incubation was carried out overnight at 4 °C. The following day, the membranes were washed in TTBS and incubated with horseradish peroxidase (HRP)-conjugated secondary antibodies for 1 h at room temperature. Then, the membranes were washed in TTBS and incubated with a SuperSignal West Pico Chemiluminescent Substrate (Thermo Scientific). The chemiluminescence signals were captured using a ChemiDoc® XRS+ System (BioRad). The experiments were repeated at least four to five times and the densitometric analysis was performed using ImageJ software (Wayne Rasband, National Institutes of Health, USA).

2.10. Transmission electron microscopy and in vivo toxicology

Ten adult specimens of *D. melanogaster* of variation y, w (I); 43.4, y +, (II) obtained from the Vienna Resource Center were cultured in the laboratories of the University of Silesia in Katowice using Nutri-Fly® Grape Agar. The animals were divided into two groups: FC, the control group, which were cultured under laboratory conditions and fed ad libitum with yeast paste devoid of gadofullerenes for one week, and F1W, which were cultured under laboratory conditions and fed ad libitum with yeast paste supplemented with gadofullerene Gd@C_{82}EDA-ERL (c = 1 mg/mL) for one week. The precise laboratory culture of *D. melanogaster* was previously described in our paper [31]. The total number of adult specimens (both males and females) was 10. The insects were anesthetized with CO_2. The midgut (middle region of the digestive system) after isolation, was fixed, washed, dehydrated, and embedded in epoxy resin (Epoxy Embedding Medium Kit; Sigma) according to standard protocols [32,33]. Ultrathin sections were cut using Leica EM UC7 RT (70 nm) and, after contrasting, were examined using a Hitachi H500 transmission electron microscope at 75 kV.

3. Results

3.1. Synthesis and characterization

Three aminofullerenes, C_{60}BUT, C_{70}BUT, and Gd@C_{82}EDA, were synthesized through a straightforward liquid-liquid reaction at room temperature. Their molecular structure was characterized using FT-IR, UV-VIS, ^{13}C-NMR, and XPS. The number of amines attached to fullerene cores was estimated using elemental analysis. For 1,4-diaminebutane fullerene derivatives, the nitrogen-to-carbon ratio (*N/C*) was used to calculate the amount of added amine units as three. For Gd@C_{82}, the calculation confirmed the formation of octakis adduct with EDA Gd@C_{82}(EDA)$_8$ (Table S1, Supporting Information). The ^{13}C-NMR spectra of two BUT derivatives of fullerenes showed four characteristic signals of alkyl chains around 70 and 20 ppm as well as one weak signal of [60]fullerene core around 146 ppm and two signals of [70]fullerene core around 150 and 147 ppm, respectively (Figures S4-S5, Supporting Information). The FT-IR analysis of the synthesized aminofullerenes (C_{60}BUT, C_{70}BUT, and Gd@C_{82}EDA) showed notable absorption bands between 1750 to 1400 cm^{-1} corresponding to N – H bending vibrations of primary amines (Figures 2(d–f)). Moreover, the vibrational bands of N-H (3500–3800 cm^{-1}) and C-H (2800–3000 cm^{-1}) of the carbon cage were observed for all water-soluble fullerene derivatives. If we consider the obtained aminofullerenes as primary amine hydrochlorides with terminal -NH_3 units, they all presented broad intense -NH_3^+ stretching envelopes. In general, for primary amine salts, this envelope falls from in the spectrum region between 3300 to 2800 cm^{-1}. Additionally, C – N stretch signals presented between 1250–1020 cm^{-1} were characteristic of aliphatic amines and were observed in all synthesized aminofullerenes.

The synthesized erlotinib carboxylic acid (ERL-COOH)) was examined further using ^{13}C-NMR spectroscopy which revealed the absence of two characteristic triple bond signals (around 82 and 77 ppm) and the formation of a triazole ring (two signals around 146 and 132 ppm) with an additional strong signal of carboxylic acid around 170 ppm (Figure S2). The high-resolution mass spectrometry confirmed the presence of a molecular peak of ERL-COOH at 493.1829 Da in negative polarization [M-H]- (calculated mass: 493.1841 Da).

In the analysis of nanoconjugation products by FT-IR spectroscopy, we observed the characteristic signals of secondary amide functional groups, which were only present in the expected products. For the compound C_{70}EDA-ERL, we observed the C=O stretch of our secondary amide (Figure 2(e)) at 1641 cm^{-1} close to the signals of N – H bending vibrations of primary amines (1635 cm^{-1}). The companion peak shown in Figure 2(e) around 1521 cm^{-1} was associated with the in-plane N-H bend of the secondary amide group, which is normally found from 1570 to 1510 cm^{-1}. Additionally, for compound Gd@C_{82}EDA-ERL, we observed strong and intense bands at 1700 cm^{-1} as stretching vibrations of the carbonyl group present in the secondary amide, whereas a band near 1530 cm^{-1} is characteristic of the in-plane N–H bends of the secondary amide group (Figure 2(f)). Unfortunately, the presence of a triazole ring (weak signals around 3100 cm^{-1}) could not be confirmed by an analysis of the infrared spectrum of synthesized nanoconjugates because of the dominating signals of N-H and C-H functional groups in that region. Furthermore, the unequivocal evidence for the attachment of the erlotinib derivative to selected aminofullerenes was the comparison of their electronic spectra. Unmodified fullerene nanomaterials possess a characteristic UV-VIS spectrum with exponential decay and without a distinct absorption maximum (Figures 2(a)). In the case of both nanoconjugates, signals at 245 and 320 nm corresponding to the erlotinib fragment can be observed (Figure 2(b,c)).

High-resolution XPS was used to further investigate the electronic structure of C_{60}BUT, C_{70}BUT-ERL, and Gd@C_{82}EDA-

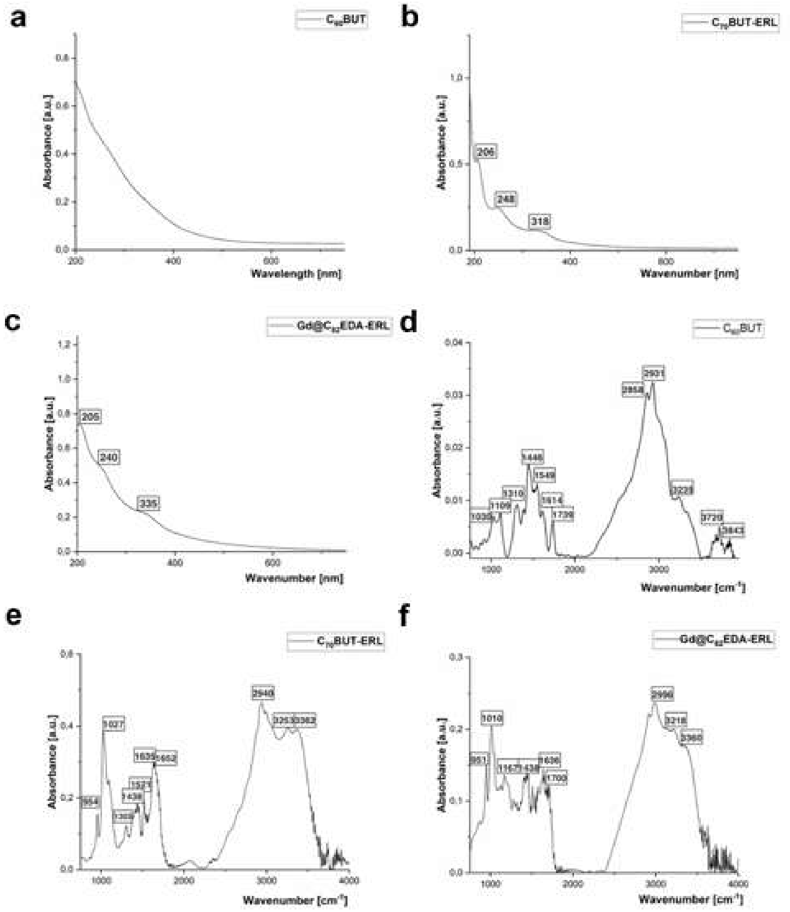

Figure 2. Spectroscopic characterization of synthesized aminofullerenes: UV-VIS spectra of obtained fullerene nanomaterials (a–c), and FT-IR spectra of synthesized compounds (d–f).

ERL fullerenes. The analysis of the chemical composition included the identification of elements, chemical bonding, and calculations of atomic concentrations. Trace contamination of silicon was observed in addition to the lines corresponding to the elements of the compound. These traces can be considered as resulting from synthetic impurities or sample preparation. Figure 3 shows the XPS spectra of the C 1s, N 1s, Cl 2p, and Gd 3d5/2 regions together with the corresponding deconvolution. The C 1s peak was decomposed into three or four lines, representing carbon atoms in various functional groups. The line with a binding energy of 284.9 eV indicates the presence of unoxidized graphitic carbon in the C-C, C=C, or C-H bonds [34]. The chemical state with a binding energy of 286.4 eV is associated with groups containing C-N and C-NH bonds. This line exhibits higher intensity for C_{70}BUT-ERL and Gd@C_{82}EDA-ERL fullerenes compared to the C_{60}BUT sample and may be additionally ascribed to the groups containing carbon-oxygen bonds (C-O). Furthermore, for these two samples, carbonyl C=O and C=N groups were identified by the third line at 288.4 eV [35]. The N 1s peak can be deconvoluted into three components. The first chemical state, occurring at the energy of 398.4 eV, is assigned to basic nitrogen of the pyridine type [36]. The second line observed at a binding energy of 399.8 eV is associated with the C-N and -NH bonds (free amino groups) in all fullerenes, as well as with the *N*-(C=O) bond and nitrogen atoms of the triazole ring in the C_{70}BUT-ERL and Gd@C_{82}EDA-ERL samples [37]. The third line localized at 401.5 eV is attributed to the partially protonated amino group $-NH_3^+$. This group is expected to be shifted to a higher binding energy compared to the original nitrogen due to the creation of a positive center [38]. The analysis of the N 1s spectrum depicted in Figure 3 revealed that the number of $-NH_3^+$ bonds calculated using the peak area ratio relative to the C-N, -NH bonds was comparable for the C_{60}BUT fullerene and decreased slightly in relation to C-N, -NH, N-N=N, *N*-(C=O) bonds for the C_{70}BUT-ERL and Gd@C_{82}EDA-ERL fullerenes. The Cl 2p peak could be fitted to one chlorine atom environment with binding energy values of 197.5 eV and

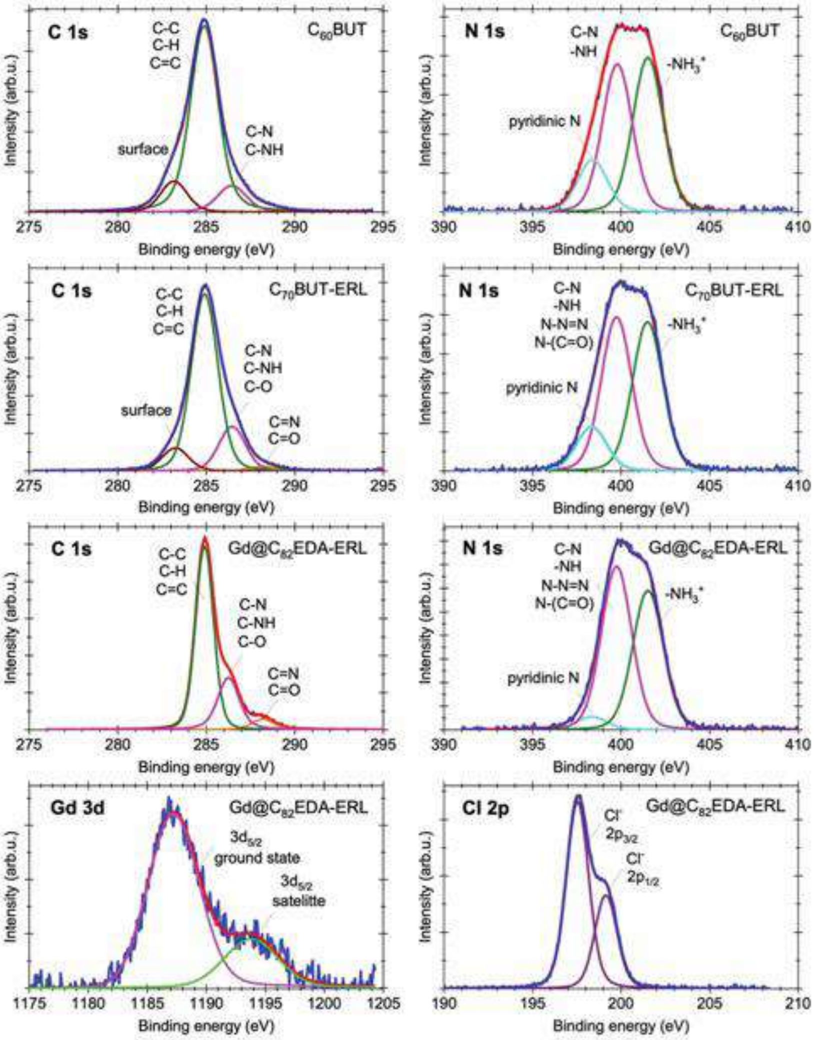

Figure 3. The XPS C 1s, N 1s, Gd 3d5/2, and Cl 2p lines of C_{60}BUT, C_{70}BUT-ERL, and Gd@C_{82}EDA-ERL fullerene derivatives.

199.1 eV for two lines splitting by spin-orbit interaction and corresponding to chloride anions presented in the fullerene nanomaterials [39]. Moreover, the XPS spectrum of the Gd 3d5/2 line for Gd@C_{82}EDA-ERL, located at 1187.0 eV, proves that fullerene C_{82} contains Gd inside the carbon core [40].

Interestingly the EDS results aligned with the elemental composition, including C, N, Gd, and O, providing additional confirmation of successful conjugation with ERL-COOH. Subsequent investigations aimed to understand the dispersion behavior of the obtained CNs in aqueous solutions, recognizing their paramount importance for future biological evaluations. Our findings revealed that C_{60}BUT nanomaterials demonstrated the propensity to form two distinct types of aggregates, with diameters of approximately 110 nm and significantly larger aggregates around 4400 nm (constituting about 1% of the aggregates, Figure S12). In contrast, C_{70}BUT-ERL samples predominantly formed smaller aggregates approximately 6.5 nm in diameter (representing about 5% of the aggregates), with the main fraction being around 140 nm (Figure S13). Moreover, the gadolinium-incorporated fullerenes exhibited the capability to form singular aggregate types with an average diameter of 200 nm. Importantly, for all synthesized aminofullerenes, the polydispersity index remained below 0.3, indicating a narrow size distribution.

3.2. Cytotoxicity assay

The potential of the synthesized fullerene nanomaterials for inhibition of the proliferation of three pancreatic cancer cell lines (PANC-1, PAN02, and AsPC-1) and a normal fibroblast cell line (NHDF) is presented in Figure 6(a). IC_{50} value for C_{60}BUT incubated with PANC-1 cell line equals 16.88 μM. This fullerene showed the highest effectiveness also against AsPC-1, with an IC_{50} value of 31.51 μM. For the mouse PAN02 cell line, the IC_{50}

value was 45.56 µM. IC_{50} values for C_{70}BUT-ERL fullerene for PAN02 and AsPC-1 cell lines amounted to 65–66 µM, while for PANC-1 was above 300 µM. Gadofullerene nanomaterial showed activity between 193.52 and above 425 µM. The ligand ERL-COOH exhibited the weakest activity with the IC_{50} values from 234.82 to 574.90 µM. Moreover, the nanomaterials tested showed much weaker activity against NHDF normal cells. The calculated IC_{50} values for C_{60}BUT and C_{70}BUT-ERL on fibroblast cells were 158.55 µM and 247.21 µM, respectively. While gadofullerene, ligand ERL-COOH, and erlotinib showed no activity.

3.3. Cell cycle inhibition

The impact of fullerene nanomaterials on the cell cycle progression in PAN02 and AsPC-1 cells was determined by flow cytometry. The results are presented in Figure 6(b), and representative histograms for each nanomaterial in Figure S16. For the PAN02 cell line incubated with C_{60}BUT and Gd@C_{82}EDA-ERL, a statistically significant increase (about 8–11% compared to the control) in the cell population in the G0/G1 phase was observed. For the AsPC-1 cell line an increase in the cell population in the G0/G1 phase was recorded in all cases.

3.4. Apoptosis induction

The potential of the tested materials to generate apoptosis in PAN02 and AsPC-1 was determined by Annexin V-FITC and 7-ADD staining using flow cytometry. The results are shown in Figure 6(c), with representative histograms depicted in Figure S17. In the PAN02 cells, the biggest increase (from 7.27% in control to 16.40%) in the population of the apoptotic cells was detected for Gd@C_{82}EDA-ERL at 320 µM. Greater increases were observed for the AsPC-1 cell line, with the biggest for C_{70}BUT-ERL at 67 µM, namely from 11% in control to 44.24%.

3.5. Western blot analysis

Basal levels of proteins associated with the EGFR signaling pathway were determinated by the Western Blot technique (Fig. S15). A high level of EGFR was detected in AsPC-1 and PANC-1 cell lines, with a high level of phospho-EGFR (Y1068) only for AsPC-1, in contrast to PAN02 cells with no expression of both proteins. An increased level of Akt and phospho-Akt (S473) was registered only for PANC-1 and PAN02 cell lines. In turn elevated level of IDH1 protein was observed for both PAN02 and AsPC-1 cell lines. Also, a high level of PI3K was detected in PAN02 cells.

Analysis of protein expression after incubation of pancreatic cells with the tested nanomaterials (Figure 7 and S18) indicates an increased level of $p27^{Kip1}$ in PAN02 cells treated by the C_{60}BUT and Gd@C_{82}EDA-ERL. For AsPC-1 cells, enhancement of the $p27^{Kip1}$ protein was also registered for the C_{60}BUT at 35 µM (5-fold increase), C_{70}BUT-ERL at 17 µM and Gd@C_{82} EDA-ERL at 160 µM (3-fold increase). All of the tested nanomaterials reduced the cyclin E1 activity by at least 2-fold in the AsPC-1 cell line. PARP cleavage was registered on the PAN02 cell line after treatment with Gd@C_{82}EDA-ERL, while it was not detected in the AsPC-1 cell line. A downregulation in mTOR protein levels after treatment with C_{60}BUT and C_{70}BUT-ERL was observed in PAN02 cells. Moreover, both nanomaterials reduced p-mTOR activation. In contrast incubation of both cell lines with gadofullerene caused an increase in mTOR and p-mTOR levels. The level of EGFR protein was markedly lower after incubation with C_{60}BUT (45 µM) and C_{70}BUT-ERL in mouse pancreatic cancer. P-EGFR expression was also reduced in PAN02 cells by all of the tested fullerenes, except C_{70}BUT-ERL (13 µM). For the second AsPC-1 cell line tested, the decrease in the concentration of these proteins was much lower. A reduction in the protein levels of Akt and phosphorylated Akt on serine 473 was observed after incubation with all of the tested fullerenes for both cell lines. Namely, C_{60}BUT resulted in more than 3-fold, while C_{70}BUT-ERL and Gd@C_{82} EDA-ERL induced a 6.5-fold decrease in p-Akt levels in the AsPC-1 cell line. In the case of PAN02 cell line, C_{60}BUT and C_{70}BUT-ERL induced over 1.5-fold decrease in p-Akt activation, while gadofullerene reduced expression by almost 4-fold. Reduced levels of PI3K p85 were detected in the PAN02 cells, while in the AsPC-1 it was not detected. Downregulation of PTEN was detected in PAN02 after incubation with C_{60}BUT and C_{70}BUT-ERL, and in AsPC-1 only for gadofullerene. IDH1 protein was decreased in PAN02 after treatment with C_{60}BUT and gadofullerene. Ras protein level in AsPC-1 cells treated with all of the tested fullerenes was reduced, except for C_{60}BUT (35 µM).

4. Discussion

The reaction of fullerene nanomaterials with amines can lead to the formation of structurally diverse compounds, depending on factors such as the reaction conditions, light illumination, type of amine, or catalyst [41–43]. For instance, primary amines have been shown to undergo reactions with the fullerene core, yielding straightforward multi-addition derivatives. Nonetheless, even minor alterations in the amine structure can facilitate the synthesis of various fulleropyrrolines. This phenomenon was observed in the reaction of [60]fullerene with β-substituted ethylamine derivatives in the presence of oxygen [44]. Moreover, it has been observed that a secondary amine can also undergo a single-step, multi-addition process with [60]fullerene under photochemical aerobic conditions, resulting in the formation of tetra(amino)fullerene epoxides [45]. However, numerous studies have shown that SET (single electron transfer)-facilitated excited-state addition reactions involving tertiary alkyl and aromatic amines with C_{60} are inefficient [46]. Aminofullerenes obtained from these reactions are extensively used in biomedical applications, such as drug delivery vehicles, photosensitizers for the inactivation of bacteria and viruses, and carriers of nucleic acids, including siRNA [47–49].

In the course of developing fullerene-derived inhibitors of EGFR protein, we decided to modify the structure of erlotinib by incorporating a carboxyl moiety within the triple bond fragment, taking into account the preservation of biological activity, in particular the interactions with the molecular target. Previously, Satpati and coworkers proposed modifications of the terminal alkyne function in the erlotinib structure to form ^{177}Lu-labeled erlotinib conjugates, without decreasing its efficacy as a tyrosine kinase inhibitor [50]. Building on our previous research on fluorescent fullerene triazoles, we used a copper-catalyzed azide-alkyne cycloaddition between the terminal alkyne fragment in the phenyl ring of erlotinib and 2-azidoacetic acid, to form erlotinib disubstituted 1,2,3-triazole derivative with carboxyl functional group (shown in Figure S1, alongside spectral characterization depicted in Figures S1-S3 within the Supporting Information) [51].

The process of conjugating water-soluble aminofullerenes (C_{60}BUT, C_{70}BUT, and Gd@C_{82}EDA) with erlotinib carboxylic acid was performed using one equivalent of water-soluble carbodiimide EDCI and *N*-hydroxysuccinimide. This ensured the nanoconjugation of one equivalent of the erlotinib derivative. This procedure was based on our previous work, where saturation of all available amines resulted in loss of solubility as well as stability of the obtained fullerene nanoconjugates. To purify the final aminofullerene nanoconjugates, we used membrane dialysis with dedicated membranes (molecular cutoffs 3k) to remove all small molecular impurities. The success of the ERL-COOH conjugation was confirmed using FT-IR and UV-VIS analysis. Unfortunately, we were not able to synthesize and further test the erlotinib conjugate with C_{60}BUT due to its extremely low water-solubility and stability of formed nanoconjugate. However, we decided to assess and describe its anticancer activity and model of action due to its very promising biological activity.

The morphological characteristics of chemically modified aminofullerenes and their nanoconjugates with ERL-COOH were systematically investigated using SEM and cryo-EM. Our observations revealed the formation of spherical aggregates in engineered CNs, particularly in C_{60}BUT (as depicted in Figure 4(a)) and the C_{70}EDA-ERL nanoconjugate (illustrated in Figure 4(b)). For larger fullerene cores such as gadolinium-containing fullerene Gd@C_{82}EDA-ERL, we detected the formation of fluffy aggregates and confirmed their derivatization through nanoscale elemental compositional analysis conducted *via* EDS mapping in the SEM, as depicted in Figure 4(d).

The use of water-soluble nanomaterials as theranostic agents has increased significantly. One area that has received particular attention is the use of engineered gadofullerenes (Gd@C_{82} and Gd_3N@C_{80}) and iron oxide nanoparticles [52,53]. Gadofullerene nanoparticles are highly effective in enhancing MRI relaxivity by one to two orders of magnitude, offering a substantial improvement over conventional method. They protect the encapsulated gadolinium atoms from metabolic degradation, which effectively reduces the risk of gadolinium leakage. Recent advances in synthetic methods, such as hydroxylation, Bingel-Hirsch, and Prato reactions, have enabled the formulation of water-soluble gadofullerenes that are highly biocompatible [21,54]. To assess the MRI-contrast properties of synthesized gadofullerene Gd@C_{82}EDA-ERL, we first measured the concentration of gadolinium in the sample using the TXRF method (Table S2). We then measured the T1 and T2 relaxation times of the synthesized gadofullerenes and calculated r_1 and r_2 relaxivities (Figure 5). It was found that the obtained nanotheranostic molecule Gd@C_{82}EDA-ERL had a relaxivity parameter r_1 of 7.15 $mM^{-1}s^{-1}$ (at 1 T), which was lower than that of previously described gadofullerenes containing β-alanine units (13 $mM^{-1}s^{-1}$). However, the r_1 values of the clinically used Gd chelates are much lower, generally about 3–6 $mM^{-1}s^{-1}$ under similar measurement conditions. Moreover, the described gadofullerenes contain conjugated small molecules with biological activity, making them truly theranostic nanomaterials.

4.1. Biological studies of aminofullerenes and their nanoconjugates with erlotinib derivative

Biological evaluation was carried out on synthesized fullerene nanomaterials to determine their antiproliferative activity on three pancreatic cancer cell lines, namely PANC-1, PAN02, and AsPC-1. The results are presented in Figure 6(a). Overall, C_{60}

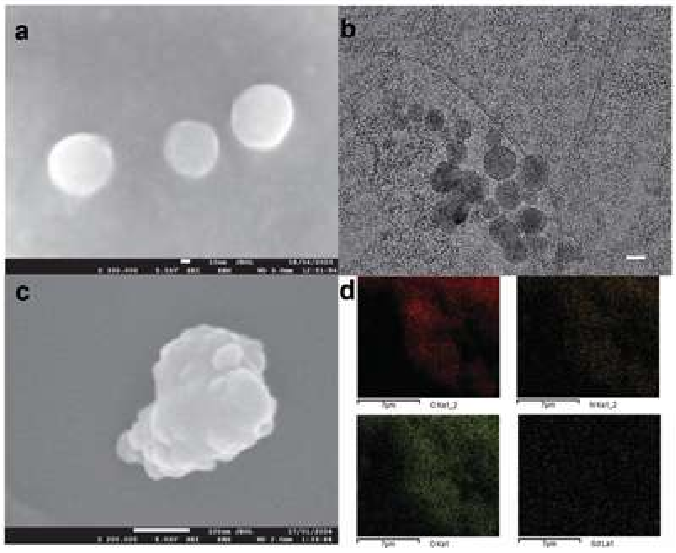

Figure 4. The SEM (a–c), cryo-EM (b, scale bar 20 nm), and EDS images (d) of synthesized aminofullerenes. The spherical aggregates of C_{60}BUT (a) and C_{70}BUT-ERL (b) as well as fluffy-type aggregates of Gd@C_{82}EDA-ERL (c) were observed.

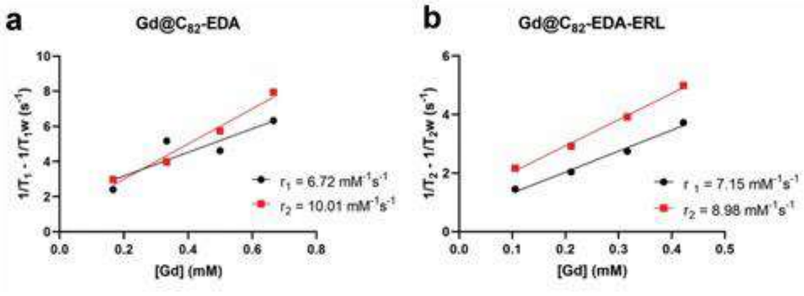

Figure 5. The r_1 and r_2 relaxivities of synthesized gadofullerenes.

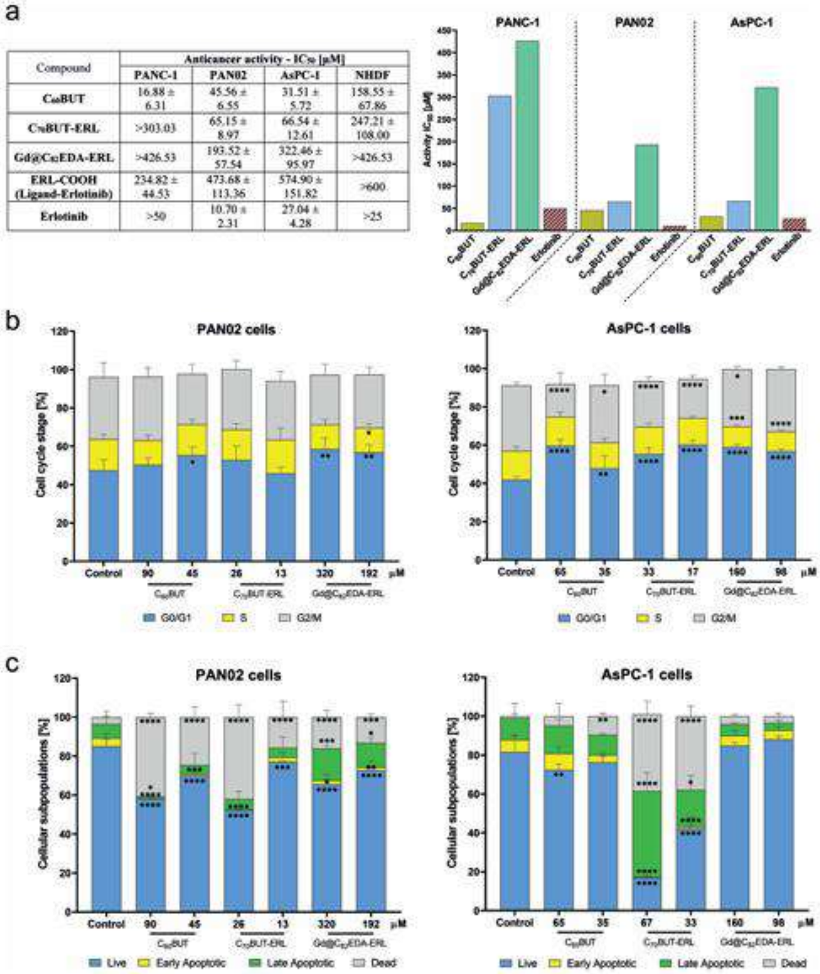

Compound	Anticancer activity - IC_{50} [µM]			
	PANC-1	PAN02	AsPC-1	NHDF
$C_{60}BUT$	16.88 ± 6.31	45.56 ± 6.55	31.51 ± 5.72	158.55 ± 67.86
$C_{70}BUT$-ERL	>303.03	65.15 ± 8.97	66.54 ± 12.61	247.21 ± 108.00
Gd@C_{82}EDA-ERL	>426.53	193.52 ± 57.54	322.46 ± 95.97	>426.53
ERL-COOH (Ligand-Erlotinib)	234.82 ± 44.53	473.68 ± 113.36	574.90 ± 151.82	>600
Erlotinib	>50	10.70 ± 2.31	27.04 ± 4.28	>25

Figure 6. The antiproliferative activity of tested nanomaterials (C_{60}BUT, C_{70}BUT-ERL, and Gd@C_{82}EDA-ERL), ligand ERL-COOH and erlotinib against pancreatic cells: PANC-1, PAN02, AsPC-1, and NHDF (a). The impact of tested nanomaterials on the progression of cell cycle (b) and apoptosis induction (c) in PAN02 and AsPC-1 cells. Statistical analysis was performed using one-way ANOVA with Dunnett's post hoc test: $^*p < 0.05$, $^{**}p < 0.01$, $^{***}p < 0.001$, $^{****}p < 0.0001$ compared with the untreated cells (control).

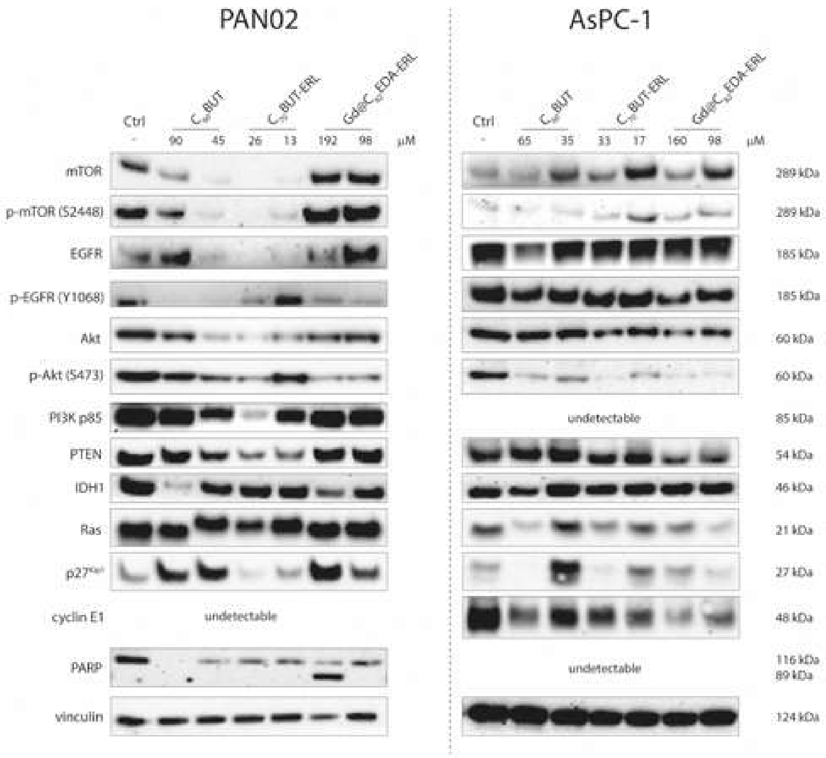

Figure 7. The level of protein expression after exposure to fullerene nanomaterials: C_{60}BUT, C_{70}BUT-ERL, and Gd@C_{82}EDA-ERL in PAN02 and AsPC-1. Densitometric analyses of these results as well as uncropped and unmodified blots were provided in the Supporting Information.

BUT showed the highest efficacy against all tested cancer cells. In particular, this fullerene was most effective against human PANC-1 cells, with an IC_{50} value of 16.88 μM. Interestingly, the FDA-approved EGFR inhibitor, erlotinib, was not effective (IC_{50} >50 μM). It is important to note that PANC-1 cells were resistant to other tested nanomaterials, C_{70}BUT-ERL and Gd@C_{82} EDA-ERL. For the second tested human pancreatic cancer cell line, AsPC-1, the antiproliferative activity of C_{60}BUT was similar to erlotinib, with IC_{50} values of 31.51 μM for fullerene and 27.04 μM, respectively. However, for mouse PAN02 cells, erlotinib was more effective (IC_{50} = 10.7 μM). Although C_{60}BUT had more than 4-fold lower efficacy than erlotinib, it still displayed high activity (IC_{50} = 45.56 μM). Moreover, the C_{70}BUT-ERL fullerene, with conjugated erlotinib, exhibited good antiproliferative activity against PAN02 and AsPC-1 cells (IC_{50} = 65–66 μM). On the other hand, the gadofullerene nanomaterial primarily inhibited cell proliferation of the murine pancreatic cells (IC_{50} = 193.52 μM), while being more resistant against both human pancreatic cancers. It is worth noting that the ligand ERL-COOH, which is erlotinib with triazole group with carboxyl function attached to phenyl ring (instead of ethynyl group), subsequently linked to C_{70} and Gd@C_{82} aminofullerenes, showed negligible activity, especially in PAN02 and AsPC-1 cell lines. It is worth noting that our nanomaterials had a high specificity against pancreatic cancer cells.

We conducted further studies on the molecular mechanism of action of the three nanomaterials- C_{60}BUT, C_{70}BUT-ERL, and Gd@C_{82}EDA-ERL – to understand their impact on cell cycle progression, apoptosis induction, and regulation of EGFR cell signaling pathway. For this, we used two pancreatic cancer cell lines – PAN02 and AsPC-1—based on the activity of tested nanomaterials and the landscape of basal protein expression levels. Our Western Blot experiments confirmed large diversity in the expression proteins associated with the EGFR signaling pathway in tested pancreatic cancer cells (Figure S15). Namely, the AsPC-1 cells show a high level of EGFR and phospho-EGFR (Y1068) expression, while their expression is relatively deficient in the PAN02 cells. Of note, the observation of high EGFR receptor expression in AsPC-1 cells has been confirmed in reports [55,56]. The complete opposite pattern is observed in the basal expression levels of Akt and phospho-Akt (S473) in these pancreatic cell lines. Both PAN02 and AsPC-1 cells display elevated expression of the IDH1 protein (compared to PANC-1), which is one of the components of the tricarboxylic acid cycle and is involved in cellular metabolism, proliferation, and energy production [57]. Interestingly, we detected a very high level of PI3K expression in PAN02 cells, while it was absent in the AsPC-1 cell line. In light of this diversification, the behavior of the tested nanomaterials in cells is crucial for understanding the interactions of signaling networks, which may have implications for therapeutic efficacy and further potential clinical relevance.

The impact of fullerenes on the cell cycle progression and apoptosis induction in PAN02 and AsPC-1 cells was determined using flow cytometry. The charts are presented in Figures 6(b,c), and representative histograms for each nanomaterial in Figures S16-S17. Our results showed that the tested fullerenes arrested the cell cycle in the G0/G1 phase (Figure 6(b)). In PAN02 cells, the C_{60}BUT and gadofullerene induced a statistically significant increase in the cell population in the G0/G1 phase by about 8%–11% compared to the control (untreated cells), with a simultaneous decrease in the number of cells in S and G2/M phases. Interestingly, a greater degree of inhibition was observed in AsPC-1 cells. Treatment with C_{60} BUT at 65 µM caused a significant increase in the percentage of cells in the G0/G1 phase from 41.93% (in control) to 59.73%. Similar effects were observed in AsPC-1 cells after administration of C_{70}BUT-ERL at 17 µM and Gd@C_{82}EDA-ERL at 160 µM. It is worth noting that our previous studies on the anticancer activity of glycofullerenes did not indicate their effect on cell cycle inhibition, despite their ability to inhibit tyrosine kinase and redox imbalance [58]. Therefore, we determined the expression of $p27^{Kip1}$ and cyclin E1 in cells after exposure to tested fullerenes. Both proteins are closely related to the ability of the cell cycle to enter from the G0/G1 to the S phase. The activity of the cyclin E1-cdk2 complex can be inhibited by $p27^{Kip1}$, which is a negative regulator of the cell cycle and blocks the transition to the DNA synthesis phase [59]. As depicted in Figure 7, the C_{60}BUT induced a more than 2-fold increase in the expression of $p27^{Kip1}$ in PAN02 cells. In addition, this protein was almost 3.5-fold upregulated after exposure to Gd@C_{82}EDA-ERL.

After incubation with tested nanomaterials, the $p27^{Kip1}$ protein level was found to be higher in AsPC-1. The C_{60}BUT at 35 µM induced a marked 5-fold increase in the expression of cyclin-dependent kinase inhibitor, while the C_{70}BUT-ERL at 17 µM and Gd@C_{82}EDA-ERL at 160 µM caused a more than 3-fold enhancement of p27 production (Figures 7 and S18). Since there were more prominent changes in cell cycle inhibition in AsPC-1 cells, we also examined the compounds' effect on cyclin E1 expression. As expected, all of the tested fullerenes reduced the cyclin E1 activity by at least 2-fold. These results are consistent with flow cytometry measurements and prove that aminofullerenes have a significant effect on arresting the cell cycle in the G0/G1 phase.

The studies on apoptosis were performed using Annexin V-FITC and 7-ADD staining to detect early and late apoptotic cell populations. Annexin V is an important protein marker of the onset of apoptotic cell death that binds with phosphatidylserine, which is a phospholipid that changes its location from the inner side of the cell membrane to the outer surface side during the early phase of apoptosis. Thus, the cellular protein Annexin V conjugated with a fluorescence dye can bind to it. Our data indicate clear changes in live and dead populations in the PAN02 cells. However, the percentage of cells in the early and late apoptosis phases was quite low (Figure 6(c)). For example, the number of cells in the late apoptosis phase increased from 7.27% in control to 16.40% after treatment with Gd@C_{82}EDA-ERL at 320 µM. A similar situation was observed in AsPC-1 cells, with one exception. C_{70}BUT-ERL at 67 µM induced a significant increase in the population of late apoptotic cells from 11% in control to 44.24%.

Protein analysis unequivocally indicates that after treatment with Gd@C_{82}EDA-ERL, cleaved PARP was registered on the PAN02 cell line (Figure 7). The results coincide with flow cytometer data where an increase in apoptotic cells was observed in the PAN02 line despite moderate levels, in contrast to the AsPC-1 cell line where (except in one case) the increase was negligible and PARP cleavage was not registered in Western Blot. Nevertheless, it seems that apoptosis is not the primary type of cell death induced by tested fullerenes. Instead, autophagic cell death may be more relevant. In our previous reports, glycofullerenes and glycine-derived [60]fullerene could activate autophagosome formation and induce autophagy through the regulation of LC3 and p62 [58,60]. Zhang et al. also described the role of the Nano-C_{60} in inducing ROS-dependent autophagy and doxorubicin chemosensitization in Hela cells by regulating Atg5 expression [61]. The activation of autophagy flux through up-regulation of cathepsin D, which caused cyclin D1 degradation and G0/G1 cell cycle arrest, has been reported for C_{70}-EDA [26]. Interestingly, the functionalization of the surface of fullerenes may determine their special properties, as well as the induction of the cell death mechanism through apoptosis or autophagy [62].

The role of autophagy induction in cancer treatment is still controversial. However, recent reports have suggested that this therapeutic approach may be effective as it positively regulates and promotes the immune response [63]. One of the crucial complexes that regulate the survival signaling pathway and block autophagy stimulation is mTOR. To investigate this, we analyzed the expression of this protein and the activation of p-mTOR after treatment with tested nanomaterials at the cellular level (Figure 7). We observed a downregulation in mTOR protein levels after treatment with C_{60}BUT and C_{70}BUT-ERL in PAN02 cells. Additionally, both fullerenes induced a significant reduction in p-mTOR activation. C_{60}BUT (45 µM) and C_{70}BUT-ERL (26 µM) showed a 4-fold and 7.6-fold decrease in phosphorylation of mTOR at the serine 2448 site, respectively. In AsPC-1 cells, we also detected reduced levels of p-mTOR protein after exposure to C_{60}BUT at higher concentrations. Surprisingly, both protein levels increased after exposure to gadofullerene in PAN02 and AsPC-1 cell lines.

We proceeded to analyze the impact of C_{60}BUT, C_{70}BUT-ERL, and Gd@C_{82}EDA-ERL on the regulation of the EGFR protein and its downstream pathway targets such as Akt, p-Akt, PI3K, and PTEN. The activation of EGFR/Akt signaling can mediate cellular responses and influence mTOR expression to control metabolism, proliferation, cell size, survival, and motility [64]. The results are presented in Figure 7, and the densitometric analyses of the tested proteins are depicted in Figure S18. It is noteworthy that the effect of the tested nanomaterials on the total level of EGFR and its activation was much higher in mouse pancreatic cancer than in the case of AsPC-1. In PAN02 cells, the total level of EGFR protein was markedly lower after incubation with C_{60}BUT and C_{70}BUT-ERL. In the second cell line tested, there were less noticeable changes only after administration of C_{60}BUT at a concentration of 65 µM. The activation of EGFR by tyrosine phosphorylation at the 1068 site was significantly inhibited by all of the tested fullerenes in PAN02 cells. The highest inhibitory effect was observed for C_{60}BUT at both tested concentrations (10-fold decrease). C_{70}BUT-ERL (26 µM) and gadofullerene (98 µM) caused a 2-fold reduction in p-EGFR protein expression.

Once EGFR is activated, the main effectors of its signaling cascade are Akt and PI3K proteins. As expected, a reduction in the protein levels of Akt and phosphorylated Akt on serine 473 was observed after incubation with fullerenes. C_{60}BUT and C_{70} BUT-ERL induced over 1.5-fold decrease in p-Akt activation, while gadofullerene reduced expression by almost 4-fold.

Interestingly, fullerenes had a greater impact on p-Akt levels in AsPC-1 cells. Specifically, C_{60}BUT resulted in more than 3-fold, while C_{70}BUT-ERL and Gd@C_{82}EDA-ERL induced at least a 6.5-fold decrease in p-Akt levels. In addition, slightly reduced levels of PI3K p85 were detected in PAN02 cells. Notably, the PI3K activation leads to the transformation of phosphatidylinositol 4,5-bisphosphate (PIP2) to phosphatidylinositol 3,4,5-trisphosphate (PIP3), which mediates the direct launch of Akt signaling [65]. There were also interesting changes observed for the PTEN protein, which acts as an antagonist of PI3K activity. The use of C_{60} BUT and C_{70}BUT-ERL in PAN02 led to the downregulation of PTEN.

In contrast, gadofullerene caused a reduction of PTEN levels in AsPC-1. This reduction should have allowed Akt signaling to

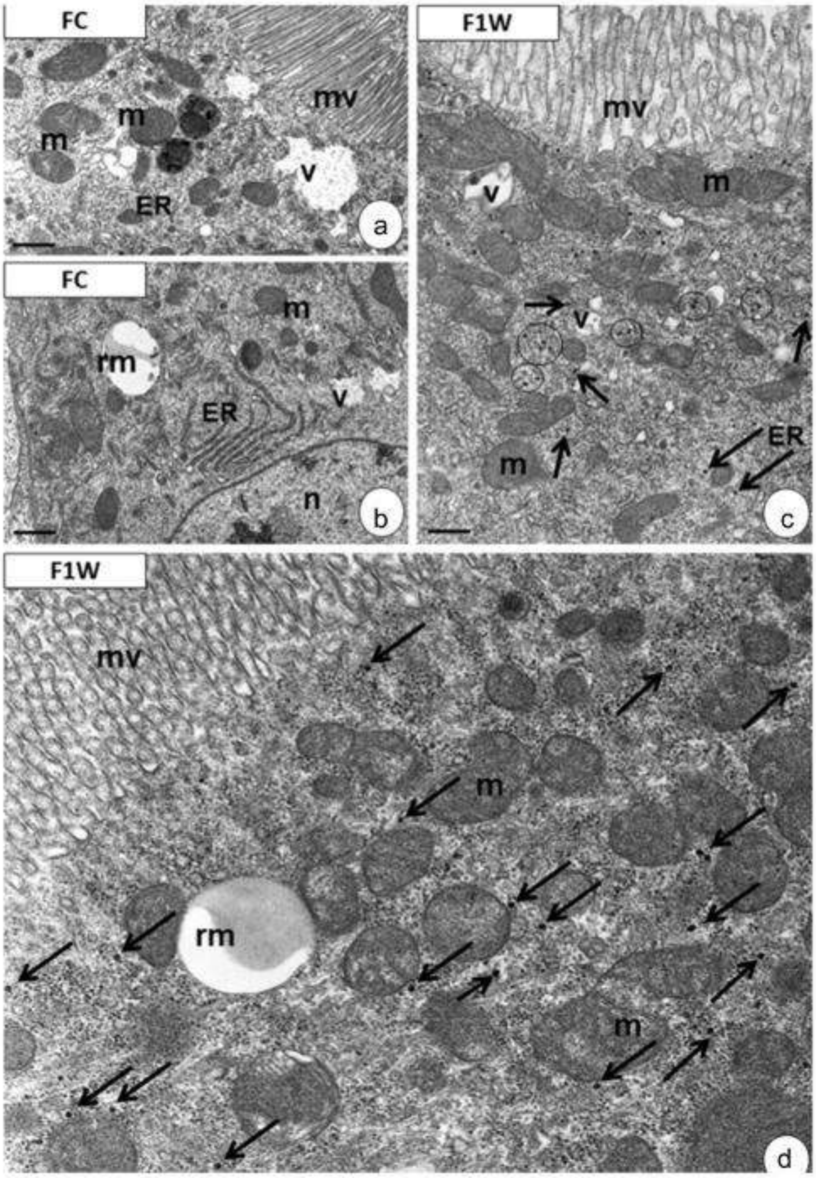

Figure 8. Midgut of *D. melanogaster*. (a-b) FC group (control group). Apical (a) and perinuclear (b) cytoplasm of midgut enterocytes. (c-d) F1W experimental group. Specimens fed with fullerenes for 1 week. Mitochondria (m), microvilli (mv), nucleus (n), cisterns of endoplasmic reticulum (ER), vesicles (v), reserve material (rm), electron-dense granules (black arrows). (a) Scale bar = 1.2 µm. (b) Scale bar = 1.2 µm. (c) Scale bar = 1 µm. (d) Scale bar = 0.8 µm.

be maintained. However, it was noted that due to the multilevel impact of fullerenes and their ability to interact with and inhibit the entire EGFR/Akt/mTOR signaling pathway, it may induce its suppression.

Moreover, IDH1 and Ras proteins play pivotal roles in cellular metabolism and the regulation of proliferation. In PAN02, we observed a significant decrease in IDH1 expression following treatment with C_{60}BUT and gadofullerene. Notably, the Ras protein, alongside other proteins within the RAF-MEK-ERK-MAPK signaling pathway, serves as a critical mediator of the EGFR response. The interaction of ERK and MAPK proteins with various substrates initiates cellular responses regulating cell growth, proliferation, differentiation, and apoptosis evasion [66]. Additionally, Ras protein can bind to PI3K via the p110 subunit, influencing the activation of cellular events associated with the Akt pathway [67]. Our analyses revealed that the tested fullerenes can modulate the Ras protein levels in AsPC-1 cells. Specifically, C_{60}BUT and gadofullerene caused a more than 2.5-fold reduction in Ras expression, while C_{70}BUT-ERL decreased protein levels to a slightly lesser extent. However, significant changes were not observed in mouse pancreatic cells. Comparing the complexity of the regulation of cellular molecules and pathways, as well as the rate of cellular responses, despite the lack of clear changes in the AsPC-1 cell line, it appears that fullerenes can suppress EGFR signaling pathway activity, as evidenced by substantial changes in p-Akt and Ras protein activity.

In further toxicological research at the *in vivo* level, we chose to study the gadofullerene Gd@C_{82}EDA-ERL nanomaterial due to its potential for translational studies (Figure 8). We used the fruit fly model (*Drosophila melanogaster*) for this purpose, as it has a short lifespan and is an excellent choice for genetic and cell biology research [68]. However, there are limited studies on how water-soluble fullerene nanoparticles interact with fruit flies [31]. We observed no changes in cell ultrastructure in the midgut epithelium of *D. melanogaster* individuals (males and females) compared to the control group (Figures 8(a,b)). All organelles had the correct structure. After one week of the experiment, TEM revealed the presence of electron-dense, homogenous granules distributed throughout the cytoplasm (Figures 8(c,d)). These granules were not observed in the cytoplasm of midgut enterocytes of control specimens.

5. Conclusions

In summary, we have successfully created versatile fullerene nanomaterials and their conjugates with erlotinib derivative to improve the treatment accuracy for pancreatic cancer. Our innovative aminofullerenes C_{60}BUT, C_{70}BUT-ERL, and Gd@C_{82} EDA-ERL formed spherical or fluffy-type aggregates in water. The structures were confirmed using several spectroscopic techniques such as FT-IR, NMR, UV-VIS, XPS, and high-resolution ESI MS. We also conducted detailed biological analysis of fullerene nanomaterials of *in vitro* and *in vivo* models. Cytotoxicity studies on pancreatic cancer cell lines revealed high anticancer activity of C_{60}BUT and C_{70}BUT-ERL. The C_{60}BUT nanomaterial showed similar biological activity to erlotinib (IC_{50} in the range of 16–45 μM). Further cellular studies on PAN02 and AsPC-1 cell lines showed the ability of the tested fullerene nanomaterials to arrest the cell cycle in the G0/G1 phase, which was also confirmed by changes in the expression of p27 and cyclin E1 proteins. Moreover, induction of cell death by autophagy for C_{60}BUT and C_{70}BUT-ERL and apoptosis for Gd@C_{82}EDA-ERL were indicated. Most importantly, we revealed the impact of the tested fullerene nanomaterials on the inhibition of the EGFR signaling pathway by reducing the expression of p-EGFR, p-Akt, PI3K, and Ras proteins. Finally, we confirmed the lack of toxicity of Gd@C_{82}EDA-ERL on *Drosophila melanogaster*.

Disclosure statement

The authors have no relevant affiliations or financial involvement with any organization or entity with a financial interest in or financial conflict with the subject matter or materials discussed in the manuscript. This includes employment, consultancies, honoraria, stock ownership or options, expert testimony, grants or patents received or pending, or royalties.

No writing assistance was utilized in the production of this manuscript.

Author Contributions

Conceptualization: MS and KM; methodology: KM, JK, AMW, MSz, FH, TS, MRR, MS; investigation: PR, DD, KK, KMał and AH; funding acquisition: MS and KM; project administration: MS; supervision: AMW, MS, RM; writing – review & editing: KM, JK, MSz, AMW, MRR, RM and MS. All authors reviewed the data and analysis.

Funding

This work was supported by National Science Centre (Poland) grants [2019/35/B/NZ5/04208 (KM) and 2019/35/B/NZ7/02459 (MS)].

ORCID

Magdalena Rost-Roszkowska http://orcid.org/0000-0001-7124-8423
Maciej Serda http://orcid.org/0000-0003-4926-5782

References

Papers of special note have been highlighted as either of interest (•) or of considerable interest (••) to readers.

1. Kamisawa T, Wood LD, Itoi T, et al. Pancreatic cancer. The Lancet. 2016;388(10039):73–85.
2. Klein AP. Pancreatic cancer epidemiology: understanding the role of lifestyle and inherited risk factors. Nat Rev Gastroenterol Hepatol. 2021;18(7):493–502.
3. Yu S, Zhang C, Xie K-P. Therapeutic resistance of pancreatic cancer: Roadmap to its reversal. Biochim Et Biophys Acta (BBA)-Rev On Cancer. 2021;1875(1):188461.
4. Chand S, O'Hayer K, Blanco FF, et al. The landscape of pancreatic cancer therapeutic resistance mechanisms. Int J Biol Sci. 2016;12 (3):273.
5. Qin C, Yang G, Yang J, et al. Metabolism of pancreatic cancer: paving the way to better anticancer strategies. Mol Cancer. 2020;19(1):1–19.
6. Springfeld C, Jäger D, Büchler MW, et al. Chemotherapy for pancreatic cancer. La Presse Medicale. 2019;48(3):e159–e174.
7. Sigismund S, Avanzato D, Lanzetti L. Emerging functions of the EGFR in cancer. Mol Oncol. 2018;12(1):3–20.
8. Dorman K, Boeck S, Snijder RJ, et al. Integrated analysis of the RASH study with the use of the "Burden of Therapy"(BOTh® TM) methodology—a novel tool for assessing adverse events in metastatic pancreatic cancer. Curr Oncol. 2023;30(6):5828–5834.

9. Wang JP, Wu C-Y, Yeh Y-C, et al. Erlotinib is effective in pancreatic cancer with epidermal growth factor receptor mutations: a randomized, open-label, prospective trial. Oncotarget. 2015;6(20):18162.
10. Desai N. Nanoparticle Albumin-Bound Paclitaxel (Abraxane®). In: Albumin in Medicine. Singapore: Springer; 2016. p. 101–119.
11. Passero FC Jr, Grapsa D, Syrigos KN, et al. The safety and efficacy of Onivyde (irinotecan liposome injection) for the treatment of metastatic pancreatic cancer following gemcitabine-based therapy. Expert Rev Anticancer Ther. 2016;16(7):697–703.
12. Gong H, Peng R, Liu Z. Carbon nanotubes for biomedical imaging: the recent advances. Adv Drug Deliv Rev. 2013;65(15):1951–1963.
13. Saleem J, Wang L, Chen C. Carbon-based nanomaterials for cancer therapy via targeting tumor microenvironment. Adv Healthc Mater. 2018;7(20):1800525.
14. Yan L, Zhao F, Li S, et al. Low-toxic and safe nanomaterials by surface-chemical design, carbon nanotubes, fullerenes, metallofullerenes, and graphenes. Nanoscale. 2011;3(2):362–382.
15. Maggini M, Scorrano G, Prato M. Addition of azomethine ylides to C60: synthesis, characterization, and functionalization of fullerene pyrrolidines. J Am Chem Soc. 1993;115(21):9798–9799.
16. Muñoz A, Sigwalt D, Illescas BM, et al. Synthesis of Giant Globular Multivalent Glycofullerenes as Potent Inhibitors in a Model of Ebola Virus Infection [Article]. Nat Chem. 2015;8:50.
17. Illescas BM, Pérez-Sánchez A, Mallo A, et al. Multivalent cationic dendrofullerenes for gene transfer: Synthesis and DNA complexation. J Mater Chem B. 2020;8(20):4505–4515.
18. Liu Y, Chen C, Qian P, et al. Gd-metallofullerenol nanomaterial as non-toxic breast cancer stem cell-specific inhibitor. Nat Commun. 2015;6(1):5988.

•• **The studied gadofullerene nanomaterial $Gd@C_{82}(OH)_{22}$ exhibits negligible toxicity towards normal mammary epithelial cells yet demonstrated pronounced inhibitory effects on triple-negative breast cancer cells. Moreover, $Gd@C_{82}(OH)_{22}$ effectively disrupted the epithelial-to-mesenchymal transition, leading to the efficient eradication of breast cancer stem cells.**

19. Kang S-G, Zhou G, Yang P, et al. Molecular mechanism of pancreatic tumor metastasis inhibition by $Gd@C_{82}(OH)_{22}$ and its implication for de novo design of nanomedicine. Proc Natl Acad Sci USA. 2012;109(38):15431–15436.
20. Liu Y, Jiao F, Qiu Y, et al. The effect of Gd@ C82 (OH) 22 nanoparticles on the release of Th1/Th2 cytokines and induction of tnf-α mediated cellular immunity. Biomaterials. 2009;30(23–24):3934–3945.
21. Toth E, Bolskar RD, Borel A, et al. Water-soluble gadofullerenes: toward high-relaxivity, pH-responsive MRI contrast agents. J Am Chem Soc. 2005;127(2):799–805.

••• **The first example of water-soluble gadofullernes used as MRI contrast agent.**

22. Li X, Wang C. The potential biomedical platforms based on the functionalized Gd@ C82 nanomaterials. View. 2020;1(1):e7.
23. Fatouros PP, Shultz MD. Metallofullerenes: a new class of MRI agents and more? Nanomedicine. 2013;8(11):1853–1864.
24. Li J, Wang T, Feng Y, et al. A water-soluble gadolinium metallofullerenol: facile preparation, magnetic properties and magnetic resonance imaging application. Dalton Trans. 2016;45(21):8696–8699.
25. Shu C-Y, Zhang E-Y, Xiang J-F, et al. Aggregation studies of the water-soluble gadofullerene magnetic resonance imaging contrast agent: [gd@ C82O6 (OH) 16 (NHCH2CH2COOH) 8] x. The J Phys Chem B. 2006;110(31):15597–15601.
26. Zhang X, Zhou W, Liu Y, et al. Nanosize aminated fullerene for autophagic flux activation and G0/G1 phase arrest in cancer cells via post-transcriptional regulation. Nano Res. 2022;15:1–10.
27. Zhang B, Yang L, Jin Y, et al. Ferritin-based supramolecular assembly drug delivery system for aminated fullerene derivatives to enhance tumor-targeted therapy. Adv Sci. 2024;2413389.
28. Zhou W, Huo J, Yang Y, et al. Aminated fullerene abrogates cancer cell migration by directly targeting myosin heavy chain 9. ACS Appl Mater Interface. 2020;12(51):56862–56873.

• **The myosin heavy chain 9, a critical molecular target for C_{70}EDA, was identified here via experimental screening. It specifically binds to the tail domain near the C-terminal end of MYH9, probably attributed to the electrostatic interaction between cationic fullerene and the negatively charged region on the C-terminal.**

29. Serda M, Ware MJ, Newton JM, et al. Development of Photoactive Sweet-C60 for Pancreatic Cancer Stellate Cell Therapy. Nanomedicine (Lond). 2018;13(23):2981–2993.
30. Dyke J, Groves A, Morris A, et al. Study of the thermal decomposition of 2-azidoacetic acid by photoelectron and matrix isolation infrared spectroscopy. J Am Chem Soc. 1997;119(29):6883–6887.
31. Dreszer D, Szewczyk G, Szubka M, et al. Uncovering nanotoxicity of a water-soluble and red-fluorescent [70]fullerene nanomaterial. Sci The Total Environ. 2023;879:163052.

•• **The water-soluble and red-fluroescent [70]fullerene derivative produces reactive oxygen species after illumination and shows no toxicity on fruit fly model.**

32. Rost-Roszkowska M, Poprawa I, Chajec Ł, et al. Influence of soil contaminated with cadmium on cell death in the digestive epithelium of soil centipede Lithobius forficatus (Myriapoda, Chilopoda). The Eur Zoological J. 2020;87(1):242–262.
33. Rost-Roszkowska M, Poprawa I, Chajec Ł, et al. Effects of cadmium on mitochondrial structure and function in different organs: studies on the soil centipede Lithobius forficatus (Myriapoda, Chilopoda). The Eur Zoological J. 2021;88(1):632–648.
34. Yu J, Guan M, Li F, et al. Effects of fullerene derivatives on bioluminescence and application for protease detection. Chem Commun. 2012;48(89):11011–11013.
35. Li C, Cui R, Feng L, et al. Synthesis of a UCNPs@ SiO 2@ gadofullerene nanocomposite and its application in UCL/MR bimodal imaging. RSC Adv. 2016;6(101):98968–98974.
36. Serda M, Gawecki R, Dulski M, et al. Synthesis and applications of [60] fullerene nanoconjugate with 5-aminolevulinic acid and its glycoconjugate as drug delivery vehicles. RSC Adv. 2022;12 (11):6377–6388.
37. Avdeev YG, Nenasheva TA, Luchkin AY, et al. Thin 1, 2, 4-triazole films for the inhibition of carbon steel corrosion in sulfuric acid solution. Coatings. 2023;13(7):1221.
38. Cao T, Huang P, Zhang K, et al. Interfacial engineering via inserting functionalized water-soluble fullerene derivative interlayers for enhancing the performance of perovskite solar cells. J Mater Chem A. 2018;6(8):3435–3443.
39. Wilson M, Kore R, Ritchie A, et al. Palladium–poly (ionic liquid) membranes for permselective sonochemical flow catalysis. Colloids and surfaces A: physicochemical and engineering aspects. 2018;545:78–85.
40. Jana D, Maikap S, Prakash A, et al. Enhanced resistive switching phenomena using low-positive-voltage format and self-compliance IrO x/GdO x/W cross-point memories. Nanoscale Res Lett. 2014;9:1–8.
41. Wu J, Liu C-X, Wang H-J, et al. Cu (OAc) 2-mediated reaction of [60] fullerene with aldehydes and primary amines for the synthesis of fulleropyrrolines. J Org Chem. 2016;81(19):9296–9307.
42. Sun YP, Liu B, Lawson GE. Photochemical Preparation of Highly Water-Soluble Pendant [60] Fullerene-Aminopolymers. Photochem Photobiol. 1997;66(3):301–308.
43. Serda M, Szewczyk G, Krzysztynska-Kuleta O, et al. Developing [60] Fullerene Nanomaterials for Better Photodynamic Treatment of Non-Melanoma Skin Cancers. ACS Biomater Sciamp; Eng. 2020;6 (10):5930–5940.
44. Xiang J-J, Huang C, Wang H-J, et al. Metal-free-mediated synthesis of fulleropyrrolines by the reaction of [60] fullerene with β-substituted ethylamines. New J Chem. 2017;41 (17):8725–8728.
45. Isobe H, Tomita N, Nakamura E. One-step multiple addition of amine to [60] fullerene. synthesis of tetra (amino) fullerene epoxide under photochemical aerobic conditions. Org Lett. 2000;2 (23):3663–3665.
46. Lim SH, Yi J, Moon GM, et al. Method for the synthesis of amine-functionalized fullerenes involving set-promoted

photoaddition reactions of α-silylamines. J Org Chem. 2014;79 (15):6946–6958.

47. Korzuch J, Rak M, Balin K, et al. Towards Water-soluble [60] Fullerenes for the Delivery of SiRNA in a Prostate Cancer Model. Sci Rep. 2021;11(1):1–10.
48. Zhang J, Xu J, Ma H, et al. Designing an amino-fullerene derivative C70–(EDA) 8 to fight superbacteria. ACS Appl Mater Interface. 2019;11(16):14597–14607.
49. Kazemzadeh H, Mozafari M. Fullerene-based delivery systems. Drug Discov Today. 2019;24(3):898–905.
50. Jain A, Kumar A, Vasumathy R, et al. Preparation of radiolabeled erlotinib analogues and analysis of the effect of linkers. Bioorg Med Chem Lett. 2022;76:128995.
51. Serda M, Malarz K, Korzuch J, et al. In Situ Cellular Localization of Nonfluorescent [60] Fullerene Nanomaterial in MCF-7 Breast Cancer Cells. ACS Biomater Sciamp; Eng. 2022;8(8):3450–3462.
52. Han Z, Wu X, Roelle S, et al. Targeted gadofullerene for sensitive magnetic resonance imaging and risk-stratification of breast cancer. Nat Commun. 2017;8(1):692.
53. Wei H, Bruns OT, Kaul MG, et al. Exceedingly small iron oxide nanoparticles as positive MRI contrast agents. Proc Natl Acad Sci. 2017;114(9):2325–2330.
54. Wang L, Zhu X, Tang X, et al. A multiple gadolinium complex decorated fullerene as a highly sensitive T 1 contrast agent. Chem Commun. 2015;51(21):4390–4393.
55. Durkin AJ, Bloomston PM, Rosemurgy AS, et al. Defining the role of the epidermal growth factor receptor in pancreatic cancer grown in vitro. The Am J Surg. 2003;186(5):431–436.
56. Patra CR, Bhattacharya R, Wang E, et al. Targeted delivery of gemcitabine to pancreatic adenocarcinoma using cetuximab as a targeting agent. Cancer Res. 2008;68(6):1970–1978.
57. Ni Y, Shen P, Wang X, et al. The roles of IDH1 in tumor metabolism and immunity. Future Oncol. 2022;18(35):3941–3953.
58. Serda M, Malarz K, Mrozek-Wilczkiewicz A, et al. Glycofullerenes as Non-receptor Tyrosine Kinase Inhibitors-Towards Better Nanotherapeutics for Pancreatic Cancer Treatment. Sci Rep. 2020;10 (1):1–11.
59. Xu X, Nakano T, Wick S, et al. Mechanism of Cdk2/Cyclin E inhibition by p27 and p27 phosphorylation. Biochemistry. 1999;38(27):8713–8722.
60. Malarz K, Korzuch J, Marforio TD, et al. Identification and biological evaluation of a water-soluble fullerene nanomaterial as BTK kinase inhibitor. Int J Nanomedicine. 2023;18:1709–1724.
61. Zhang Q, Yang W, Man N, et al. Autophagy-mediated chemosensitization in cancer cells by fullerene C60 nanocrystal. Autophagy. 2009;5(8):1107–1117.
62. Wong C-W, Zhilenkov AV, Kraevaya OA, et al. Toward understanding the antitumor effects of water-soluble fullerene derivatives on lung cancer cells: Apoptosis or autophagy pathways? J Med Chem. 2019;62(15):7111–7125.
63. Long X, Yan J, Zhang Z, et al. Autophagy-targeted nanoparticles for effective cancer treatment: advances and outlook. NPG Asia Mater. 2022;14(1):71.
64. Wee P, Wang Z. Epidermal growth factor receptor cell proliferation signaling pathways. Cancers (Basel). 2017;9(5):52.
65. Carnero A, Blanco-Aparicio C, Renner O, et al. The PTEN/PI3K/AKT signalling pathway in cancer, therapeutic implications. Curr Cancer Drug Targets. 2008;8(3):187–198.
66. Roberts PJ, Der CJ. Targeting the Raf-MEK-ERK mitogen-activated protein kinase cascade for the treatment of cancer. Oncogene. 2007;26(22):3291–3310.
67. Krygowska AA, Castellano E. PI3K: a crucial piece in the RAS signaling puzzle. Cold Spring Harb Perspect Med. 2018;8(6):a031450.
68. Vecchio G. Afruit fly in the nanoworld: once again Drosophila contributes to environment and human health. Nanotoxicology. 2014:135–137.

Author's academic achievements

Personal data:
Julia Korzuch
address: ul. Kochanowskiego 3a/12, 43-100 Tychy, Poland
e-mail: julia.korzuch@us.edu.pl
phone number: +48510696643

Education:
2014-2017 – BSc in medicinal chemistry, University of Silesia in Katowice
2017-2019 – MSc in chemistry, University of Silesia in Katowice
2019 – now – PhD studies in Doctoral School at University of Silesia in Katowice

Publications:

1. Serda M., Szewczyk G., Krzysztyńska-Kuleta O., Korzuch J., Dulski M., Musiol R., Sarna T., (2020) Developing [60]fullerene nanomaterials for better photodynamic treatment of non-melanoma skin cancer, *ACS Biomaterials Science & Engineering,* 6, 5930-5940.

2. Korzuch J., Rak M., Balin K., Zubko M., Głowacka E., Dulski M., Musioł R., Madeja Z., Serda M., (2021) Towards water-soluble [60]fullerenes for efficient siRNA delivery in a prostate cancer model, *Scientific Reports,* 11, 10565.

3. Serda M., Malarz K., Korzuch J., Szubka M., Zubko M., Musioł R. (2022) In situ cellular localization of non-fluorescent [60]fullerene nanomaterial in MCF-7 breast cancer cells, *ACS Biomaterials Science and Engeneering,* 8, 3450–3462.

4. Malarz K, Korzuch J, Marforio TD, Balin K, Calvaresi M, Mrozek-Wilczkiewicz A, Musiol R, Serda M., (2023) Identification and Biological Evaluation of a Water-Soluble Fullerene Nanomaterial as BTK Kinase Inhibitor, *Int J Nanomedicine*, 18:1709-1724.

5. Serda M, Korzuch J, Dreszer D, Krzykawska-Serda M, Musioł R., (2023) Interactions between modified fullerenes and proteins in cancer nanotechnology, *Drug Discovery Today*, (9):103704.

6. Malarz K, Korzuch J, Mrozek-Wilczkiewicz A, Szubka M, Rurka P, Małota K, Herraiz A, Dreszer D, Kocot K, Herranz F, Rost-Roszkowska M, Sun T, Musioł R, Serda M., (2025) Aminofullerenes as targeted inhibitors of EGFR: from pancreatic cancer inhibitors to *Drosophila m*. Toxicology, *Nanomedicine* (Lond) 20(6):585-601.

Patent applications:

1. Fullerene nanomaterials factionalized with 5-aminolevulenic acid - synthesis and application thereof, Polish Patent Application, P.437483.

2. Fullerene glycoconjugate functionalized with 5-aminolevulinic acid, preparation and application thereof, Polish Patent Application, P.437482.

Internship:
07-09.2019 internship in “i-petrol” Sp. z.o.o. Katowice
09.2022 University of Bologna, Italy, Matteo Calvaresi research team

Conferences:

1. XLVIII Winter School “From proton to proteome”; XLVIII Winter School FBBB Jagiellonian University, Kraków, 11 13.02.2021; Developing [60]fullerene nanomaterials for better photodynamic treatment of non-melanoma skin cancer; poster

2. Paul Ehrlich (PE) Euro-PhD Network virtual meeting; 19-24.07.2021; Water-soluble aminofullerenes as efficient delivery agents for siRNA transfection; poster

3. Elimination of the Polish representative to make a statement at 8th EFMC-YMCS; PTChem, 15.05.2021; Water-soluble aminofullerenes for siRNA transfection and photodynamic therapy; presentation

4. 3th International Workshop on Functional Nanostructured Materials 3 –FuNaM3, Faculty of Chemistry Jagiellonian University in Krakow, Kraków, 6-8.10.2021, Water-soluble aminofullerenes as efficient delivery agents for siRNA transfection, poster

5. XV Copernican Seminar of Doctoral Students, Nicolaus Copernicus Univeristy in Toruń, 20-22.06.2022 Toruń; Opracowanie metody lokalizacji komórkowej materiału fullerenowego na ludzkim modelu raka piersi; poster

6. 10th EFMC Young Medicinal Chemists' Symposium, 7-8.09.2023 Zagrzeb, In Situ Cellular Localization of Nonfluorescent [60]Fullerene Nanomaterial in MCF-7 Breast Cancer Cells, poster

7. Young Research Fellows Meeting YRFM, 26-28.02.2025 Paryż, The novel aminofullerenes targeting epidermal growth factor receptor. From pancreatic cancer inhibition to toxicological studies on the Drosophila m. model, poster

Outside activities

Athlete on the Polish national team (400m hurdles); represented Poland at the 2023 European Team Championships

Multiple-time medalist at the Polish National Championships in 400m hurdles

Passionate about blues and rock music, literature enthusiast